University of the Witwatersrand, Johannesburg
School of Mechanical, Industrial and Aeronautical Engineering

MECN 7018: MSc Research Project

Oil Film Interferometry Visualisation of Surface Flow Patterns Generated by Impinging Jets

Author: Louis Biebuyck (0506398W)

Supervisor: Prof. B. W. Skews

I Declaration

I hereby declare that, unless otherwise stated or referenced, all work contained within this report is that of myself, Louis Pierre Biebuyck, student number 0506398W, ID number 8606015167089.

Signature______________________ Date _______________

II Abstract

The main purpose of the investigation detailed here was to determine whether or not oil film interferometry techniques could be applied to impinging sonic and supersonic flows. Experimentation was limited to the flow fields generated by impinging jets emanating from convergent nozzles with square and rectangular cross sections. The impingement plate was coated with polished aluminium sheeting to provide the required reflective surface. Interferometry images were generated by the application of Dow Corning PMX 200 silicone fluid to the plate, which was illuminated by a monochromatic sodium light source. Images were captured using a Nikon D90 DSLR camera with a standard 18-55mm lens. The shear force at various points on the plate was determined by analysing the resultant images using the MATLAB image processing toolbox. The experimental results were then compared to results from CFD simulations that were carried out using the Fluent components of ANSYS v.13. A quantitative examination of the two sets of results revealed that the experimental results were consistently lower than the shear forces predicted by CFD simulations, particularly in the high shear areas near the centre of impingement. However, a qualitative examination of the interferometry images showed interesting results. These images gave a good representation of the overall flow patterns over the plate, with clearly defined fringe patterns visible in the oil coating. Therefore the investigation discussed here was determined to be a successful proof of concept for the utilisation of oil film interferometry techniques in this application. It is believed that the methodology utilised in this investigation can be successfully developed to significantly improve the accuracy of the quantitative results.

III Table of Contents

IV List of Figures

V List of Tables

VI List of Equations

VII Nomenclature

P_0 – Inlet Pressure

P_∞ – Atmospheric Pressure, Back Pressure

P_e – Pressure at Nozzle Exit

NPR – Nozzle Pressure Ratio

n – Distance from Nozzle Exit to Impingement Plate

d – Nozzle Exit Diameter

n/d – Ratio of Plate Distance to Nozzle Diameter

h – Oil Height

t – Run Time

τ_x – Shear Force in x-direction

τ_z – Shear Force in z-direction

μ_0 – Oil Viscosity

ρ – Oil Density

V – Oil Volume

$\%_V$ – Oil Volume Percentage

W – Oil Weight

$\%_W$ – Oil Weight Percentage

k – Positive Integer Multiplication Factor

λ_0 – Light Wavelength

n_1 – Refractive Index of Air

n_f – Refractive Index of Oil

θ_i – Angle of Incidence of Light

a – Speed of Sound

γ – Specific Heat Ratio

R – Specific Gas Constant

T – Temperature

μ = Fluid dynamic viscosity

$\frac{\partial v}{\partial x}$ = Velocity gradient in the direction of flow

1 Introduction

1.1 Background and Motivation

The impingement of an under-expanded sonic jet onto a flat surface has been the subject of research for a number of years, and has possibilities for application in a number of fields: During the takeoff and landing phases of Vertical Take Off and Landing (VTOL) aircraft, such as the Harrier and the F35 Lightning II, the impingement of airflow from the lift nozzles creates flow patterns that can adversely affect the performance of the engines and the overall lift generated. When launching missiles and rockets, the impingement of the high-temperature, high-pressure jet often causes significant damage to the launch platform. Having a better understanding of the flow patterns of these impinging jets could allow for better nozzle and air intake designs in VTOL aircraft and better ways to redirect the most damaging parts of the jet flow during rocket launches.

Jet impingement is not only utilized in the aerospace sector. In manufacturing, a high energy air jet is used to deposit metal particles onto a substrate. Understanding the impingement process could help make this process more effective and efficient. New high performance computers utilize jet impingement to increase the heat flux through CPU heat exchangers. Whilst the majority of these use water as the working fluid, a lot of the basic impingement flow fields observed in subsonic air jet impingement can be extended to water jets.

Until recently, investigations into the behaviour of impinging jets have been limited to the case of jets emanating from axisymmetric nozzles. Studies performed by Donaldson and Snedeker [1], Carling and Hunt [2], Kalghatgi and Hunt [3], and Lamont and Hunt [4] have provided important insight into the pressure and velocity distributions over the impingement surface as well as the flow patterns in and around the impingement area.

Although understanding the behaviour of axisymmetric jets is important, there are many cases where the impinging flows originate from non-axisymmetric nozzles. However, as stated above, there has not been much focus on the behaviour of these flows. Previous work performed by Menon and Skews has given important insight into the flow fields generated by the impingement of square jets [5] as well as the structure of jets emanating from rectangular nozzles [6]. Their work has shown that non-axisymmetric nozzles generate complex, three-dimensional flow patterns in the jet core as well as over the impingement surface.

In order to better understand the flow patterns observed by Menon and Skews, as well as that of other non-axisymmetric jets, the behaviour of the airflow over the impingement surface needs to be visualised. Several methods have been used previously to visualise the flow fields on the impingement surface. These methods usually involve coating the impingement surface with a brightly-coloured, viscous fluid. Although these methods have produced promising results, the visualisations are often blurred, and subject to interpretation.

Another important limitation of these visualisation methods is that they only generate qualitative results and yield no numerical data about the flow patterns over the surface. This problem can be solved by drilling pressure ports in the surface and attaching a manometer or data acquisition system to gather pressure data. Although this method generates positive results, it is complex and time-consuming to set up and introduces inconsistencies in the surface that can adversely affect the flow pattern and skew the results. A second method that has recently seen increased use is that of pressure sensitive paints (PSP). These paints contain crystals that effect a colour change when subjected to an increase in pressure. Once again, this method has yielded positive results in the past and has the added benefit of not introducing any obstacles that could affect the flow pattern. Unfortunately these PSP’s are prohibitively expensive for use in the current study.

The method of flow visualisation that was of particular interest for this study was that of oil film interferometry. This method utilises the principles of thin film interference to determine the variation in thickness of a film of oil covering a surface. This information can in turn be used to determine the shear-force experience by the oil due to the flow of air over the surface.

Since this method of visualisation relies on constructive and destructive interference of light, there is no need to alter the surface of interest to allow for mounting of pressure transducers or any other electronic instrumentation. This method is therefore relatively inexpensive and, more importantly, has minimal effect on the usual flow patterns over the surface.

Oil film interferometry is a well-established method for flow visualisation over a surface. However it has seen limited use in the field of jet impingement. That being said, it was used successfully by Davy, Alvi and Naughton [7] to generate data on surface flow patterns of micro-supersonic impinging jets. Although this study was limited to investigating jets originating from axisymmetric nozzles with a maximum diameter of 1000µm, all the underlying principles are the same as those of the current study.

1.2 Statement of Task

Develop a method to generate images of the flow fields on a flat plate generated by an impinging, non-axisymmetric sonic jet. These images should allow for the generation of both qualitative and quantitative data about the flow fields over the surface.

1.3 Project Scope

As discussed above, there are numerous flow visualisation methods available for use in such an investigation. However due to the relative simplicity and low cost, it was decided that the oil film interferometry technique was most promising and therefore would be the focus of this study.

The initial aim of this investigation was to utilise the methodology set out by Davy and Alvi to generate similar interferograms on a macro scale using a 10mm diameter nozzle. Provided that this set of experiments yielded positive results, the set up would then be modified to allow for the capture of real-time images during the impingement process. This set of interferograms would allow for the visualisation of the three main phases of the impingement process, namely start-up, steady-state operation, and shutdown. This methodology would then be utilised to generate data about the impingement of non-axisymmetric jets.

2 Objectives

- Develop a method to successfully capture images of fringes on a reflective plate after impingement from an axisymmetric nozzle.
- Extend this method to allow for capture of images during the impingement process. This includes the start-up, steady-state and shutdown phases of the jet flow.
- Utilise this methodology to capture images of impingement of non-axisymmetric jets at various and plate distances and nozzle pressure ratios.
- Develop an image processing algorithm based on work done by Davy, Alvi and Naughton [7], and Decker and Naughton [8] to analyse interferometry images.
- Cross-check experimental results with results from Computational Fluid Dynamics simulations to determine that accuracy and validity of the CFD models as well as the image processing algorithm.

3 Literature Review

3.1 The Free Jet

Consider a convergent nozzle secured to the end of an outlet from a pressure vessel, in which the pressure can be varied as desired (illustrated in Figure 3-1 below). The nozzle is vented to atmosphere, providing a sink of constant pressure. If the pressure in the vessel (P_0) is greater than atmospheric pressure (P_∞), the net pressure difference will cause air to flow from the pressure vessel, through the outlet and nozzle, into the atmosphere.

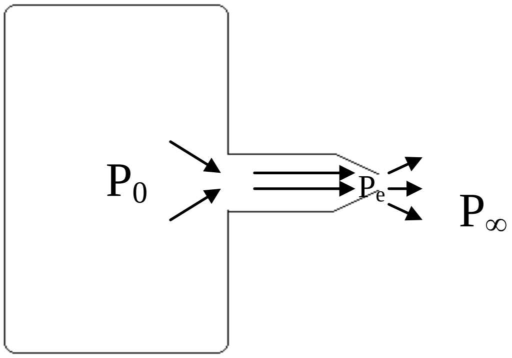

Figure 3-1: Schematic drawing of high pressure vessel with a convergent nozzle fitted to the outlet

As the air flows through the convergent nozzle, the decrease in area forces the airflow to accelerate in order to maintain a constant mass flow rate. This results in a high-velocity air jet forming at the nozzle exit. For subsonic flows, the velocity of this jet is determined by the pressure difference between the vessel and the atmosphere, since the pressure at the nozzle exit (P_e) must be equal to the back pressure in the exit plane, in this case atmospheric pressure, P_∞. Therefore, as P_0 is increased, the velocity of the jet also increases, since the air needs to undergo a larger decrease in pressure before it reaches the exit plane.

This increase in exit velocity with increased inlet pressure continues until the flow at the nozzle exit reaches sonic conditions. This occurs at a pressure ratio of 1.8929. This is known as the Critical Pressure Ratio, since it is the limiting condition for flow through convergent nozzles. The critical pressure ratio is given in Equation 3-1 below.

$$\frac{P_0}{P_\infty} = 1.8929$$

Equation 3-1

An examination of the continuity and conservation equations shows that for a purely convergent nozzle it is impossible for the flow velocity at the exit plane to accelerate past Mach 1. Since any further increase in the pressure ratio across the nozzle will not result in an increase in flow velocity, the nozzle is considered to be 'Choked'.

Once the nozzle has been choked, the pressure ratio between the inlet and the nozzle exit remains at the critical pressure ratio. The pressure at the exit plane can thus be determined by Equation 3-2:

$$P_e = \frac{P_0}{1.8929}$$

Equation 3-2

Thus any further increase in the inlet pressure past the sonic condition results in the exit pressure being greater than the atmospheric pressure. The ratio between nozzle exit pressure and atmospheric pressure is defined as the nozzle pressure ratio (NPR) and is given by Equation 3-3.

$$\boldsymbol{NPR = \frac{P_e}{P_\infty}}$$

Equation 3-3

Where:
NPR – Nozzle Pressure Ratio
P_e – Pressure at the Nozzle Exit
P_∞ – Back Pressure

The nozzle pressure ratio, as defined above, can be used to classify the type of flow pattern that will be obtained:

If NPR=1, the jet is considered to be perfectly expanded. The exit pressure is equal to the back pressure and the flow does not have to go through any compression or expansion. The flow along the central axis of the jet remains constant at Mach 1 for the entire extent of the jet core. This is the ideal case and the jet behaves exactly like a subsonic jet, with no complex flow patterns in the jet core, as is shown in Figure 3-2 (a) below. Unfortunately this case is extremely difficult to obtain in reality, since any pressure fluctuation in either the inlet or back pressure will result in the flow field moving into either the subsonic region or becoming under-expanded.

If NPR<1, the jet is classified as being over-expanded. In this case, since the exit pressure P_e is less that the back pressure P_∞, the jet core is initially forced inwards by the higher P_∞. In an attempt to equalise this pressure difference the air flow in the jet core goes through a series of shock waves and expansion fans until the jet core has fully mixed with the surrounding atmosphere. However since the back pressure must be higher than the exit pressure for this type of flow to occur, these over-expanded jets are not very common.

Therefore only the more common case of the under-expanded sonic jet will be considered further in this study. A sonic jet is considered to be under-expanded when the exit pressure P_e is greater than the back pressure P_∞, resulting in a pressure ratio greater than 1. Under-expanded flows can be classified further depending on this pressure ratio, namely moderately under-expanded and highly under-expanded. The flow patterns generated by these conditions are illustrated schematically in Figure 3-2 below, along with a subsonic jet for comparison purposes:

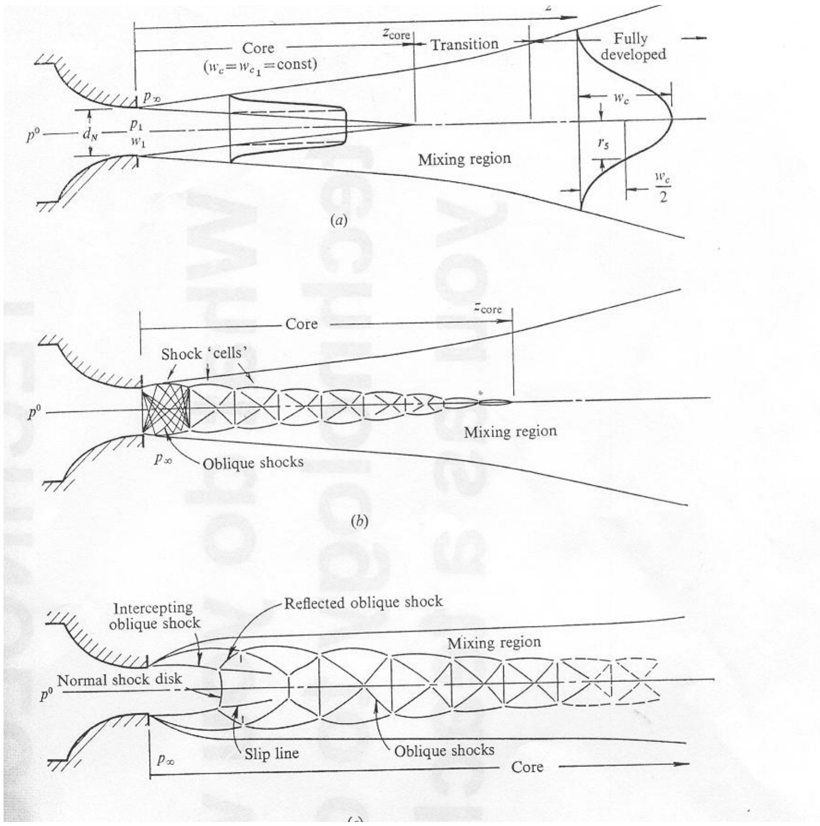

Figure 3-2: Schematic drawing showing the structure of (a) subsonic jets, (b) moderately under-expanded jets and (c) highly under-expanded jets. [1]

The subsonic jet (Figure 3-2 a), occurs for pressure ratios of P_∞/P_0 between 1 and 0.528. This is characterised by a core region, surrounded by a mixing region in which a portion of the jet mixes with the surrounding fluid. Moving downstream of the nozzle exit, the size of the jet core decreases as the mixing region spreads inwards towards the centre line of the jet, until it eventually reaches the centre of the jet and the core no longer exists. Beyond this point the mixing region continues to grow as the velocity decreases until the air in the jet matches atmospheric conditions[1].

The moderately under-expanded jet (Figure 3-2 b) occurs with under-expansion ratios of between 1 and 2 (1<PR<2). As the airflow exits the nozzle, it passes through a series of expansion fans to try to bring the pressure down to match atmospheric conditions through acceleration. As the air passes through these expansion fans it is turned away from the jet centre line. In order to turn the flow back towards the centre line, it must pass through a second set of expansion fans that emanate from the intersection point of the first set of expansion fans. Since the air has now passed through two sets of expansion fans of similar strength, the pressure is now lower than the back pressure. The necessary increase in pressure results in the formation of a set of shock waves, angled towards the jet centre. These shocks meet at the jet centre and reflect back towards the jet boundary as a second set of shock waves. However the air pressure downstream of these shocks is now higher than the back pressure, leading to the formation of further expansion fans [9].

This process of successive expansion and recompression result in the characteristic diamond pattern that can often be seen in the jet plume of rockets and missiles. This flow pattern is clearly illustrated in the first two rows of images in Figure 3-3 below. The first two rows of images also show the increase in the length of the shock cells or ‘diamonds’ as the under-expansion ratio is increased from 1 to 2. The formation of these shock cells continues, with ever decreasing magnitude, until the jet flow reaches equilibrium with the surrounding atmosphere [1].

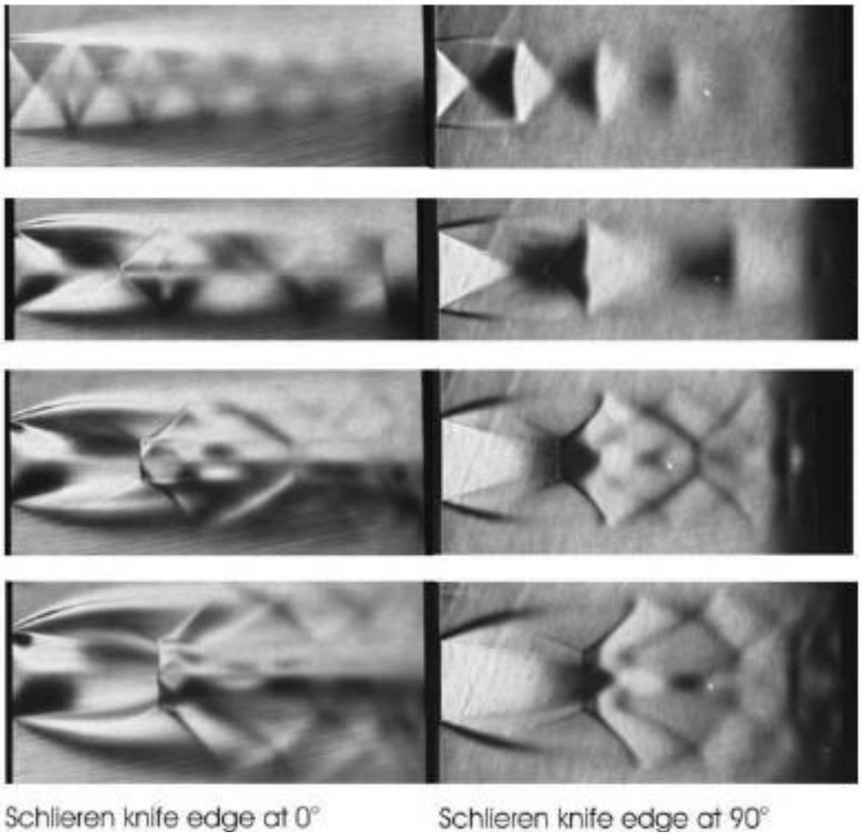

Figure 3-3: Schlieren photographs of the flow patterns in an under expanded jet [5]

The highly under-expanded jet (Figure 3-2 c) occurs with under-expansion ratios greater than 2. At higher under-expansion ratios the intersecting shock waves within the core undergo Mach reflection rather than regular reflection. This is characterised by the occurrence of a normal shock, or 'Mach disk', within the first shock cell. A highly under-expanded jet is defined by the occurrence of this Mach disk [6].

The formation of this normal shock in the jet causes an area of subsonic flow immediately behind the Mach disk. The large difference in airflow velocities between this subsonic region and the surrounding supersonic regions leads to the complex flow patterns that can be seen in the last two rows of images in Figure 3-3. At very high under-expansion ratios a second, weaker Mach disk can occur within the second shock cell [1].

As can be seen from the figures above, the behaviour of under-expanded jets is well understood and has been the focus of research for a number of years. However the vast majority of these studies have been limited to the study of jets emanating from axisymmetric nozzles. It was not until recently that studies were performed on non-axisymmetric jets. Numerical and experimental studies performed by Menon and Skews investigated the flow structures of jets issuing from square [5] and rectangular nozzles [6]. Along the major and minor axis of the jets, the flow features were shown to be the same as for an axisymmetric jet, as is evident in Figure 3-3 above. However, along the diagonal axis the jets were shown to behave as over-expanded jets, with convergent shock waves forming at the corners of the nozzle exits.

3.2 Impinging Jets

Now consider the case of a jet as described above being directed onto a flat plate. In the case of the axisymmetric jet, there are three distinct flow regions that can be observed:

As the jet reaches the surface the flow is forced to decelerate rapidly. This deceleration is most prevalent in the jet core where the air is bounded by the plate in front of it and high-velocity airflow surrounding it in the mixing region. Since this air has nowhere to go, it forms a bubble of slowly recirculating air known as the **Recirculation Zone**. At the very centre of the recirculation zone, the air cannot flow in any direction along the plate due to the surrounding flow and is thus forced to decelerate to zero flow velocity, generating the **Stagnation Point.** The bubble formed by the recirculation zone acts as a secondary boundary for the airflow entering the vicinity of the impingement zone. Thus the airflow on the outside of the jet core as well as in the mixing region is deflected around the recirculation zone and forced to flow along the plate surface, forming the **Wall Jet**. Since the recirculation zone forms a convex boundary for the air, this portion of the flow is not decelerated as much or as rapidly as the initial flow that formed the recirculation zone. Thus the airflow in the wall jet retains most of its initial flow velocity. Since the boundary formed by the recirculation zone is not solid, some of the air flowing into the area from the jet core enters the recirculation zone. But since the zone is bounded by the wall jet, it cannot grow any further. Thus to maintain mass flow, some air must exit the recirculation zone. This air exiting the zone must rapidly accelerate to match the flow velocity of the wall jet.

In the case of sonic flows there are two more flow patterns that appear as a result of the compressible nature of these types of flows (as shown in Figure 3-4 below). Because air in the jet is flowing at a velocity of Mach 1 or greater, rapid deceleration that occurs within the recirculation zone results in the formation of a normal shockwave at or above the boundary of the recirculation zone. This normal shock is known as the **Standoff Shock**. The second flow field that results from the sonic nature of the jet is the formation of a wall expansion fan at the boundary between the recirculation zone and the wall jet. This expansion fan forms when the air exiting the recirculation zone accelerates rapidly to join the sonic or supersonic wall jet.

When considering axisymmetric jets, all the flow regions described above have a predictable circular pattern, as shown in Figure 3-5 below. However as soon as the jet nozzle is anything but circular, the flow regions occur along specific lines of symmetry, which are usually aligned with either the main or diagonal axes of the jet nozzle. Figure 3-6 below, taken from Menon and Skews [5], shows the impingement zone of a jet emanating from a square convergent nozzle. As is shown in the image, the impingement zone exhibits some interesting flow patterns. As well as the expected stagnation point at the centre, four other stagnation points occur farther out into the impingement zone. These extra stagnation points are aligned with the main axes of the jet nozzle. Emanating out from the central stagnation point, along the diagonal axes of the nozzle, are four lines of recirculation.

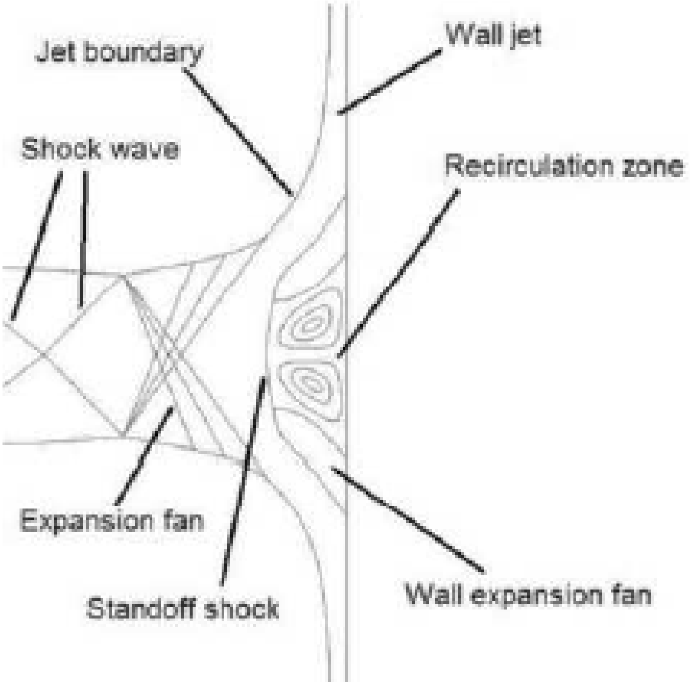

Figure 3-4: Schematic representation of the impingement zone for a jet with PR = 2 [5]

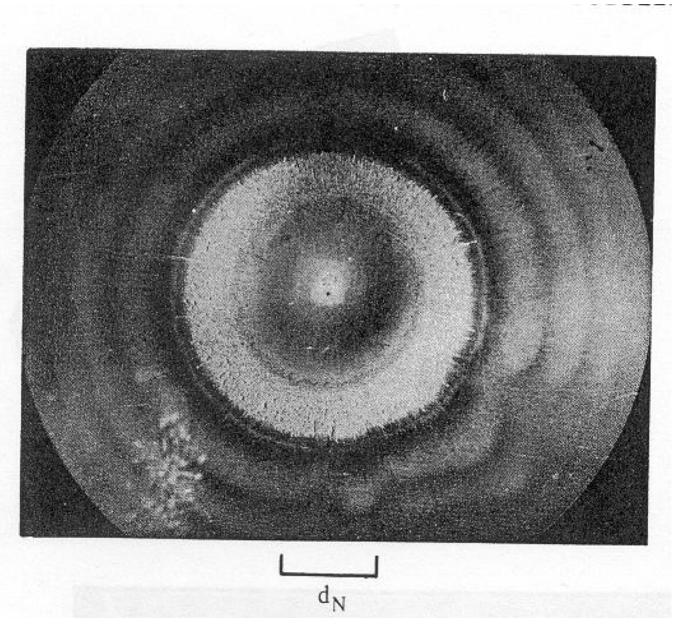

Figure 3-5: Photograph of impingement plate with oil flow visualisation [3]

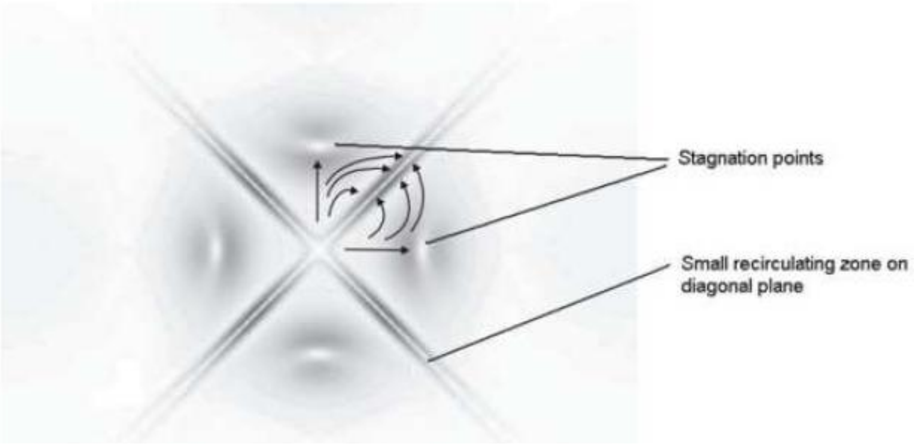

Figure 3-6: Numerical Schlieren of flow patterns on the impingement plate, PR=3, square nozzle [5]

3.3 Flow Visualisations

As mentioned in the project scope section above, it was decided that this investigation would focus on utilising the method of oil film interferometry to generate experimental data.

Consider a drop of clear oil on a smooth, reflective surface. The surface is held horizontal, ensuring the force of gravity acts uniformly in all directions. The oil is also of sufficient viscosity such that the spreading of the drop over the surface is slow enough to be ignored. Thus the oil drop can be considered to be stationary. This oil drop is then subjected to airflow parallel to the surface upon which the drop sits.

The oil will be subjected to a shear force due to the airflow and will begin to spread out along the surface in the direction of the air flow. This is represented by the diagram in Figure 3-7. Obviously the higher the shear force, and the lower the viscosity of the oil, the more the oil will spread out. Thus if the thinning rate of the oil is known, the shear force acting on the oil due to the air flow can be determined. Therefore the first step in utilising the oil film interferometry method is to develop an expression relating the shear force acting on the oil to other known properties. The thin film equation below, taken from Brown and Naughton [10], gives the relationship between oil thickness (h), oil viscosity (μ_0) and shear force (τ). The full derivation of this equation can be found in Appendix A.

$$\frac{\partial h}{\partial t}+\frac{\partial}{\partial x}\left(\frac{\tau_x h^2}{2\mu_0}\right)+\frac{\partial}{\partial z}\left(\frac{\tau_z h^2}{2\mu_0}\right)=0$$

Equation 3-4

Where:

h – oil thickness

t – run time

τ_x – shear force in the x-direction

τ_z – shear force in the z-direction

μ_0 – oil viscosity

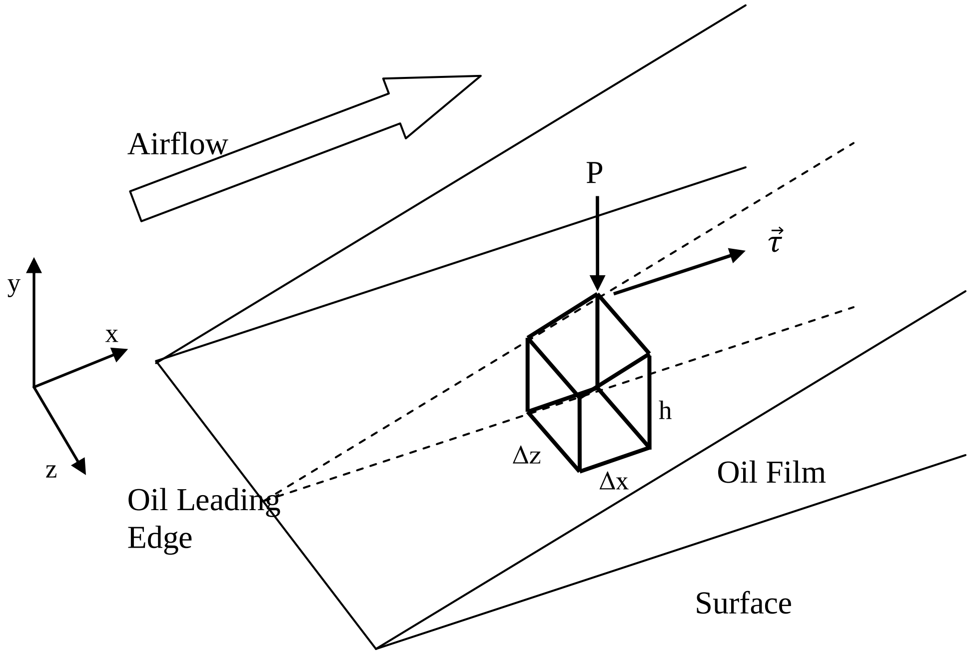

Figure 3-7: Thin oil film on a surface subjected to aerodynamic forces

In order to solve the partial differential equation as shown above, the methodology described by Brown and Naughton [10] was employed:

Under steady-state conditions the oil film thickness, *h*, can be assumed to be self-similar, or linear, with time. Therefore:

$$h(x,z,t) = \frac{H(x,z)}{t}$$

$$\Rightarrow \frac{\partial h}{\partial t} = -\frac{H}{t^2}$$

Equation 3-5

Substituting this into Equation 3-4:

$$-\frac{H}{t^2} + \frac{\partial}{\partial x}\left(\frac{\tau_x H^2}{2\mu_0 t^2}\right) + \frac{\partial}{\partial z}\left(\frac{\tau_z H^2}{2\mu_0 t^2}\right) = 0$$

Since *t* is independent of both *x* and *z*, it can be taken out of the partial differentials and thus removed from the equation:

$$\Rightarrow -H + \frac{\partial}{\partial x}\left(\frac{\tau_x H^2}{2\mu_0}\right) + \frac{\partial}{\partial z}\left(\frac{\tau_z H^2}{2\mu_0}\right) = 0$$

Equation 3-6

For the simplest case of 1-dimensional flows, as shown in Figure 3-7, the aerodynamic shear force acts only in one direction. Taking this to be the x-direction, Equation 3-6 can be simplified down to:

$$-H + \frac{\partial}{\partial x}\left(\frac{\tau H^2}{2\mu_0}\right) = 0$$

$$H = \frac{\partial}{\partial x}\left(\frac{\tau H^2}{2\mu_0}\right)$$

Integrating from the oil leading edge to a position *x* along the oil film:

$$\frac{\tau H^2}{2\mu_0} = \int_0^x H dx$$

$$\tau = \frac{2\mu_0}{H^2}\int_0^x H dx$$

Taking the definition for *H* given in Equation 3-5 and substituting:

$$h = \frac{H}{t} \Rightarrow H = ht$$

$$\Rightarrow \tau = \frac{2\mu_0}{(ht)^2}\int_0^x (ht)dx$$

Since t is independent of x it can be removed from the integral. This gives the final expression for shear force:

$$\tau = \frac{2\mu_0}{h^2 t}\int_0^x h\,dx$$

Equation 3-7

The equation above was derived using the assumption that the flow was 1-dimensional, or in a single direction. In order to apply Equation 3-7 to the two dimensional flows that occur on an impingement surface, the data analysis technique was developed to reduce the apparent flow in each area of interest down to a one-dimensional case. A brief description of this technique is given below, with the full details given in Section 7 of this report.

Once each experiment had been run, and the oil coating on the impingement plate photographed, the resultant images were examined in detail. Based on the overall flow patterns visible in the oil coating, as well as the initial placement of the oil on the plate, a number of areas of interest were identified in each image. Each area of interest was then magnified and the fringe pattern along the apparent streamlines were analysed. By analysing the fringe pattern one streamline at a time, the apparent flow along each streamline can be taken to be one dimensional. Therefore it is valid to utilise the one dimensional shear force equation given above to analyse the data.

In the expression above, the dynamic viscosity is a known property of the oil. The run time and the distance along the surface can be determined via direct measurement. However a certain amount of work is required to determine the oil thickness (h). The technique used to find the oil thickness is based on the principle of Thin Film Interference:

Consider the same drop of oil on the reflective surface discussed above. The oil has been subjected to the airflow and has spread out over the surface due to the shear force acting on it. If the shear force is sufficiently large, or the flow continues for a sufficient time, the oil will be thinned out to a point that its thickness is in the order of nanometres. Now consider this extremely thin film of oil being illuminated by a monochromatic, or single wavelength, light source, as shown in Figure 3-8 below.

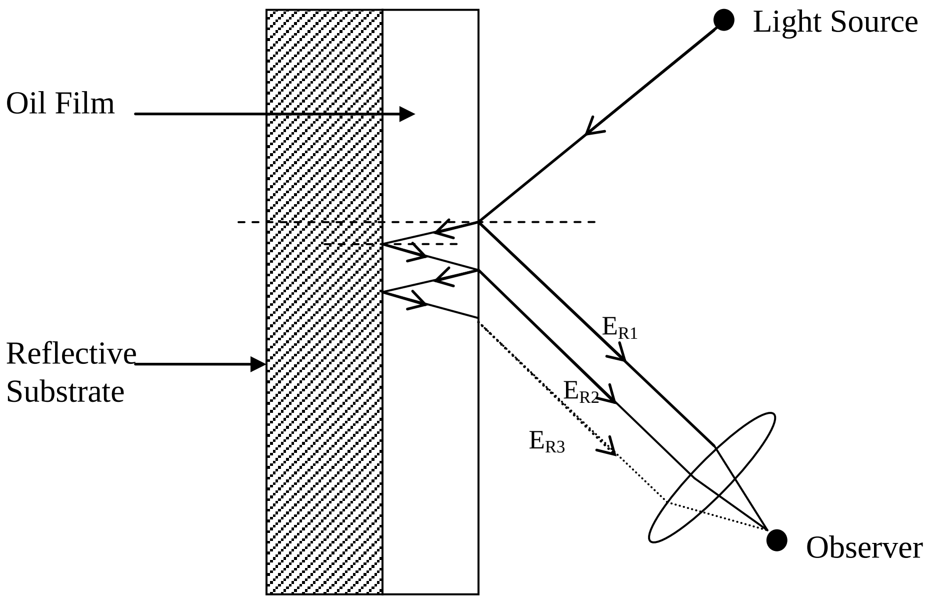

Figure 3-8: Schematic showing the path of light through the oil film

As the light hits the oil surface, a certain amount of it will be reflected off the surface, and the rest of it will be transmitted through the oil. Since the oil is a more optically dense medium than air, the portion of light that is transmitted through the oil will be refracted and slowed down. This portion of light will then be reflected off the back surface, travel through the oil once again and meet up with the initial reflected portion of light. Because the light that passed through the oil was slowed down, the wave forms of the two beams are no longer in phase although the two resultant beams of light are parallel to one another. Depending on the magnitude of the phase shift, the interaction of the two beams will lead to either constructive or destructive interference. Since the phase shift is determined by the thickness of the oil that the light has to travel through, if the phase shift can be determined, the thickness of the oil can be found. Although this is not possible all the way along the oil surface, it is possible at certain points in the oil. If the phase shift of the refracted light is 180 deg, the result will be total destructive interference between the two light beams. If the phase shift is 360 deg, there will be total constructive interference. This results in the appearance of successive light and dark lines along the surface of the oil.

Assuming that the oil starts off with a thickness of zero, the oil thickness at each light or dark band should be a multiple of a specific function. Based on the derivation described by Hecht in *Optics* it can be shown that this function is:

$$h = \frac{k\lambda_0}{4}\frac{1}{\sqrt{n_f^2 - n_1^2 \sin^2 \theta_i}}$$

Equation 3-8

Where:
h – oil thickness
k – multiplication factor ($k \in \mathbb{N}$)
λ_0 – light wavelength
n_f – refractive index of oil
n_1 – refractive index of air
θ_i – light incident angle

The full derivation of this equation can be found in Appendix A. Referring to this derivation it can be shown that total constructive interference occurs when k is odd and total destructive interference occurs when k is even. Thus utilizing this equation the oil thickness at each light and dark band can be determined. Once the thickness at each line is found, the shear equation above can be used to find the shear force at these points.

During the evolution of the technique of thin film interferometry, a number of different light sources have been used. Naughton and Sheplak [11] give examples of the most common light sources used for interferometry investigation. Table 3-1 below was taken from this paper:

Table 3-1: Light sources used for oil film interferometry [11]

Light Source	**Wavelength (nm)**
He-Ne Laser	632.8
Fluorescent Lamp	Green – use with filter
Sodium Lamp	589
Mercury Lamp	546.1
Xenon Flash	Broad Band

This table, as well as other information from [11], was used to determine the best light source to use in this investigation. The xenon flash and fluorescent lamp were ruled out as they would require the use of a filter which, according to Naughton and Sheplak [11], results in a great reduction in the light intensity. The use of the He-Ne laser was also ruled out due to the fact that it has a longer wavelength, reducing the resolution of the fringe images. Also, as noted by Naughton and Sheplak, the coherent properties of the light from a laser introduce speckling into the images. A coherent light source such as a laser would also mean that the entire plate surface could not be photographed at the same time. Thus the two most promising options for a light source were a sodium lamp or a mercury lamp. A review of the literature revealed that the majority of recent interferometry experimentation has been carried out using a sodium lamp, making this light source the preferred choice. The sodium lamp used is shown in Figure 4-4 below.

4 Apparatus

4.1 Jet flow apparatus

4.1.1 Settling Chamber

The impinging jet flows used for this investigation were generated by a convergent nozzle plate mounted at the end of a 2m long settling chamber. The settling chamber was fed by a 15 bar high pressure receiver in the basement of the Mechanical Engineering Laboratories at University of the Witwatersrand. An air dryer was used to remove the moister from the air that collected in the receiver due to the compression process. A series of valves in the supply line were used to control the air pressure in the settling chamber, which was monitored via a static pressure port in the side of the chamber.

Nozzle plates were secured to the end of the settling chamber using cap screws allowing for any number of nozzle profiles to be tested. The entire settling chamber was mounted on bullet hinges allowing for it to be rotated out of plane giving easy access to the impingement plate directly below. The entire settling chamber set-up is shown in Figure 4-1 below.

Figure 4-1: Photograph of the settling chamber in its 'open' position

4.1.2 Nozzle Plates

A total of three convergent nozzle plates were used in this investigation. An axisymmetric nozzle, with an exit diameter of 10mm, was used in the initial investigation phase. Non-axisymmetric flow investigations were carried out using a square nozzle plate, with 10mm sides at the exit, as well as a rectangular nozzle with an aspect ratio (AR) of four (the ratio of the length of the long side to the short side). The rectangular nozzle was sized to ensure the overall cross-section was the same as the square nozzle, allowing for direct comparisons between results. The square nozzle is shown in Figure 4-2 for illustration. Full manufacturing drawings of all nozzle plates used can be found in Appendix B

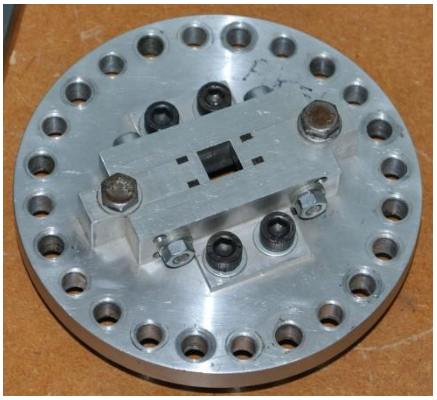

Figure 4-2: Photograph of the square nozzle plate

4.2 Impingement Apparatus

The impingement plates were mounted directly below the nozzle exit. The plate mount, shown in Figure 4-3 below, allowed for the plate distance from the nozzle, as well as the angle from the horizontal, to be altered. The manufacturing drawings for the plate mount can be found in Appendix B.

Figure 4-3: Photograph of the impingement plate mount with aluminium impingement plate

The actual impingement plates were mounted on a collar made from a section of PVC pipe and secured with three metal clamps around the circumference. Impingement plates could thus be changed out with relative ease, allowing for the testing of different materials and surface finishes. The hollow PVC pipe allowed for real-time images of the impingement surface to be captured when using the glass plate.

Base on investigations performed by Naughton and Sheplak [11] the best surface for imaging of fringe patterns is SF 11 optical glass. Unfortunately this specialised type of glass proved difficult to obtain. Therefore it was decided that for the initial investigations standard lead float glass would be used. If this glass gave promising results then a plate of SF 11 glass would be sourced. The glass impingement plate was 10mm thick with a diameter of 160mm. It was decided to utilise quite a thick section of glass to ensure that there was no chance of the plate breaking when subjected to the high pressure flows from the jet, especially at small plate distances (<20mm).

A second impingement plate of steel coated with highly polished aluminium was also used. Although Naughton and Sheplak [11] stated that polished aluminium is not the ideal surface for fringe imaging the decision to use this surface was made based on practicality:

Purchasing a plate of stainless steel 4-5mm thick with a diameter of 160mm would be rather expensive. Making the plate any thinner would run the risk of it bending and warping under the pressure of the jet. The second, and rather more important issue with using polished stainless steel, is the fact that there are no in-house facilities to perform the polishing process. It would thus need to be sent out to an external company for polishing which would be a time consuming process. Whilst this is not a problem the first time, it would incur significant delays in experimentation if the plate needed re-polishing during experimentation. Due to the fine finish required on the surface and the fact that stainless steel is significantly softer than standard steel this was a concern. Therefore it was decided to manufacture the plate from plain carbon steel with a sheet of polished aluminium bonded to the surface.

The material selected for the plate coating was MIRO 27 extra bright rolled aluminium. This is the trade name of the material which is manufactured by the ALANOD Company based in Germany. Unfortunately the MIRO range of products appears to be a company specific material and no generic was found for this material. Based on their website [12] the MIRO product is used mainly in lighting applications. The data sheet for this range can be found in Appendix C. The MIRO 27 was chosen due to the extremely high reflective properties, with 95% total reflection and less than 6% diffuse reflection. The manufacturer also claims that this material has a high hardness, making it less susceptible to surface damage.

Unfortunately it became apparent through the course of this investigation that the aluminium coating was not as rugged as was hoped and was in fact highly susceptible to surface scratches and pitting due to the high pressure airflow from the impinging jet. However since the coating was a separate sheet bonded to the steel sub plate with contact adhesive, applying a new surface coating was relatively quick and straight forward with a turn-around time of approximately 24 hours.

4.3 Imaging Apparatus

4.3.1 Camera

Interferometry images were captured using a Nikon D90 DSLR camera and a standard 18-55 AF lens. This is a 12 mega pixel camera that allows for full manual control over the sensor exposure and aperture settings. This made it ideal for use in this investigation, since all camera settings could be adjusted to ensure the best possible images were captured.

The camera was mounted on a tripod to ensure the ideal camera positioning was maintained throughout each test. A remote trigger was used to remove any chance of jarring or shaking of the camera. This was of particular concern during long-exposure image capture.

4.3.2 Light Source

As mentioned in section 1, it was decided to make use of a sodium lamp as the light source for this investigation. A photograph of the light source with a shroud to reduce the light intensity is shown in Figure 4-4 below.

Figure 4-4: Photograph of sodium lamp with shroud

As is visible in the figure, the light source is mounted on a small retort stand with a movable shroud partially covering it. To further decrease the amount of light the shroud lets out a piece of black cardboard was secured to the top of the shroud, which was originally open. This also served to minimise the amount of illumination of the surrounding apparatus. This illumination was found to cause problems when photographing the plate since reflections of the apparatus on the highly polished plate surface distorted the imaging of the fringe patterns on the plate.

A second hole in the side of the shroud was covered with opaque plastic, visible as the white section on the shroud. This opaque plastic served as a light diffuser reducing the focused intensity of the light coming through this hole. Originally this hole in the side of the shroud gave an intense spotlight effect which was not conducive to capturing fringe images.

It should be noted at this point that a beam splitter was not utilised in this investigation. Although it is mentioned in a number of the previous investigations reviewed, it was not used in this case due to space limitations. The position of the large settling chamber directly above, and in close proximity to, the impingement plate meant that there was no space for the mounting of a beam splitter. Although, as mentioned above, the settling chamber was mounted on hinges to allow it to be moved out of the way, it should be noted that one of the objectives of this investigation was to generate real-time images of the impingement plate. During the operation of the jet the positioning of a beam splitter was not possible. Therefore in an attempt to maintain consistency throughout the investigation it was decided to alter the intensity of the light at the source using a shroud. It was also hoped that the effect of the beam splitter could be reproduced by altering the camera aperture and shutter speed.

4.3.3 Oils

Dow Corning PMX 200 fluid was used as the oil coating in this investigation. This is a clear silicon-based fluid usually used as a base for lubricants in the medical field. However it has become the norm for use in interferometry investigations due to its clarity and the thermal stability of its viscosity and optical properties. The data sheet for this oil is attached in Appendix C.

Over the course of this investigation a large variety of viscosities were used. The desired oil viscosity was obtained by mixing predetermined amounts of high viscosity (1000cSt) and low viscosity (50cSt) fluids. The required amount of each fluid was determined from the mixing table shown in Appendix C.

Although this type of oil has become the standard for use in the interferometry field, there is quite a large drawback to using it. As is shown in the data sheet this fluid is only soluble in organic solvents such as chloroform, toluene or xylene; all of which are highly volatile chemicals and the fumes can be harmful if inhaled. A number of these solvents are also suspected carcinogens. Unfortunately, due to the fact that the interferometry method relies on oil coatings in the scale of nanometres, any residual oil left on the test surface could skew the data. Therefore before each test could be carried out all traces of oil coatings from the previous test had to be removed from the surface. Since the best method to do so is to clean it off with a solvent, one of these organic solvents had to be used.

After consulting the relevant Material Safety Data Sheets (MSDS) for a range of these solvents it was decided that Toluene was the best option. Whilst Toluene is harmful if inhaled, it is not absorbed through the skin and is not stated as being harmful to the environment. This being said, all relevant Personal Protective Equipment (PPE) should be used when working with Toluene (eye protection and a respirator). Wherever possible it should be used outdoors or under a fume hood. Toluene is also extremely flammable and should be kept away from all sources of ignition and where possible should be stored in a flame proof fume cupboard. The MSDS data can be found in Appendix C

4.3.4 Oil Application

There were two methods of oil application used in this investigation. For some tests a single large globule of oil was poured at the centre of the plate. However some tests required a rather more accurate method of oil application. In these cases a medical dropper bottle was used in conjunction with the spacing apparatus shown in Figure 4-5 below. This apparatus consists of a cross of plate steel with holes drilled at 10mm intervals. The edges of the cross are bent down such that it fits snugly over the 160mm impingement plate. This ensured that the central hole in the plate was over the centre of the plate. Thus each drop placed would be a known distance from the plate centre.

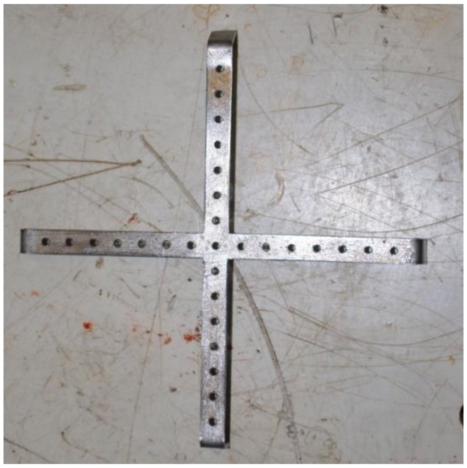

Figure 4-5: Photograph of the oil application apparatus

Unfortunately, due to errors when securing the plate stand to the floor, the centre of the plate did not line up exactly with the centre of the jet nozzles. Therefore it was necessary to bend up the one edge of the applicator so it could be shifted across the plate ensuring that the centre hole of the applicator lined up with the centre of impingement. Although it was possible to estimate the centre of impingement on the plate, this obviously introduced unwanted uncertainties into the data.

4.4 Computational Simulations

The other important aspect of this investigation was computational simulation. This was carried out through Computational Fluid Dynamics (CFD).

The CFD models used for this investigation were generated using the Fluent module of ANSYS v.13. 3-D models of the geometry of each flow case were first constructed in Solid Edge V. 19 and then imported into the Fluent environment. A sample model is shown in Figure 4-6 below. When creating these models it is important to remember that the CAD model must represent the air space within the geometry being investigated and not the physical pipes and plates. Once imported the CAD models were used to generate the flow mesh in ANSYS.

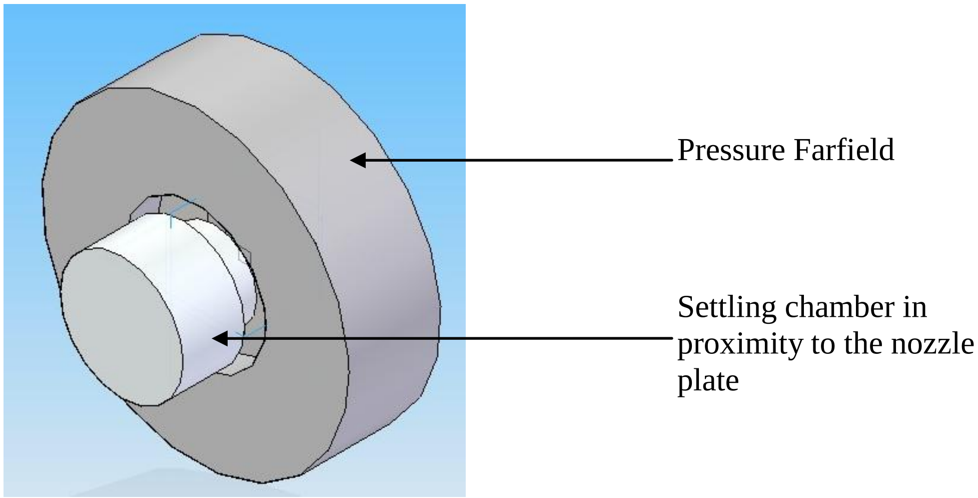

Figure 4-6: Solid Edge model used to simulate the square nozzle n/d=2 flow conditions

As is to be expected, there must be a certain amount of trade-off between desired accuracy and simulation run time when developing the mesh. Therefore in the areas of low flow velocity and gradient, such as the settling chamber inlet and the pressure-far-field boundary, the mesh was made very coarse, with an average cell size of 10mm. However within the areas of interest, where the magnitude and gradient of the flow variables are very high, the mesh was made very fine, using cells with an average size of 0.5mm. These areas of high mesh density were the area approaching the nozzle inlet, the nozzle throat, the jet core and the plate impingement zone.

Once the mesh had been generated it was passed into Fluent for the actual flow calculations. A density-based solver was used, with air treated as an ideal gas, since the flow cases being simulated had flow velocities well into the compressible region. Calculations were performed using a realisable k-ε turbulence model, since this model is known to give good resolution of shock waves and expansion fans. All constants in this turbulence model were left at their default values. The results from the simulations were accurate enough for this investigation, and the amount of time required analysing empirical data to determine the actual values for these constants did not justify the small increase in accuracy it would generate.

The inlet boundary, at the top of the settling chamber, was set as a pressure inlet, since the flow velocity at this point was not known, but all pressure conditions at this point could be calculated easily. Since the nozzle vents to atmosphere, the impingement plate was modelled inside a secondary body with pressure far-field boundary conditions around the outer edge of the model.

Calculations were carried out using a second-order upwind, Green-Gauss node-based solver. Although this does increase the solution run time slightly, the increased accuracy achieved made this sacrifice justifiable. Also, since once the simulation has been set up it can be left to its own devices whilst performing the calculations, this increase in run time was not a large concern. Since the results from these simulations would eventually be compared to experimental shear data, the simulation was run under steady-state conditions.

Examining the residuals of the simulations, the majority converged down to a magnitude of 10^{-5} or 10^{-6}. However the x and y velocity residuals, representing flow in the same plane of the impingement plate, only reached a minimum order of magnitude of 10^{-3}. This gives an uncertainty of approximately 1% in the simulated data on this plane. Compared to the level of uncertainty in the experimental data, which is discussed later, this uncertainty was well within acceptable limits.

5 Methodology

5.1 Scope and Limitations

Leaks in the air supply system meant that even with the receiver charged to full pressure of 15 bar, the peak settling chamber pressure possible was limited to 380 kPa, which is 10 kPa less than that required to obtain an NPR value of 2.5. Operating the apparatus at this high pressure caused the inlet pressure in the system to drop too rapidly to be able to run the jet for enough time to generate useful data. Therefore it was decided to limit this investigation to moderately under expanded jets with a maximum NPR of 2.

5.2 Experimental Procedure

5.2.1 Apparatus Set Up

The first step in setting up for experimentation was to charge the air receiver. This involved the following steps:

- Ensure all outlet valves are closed, including the valves on the air dryer.
- Turn on the water flow to cool the compressor.
- Turn on the circuit for the pressure relief valves.
- Finally turn on the compressor.

Once the receiver was charged up to 10-15 bar the compressor was shut down and the water flow and pressure relief valves were closed. Although the large size of the receiver meant that it took between 1 and 2 hours to get up to pressure, the pressure in the receiver was checked periodically to ensure it was not over pressurised, since it is only rated to 15 bar.

The next step was then to run the air dryer to remove moisture from the system. During the charging process the air dryer chamber also becomes pressurised. Therefore, when opening the dryer's outlet vent care should be taken to not open the valve too quickly, as this would result in the silicon granules being blown out of the chamber. Ear protection should also be worn since the venting of the high pressure air through the outlet valve creates a high velocity air jet. Once the chamber has been vented to atmosphere the second valve at the bottom of the chamber was opened and the dryer's heating elements were turned on. The dryer runs for 3 hours, which is sufficient to remove the majority of the moisture from the system.

Once the air receiver had been charged and the moisture removed from the system the rest of the testing procedure was relatively quick. The local atmospheric pressure was recorded from the digital manometer in the laboratory. This pressure reading was used to determine the required pressure in the settling chamber to obtain the desired nozzle pressure ratio (NPR). This was calculated using Equation 3-1 and Equation 3-3, an example of which is given below.

For NPR=1 and atmospheric pressure P_∞=828 mbar

$$NPR = \frac{P_e}{P_\infty}$$

$$P_e = NPR \times P_\infty = 828mbar$$

$$\frac{P_0}{P_e} = 1.8292$$

$$\Rightarrow P_0 = 1567mbar$$

Therefore for the jet to be operating at sonic conditions the pressure in the settling chamber should be set to 1567 mbar, or 156.7 kPa. Since the pressure gauge on the settling chamber had a resolution of 5kPa this value was rounded down to 155 kPa.

Although each day's atmospheric pressure was used to calculate the settling chamber pressure, the necessary rounding due to the resolution of the pressure gauge negated any of these day to day variations. Over the course of the six months of experimentation the atmospheric pressure variation was found to be a maximum of 8 mbar, or 0,8 kPa, with a minimum pressure reading of 827 mbar and a maximum of 835 mbar. For an NPR of 2, a P_∞ of 827 mbar gives a P_0 of 313 kPa and a P_∞ of 835 mbar gives a P_0 of 316 kPa, both of which round to 315 kPa. The following table was constructed using the rounded figures for the settling chamber pressure. As discussed previously it was decided to limit the testing to a pressure ratio of 2.

Table 5-1: Nozzle Pressure Ratio versus Required Settling Chamber Pressure

NPR	P_0 (kPa)
1	155
1.5	235
2	315

5.2.2 Testing Procedure

At the beginning of each experimental run the ball valve was opened and the throttling valve was set to a position giving the required pressure in the settling chamber. The ball valve was then closed and the rest of the apparatus was set up for the experiment. The use of the ball valve thus ensured that the jet flow was operating at the desired pressure right from the start.

Once all the valves had been set to give the correct pressure in the settling chamber, the settling chamber was unclamped and rotated out of the way of the impingement plate. The oil coating was then applied to the surface, either in a large globule at the centre of the plate or as a series of drops placed at 10mm intervals away from the jet centre using the cross applicator shown in Figure 4-5 in the previous section.

When using the applicator it is important to ensure that it is correctly aligned with the axes of the jet nozzle, as well as ensuring the centre of the apparatus is directly above the centre of impingement. As discussed previously the applicator had to be modified slightly to ensure this since the centre of impingement was not exactly in line with the centre of the plate.

Another consideration to be made when applying the oil in single drops is to ensure that only one drop is placed on each axis. This is because, due to the high velocities and shear forces, the oil drops placed on the surface were found to spread out from their leading edge all the way to the outer rim of the plate. Thus if two drops are place on the same axis, the oil from the first drop will flow into the second, causing the flow patterns in both oil coatings to be compromised.

Once the oil had been applied to the plate the camera was set up on the tripod at the correct angle and distance from the plate. Due to the reflection from the impingement plate the autofocus function on the camera could not be used. Therefore the initial position of the oil drops on the plate was used to ensure the camera was in focus. Photographing the initial position also generated the datum image needed for the data analysis procedure, as discussed later in section 7. After testing the camera focus, the lens cap was replaced and the settling chamber was clamped back in place above the impingement plate.

After blowing the warning whistle to warn anybody in the area of the impending noise, the ball valve was opened to start the jet flow. Simultaneously the digital stopwatch was started to ensure the jet ran for the desired time. Once the jet had run for the required time, the ball valve was closed, shutting down the flow.

The other two gate valves were also closed to ensure that there was no chance of the jet flow being reactivated accidentally. Apart from the health and safety concerns, the running of the jet accidentally could skew any oil film results.

The settling chamber was then unclamped and rotated out of the way and the overhead lights were turned off to ensure the only illumination came from the monochromatic sodium lamp. The resulting oil flow patterns were then photographed a number of times. The overhead transparency reference circles were then place on the plate and photographed to generate the required error of parallax conversion image.

Finally the excess oil was wiped off the plate using a glasses cleaning cloth, and any residue was removed by a final cleaning with toluene.

5.3 Oil preparation

As mentioned in the previous section, the oils used in this investigation had to be mixed by hand from the two samples obtained from the supplier. The best way of explaining this mixing process is by way of example. Detailed below is the mixing process to obtain an oil viscosity of 550cSt.

The first step in mixing the oil was to read off the mixing table the percent per weight of each of the two substrate oils. Reading off the graph, to obtain a final viscosity of 550cSt, 20% by weight of the mix must be made up of the 50cSt oil. Obviously the remaining 80% is the 1000cSt oil. However it was much more convenient to mix the oils by volume rather than weight. The relationship between the percentage per volume and the percentage per weight was calculated as shown below:

$$\%_{v1} = \frac{\%_{w1}}{\rho_1 V}$$

Equation 5-1

Where:

$$V = \frac{\%_{w1}}{\rho_1} + \frac{\%_{w2}}{\rho_2}$$

Equation 5-2

Where:
$\%_v$ = volume percentage required
$\%_w$ = weight percentage required
ρ = density of oil (g/ml)
V=volume required to make 1g of oil (ml)
Subscript 1 represents the 50cSt oil, subscript 2 the 1000cSt oil.

Using the weight percentage values as stated above, and the quoted densities for the two oils, which were 0.96g/ml for the 50cSt oil and 0.97g/ml for the 1000cSt oil, the respective volume percentages were calculated to be:

$\%_{v1}=0.2017$

$\%_{v2}=0.7983$

The test oils were mixed in 10ml batches, meaning the required volume percentage of each oil simply had to be multiplied by ten to give the required volume in millilitres. Performing this calculation, the respective volumes for the oils were calculated as:

$V_1=2.02ml$

$V_2=7.98ml$

The required volume of each oil was then measured out using 10*ml* syringes. The syringes used had graduations every 0.2*ml*, meaning the maximum possible accuracy in measurement was 0.1*ml*. The required volumes where thus rounded to the nearest 0.1*ml*, giving the final volumes of:

$V_1=2.0ml$

$V_2=8.0ml$

This amount of each oil was measured out and mixed in a medicine dropper bottle. To ensure that there was no contamination of either the original oil or the resultant fluid, the two oils were measured out using two separate dedicated syringes. The dropper bottles were also labelled with the viscosity of the oil contained to ensure there was no cross-contamination.

5.4 Precautions

There were a number of precautions that had to be taken into account during the testing process. As mentioned in the previous section, toluene is a hazardous material and needs to be used with extreme caution. Where possible it should be used in a fume chamber or under a fume hood. Unfortunately this was not possible in the current laboratory room, so when working with it care was taken to always wear gloves, a long-sleeve lab coat, a respirator and safety glasses.

When performing the jet impingement tests, safety glasses and hearing protection should always be worn. As mentioned above a warning whistle was also blown prior to each test run to warn anyone in the immediate vicinity that a test is about to begin.

Other not-so-obvious things to note when performing these interferometry tests include wearing gloves when working with the oil and ensuring the settling chamber is clamped in place when performing the initial pressure runs. It was noticed when performing the initial pressurisation tests that the if the settling chamber was not secured above the plate, the setting on the gate throttling valve that gave the correct settling chamber pressure was much lower than the setting required to give the same pressure when the nozzle was positioned over the impingement plate. At first glance this observation was not easily explainable, since the choked nozzle should block any pressure signals going back into the settling chamber. It was assumed that this occurrence was due to the presence of a subsonic region within the boundary layer allowing for the transmission of pressure signals.

6 Observations

It should be noted that the overall objective of this investigation was to determine whether or not the techniques of oil film interferometry could be applied successfully in this high-velocity environment. The data presented in this section details the evolution of the experimental procedures used to reach this objective. Therefore the majority of the initial data show the results of experimentation that failed to generate fringe images. Despite not showing fringe patterns, the initial data detailed here still gave important insights into the behaviour of the airflow over the plate surface. The initial results also serve to highlight which experimental parameters were found to be most important to the final success of the investigation.

Even though there have been numerous papers published on the subject of oil film interferometry there were still a number of parameters that had to be considered when designing this experiment:

Based on previous research the type of oil to be used was selected as Down Corning PMX 200 silicon fluid. However the oil placement on the test surface, application method, amount of oil applied at each point and optimal oil viscosity had yet to be determined.

Similarly the light source was selected as a sodium lamp with dominant wavelength of 589nm. However the correct light intensity and light positioning relative to the test surface was unknown.

Other parameters that had to be considered during the initial phase of experimentation were:

- Camera Placement and Focal Length
- Camera Settings in terms of ISO sensitivity, aperture size and exposure time
- Jet run time

- Impingement surface: Glass or Aluminium

Therefore the first phase of experimentation was focused on determining which of the stated parameters were most important to generating data as well as narrowing down the possible effective range of each of these parameters.

As stated in the objectives section, the first objective of this investigation was to utilise existing interferometry methods to generate fringe images from the impingement of an axisymmetric jet. Thus the first round of experimentation was carried out using the 10mm axisymmetric convergent nozzle.

The first parameters that were tested were light source placement, intensity and oil viscosity. The other parameters for these experiments were set as follows:

Jet run time – 2-4 seconds
n/d – 10
NPR – 1
Oil application – drops at various intervals from the centre of the plate
Camera Placement – directly above the plate
Camera settings – Auto
Reflective aluminium plate

The four photographs in Figure 6-1 below clearly demonstrate the effect of light placement on what is visible on the plate. Although no fringes are visible in any of these images it is clear that the light intensity is too great when the lamp is placed directly over the plate, as shown in the first two images.

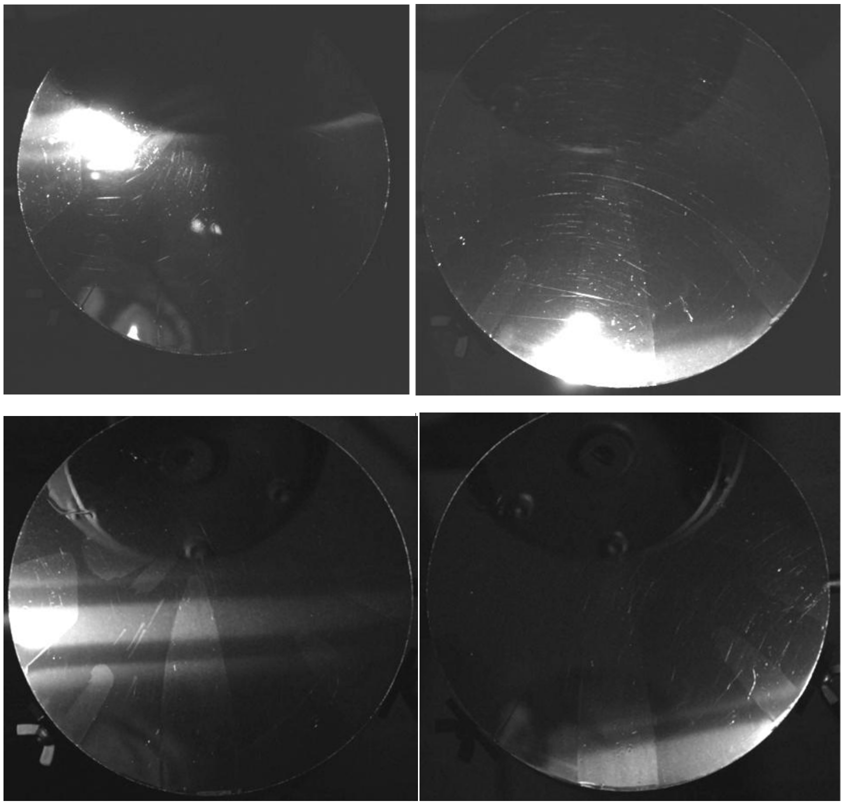

Figure 6-1: Axisymmetric nozzle, n/d=10, NPR=1, oil ν=200 cSt, t=2s

The other two photographs, taken with the light source slightly off to the side of the plate show the flow patterns of the oil much more clearly. However the light diffusion and intensity is still too great, as is evident by the reflection of the settling chamber on the plate. Therefore the light was covered with the shroud to decrease the intensity as well as focus the light onto the plate.

A series of test runs were performed using various combinations of oil viscosity and light positioning to try find the combination that would generate fringe patterns. Unfortunately no combination could be found that gave positive results. Therefore it was decided to shift the focus of the experiments to capturing real-time images of the impingement process.

With the impingement plate set orthogonal to the airflow, it was not possible to get the camera in a position to capture images of the plate during the impingement process. As mentioned above, the hinges on the settling chamber allowed for it to be moved out of the way after each run. However the experimental methodology had to be altered to enable the capturing of real-time images. The following two methods were identified as the most promising:

The first method involved angling the plate at 40^0 to the horizontal. The camera was then mounted on the tripod such that it could be focused orthogonal to the plate. The camera was then set to shoot continuously capturing images at 4.5 frames per second, giving a picture every 0.2 seconds. The set of images in Figure 6-2 show the flow of the oil through the first second of the impingement process.

Figure 6-2 (a) shows the initial placement of the oil drops just before the jet flow was started. In this image only the two drops on the lower section of the plate are visible. As soon as the air flow hits the plate, the high shear acting on the surface makes the rest of the oil drops visible as well, as evident in Figure 6-2 (b). The succeeding two images in the figure show the thinning out of the oil due to the air flow, indicating the direction of flow at each point. However because of the initial gravitational flow of the oil, determining the actual direction of airflow is rather difficult. This problem is compounded by the fact that initial position of the majority of the oil droplets is not clearly visible. The other obvious issue with these images is the fact that no fringe patterns are visible. However this could be due to the fact that these images were captured during the first second of the jet flow and thus the oil has not thinned out sufficiently to make fringes visible. Unfortunately examination of the images in Figure 6-3, which were captured during the shut-down phase of the jet, shows that this is not the case.

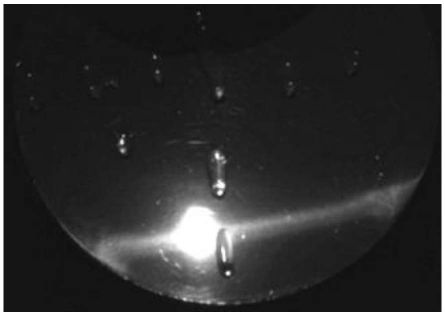

(a)

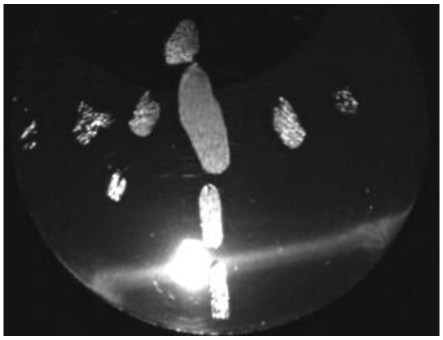

(b)

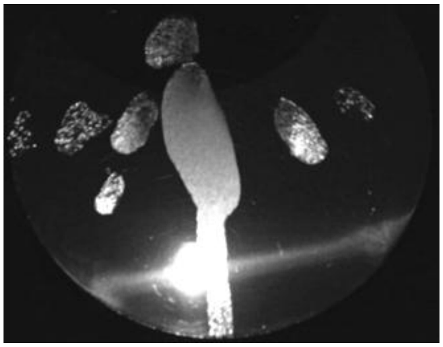

(c)

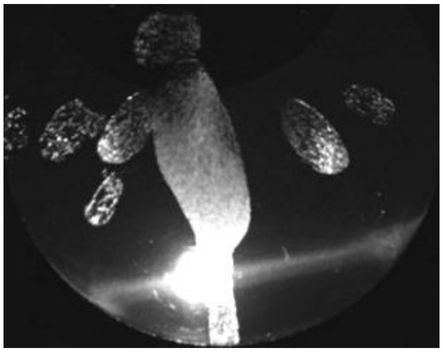

(d)

Figure 6-2: Jet Start Up Phase, Axisymmetric Nozzle, NPR =1, n/d=10, Plate 40^o, ν=200cSt

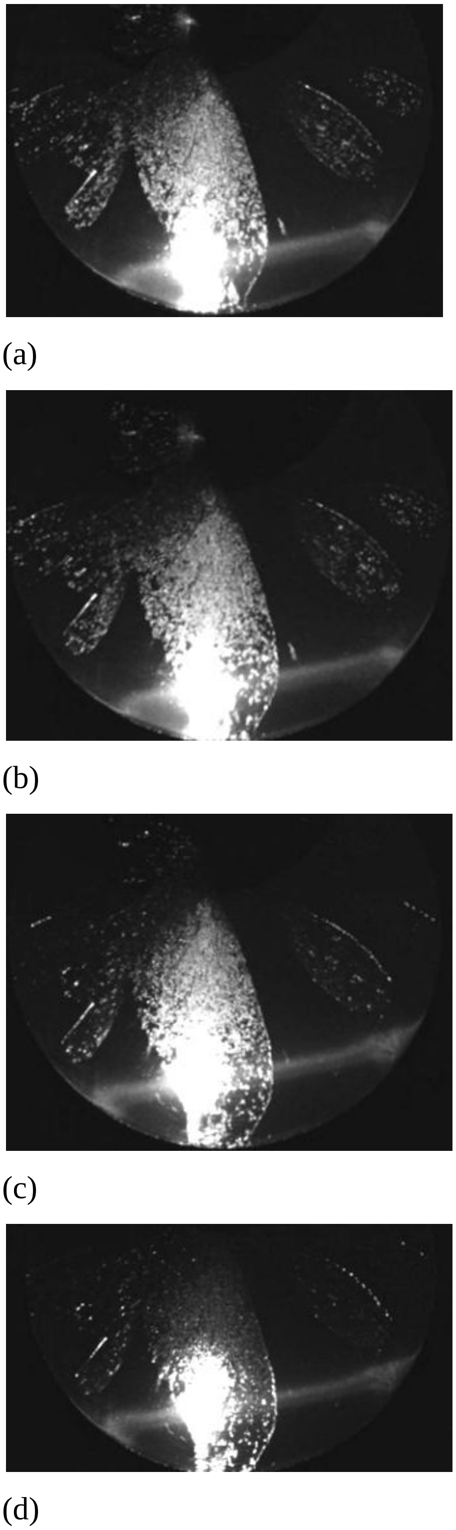
(a)

(b)

(c)

(d)

Figure 6-3: Jet Shut Down Phase, Axisymmetric Nozzle, NPR =1, n/d=10, Plate 40^{o}, ν=200cSt

The first thing that becomes immediately obvious when examining this set of images is the difference in brightness between Figure 6-3 (c) and Figure 6-3 (d). This illustrates the difference in the appearance of the oil during impingement versus after the flow has been shut down, which occurred in the time between these two images being captured. The shear force acting on the oil introduces turbulence to the surface of the oil making it highly visible. As soon as the aerodynamic forces are removed, the oil surface smoothes out and no longer reflects the incident light as brightly.

The next thing to note is the pattern of the oil film on each image. The first three images, which were captured whilst the jet was still running, show very little difference in the film coating. This shows that the flow rate of the oil has slowed down considerably. From this fact it can be assumed that the oil has thinned out to a point where, theoretically, fringe patterns should be visible. However due to the turbulence on the film surface, the light is not reflected off the oil surface in a regular and consistent manner, meaning there is no opportunity for the optical interference patterns to occur.

This being said, this initial observation cannot be considered to be conclusive in any way, since, even after the jet flow had been shut off, there were no fringe patterns visible, as illustrated in Figure 6-4.

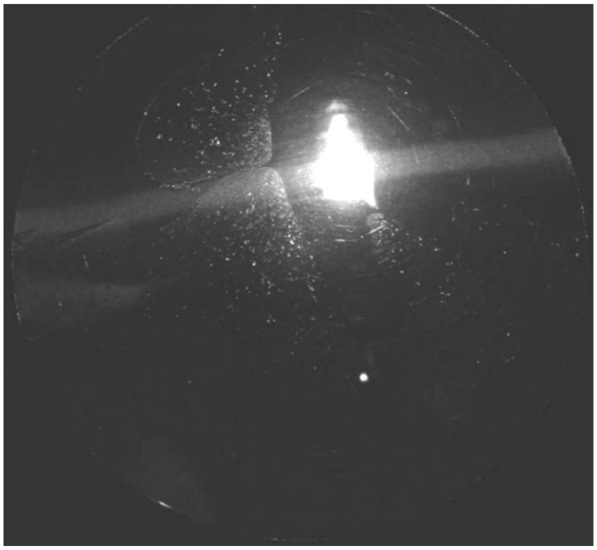

Figure 6-4: Oil Film Coating After Impingement

After numerous failed attempts to capture fringe images, this technique was abandoned in favour of the second real-time imaging method, as described below:

This next technique involved using the glass impingement plate, as detailed in the Apparatus section (section 4.2) with the camera mounted below the plate. This allowed for images to be captured orthogonal to the plate during the impingement process, with the plate set normal to the flow. However, because the images were captured through the plate, the normal method of illumination could not be used. Firstly the light source would be shining directly into the camera, saturating the detector making any small variation in intensity impossible to see. The second problem is that there is no opportunity for the reflection/refraction interference case to be set up, since the camera is only capturing the light that has been refracted through the oil and the glass. Therefore another method of illumination had to be used.

The illumination method used was what was referred to as ‘Edge Lighting’. A flexible strip of LEDs, as discussed in section 4.3.2 above, was secured around the edge of the glass plate. With the light from these LEDs shining through the edge of the plate, it was hoped that this would highlight any variations in the plate surface. Even though this method is different to that which has been proven to generate fringe images, the basic principles of thin film interference should still apply to this case. The light passing through the oil film will experience a phase shift as it passes through the oil film. This phase shift should generate some form of interference, be it constructive or destructive, when this light interacts with surrounding light rays. Whether or not this phase shift and interference is actually visible when viewed from the position of the camera was not known.

Initial tests were promising, with every scratch and blemish on the plate surface showing up very clearly. In Figure 6-5 below, showing the plate in place below the jet nozzle, surface scratches, smudges and dust particles are clearly visible. The oil droplets placed on the surface, however, are not so clearly defined. It was hoped that these would become more defined once the oil had thinned out, since the oil smudges around the outer edge of the plate are clearly visible.

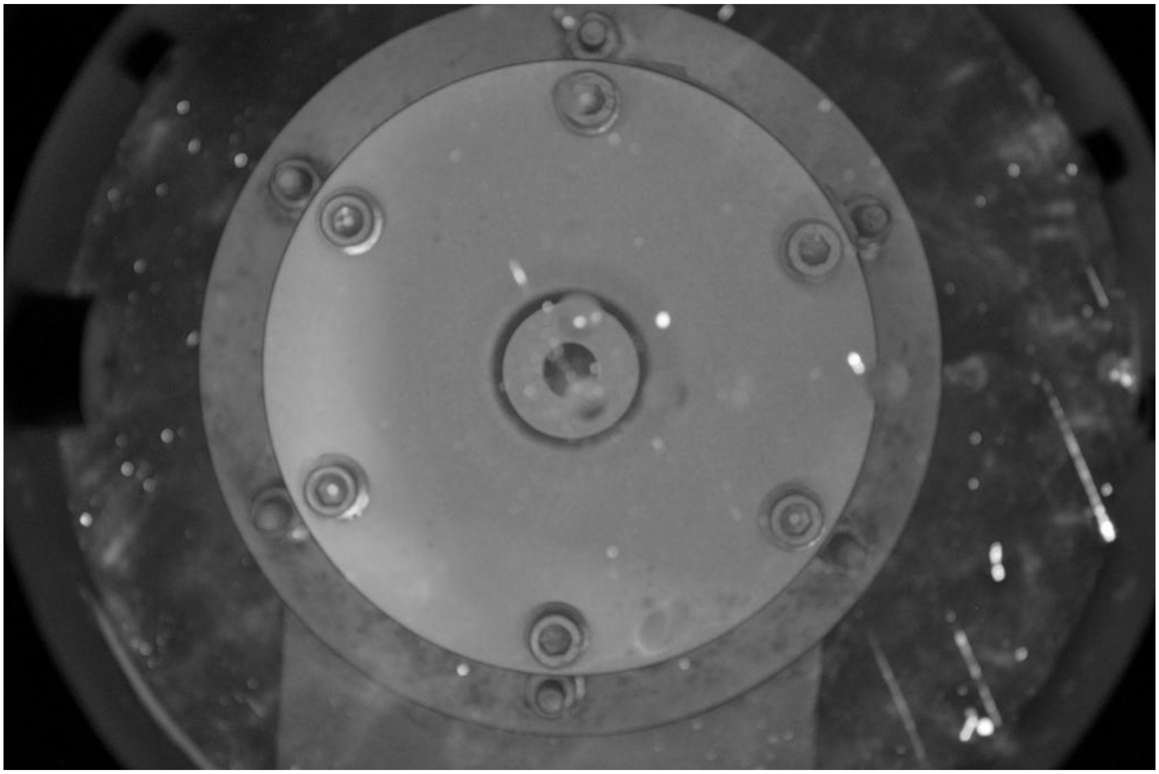

Figure 6-5: Glass Plate with Edge Lighting

Figure 6-6 shows the plate just after the start of the flow. As with the previous experiment, as soon as the jet flow hits the oil droplets, the aerodynamic shear introduces turbulence in the surface of the oil, making this surface much more reflective causing the oil coating to show up clearly in the image. The evolution of the surface flow is also visible in this image, since the droplets at the centre of the plate have been spread out more than the droplets towards the edge of the plate, which have only just begun to feel the effects of the airflow over the surface.

Examining the next series of images shown in Figure 6-7, the continuous spreading out and thinning of the oil film is clearly evident, as was noted in the images from the previous experiment.

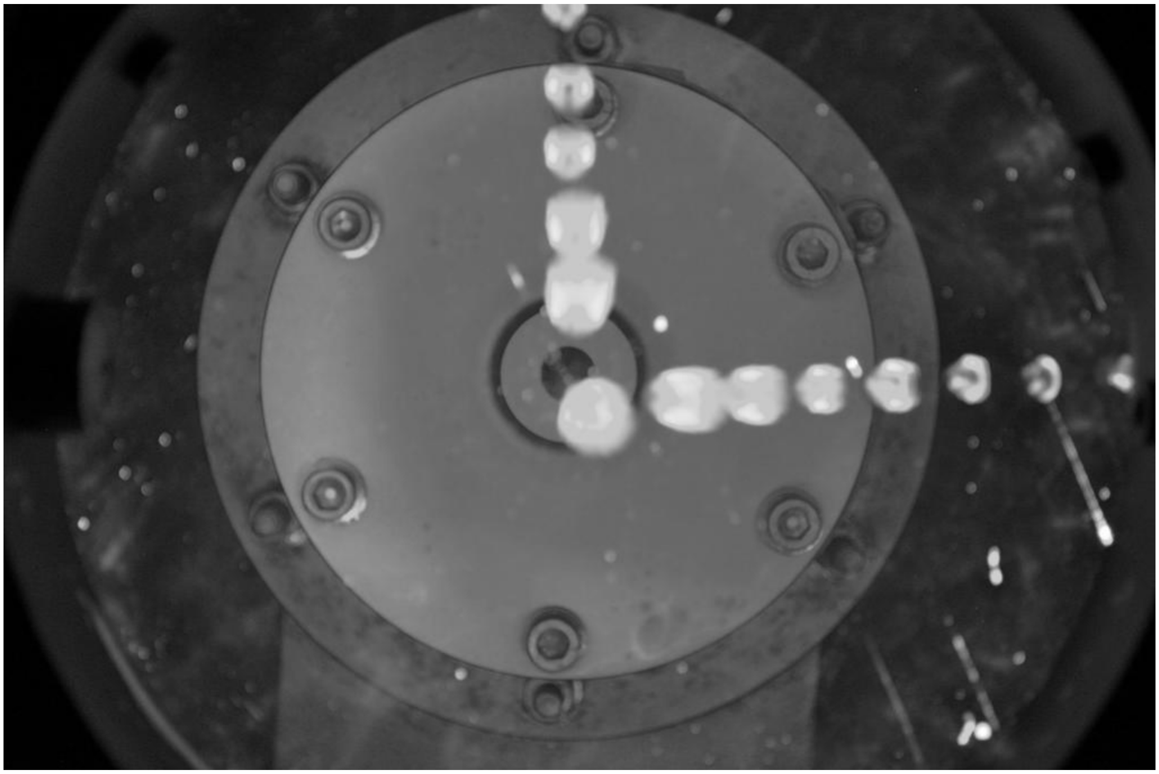

Figure 6-6: Glass Plate Approximately 0.2s after the start of the flow

The next observation made when examining these images was that the oil film becomes less visible as it thins out. Comparing Figure 6-7 (a) and Figure 6-7 (d), with specific reference to the oil along the vertical line, the oil film is not nearly as well defined in image (d) as it is in image (a). This is particularly evident when examining the leading edge of the oil, which is clearly visible in the first image, but there is almost no evidence of it in image (d).

This observation is actually a positive result of this investigation, since it means that the obscuring nature of the oil turbulence becomes reduced as the oil thins out. Therefore the light has a better chance to refract regularly through the oil setting up the interference fringes. So, given enough time to thin out sufficiently, it may be possible to capture fringe images during the impingement process.

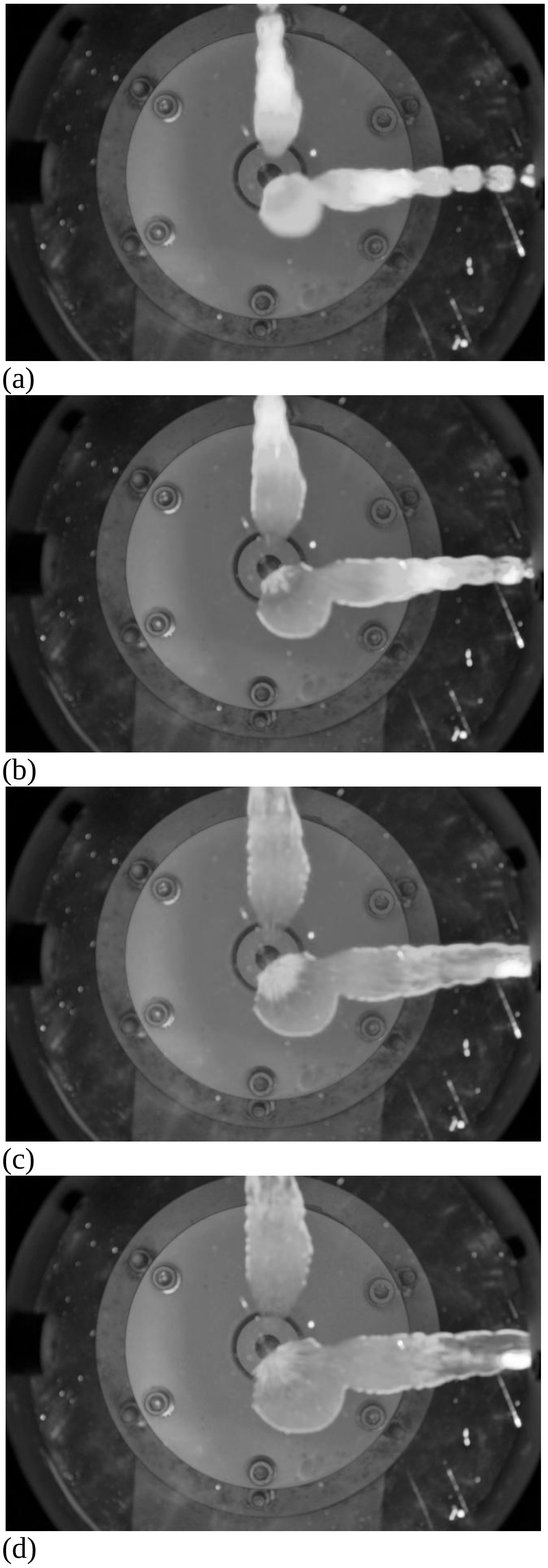
(a)
(b)
(c)
(d)

Figure 6-7: Images of the plate during the impingement process

Unfortunately, as is evident from Figure 6-7 (d), as well as the image in Figure 6-8, no interference patterns are visible in the oil film; either during the impingement process or after the jet has been shut down. Considering Figure 6-8, which shows the impingement plate after jet shut down, the oil film is just barely visible on the surface. The only thing visible in the oil film is speckles, which were assumed to be dust particles that settled in the oil after the flow had been shut down.

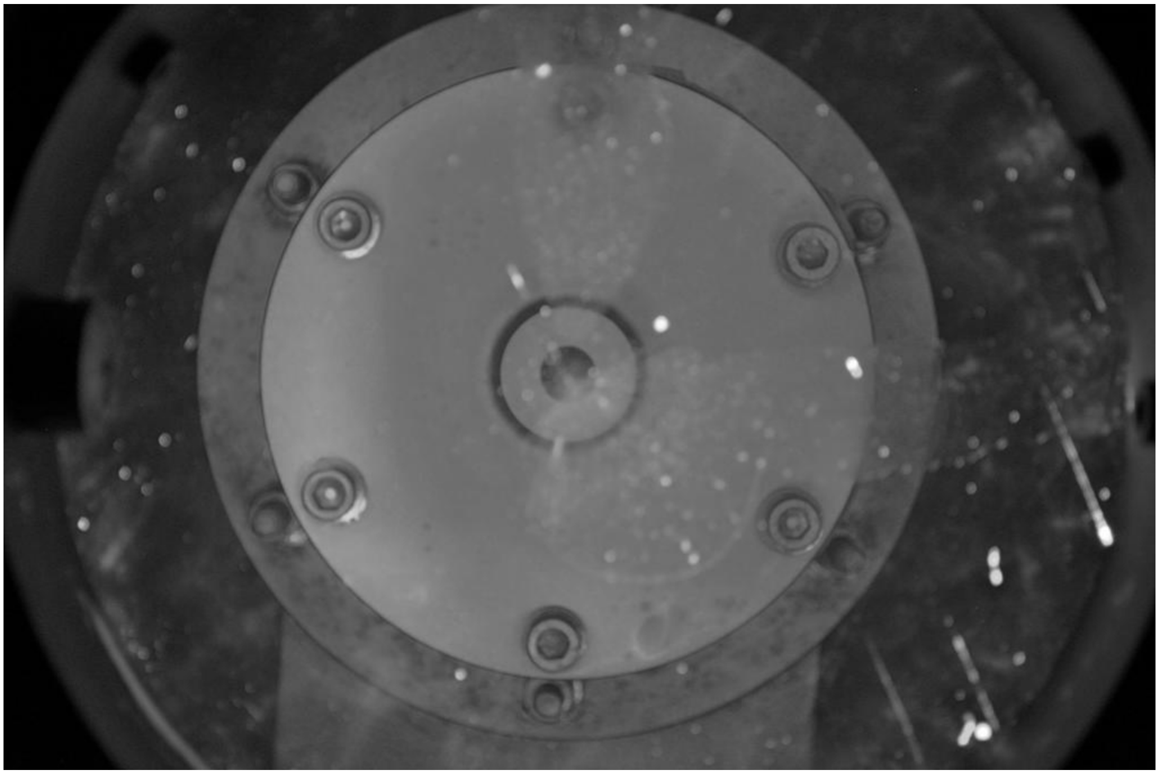

Figure 6-8: Glass Plate After Shut Down

Examining the image of the jet nozzle, which is clearly visible through the glass, a small amount of refraction is evident when comparing the part of the image that passes through the oil film versus the section visible through ‘clean’ glass. However, as with the previous experiment, there are not interference fringes visible in the oil.

One obvious problem that should be noted immediately when examining these images is the fact that the jet nozzle is so clearly visible. This will obviously have an effect on what is visible in the oil film. However it would only be necessary to find a solution to this problem if this method of edge lighting actually generated positive results. Since this technique did not generate any images that could be used for quantitative analysis, it was decided not to continue with in this direction.

Although these experiments into capturing real-time images did not generate any useable data, it did reveal some important information regarding the behaviour of the oil coating as it thins out. Initially the aerodynamic forces generate high turbulence on the surface of the oil making it completely opaque. Whilst this does make the position and movement of the oil easy to see, it is not possible to draw any quantitative data from this. Once the jet has been run for a few seconds this turbulence appears to subside, making it possible to see through the oil film, which is a requirement for the setting up of interference patterns. Although this reduction in the oil turbulence could be due to the fact that the flow has reached steady state conditions, it seems more likely that it is due to the oil having thinned out past a certain threshold value. In either case, the clearing up of the oil indicates that there is a chance for interference fringes to be visible during the impingement process and not just after the fact.

Another insight that came from these real-time experiments was that the jet flow took between three and five seconds to reach steady-state. This means that, even if the initial experimentation had generated fringe images, they would not be an accurate representation of the flow fields.

Based on this new information, it was decided to go back to the initial experimental set up, taking photographs of the plate after the impingement process. However the set up was modified slightly in an effort to improve the chances of generating fringe images.

The axisymmetric nozzle was changed for the square nozzle, since this would create more varied flow conditions over the plate. The plate was also moved up to the minimum plate distance of 20mm from the nozzle exit. This meant that the oil would experience the maximum possible shear force, giving it the best chance of thinning out to the extent that fringe patterns become visible. The jet run time was also extended from 2 seconds to 10 seconds, ensuring that the jet flow was fully evolved. Finally, the method of oil application was changed from placing several small drops across the surface to putting one large globule in the centre of the plate. This was done so that, even if no fringe patterns resulted, the resultant oil coating would at least show the overall behaviour of the airflow on the plate.

The initial results from this round of testing were promising. Figure 6-9 shows the resultant oil pattern on the aluminium impingement plate after the impingement of the jet flow for 10 seconds. In this image the boundary of the recirculation zone is clearly visible, as indicated by the dark ring pattern on the surface. This dark ring, which shows a lack of oil at this point, is most probably caused by the high speed expansion fan region.

What is even more interesting are the rectangular-shaped extensions in the ring pattern. Upon closer inspection it was noted that these rectangular extensions were in plane with the main axes of the jet nozzle (The set of axes in the left hand corner of the figure indicate the direction of these main axes). This indicates that the expansion fan is stronger along the main axes of the jet.

The definition of both the main and diagonal axes is shown in the schematic diagram in Figure 6-10. The main axes, indicated by the solid lines, are in line with the horizontal and vertical sides of the nozzle. The diagonal axes, indicated by the dashed lines, are plotted from corner to corner across the face of the nozzle.

Other patterns that are visible in the image are the white striations on the plate radiating out from the impingement zone, indicating the presence of the high-velocity wall jet, as well as the dark spot in the centre of the recirculation zone. When first observed, this dark spot generated some concern since it coincides with where the stagnation point should be.

As discussed in section 3.2, a central stagnation point is formed at the centre of the impingement zone. A stagnation point is, by definition, a point where the flow velocity is zero. However a dark area on the image is caused by a lack of any oil in that area. Since the oil was initially applied to the surface in a large globule at the centre of the plate, this dark spot means that all the oil has been pushed off of the surface at this point, which indicates a point of high-velocity flow rather than a stagnation point. However a closer examination of the theory of axisymmetric flows gave a possible explanation of these patterns:

At the very centre of the jet core, the airflow is forced to decelerate to zero. However immediately adjacent to the stagnation point, the airflow is decelerated and turned through 90 degrees and continues to flow along the plate. The close proximity of these highly curved streamlines to the stagnation point could pull the oil off the surface in the surrounding areas.

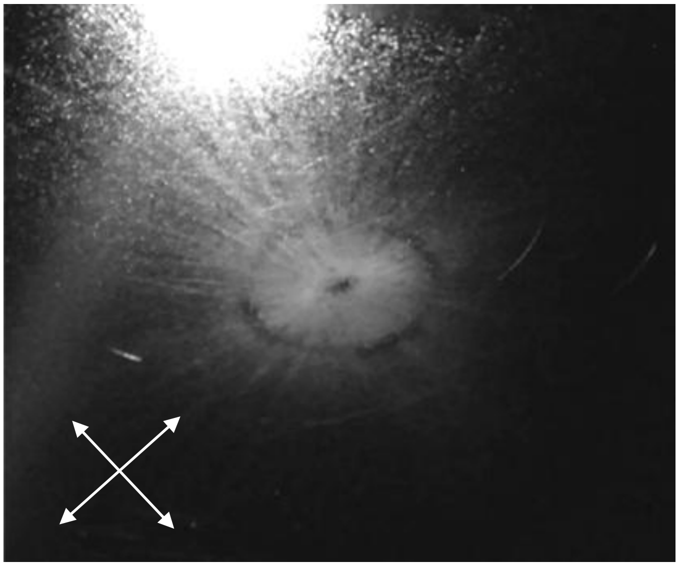

Figure 6-9: Square Nozzle, NPR =1, n/d=2, *v*=200cSt, t=10s

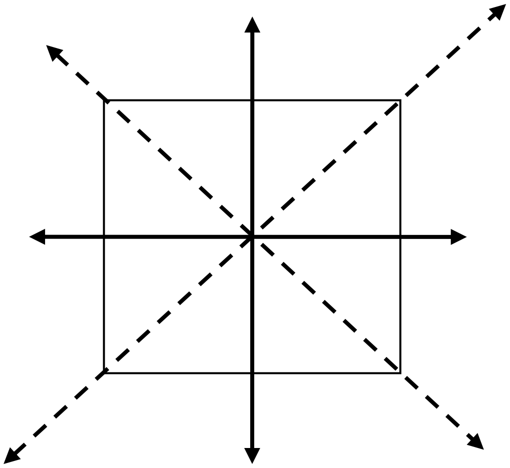

Figure 6-10: Schematic representation of the square nozzle exit with axis definitions indicated

Further testing did, however, yield images that replicated the other flow patterns noted above, as well as highlighting other phenomena in the surface flow. Figure 6-11 shows an image from another test run, taken from a very oblique angle. Once again the boundary of the recirculation zone is clearly visible, as well as the extended dark zones aligned with the main axes. But what is of particular interest in this image are the radial striations on the plate. There is a subtle difference in the density of the striations along the main axes versus those in the diagonal plane. This indicates that the wall jet has a higher velocity along the main axes of the nozzle. This agrees with the previous observation that the expansion fans are stronger along the main axes, since the air exiting the recirculation zone will have to accelerate to a greater degree if the wall jet has a higher velocity.

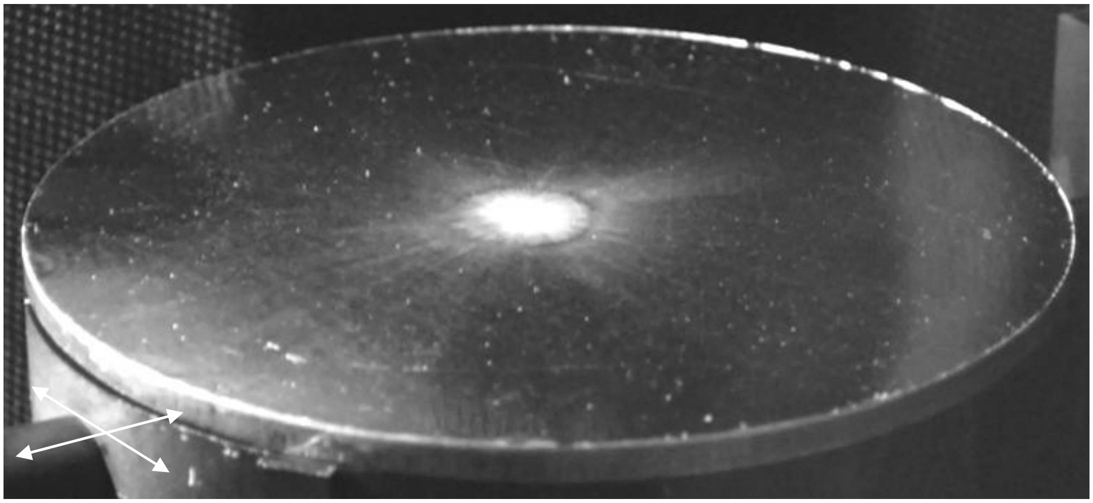

Figure 6-11: Square Nozzle, NPR =1, n/d=2, *v*=200cSt, t=10s

This round of experimentation generated some important data that highlighted some interesting flow patterns in the impingement of jets from square nozzles. Unfortunately, as with all the previous experiments, this testing did not generate any fringe images. It was therefore decided to perform the same test procedure using the glass impingement plate. As was noted previously, the background research indicated that a glass plate should generate better fringe images than a polished aluminium plate. However, as with all other tests, these experiments did not generate any fringe images. This being said results from these tests did highlight further flow patterns on the plate.

Examining the image in Figure 6-12, the border of the recirculation zone is once again apparent, as indicated by the darker ring in the centre of the plate, although it is much less well defined that in the previous images. That being said, it does appear to have a roughly square shape to it, with the corners of the square in line with the main axes of the nozzle, which was not apparent in previous tests.

Also apparent on the image are the subtly darker lines radiating out from the centre. Four of these lines are once again aligned with the main axes, indicating that the wall jet has a higher velocity along these axes, agreeing with the results from the previous experiment. The presence of the fifth line is much harder to explain, since it indicates a flow pattern completely contradictory to that which has been observed so far. This line suggests that there was a single higher-velocity wall jet radiating out along one of the diagonals. If this is in fact the case, why was this additional wall jet not visible in the previous results? Also, and this is perhaps the more critical question, why is this wall jet only present along one of the diagonals? All other flow patterns observed so far have been present in all four directions either along the main or diagonal axes.

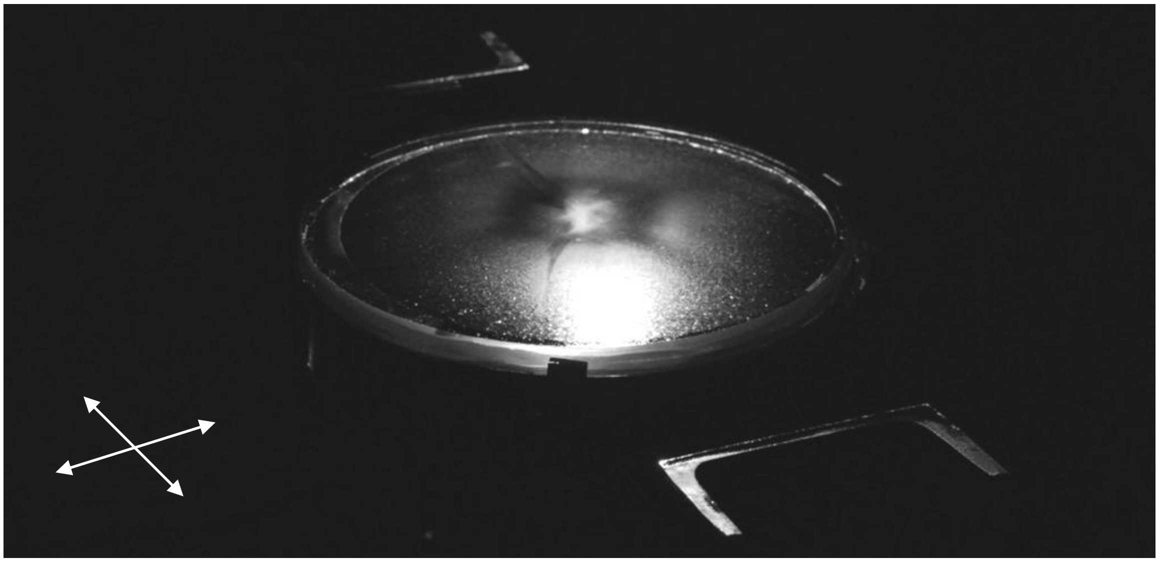

Figure 6-12: Glass plate

However upon closer inspection, the reason for the presence of this additional line became clearly evident. Zooming in on the plate, as shown in Figure 6-13, this additional dark line seems to be much more clearly defined that the two lines on either side of it. The line has well defined edges and a constant thickness along the first portion moving away from the impingement zone. The other portion of the line tapers down to a point approximately half way to the edge of the plate. Therefore it is much more likely that this additional line was caused by something being dragged across the plate after the jet had been shut down, rather than any sudden unexplained variation in the airflow. This conclusion is supported by the characteristics of the dark line in the top left of the image, which also has well defined edges and curves out away from the axis of flow. It is most likely that these patterns in the oil coating were caused by a corner of the black-out curtain lightly brushing over the plate as the settling chamber over which it was wrapped was moved out of the way.

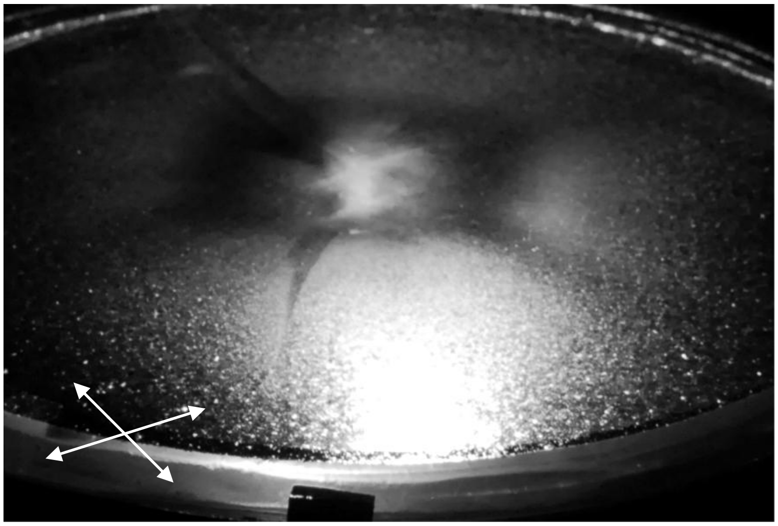

Figure 6-13: Magnified Image of Glass Plate with cross patterns

Even though the oil coating has been corrupted by this error, the images from this experiment still revealed some important information about the surface flow patterns, as well as the applicability of glass as a possible surface for interferometry imaging.

Focusing now on the centre of the plate shown in Figure 6-13, a distinct cross pattern is visible in the oil coating, aligned with the main axes of the jet. The presence of this white cross points to the presence of the lines of recirculation as predicted by Menon and Skews [5]. However as illustrated in section 3.2, the numerical simulations carried out by Menon and Skews predicts that these lines are along the diagonal plane of the nozzle rather than the main plane as shown in the figure. When viewed from a more orthogonal angle, however, the actual orientation of this cross pattern becomes much clearer.

Referring now to Figure 6-14, the cross pattern is visible at the centre of the reflection of the light source. Between the bottom two arms of the cross, one of the dark lines representing the main axis wall jet is just visible. This image, therefore, seems to indicate that this cross pattern is in fact aligned with the diagonal rather than the main plane.

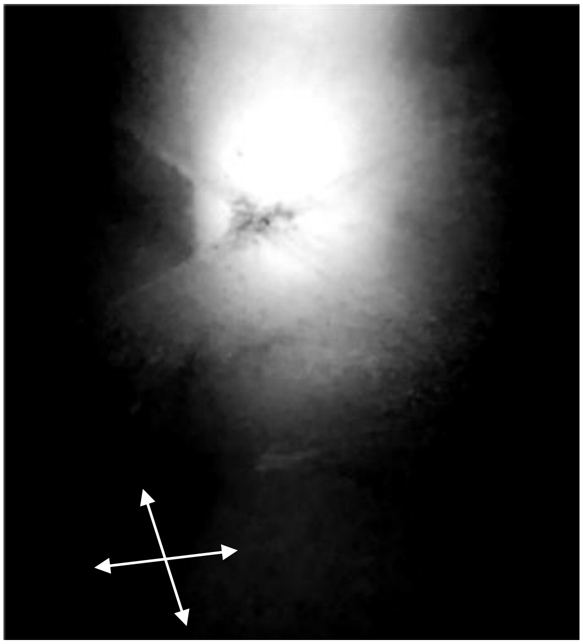

Figure 6-14: Cross Patterns in the region of the Impingement Zone

Moving back to the cross pattern visible in Figure 6-13, there is a second white patch visible just below the cross pattern. This serves to illustrate one of the potential issues with using glass as an interferometry surface: The problem of double reflection. The second white patch visible in the image is in fact the reflection of the impingement zone cross from the lower surface of the glass. Whilst the presence of this phenomenon is relatively clear in this image and the image interpretation can be altered to allow for this, it might not be so easy to compensate for this occurrence when analysing fringe images. The calculation of shear forces from fringe patterns is highly dependent on the accurate measurement of the spacing between fringes. Any double reflection of the light from the bottom surface of the plate could artificially increase the number of fringes visible, thus decreasing the calculated shear values. Therefore it was decided that no further work would be performed on this track and efforts would be better exerted in an attempt to generate usable fringe images using the aluminium impingement surface.

Whilst promising, the results from this set of experiments still failed to generate any fringe images. It was decided to perform one final batch of tests, using the aluminium plate and experimenting with greatly increased run times and testing over the whole range of oil viscosities, from 50 to 1000 cSt. The aluminium coating was also replaced, since over the course of the experimentation the polished surface had become scratched and pitted. A rather interesting observation was made at this time:

The old aluminium covering showed clear signs of pitting at the centre of the impingement zone. Evidence of this pitting is highlighted by the circle in the close-up image in Figure 6-15. According to the theory, this is the area of the central stagnation point. This pitting indicates that the airflow is hitting the plate at a high velocity or pressure causing this erosion of the surface. This erosion could possibly explain the lack of oil observed in Figure 6-9, which as mentioned above was an area of concern. If the airflow is causing erosion of the aluminium surface it is reasonable to assume that the dark spot in the oil in Figure 6-9 was caused by the oil being blasted off the surface by the airflow, much in the same way as a sand blaster removes rust and surface deposits.

Figure 6-15: Close-up of the centre of the impingement plate showing evidence of pitting

The first few tests still failed to give any positive results. Then finally, using 100 cSt oil applied in a globule at the centre, and running the jet for 30 seconds, the image in Figure 6-16 was captured. Unfortunately this image is slightly blurred and does not show very much detail or contrast, but there is still a very distinct pattern visible on the surface that is very different from anything observed in the previous experimentation. These patterns were also much more distinct when observed in the laboratory than what is shown in the image, and showed the definite presence of fringes as described by previous papers on the subject [7, 8, 11]. This image was the first evidence that the technique of oil film interferometry could in fact be used in this application.

The final step was then to refine the testing procedure to optimise the definition and resolution of the fringe patterns. This involved determining what oil viscosity gave the best results, determining the ideal jet run time, finding the optimal camera position and settings to capture the fringes, and finally attempting to generate the same results using discrete droplets rather than a single large globule.

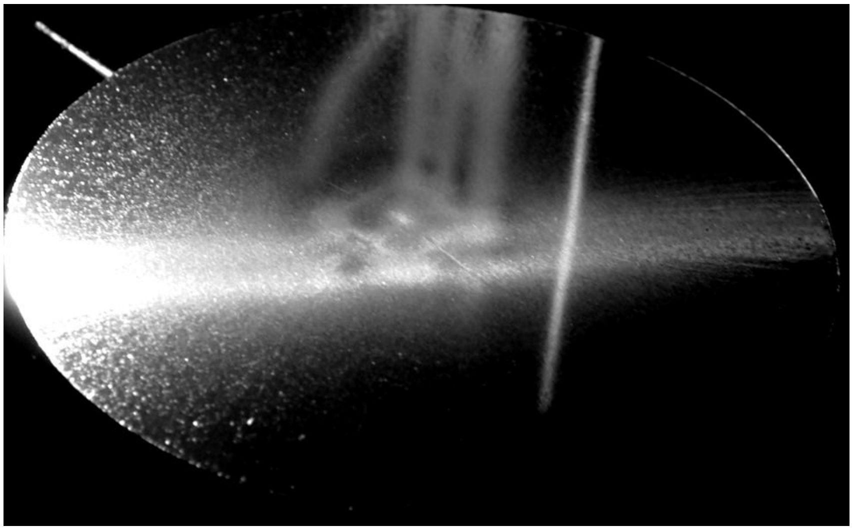

Figure 6-16: First fringe patterns generated. Oil v=100 cSt, NPR=1, n/d=2, t=30s, square nozzle

In order to determine the optimal oil viscosity for fringe imaging, a series of tests were run keeping all other variables constant and only the viscosity of the oil was varied. The constant parameters were set as follows:
Square Nozzle
NPR=1
n/d=2
run time=35s

Oil viscosities tested ranged from 200 to 1000cSt in intervals of 200cSt. Based on this set of tests it was found that the 400 and 600cSt oils produced the best images. Figure 6-17

(a) shows the clear fringes generated by the 400cSt oil test and Figure 6-17 (b) shows the comparatively poor fringe definition from the 800cSt test. This is not a totally unexpected result, since the higher the viscosity of the oil, the longer it will take to thin out to the point where fringes become visible. Conversely if the oil viscosity is too low it will thin out past the point of fringe interference before the jet has reached steady-state conditions.

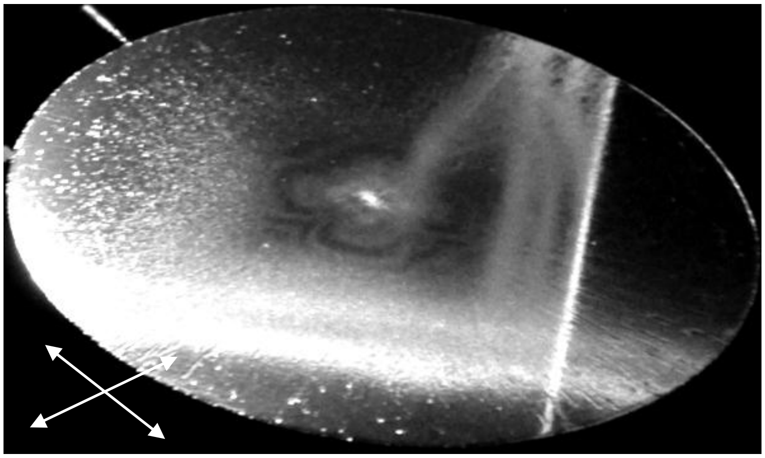

(a)

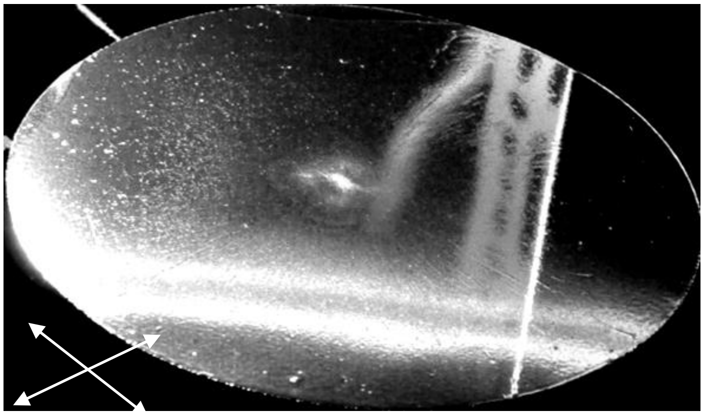

(b)

Figure 6-17: Fringe definition comparison. NPR=1, n/d=2, t=35s, square nozzle (a) *v*=400cSt (b) *v*=800cSt

What is very interesting to note about these images is the fact that the fringes are aligned with the diagonal plane and not the main axes (indicated by the cross in the bottom left corner of image (a)) as would be expected.

The presence of the fringes on the diagonal axes and not on the main axes indicates that the highest shear forces occur along the diagonal plane. This is somewhat counterintuitive, since it was noted above that the highest velocity areas where aligned with the main axes. Therefore it was expected that the highest shear would also occur in this area, since the higher the velocity, the higher the resultant shear force. This apparent high shear area along the diagonal axes is not a once off observation and is repeated in all images under these test conditions, regardless of oil viscosity. The same general pattern is also visible in the blurred image in Figure 6-16. At this point in the investigation these contradictory results could not be resolved. It was decided to push on with the refinement process in the hope that additional data would help explain this issue.

To further refine the range of optimal oil viscosities another batch of oil was mixed with viscosities ranging from 400cSt to 700cSt at intervals of 50cSt. At this point the plate covering was changed once again in an attempt to provide the best possible reflective surface for fringe imaging. The old plate covering was severely pitted at the centre, which could potentially skew results. The white oval visible at the centre of the impingement zone in Figure 6-17 indicates surface erosion, since it was still apparent after the plate surface had been cleaned.

It was found that under the test conditions mentioned above and within the range of 400-600cSt, the oil viscosity didn’t make a noticeable difference to the visibility of the fringes. The fringe patterns on the plate shown in Figure 6-18, which were generated using v=500cSt oil, look almost identical to those shown in Figure 6-17 (a).

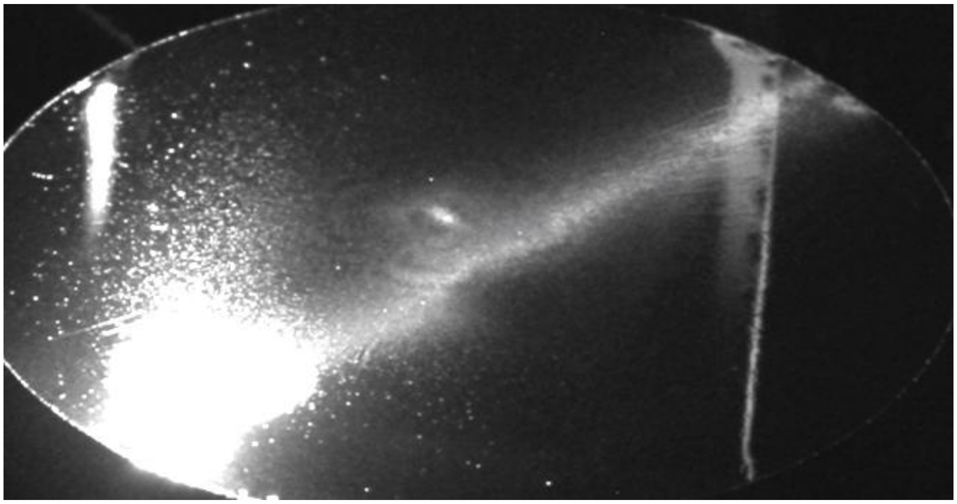

Figure 6-18: v=500cSt, NPR=1, n/d=2, t=30s, square nozzle.

The next important parameter to be optimised was the jet run time. In order to determine the effect of run time the entire plate surface was coated with a thin layer of 500cSt oil and images were captured at 20 second intervals, capturing the first image at 10 seconds, to track the development of the fringes. The reason that the method of oil application was changed for this test was due to the fact that during the above tests it was noted that it generally took between 10 to 15 seconds for the oil globule at the plate centre to spread out over the entire plate. It was hoped that by spreading the oil over the entire plate prior to turning on the jet, the area in which fringes were visible would be increased without sacrificing any fringe resolution at the centre of the plate. The series of images in Figure 6-19 shows the evolution of the fringes over a total run period of 110 seconds.

Examining the images, after 10 seconds the majority of excess oil has been blown off the plate and any large variations in the oil coating have been removed. But at this point the oil has not thinned out enough to generate fringes. 20 seconds later the oil film is sufficiently thin to allow for the interference patterns to become visible. The image in Figure 6-19 (c) possibly shows the best fringe resolution out of the sequence. After 50 seconds the fringes have broadened out significantly, however the area in which fringe patterns are visible has not increased. The final four images in the sequence show the degeneration of the fringes until, after 110 seconds, virtually no distinct fringes are visible at all.

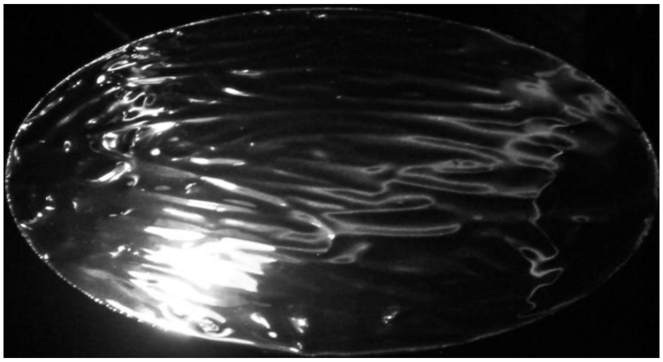

(a)

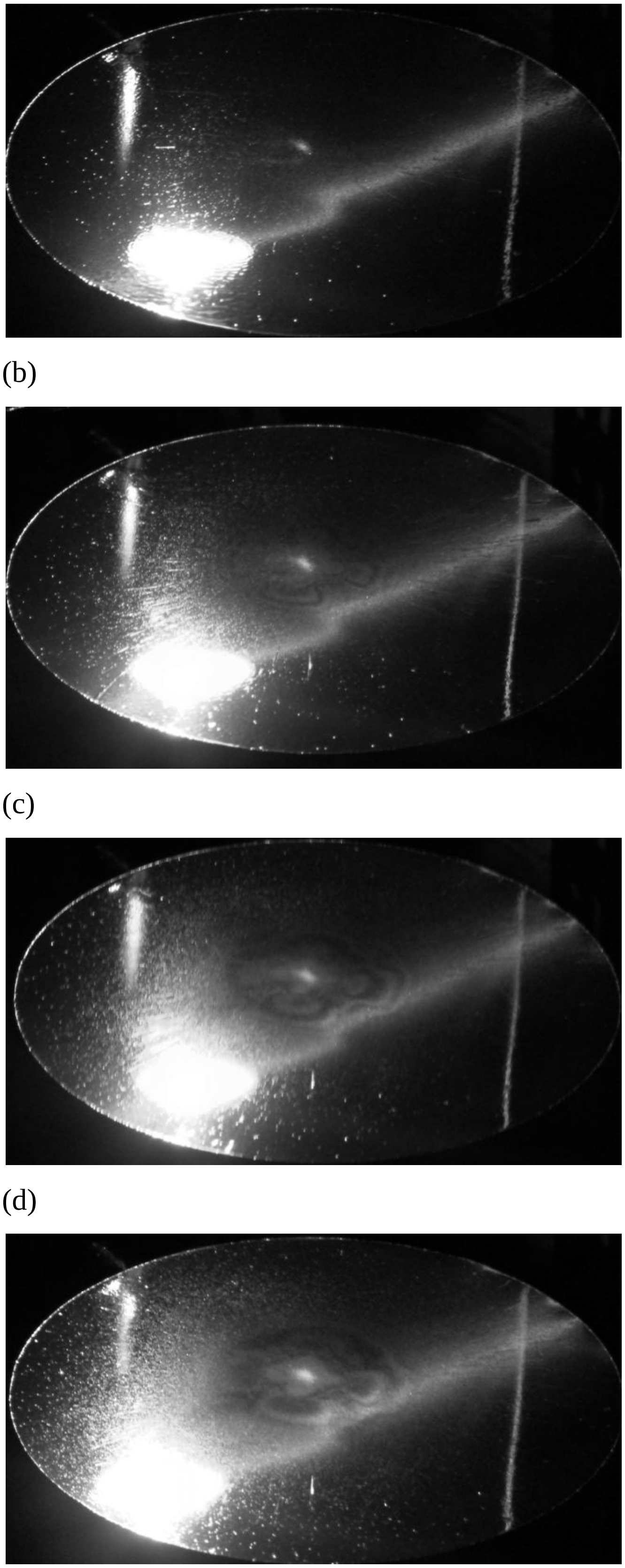

(b)

(c)

(d)

(e)

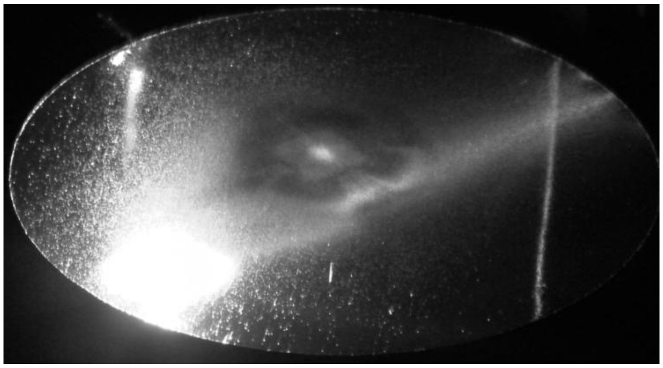

(f)

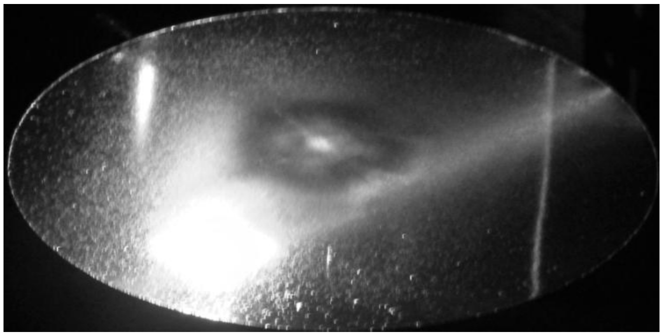

(g)

Figure 6-19: Evolution of fringes (a) initial oil coating (b) 10s (c) 30s (d) 50s (e) 70s (f) 90s (g) 110s

Although the test illustrated in Figure 6-19 was not carried out in strict accordance with the test procedure of only changing one parameter at a time, the images did serve to give a good general understanding of the effects of run time on the appearance of fringes on the plate. The pictures shown in Figure 6-19 indicate that a jet run time of approximately 30 seconds generated the best results. However the question still remains as to whether or not these results could be correlated directly to the central globule application method.

The first evidence that they can be directly correlated is shown when comparing the image in Figure 6-19 (c) to that shown in Figure 6-18. After a run time of 30 seconds, the fringe patterns for both application methods appear to be almost identical. Further evidence that the two application methods are comparable is shown in the two images in Figure 6-20. Figure 6-20 (a) shows the fringe patterns on the plate using the globule application technique; Figure 6-20 (b) shows the fringes generated by smearing the oil over the plate.

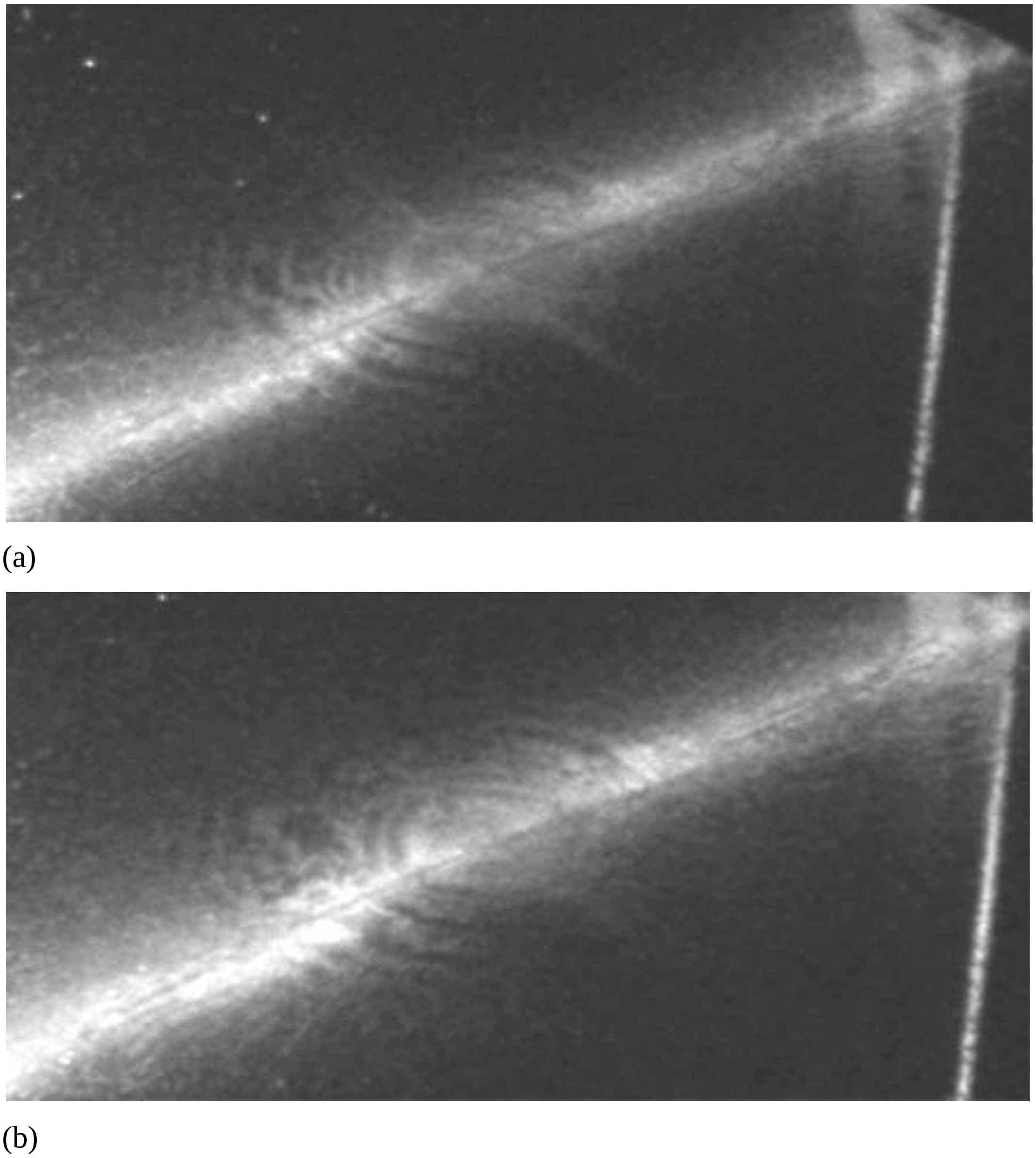

Figure 6-20: ***v*=600cSt, NPR=1.5, n/d=2, t=30s, square nozzle (a) globule (b) smear**

Comparing the two images there are obvious differences in the fringe patterns, however the overall trends displayed in both images are the same. The fringes in Figure 6-20 (a) appear to be slightly more coherent than those in Figure 6-20 (b). Therefore it was assumed that the generalised conclusions made about the time dependant appearance of fringes in the test above would hold for the other oil application techniques used in this investigation. Thus for the remainder of this investigation the jet run times were limited to a range of 20-40 seconds.

All the fringe images shown above give a good general idea of the flow fields on the plate, as has been discussed. But the main objective of this investigation was to generate images in which both qualitative and quantitative data could be disseminated. Since the images generated thus far did not allow for any quantitative analysis, the experimental procedure had to be further refined.

The problem with using a single globule at the centre of the plate is that the thin film equations detailed in section 3.3 cannot be used to analyse the images. This is because the equations require the initial position of the oil (the point where the oil thickness is zero) to be used as a datum point. Whilst this point can be determined quite easily for a single drop (it is taken as the starting edge of the original drop) it cannot be determined for a large globule. The final stage in this optimisation process was to extend the interferometry techniques that had been developed to generate fringe images using discreet droplets.

Oil drops were placed on the surface at known positions, using the apparatus discussed in section 4.3.4. The rest of the methodology was the kept identical to the previous experiments. As is visible in the image in Figure 6-21, the oil droplets gave very good fringe definition. The interference fringes in this test could finally be used to generate quantitative data.

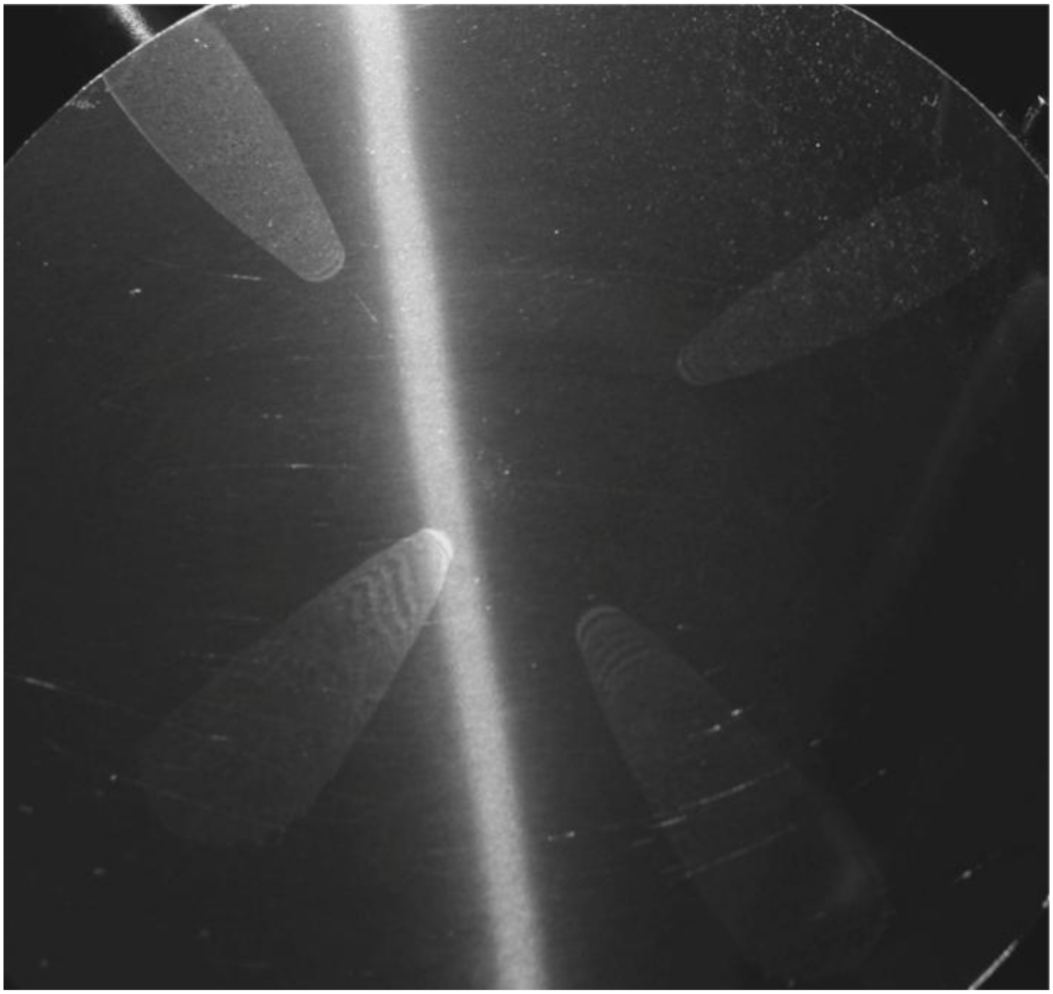

Figure 6-21: Droplets along main jet axes. NPR=1 n/d=2 v=550cSt t=20s

At this point the testing methodology was considered to be refined to an acceptable degree. The remainder of the testing was carried out to investigate the effects of varying nozzle pressure ratio and nozzle geometry on the surface flow fields. Using the square nozzle, tests were carried out for nozzle pressure ratios of 1 and 2. A rectangular nozzle with an aspect ratio of four was also used, and tests were performed with nozzle pressure ratios of 1 and 2.

7 Data Analysis

The data analysis techniques used in this investigation were based on the methods detailed by Decker and Naughton [8]. The image processing toolbox in MATLAB© was used to identify and analyse fringe patterns in the experimental images. The entire code used for image analysis can be found in Appendix D.

The final objective of this analysis process was to determine the shear forces experienced by the oil coating. This was done by using a three step analysis process:

The first step was to determine the distance between each fringe.

The image being analysed is read into MATLAB and cropped down to the area of interest. Figure 7-1 below shows the initial image and cropped images. Figure 7-1 (a) shows the entire plate with fringe patterns visible. This image was generated using drops of oil of 550cSt placed at intervals along the main axis of the jet. The drops were placed at 10, 20, 30 and 40 mm from the centre of impingement. The jet flow was emitted from the square nozzle with Nozzle Pressure Ratio (NPR) equal to 1 and the plate set 20mm or 2 Nozzle Diameters from the nozzle exit. The jet was run for 20 seconds.

It should be noted that the image shown in Figure 7-1 (b) shows a lot of graininess and pixel noise. This is due to the fact that the contrast of the image has been adjusted using the function *imadjust*. Performing this contrast adjustment seems to be rather counter-productive since it introduces unnecessary noise into the data. However this is in fact not the case. Since the objective of this step in the analysis process is to determine the spacing of the fringes, adjusting the contrast actually serves to improve the resolution of the fringes in the image. Comparing the adjusted image shown in Figure 7-1 (b) with the unadjusted image shown in Figure 7-2, the fringes are much clearer in the adjusted image.

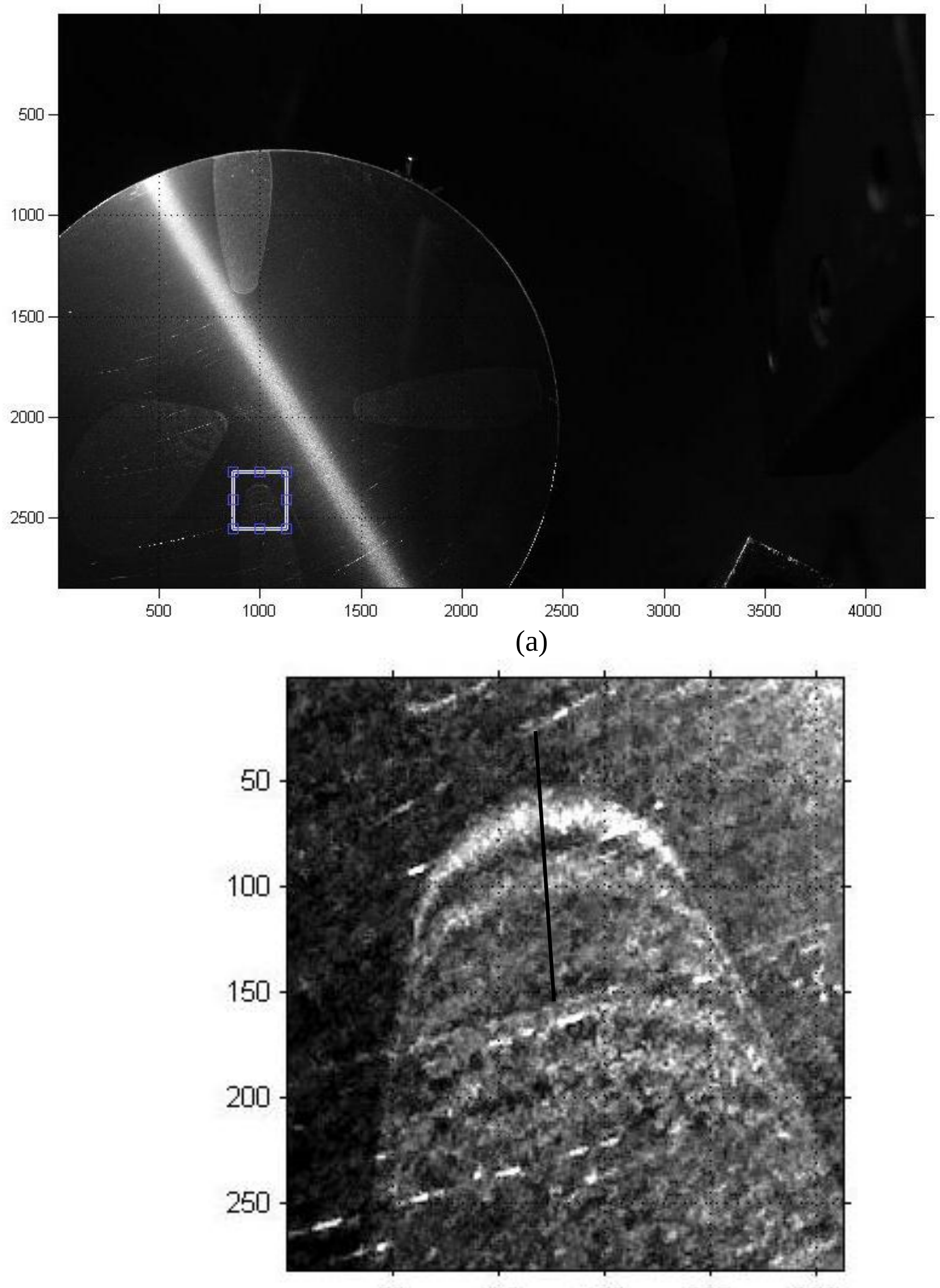

(a)

(b)

Figure 7-1: Overall and cropped interferometry image. Square nozzle NPR=1 N/D=2 t=20s ν=550cSt

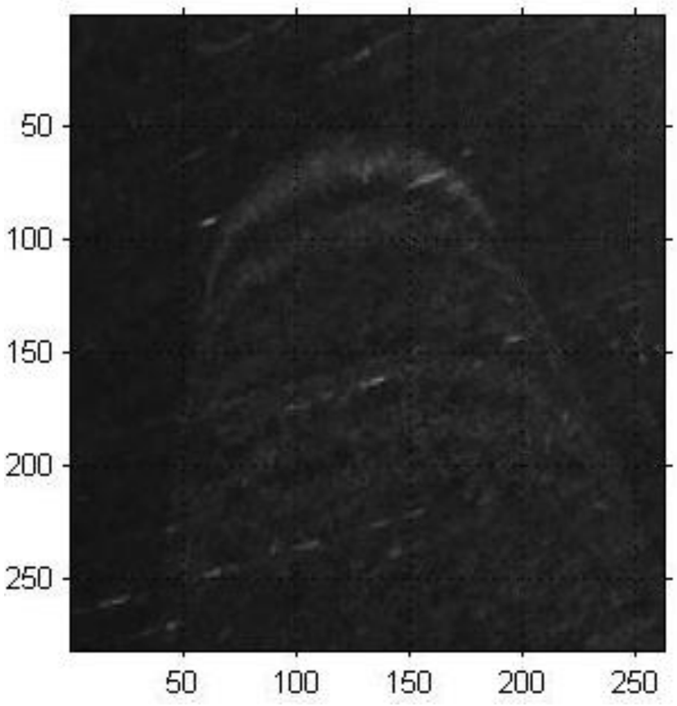

Figure 7-2: Fringe Image without Contrast Adjustment

Once the area of interest has been identified and the image cropped down to magnify this area, the next step is to find the pixel spacing between each fringe. This was done by using the *improfile* function in MATLAB.

A line is drawn across the fringes as illustrated in Figure 7-1 (b). The *improfile* function then generates a pixel intensity graph, as shown in Figure 7-3. This graph shows the pixel intensity values versus pixel distance along the line.

Whilst this graph does show a periodic oscillation due to the presence of the light and dark fringe bands, the large amount of noise makes it extremely difficult to determine the actual position of each fringe. Therefore the intensity data was passed through a low-pass filter to make fringe identification easier.

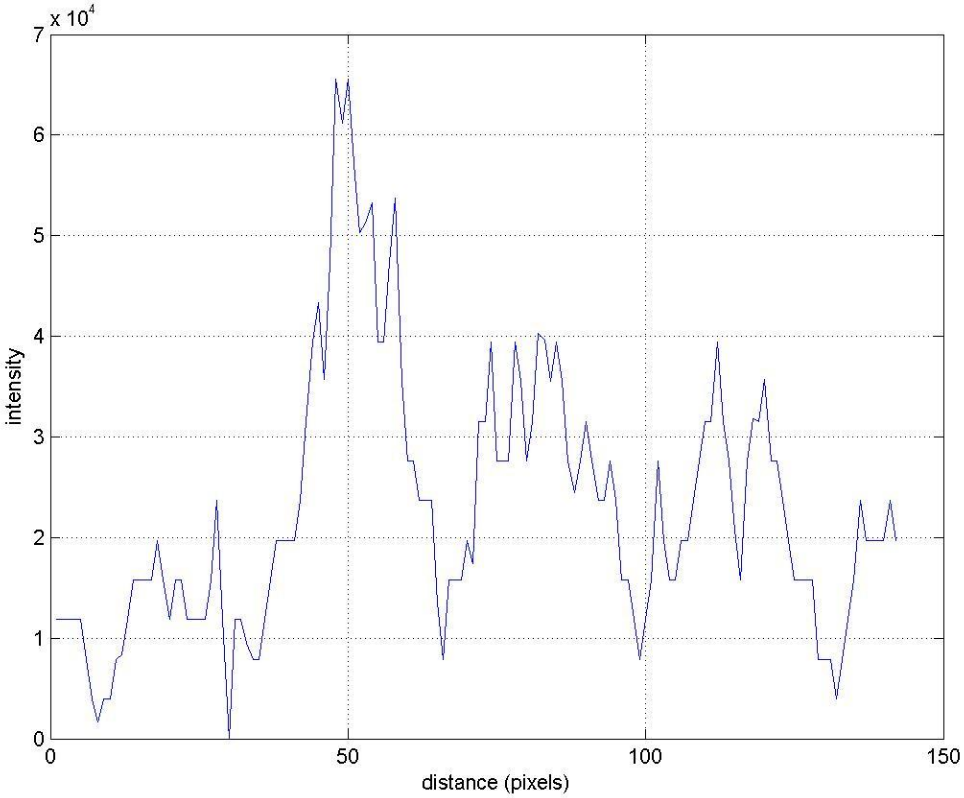

Figure 7-3: Initial Pixel Intensity Graph

A Fast Fourier Transform (FFT) was performed on the data to determine the cut-off frequency for the filter. The graph shown in Figure 7-4 shows the FFT magnitude versus the normalised frequency. The graph shows a number of peaks close to the origin with a large peak at 0.0285. The FFT magnitude drops off significantly after this peak value. Therefore this is chosen as the cut-off frequency for the low-pass filter.

Using the *filter* function, the data from Figure 7-3 was cleaned up and the high-frequency noise was removed. The filtered data is shown in Figure 7-5.

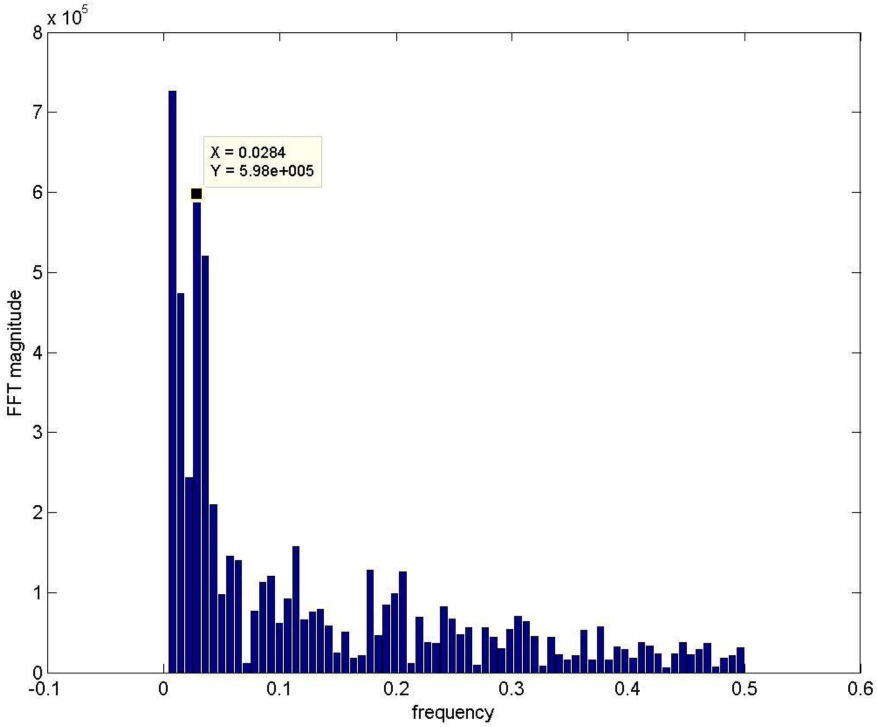

Figure 7-4: Graph of FFT magnitude versus normalised frequencies

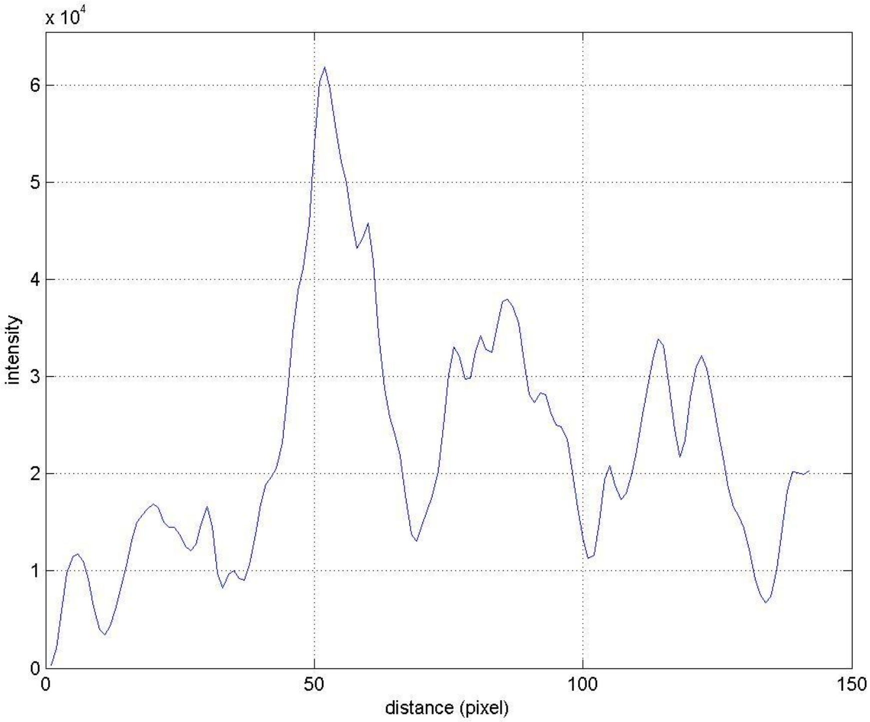

Figure 7-5: Filtered pixel intensity data

The pixel-wise position of each light and dark band now becomes much clearer. Examining this graph in conjunction with the actual fringe image shown in Figure 7-1, the three large-amplitude peaks obviously correspond to the first three light fringes visible in the image. There are a further two, possibly three, fringes visible in the image past the point of the end of the interrogation line. However scratches in the plate surface make it impossible to determine the pixel-wise position of these fringes. As is visible in the image even very light scratches that have no apparent adverse affect on the flow of the oil still show up as light streaks when photographed under interferometry conditions. Therefore if the interrogation line was drawn over these scratches they would no doubt give false positives in the intensity graph, and possibly also affect the FFT graph as well.

Using the filtered intensity graph in conjunction with the adjusted fringe image, the following vector was generated. Using the data point curser in the MATLAB figure the pixel position of each peak and trough was identified:

$$Fringe\ Spacing = [52\ 69\ 86\ 101\ 118\ 134]$$

This vector gives the pixel-wise position along the line of each maximum (light band) and minimum (dark band). However these values are in reference to the beginning of the interrogation line, which starts some distance in front of the leading edge of the oil. The pixel-wise position of the leading edge along this line was thus subtracted from these initial values to give the true pixel spacing of each fringe. The leading edge of the oil is visible in the intensity graph as the first small peak point before the first maximum fringe.

As mentioned previously the oil height theory predicts a ‘zero’ dark fringe before the first maximum intensity area. This zero fringe is visible as the drop in intensity just prior to the first maximum fringe. It can therefore be assumed that the leading edge of the oil will be at the start of this zero fringe.

The leading edge point was found to be 20 pixels from the start of the interrogation line. Subtracting this from the *Fringe Spacing* vector gives:

$$Fringe\ Spacing = [32\ 49\ 66\ 81\ 98\ 114]$$

This vector gives the distance from the leading edge of each successive fringe. However as it stands this vector cannot be used to determine any shear forces. This is because this vector gives distance values in terms of pixels, which is an entirely subjective measurement value that has no direct physical value since pixel density is dependent on the camera resolution and zoom. Thus the next step in the analysis process was to determine the physical distance represented by these pixel values. This was done using the following process:

Once all the fringe images had been captured from each experiment an over-head transparency was placed over the impingement plate. This transparency, shown in Figure 7-6 below, had a series of concentric circles printed on it. The circles are 5mm apart. This was then photographed with the camera in the same position and the same settings and zoom as the previous fringe images. This ensured that this reference picture had the same pixel density as the fringe pictures. This reference image was then taken through the same analysis process as the fringe images:

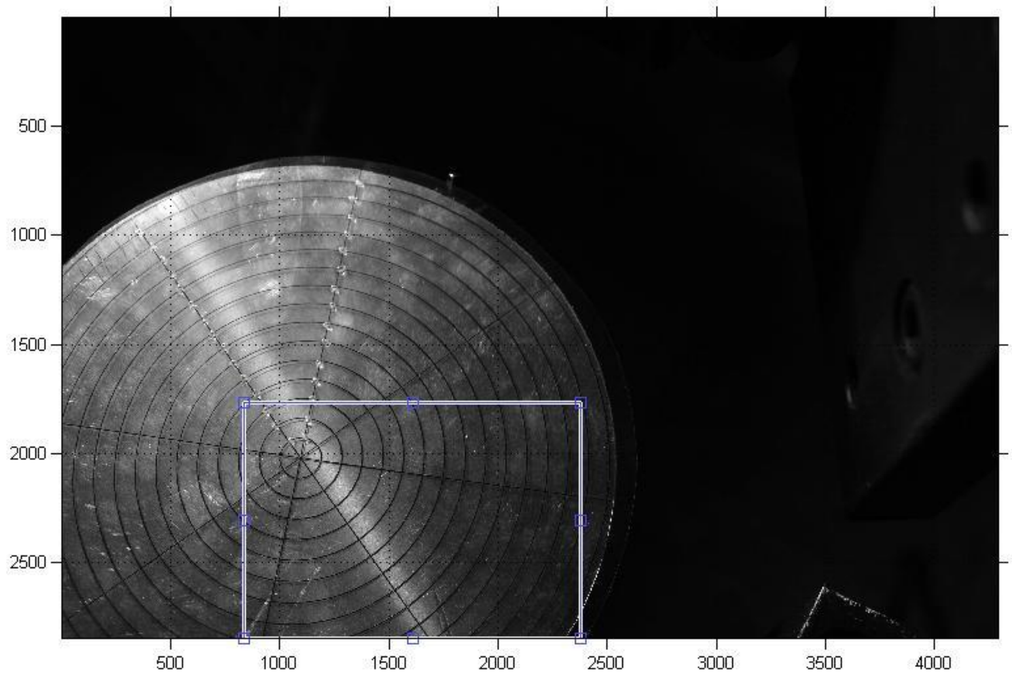

Figure 7-6: Impingement plate with reference circle

Zooming in on the area of interest of the plate the oil fringes are just barely visible through the transparency, as highlighted in Figure 7-7. This fact is important since the error of parallax caused by the images being captured at an angle means that pixel distances on different areas of the plate will represent different physical distances.

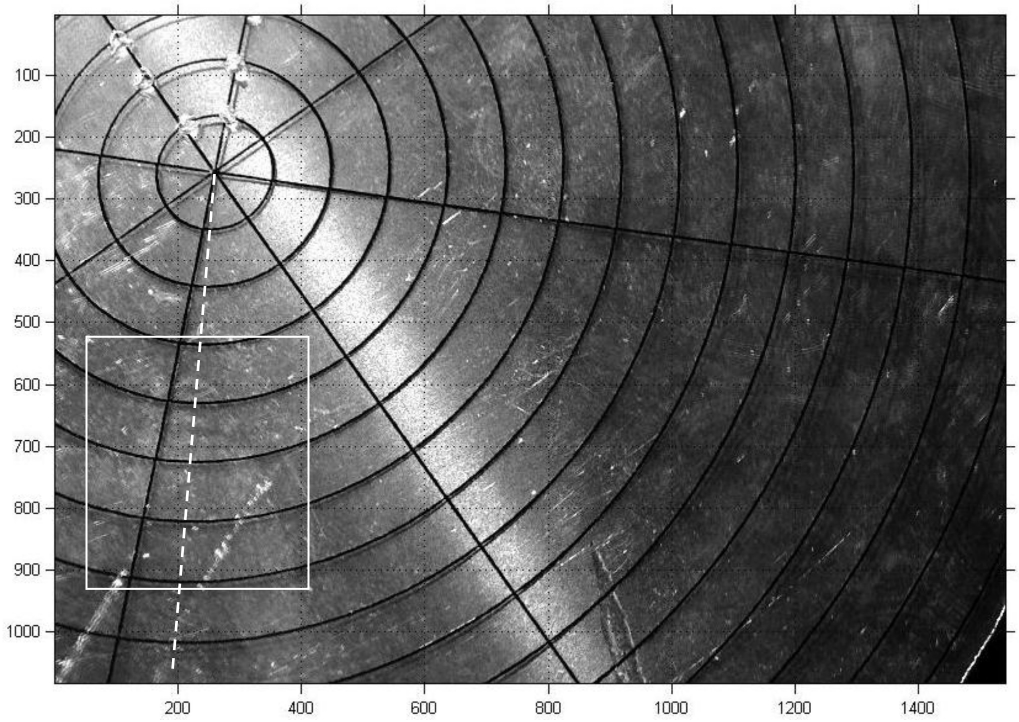

Figure 7-7: Cropped reference image

The *improfile* interrogation line, shown by the dashed line, was then taken from the centre of the circle to the edge of the image, through the visible fringes. It is important that the line starts from the centre of the reference circles since this ensures that the line cuts through all reference lines at 90^o, thus ensuring that each dark line is the same thickness.

Plotting the pixel intensity along this line generates the graph shown in Figure 7-8. The position of each of the eight reference lines along the interrogation line are represented by the sudden, large amplitude drops in the intensity.

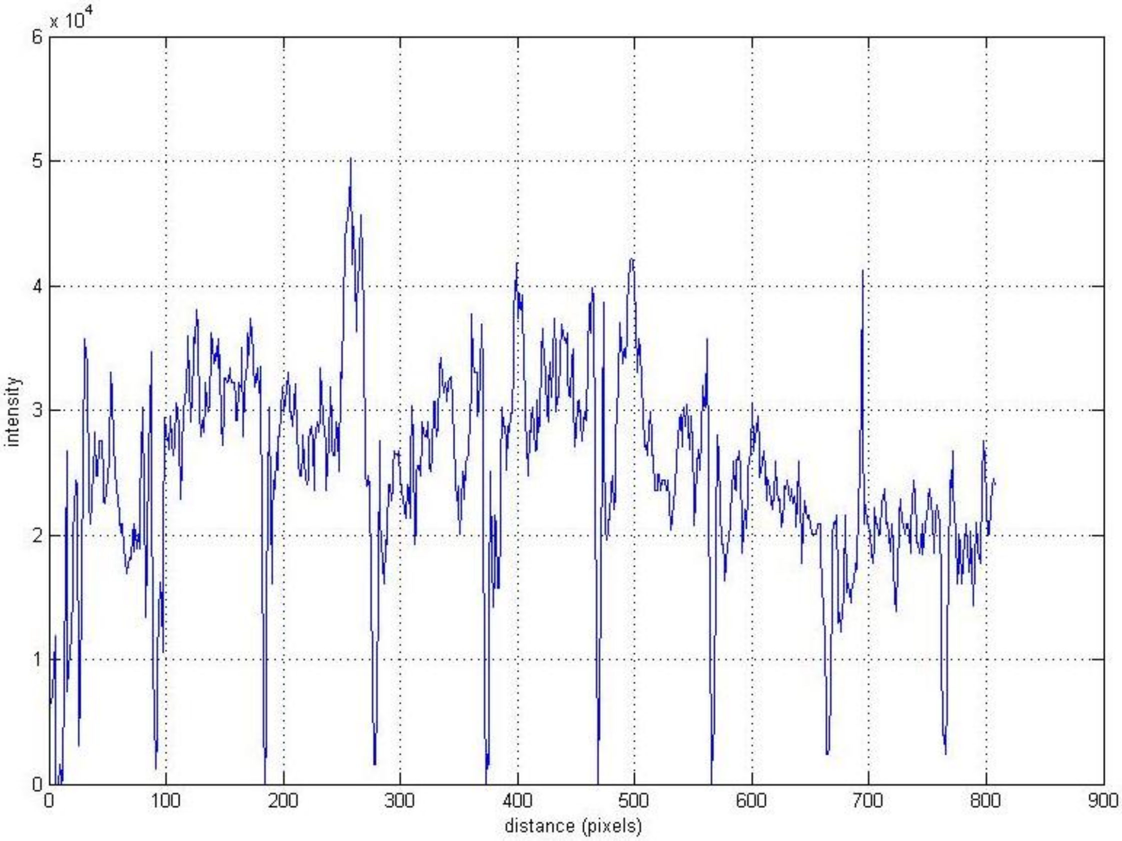

Figure 7-8: Pixel intensity plot of the reference image

Although it is not strictly necessary in this case, since the position of each local minimum is clearly visible, the intensity data is taken through the same filtering process as the fringe data. This is done because in some cases the area of interest is not very well illuminated and as such darker areas of the image may give false positives in the data.

Putting the data through the low-pass filter function gives the graph shown in

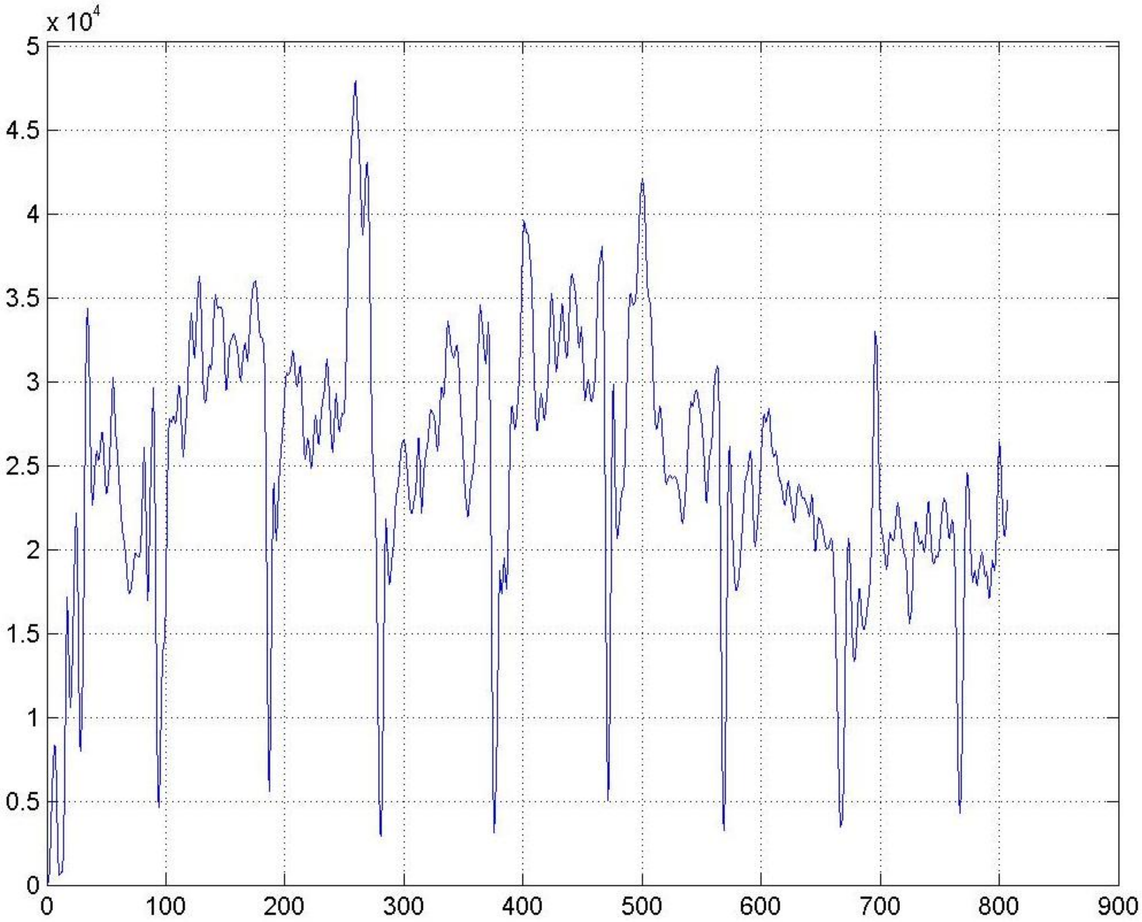

Figure 7-9. This graph is then used to find the pixel-wise position of each reference line. This gives the following vector:

$$line\ distance = [94\ 187\ 281\ 376\ 471\ 569\ 667\ 767]$$

Taking the difference between each line's pixel position gives the line spacing vector:

$$line\ space = [93\ 94\ 95\ 95\ 98\ 98\ 100]$$

Taking the average of this vector gives an average line spacing of 96.14286 pixels. Since the physical distance between each circle is known to be 5mm, dividing the pixel spacing by the physical spacing then gives the average number of pixels per millimetre in this area of the image. Thus the area of the image containing the fringe pattern being analysed has a pixel density of 19.228571 pixels per mm.

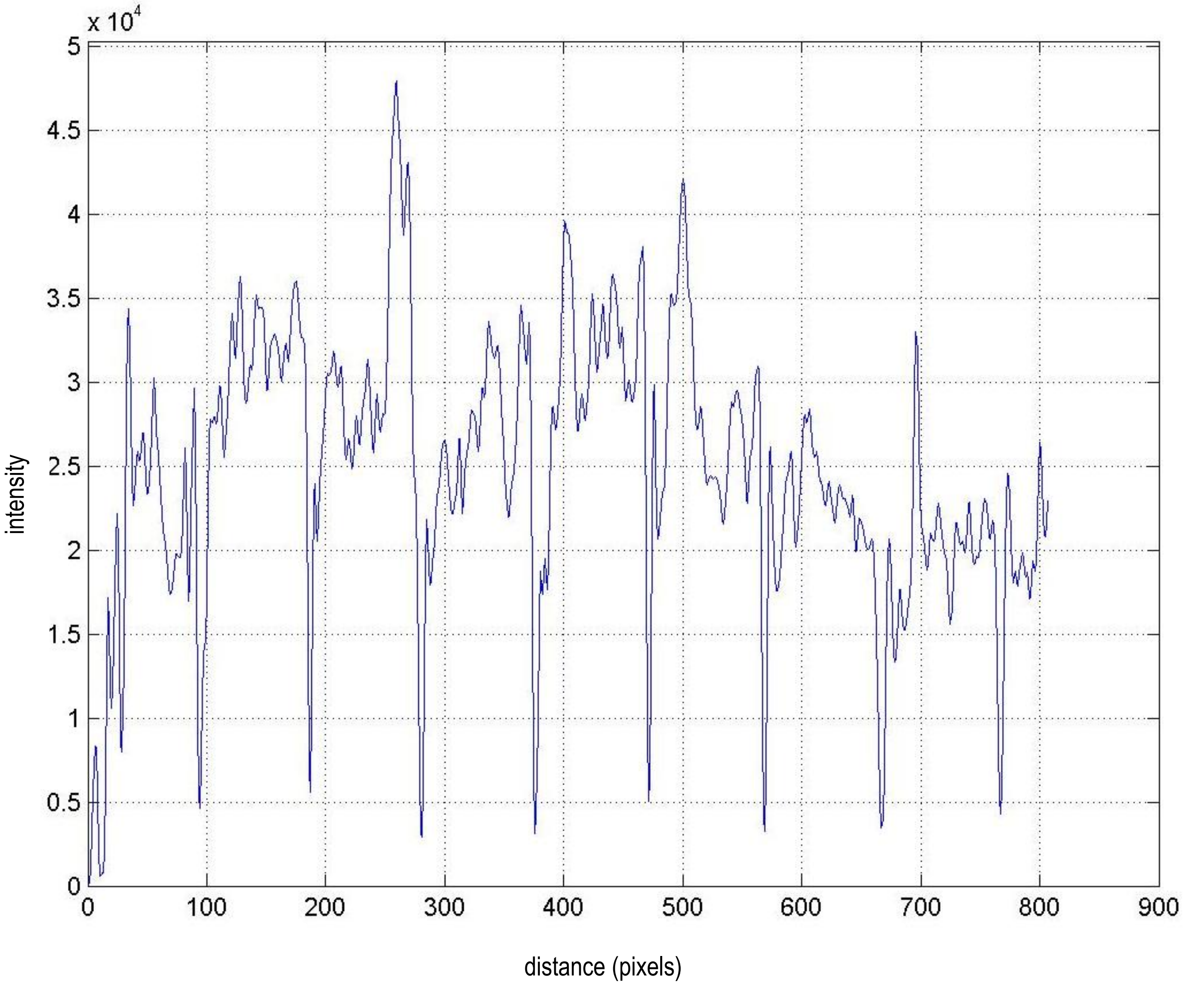

Figure 7-9: Filtered reference intensity graph

The fringe spacing vector was then divided by the pixel density to give the fringe spacing in millimetres. Converting to metres gives the fringe spacing vector:

$$fringe\ spacing = 10^{-3} \times [1.66\ 2.55\ 3.43\ 5.10\ 5.93]\ m$$

The next step is to determine the oil height at each fringe point. This was done by using the oil height equation defined in section 3.3. For ease of reference Equation 3-8 has been repeated below:

$$h = \frac{k\lambda_0}{4}\frac{1}{\sqrt{n_f^2 - n_1^2 \sin^2\theta_i}}$$

In the process of experimentation the only variable in the above equation that could vary is the angle of incidence of the light θ_i. This was determined by measuring the angle from the vertical of the camera lens using a bubble inclinometer. The angle of incidence was measured from the camera side rather than the light source side due to the fact that the light source had a short coherence length. Adding to this the fact that the sodium lamp used was an extended light source, measuring the angle of incidence from the source side would not give a realistic idea of the angle at which the light hits the plate. Measuring the angle of the camera from the vertical thus gives a better representation of the angle of incidence of the light.

In the case of the sample calculation detailed here, the angle of the camera was measured to be 20^0. The other variables in Equation 3-8 are set by the light source and oil. Since the same type of oil and the same light source were used throughout this investigation, these values can be considered to be constant. Therefore the input parameters for this Equation 3-8 were:

$\lambda_0 = 589x10^{-9}m$
$n_f = 1.40$
$n_i = 1.0$
$\theta_0 = 10^0$

As was mentioned in section 3.3, k is a positive integer multiplication factor. In this sample analysis the oil has a total of six light and dark bands. Therefore k was incremented from 1 to 6. This gives the oil height vector:

$$h = 10^{-6} \times [10.85\ 21.69\ 32.54\ 43.39\ 54.23\ 65.08]\ m$$

The data from this oil height vector and the corresponding fringe spacing vector given above were then used to calculate the shear forces using Equation 3-7. Once again for ease of reference this equation has been repeated below:

$$\tau = \frac{2\mu_0}{h^2 t} \int_0^x h\, dx$$

Before Equation 3-7 could be applied, it was necessary to determine a continuous expression for the oil height. This expression was estimated using the MATLAB *polyfit* function. This function takes the discreet x-y data and fits a polynomial curve to it, the degree of the polynomial being set by the user.

The resultant curve was then plotted with the original data to determine the goodness of fit of the function. This curve was extrapolated past the original data to ensure that the function followed the overall trend of the data. This was done because although a function may follow the data very closely within the given range, it may diverge from the data trend after this. An example of this is shown in Figure 7-10 below. Examining the first graph, which is a fifth order polynomial, the curve seems to follow the data quite well. However the curve diverges rapidly from the data set when extrapolated backwards. In comparison, the second order polynomial fit shown in Figure 7-10 (b) follows the overall trend much better when extrapolated past the data range in both directions.

Another consideration when choosing the order of the best fit curve was the fact that MATLAB warns the user when the curve is poorly conditioned. For the majority of the data processed in this investigation this usually occurred for polynomials of order five and above, sometimes as low as three when there were a small number of data points.

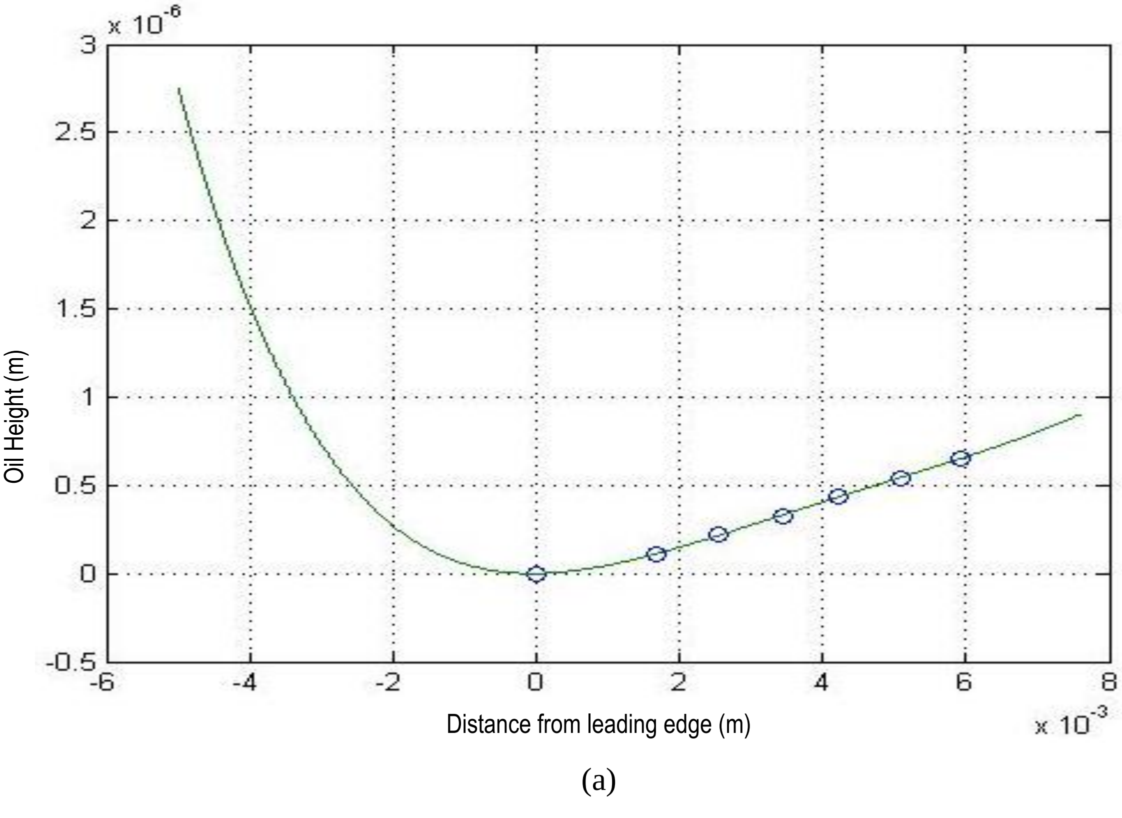

(a)

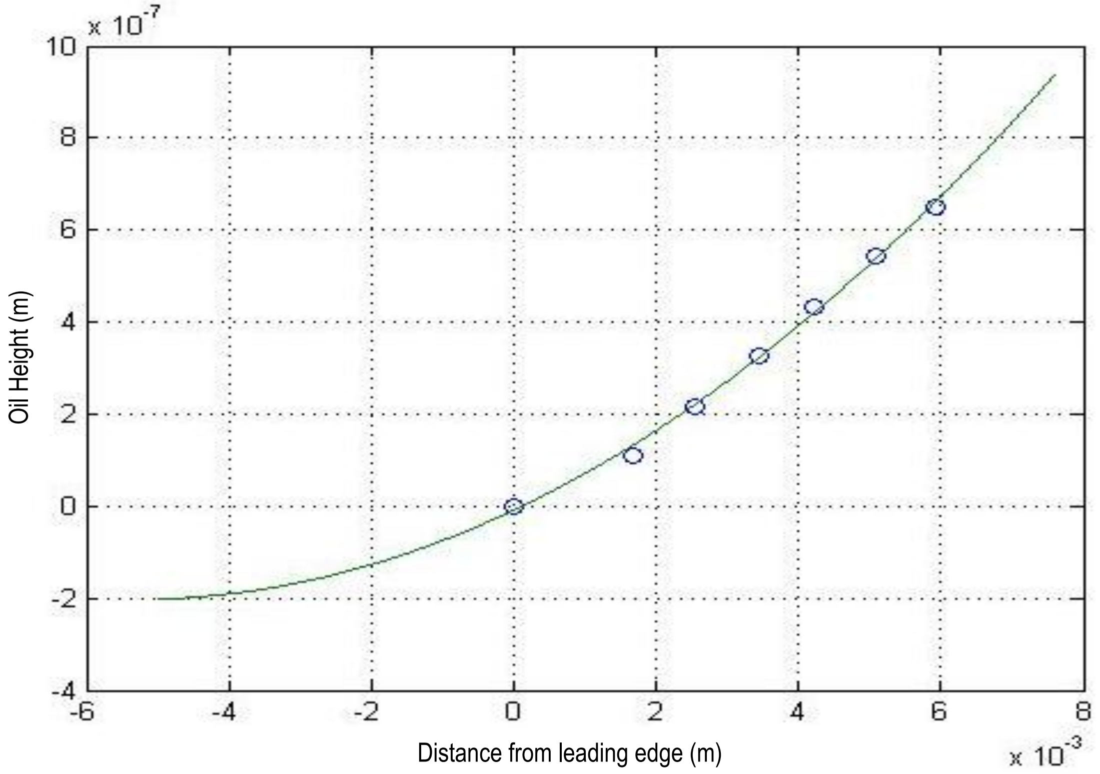

Figure 7-10: (a) Fifth order polynomial (b) Second order polynomial

Therefore, even though the curve doesn't fit the data quite as well as the fifth order polynomial, it was decided in this case to use the second order polynomial to determine the shear forces.

Using the equation of the chosen best fit curve, new oil height values were then calculated and substituted into the shear force equation.

Evaluating the equation for each fringe point, the following shear force vector was then generated

$$shear\ force = [298\ 274\ 252\ 236\ 219\ 206]$$

This analysis process gives the shear forces along the plate at each oil flow point. However this data is only valuable if it placed in reference to the rest of the experimental data. The final step in the process of analysing each fringe patterns was therefore to determine the position of each set of data from the common datum point of the centre of impingement.

Before each test was run the impingement plate with the original positions of the oil drops was photographed. Using the *imtool* function the pixel distance of the edge of each oil drop from the plate centre was measured, as illustrated in Figure 7-11.

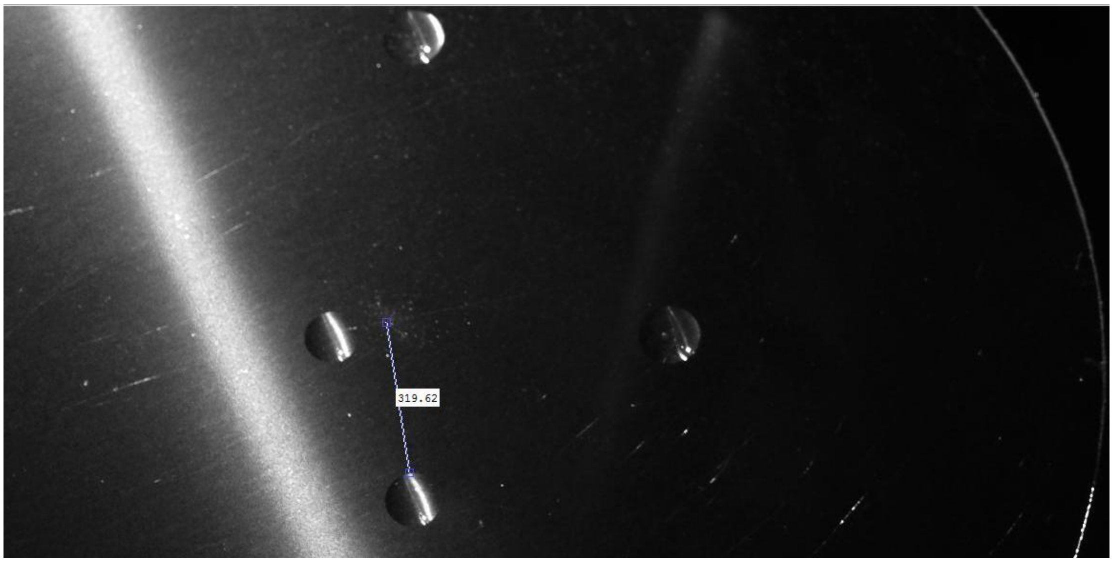

Figure 7-11: Initial position of oil drops on plate with measurement tool shown

As mentioned in Section 6 above, the soft aluminium suffers erosion and pitting at the centre of the impingement zone. Whilst this is a general concern in terms of the experimental data, in this case it serves to aid in the measurement of the position of the oil drops, giving a clear indication as to the position of the common datum point. Figure 7-11 shows the measurement line drawn from the centre to the edge of the oil drop positioned approximately 20mm from the centre. Although it is not clearly visible in the figure, the data label shown gives the pixel-wise length of the line. In this case it is found to be 319.42 pixels. Using this measurement, as well as the pixel density calculated previously, it was found that the leading edge of the oil drop under investigation is approximately 16.6mm from the centre of impingement. Adding this value to the fringe spacing vector shown previously gives the follow table of distance from jet centre versus shear force:

Table 7-1: Distance from Jet Centre vs. Surface Shear Force

Distance (mm)	Shear Force (Pa)
18.28	298.39
19.16	274.09
20.04	252.68
20.82	236.17
21.71	219.75
22.54	206.16

The identification of fringes has always been a very subjective process. Even though the analysis process described above makes it easier to identify the position of the fringes, it is still subject to interpretation by the user. Therefore in an attempt to minimise the effect of this the process described above was carried out a number of times on each fringe image to get an average shear force value. All the analysis runs were then plotted together to assess the general trend of the data, as shown in Figure 7-12 below. Comparing the behaviour of all data sets, any set that shows large deviation from the general trend was then removed from the total set before averaging.

In the case shown below all ten data sets appear to show the same general trends, save perhaps data set eight. However since this data set still does not deviate considerably from the general trend it was not removed. In general only if a data set was clearly outside of the norm was it removed. The main purpose of this step was to allow for the case when erroneous data points were entered during the analysis process. An example of this is given in Figure 7-13 below.

This graph shows the effect of mistakenly adding an extra digit to a fringe pixel distance point during data entry. The entire data set was then removed from the averaging matrix. Because the pixel distances are used to calculate the best fit curves and generate an equation for integration in the shear force equation this one bad point means that the entire data set is affected and must be removed. Once the bad data set was removed all remaining sets were re-plotted and the process was repeated until all bad data sets have been removed. The remaining data sets were then averaged to give the final distance versus shear force data. For the sample calculation given here this averaged data is given in Figure 7-14 below.

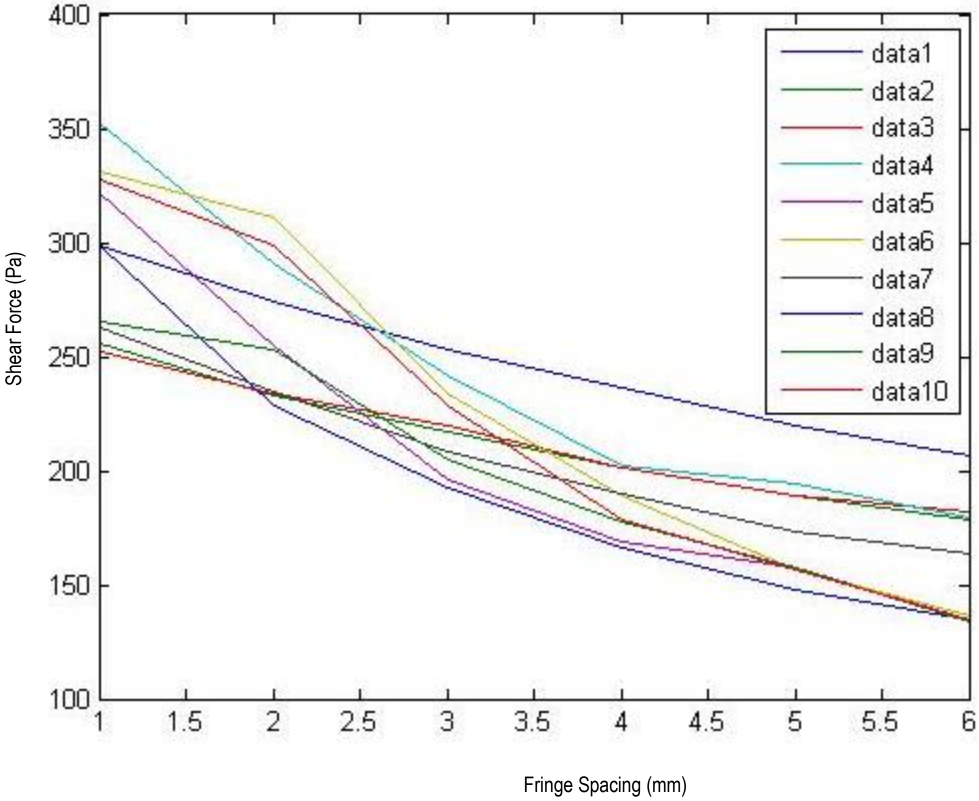

Figure 7-12: Graph of Distance versus Shear Force for all data sets

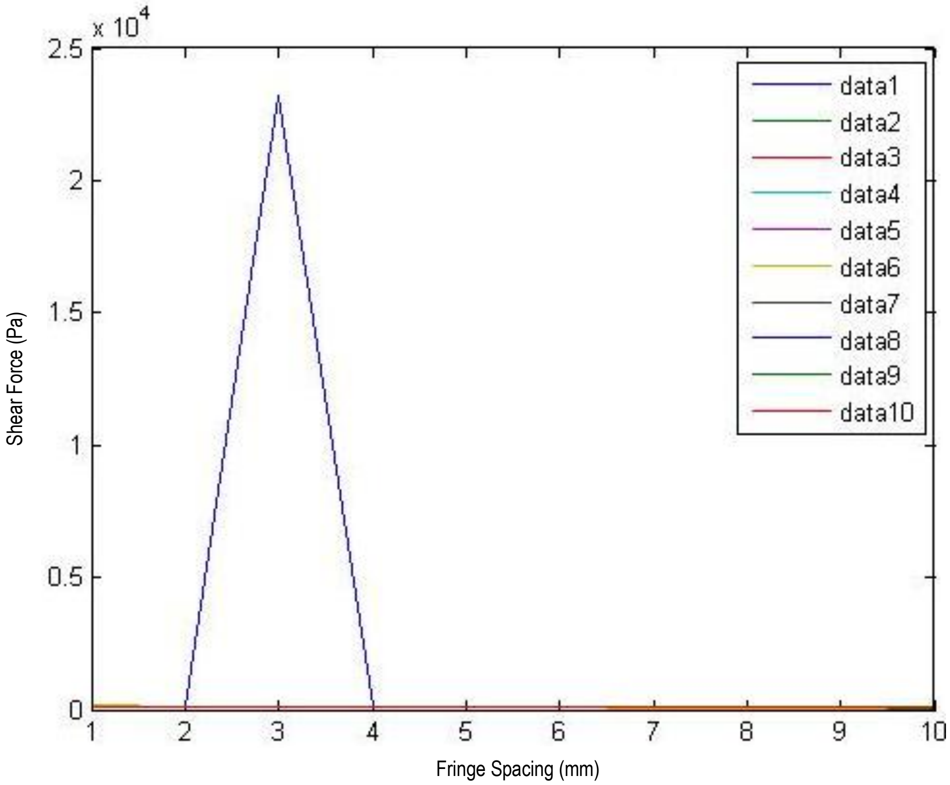

Figure 7-13: Graph of Distance versus Shear Force illustrating the effect of an erroneous data point

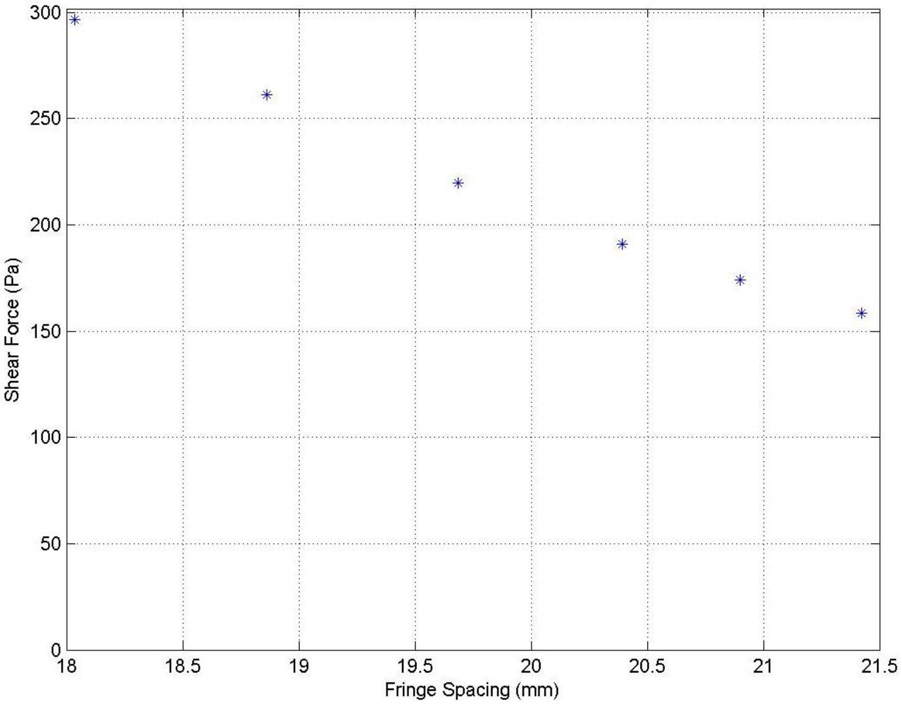

Figure 7-14: Average Distance vs. Average Shear Force

8 Uncertainty Analysis

In all measuring equipment, no matter how accurate it is, there is always a certain amount of uncertainty inherent in the data it provides. These uncertainties in the raw data gathered results in the presence of uncertainties in the final analysed data. In order to properly account for these uncertainties, the effect of these initial possible errors has to be determined. A relationship between the raw and analysed uncertainties was determined as follows:

If the resultant variable, *F*, is dependent on *n* number of independent variables x_1, x_2, x_3,…, x_n, then the resultant uncertainty, ΔF, due to uncertainties $\Delta x_1, \Delta x_2, \Delta x_3, \ldots, \Delta x_n$ can be calculated using the following equation:

$$\Delta F = \sqrt{\left(\frac{\partial F}{\partial x_1}\Delta x_1\right)^2 + \left(\frac{\partial F}{\partial x_2}\Delta x_2\right)^2 + \left(\frac{\partial F}{\partial x_3}\Delta x_3\right)^2 + \ldots + \left(\frac{\partial F}{\partial x_n}\Delta x_n\right)^2}$$

Equation 8-1 [13]

Examining the experimental process, the following areas were identified as points of potential error due to the resolution of the measuring equipment:

Starting from the apparatus set up, the first area of uncertainty is the positioning of the impingement plate below the jet nozzle. As already discussed, the initial securing of the plate mount to the floor resulted in the centre of the jet being slightly offset from the centre of the plate. The effects of this error were negated by altering the oil application apparatus, as well as measuring the position of all oil coatings on the plate from the position of the centre of impingement and not the centre of the plate.

Other points of potential error in the plate positioning were the measurement of the plate distance from the nozzle exit and the angle of the plate from the horizontal. However these errors were considered to be negligible, since the plate distance was measured by the use of vernier callipers, ensuring a plate distance error of 0.005mm, and the plate angle from the horizontal was checked at the beginning of each test day with a spirit level placed along both planes. Although a spirit level is not graduated and as such the potential error cannot be quantified, it was taken to be less than a degree in either direction. The very small potential errors in the plate set up are so small in comparison to the other sources of potential error that they were ignored.

The first point of major uncertainty was introduced when measuring the angle of the camera. As mentioned previously this measurement was performed using a bubble inclinometer. Whilst this device has an accuracy of 0.01^o, the measurement process used introduced an uncertainty several orders of magnitude greater. The size and weight of the bubble inclinometer was such that it could not be safely positioned on the camera lens itself. In order to measure the angle at which the images were captured, the camera had to be removed from the tripod. This act in and of itself has the potential to change the angle and position of the camera mount on the tripod. Adding to this was the fact that the locks on the tripod legs allowed for a small amount of slip, meaning that the relative length of the three legs could be altered slightly from their original position when the camera was in place. Finally over the course of this investigation, the floor of the laboratory became coated in a thin layer of the silicone fluid that had been blown off the apparatus during jet runs. This meant that the tripod legs could slip across the surface quite easily, thereby altering the angle and position of the camera. Taking all these factors into account, an optimistic estimation of the camera angle uncertainty was taken as 5^o.

The next point of uncertainty in the experimentation was the uncertainty in the nozzle pressure ratio. As mentioned above, for a nozzle pressure ratio of 1, the inlet pressure has to be 1.8929 times greater than the atmospheric pressure. The gauge used to measure the pressure in the settling chamber had a minimum graduation of 5 kPa, giving an uncertainty in these values of 2.5*kPa*. The atmospheric pressure was measured with a rather more accurate digital pressure gauge, which had an uncertainty of 0.01*mbar*. However the effect of these uncertainties on the nozzle pressure ratio is not immediately apparent. Therefore it was necessary to perform the uncertainty analysis shown in Equation 8-1.

For the purpose of illustration the detailed uncertainty analysis for the nozzle pressure ratio has been included below. The full set of equations used to calculate all of the uncertainties in the resultant data are given in Appendix E. Since the uncertainty analysis method used is dependent on the actual raw data values, the results will vary with each set of analysed data. The equations given in Appendix E were used in the MATLAB analysis program shown in the previous section, allowing for specific uncertainty data to be generated for each set of raw data.

Using Equation 3-1 and Equation 3-2 the equation for nozzle pressure ratio can be shown to be:

$$NPR = \frac{P_0}{1.8929P_\infty}$$

Where:
P_0 = Inlet Pressure
P_∞ = Atmospheric Pressure
NPR=Nozzle Pressure Ratio

Differentiating this equation by the two variables:

$$\frac{\partial NPR}{\partial P_0} = \frac{1}{1.8292P_\infty}$$

$$\frac{\partial NPR}{\partial P_\infty} = -\frac{P_0}{1.8292{P_\infty}^2}$$

Substituting these partial differentials into Equation 8-1:

$$\Delta NPR = \sqrt{\left(\frac{1}{1.8292P_\infty} \times \Delta P_0\right)^2 + \left(-\frac{P_0}{1.8292{P_\infty}^2} \times \Delta P_\infty\right)^2}$$

Examining the pressure gauges used, the gauge that gave the pressure in the settling chamber had an uncertainty of 2.5kPa. The gauge that gave the atmospheric pressure in the laboratory had an uncertainty of 0.01mbar. Taking a sample calculation for the rest of the values:

P_0=157.75kPa=1577.5mbar

P_∞=833.4mbar

ΔP_0=2.5kPa=25mbar

ΔP_∞=0.05mbar

Substituting these values into the above equation gives a solution of:

$$\Delta NPR = 0.015847$$

Although this sample calculation used the values for a nozzle pressure ratio of 1, performing this same calculation for NPR=1.5 and NPR=2 gave the same uncertainty value. This means that the percentage uncertainty is a maximum of 1.6% for NPR=1, and becomes significantly less as the nozzle pressure ratio is increased.

The main source of error in the experimental set up was found to be the viscosity of the oil. Since the oil had to be mixed by hand to obtain the correct viscosity there is the chance for the introduction of a number of errors.

The two points where errors can be introduced when mixing the oil are the point where the required percentages are measured off the graph and the measurement of the amount of each oil being mixed in. The graduations on the mixing table gave an uncertainty of 0.25% in the quoted weight percentages.

As mentioned in the methodology section, the oils were measured out using 10ml syringes with graduations every 0.2ml, introducing an uncertainty of 0.1ml.

Performing the uncertainty analysis through the mixing procedure, and taking the average over the whole viscosity range, it was discovered that the oil viscosity had an uncertainty of 16.5%.

Moving to the uncertainties present in the data analysis process, there are once again numerous points were potential errors can be introduced into the data.

Firstly, the error of parallax conversion process has two points of uncertainty. Considering the potential for printing errors, it was assumed that the physical spacing between each successive ring had an uncertainty of 0.25mm. Since the intensity graph used to determine the pixel-wise spacing between each reference ring was passed through a low-pass filter, which could skew the data slightly, the uncertainty in the line pixel spacing was taken to be 2 pixels. This resulted in an uncertainty in the pixel density of 5.5%

This pixel density uncertainty, coupled with the assumed potential error in the fringe position measurement of 5 pixels resulted in a potential fringe spacing error of between 5.9 and 13.2%. This uncertainty decreases with distance along the oil from the leading edge.

Since the fringe spacing values were used to calculate the oil height values, through the selected best fit equations, it was expected that the potential error in fringe spacing would be magnified in the oil height error. Whilst this is the case, the degree of this magnification was somewhat less than anticipated. Moving along the oil film from the leading edge the uncertainty varies from 17.4% to 7.7%.

Finally looking at the uncertainty in the shear force calculations, it was expected that the high uncertainties in the oil viscosity and fringe spacing would generate a very large uncertainty, especially since the fringe spacing values are used twice in the shear calculations to determine shear forces. However this is not in fact the case and once the uncertainty analysis process had been completed for the shear force equation, the average uncertainty across all shear values was calculated to be 16.7%

9 Results

As was discussed in the Observations section (Section 6), the tests performed using the axisymmetric nozzle failed to generate any usable data. Therefore this section is limited to the results obtained from the use of the square and rectangular nozzles.

9.1 Square Nozzle, NPR=1, n/d=2

The first set of results discussed below was generated using the square nozzle plate set 2 nozzle diameters from the plate surface (20mm) with the jet operating at NPR=1.

The images shown in Figure 9-1 and Figure 9-2 were generated using the central globule oil application technique. As was noted in the previous section the fringe patterns visible occur along the diagonal axes of the jet, indicating a higher shear force present along these axes (in all following images discussed in this section the alignment of the jet nozzle is indicated by the set of axes in the bottom left hand corner of each image). This conclusion is supported by CFD results, as shown in Figure 9-3. This figure shows a contour plot of the shear forces in and around the impingement zone. The red areas, indicating the highest shear forces, are aligned with the diagonal plane; a conclusion supported by the comparative graph in Figure 9-4, showing the shear forces on the plate along the main and diagonal axes of the jet.

Examining the two sets of data, the shear forces appear to peak at approximately the same distance from the jet centre: 7.6mm along the main axis and 8.1mm along the diagonal. Looking at the shear contour plot (Figure 9-3) these peaks appear to indicate the boundary of the recirculation zone.

Even though the shear force is higher along the diagonal in proximity of the impingement zone, it drops off much more rapidly than that on the main axis. After the maximum point, the diagonal shear drops to approximately the same values as the main axis shear until the diagonal plot crosses the main axis graph at 15mm. After this point the diagonal shear values are considerably lower than the main axis values across the rest of the plate. This is also shown in the shear contour plot across the whole plate shown in Figure 9-5.

Another important point to note when examining the simulated results shown in Figure 9-3 is the presence of the subtle cross pattern within the recirculation zone, extending slightly past the area of maximum shear. This pattern was also noted in the initial results discussed in Section 6 (refer to Figure 6-13 and Figure 6-14). The presence of this cross pattern along the diagonal plane supports the findings of Menon and Skews [5] that lines of recirculation occur along the diagonal plane within the recirculation bubble. The presence of these discrete recirculation zones also explains the fringe patterns visible at the centre of the plate in Figure 9-1 and Figure 9-2. Highlighted in Figure 9-1, right next to the centre of the impingement zone are four oval fringes that indicate flow from the centre of these ovals in all directions.

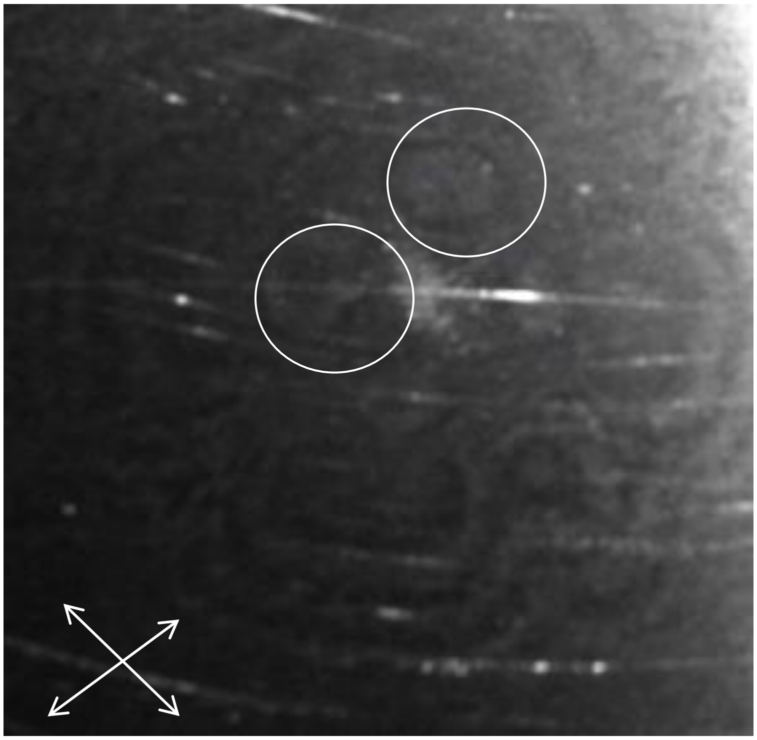

Figure 9-1: v=600cSt t=30s

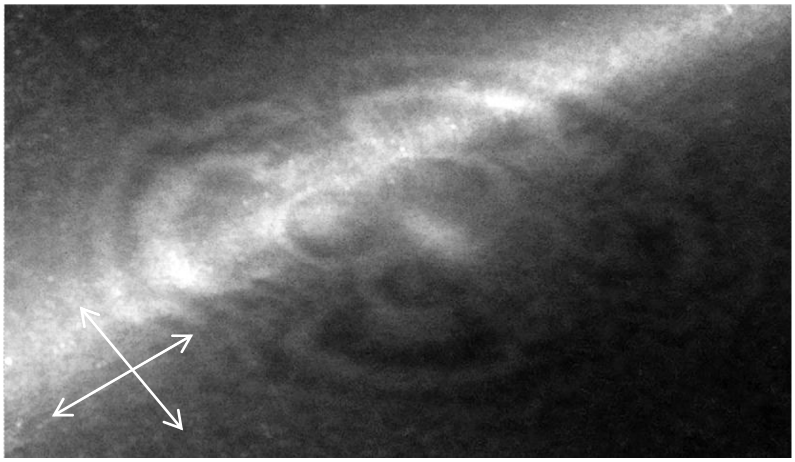

Figure 9-2: v=650cSt t=50s

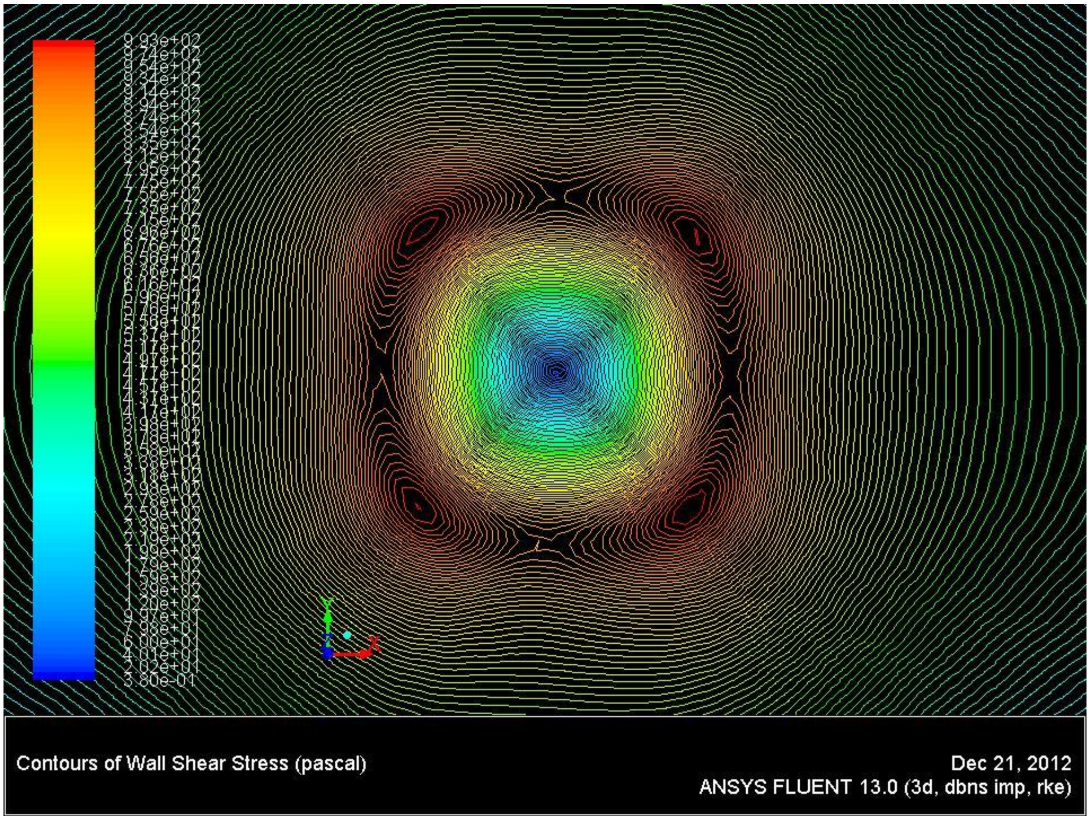

Figure 9-3: CFD Impingement Zone Predicted Shear Stress

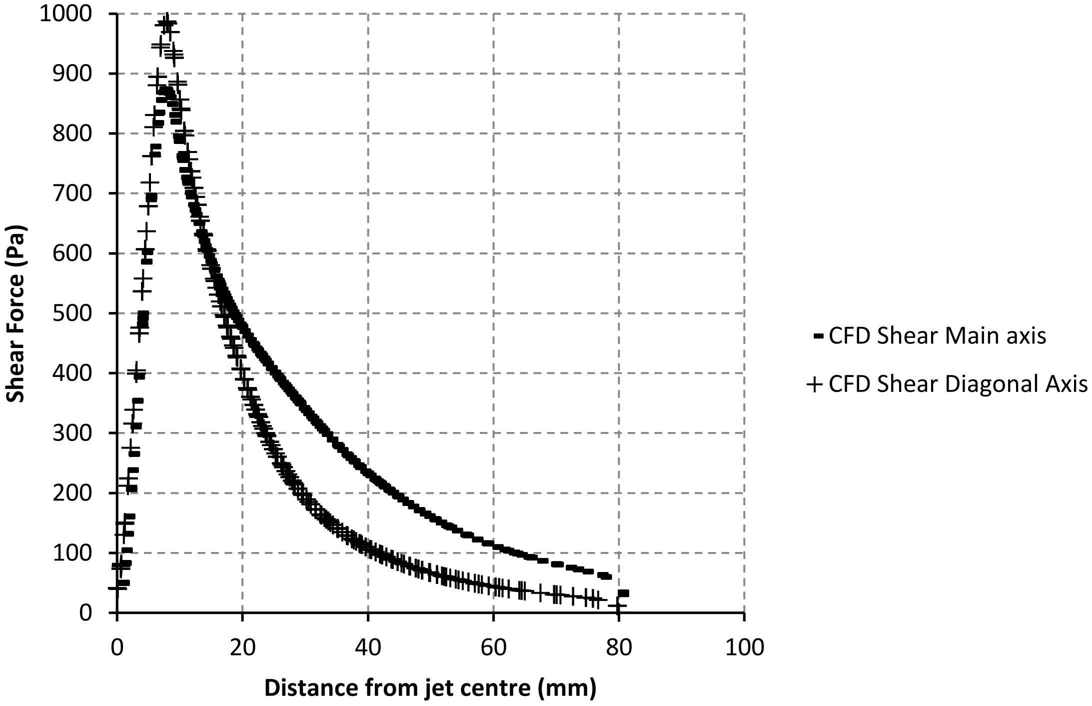

Figure 9-4: Comparative graph of shear force along the main and diagonal axes

As was discussed previously, the fact that the shear force is higher along the diagonal plane than the main axes is in direct conflict with the fact that the highest velocity wall jets occur along the main axes. The occurrence of the wall jets along the main plane was noted in reference to Figure 6-9, Figure 6-13 and Figure 6-14 (pp 54-59) and is also visible in the simulated Mach number plot shown in Figure 9-6 and the graph in Figure 9-8. The alignment of the wall jets explains the fact that the shear force along the main axes is higher than that on the diagonal on the outer portions of the plate, as evident in Figure 9-4 and Figure 9-5. However it still does not explain the higher shear forces along the diagonal within the recirculation zone.

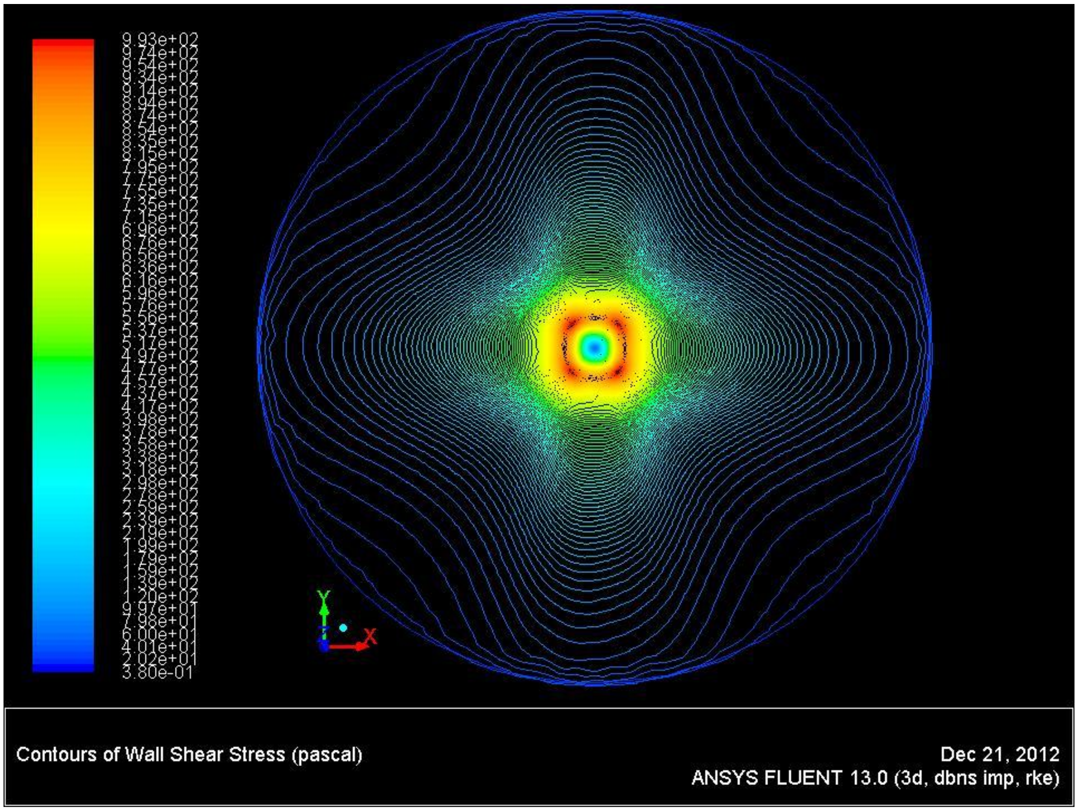

Figure 9-5: CFD Predicted Shear Stress

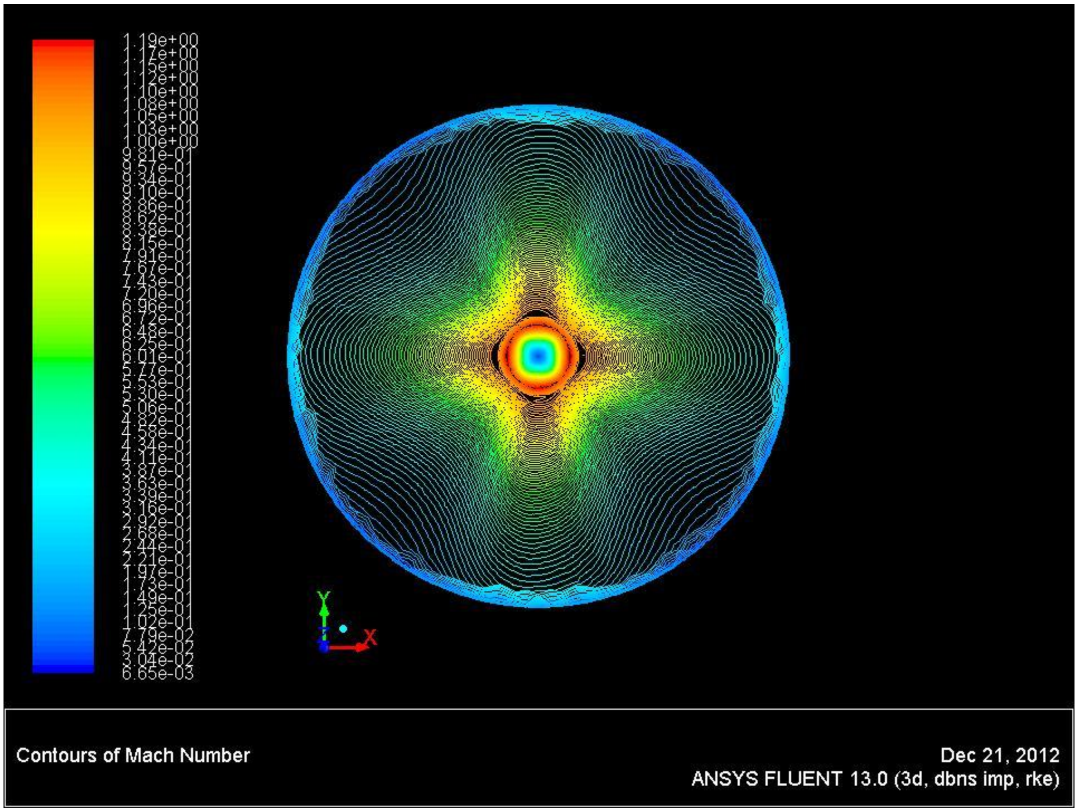

Figure 9-6: CFD Predicted Plate Mach Number

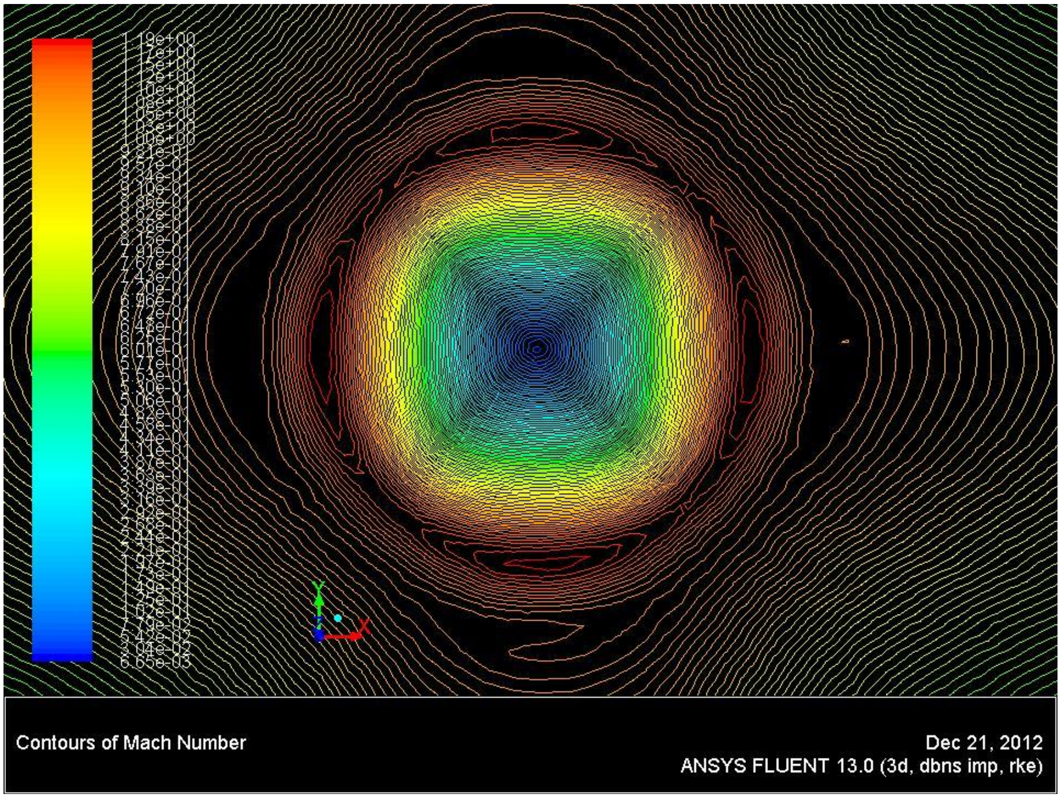

Figure 9-7: Close up of the Mach contours within the impingement zone

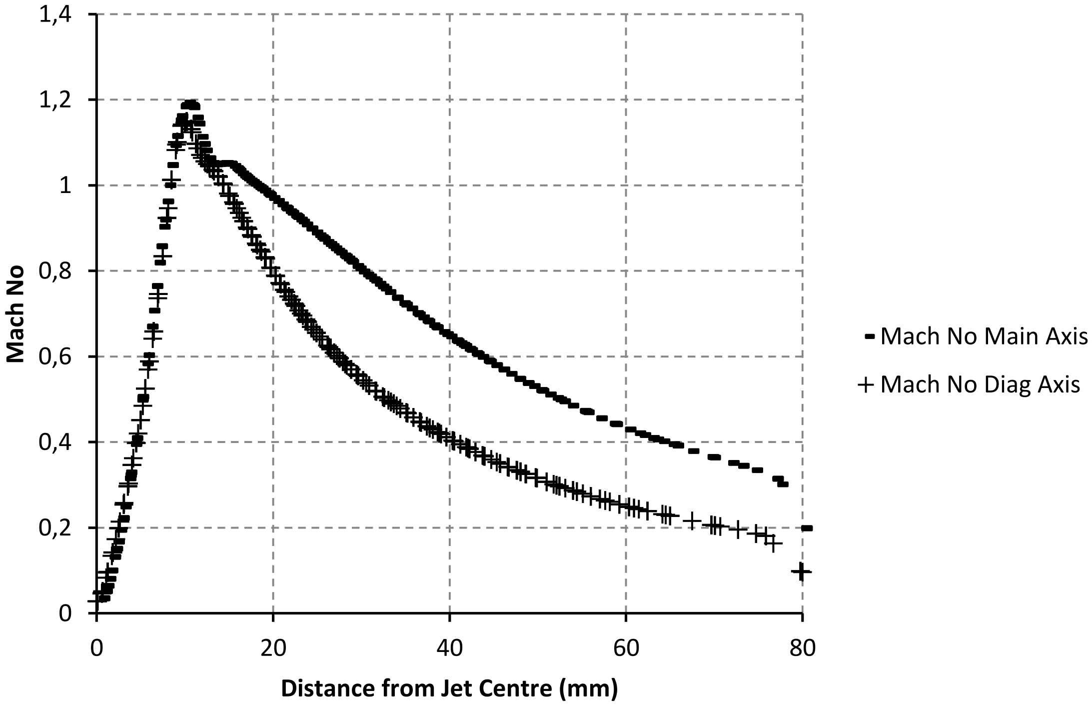

Figure 9-8: Comparative plot of Mach number along main and diagonal axes

Examining the graph in Figure 9-8, which shows the Mach number data along the two planes, the main axis curve sits significantly higher along the majority of the plate. However in the vicinity of the recirculation zone the two curves are very close together making interpretation of the data rather difficult. The Mach data has thus been re-plotted over the initial 20mm from the centre of the plate to allow for the trends in this area to be seen more easily (Figure 9-9). This close up look at the data shows that even within the recirculation zone the Mach number along the diagonal is less than that on the main axis. So whilst higher Mach numbers result in higher shear forces across the rest of the plate, they do not have the same effect at the recirculation zone boundary.

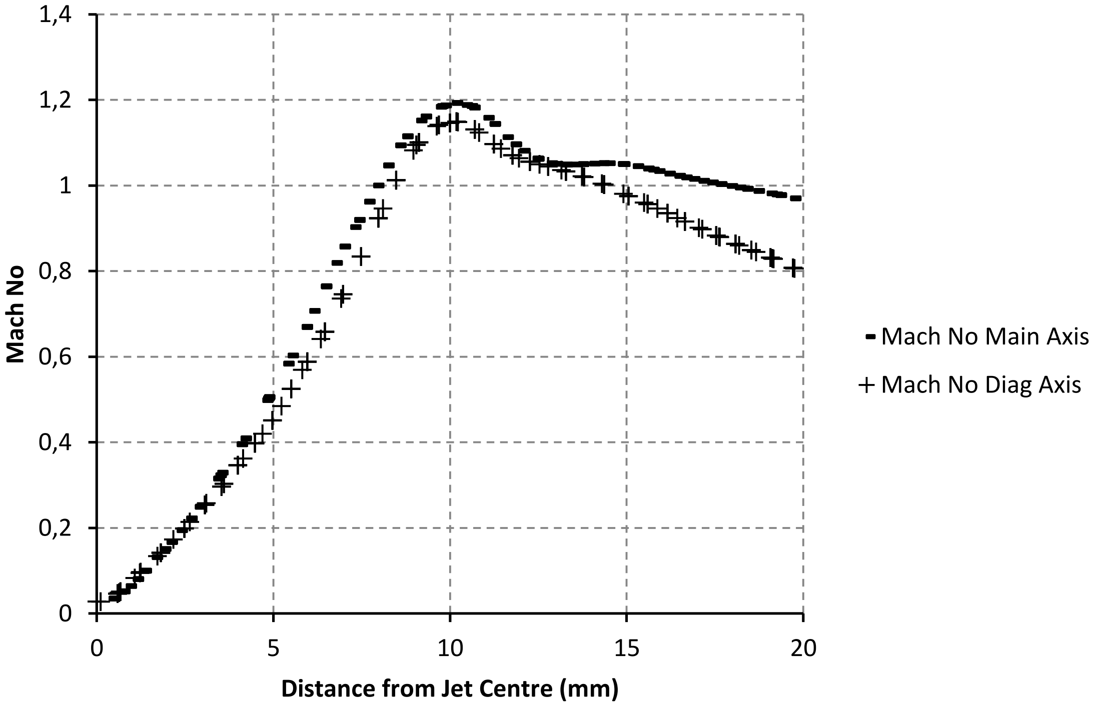

Figure 9-9: Mach number in the impingement area for the main and diagonal axes

In the search for an explanation to this disparity between data sets it was of use to turn to the shear force equations.

$$\tau = \mu \frac{\partial v}{\partial x}$$

Equation 9-1

Where:

τ = Shear Force

μ = Fluid dynamic viscosity

$\frac{\partial v}{\partial x}$ = Velocity gradient in the direction of flow

(It should be noted that the equation given above is the most generalised form of the expression for calculating shear force. Since it has been included here for illustration purposes only it was not thought necessary to include the more complex equation specific to compressible flows.)

This equation shows that the shear force is not in fact directly dependant on the flow velocity, but on the derivative of the velocity. It is also dependant on the viscosity of the fluid. In turn, the viscosity is dependent on a number of variables, including temperature, pressure and density.

Looking at the CFD data for these other variables, the only one that shows a similar pattern to that of the shear forces across the plate is that of temperature. Figure 9-10 shows the contour plot of the total temperature in proximity to the impingement zone. The cross patterns and areas of higher temperature are aligned with the diagonal plane of the jet. This increased temperature could explain the increased shear values observed. However, when examining the actual data, as shown in Figure 9-11, the temperature difference between the two planes is rather small (less than a single degree). Although the scale of the effect of the temperature is not know, a variation of that size does not seem enough to account for the large difference between shear forces on its own (approximately 100 Pa).

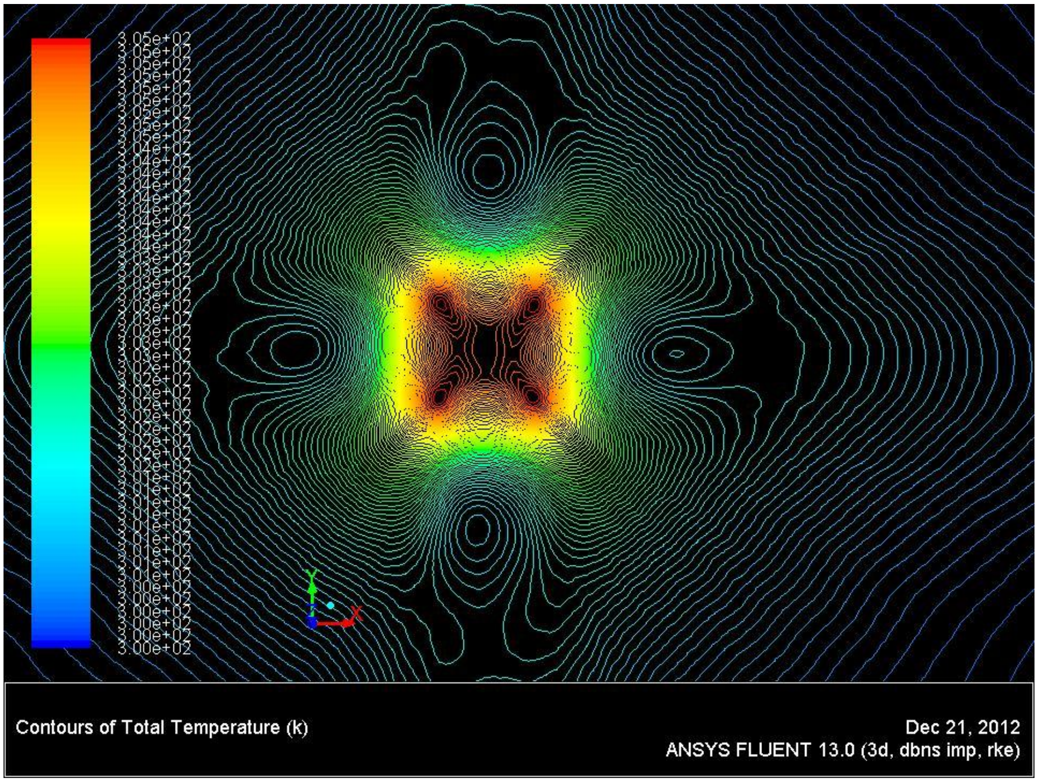

Figure 9-10: CFD plate temperature contours

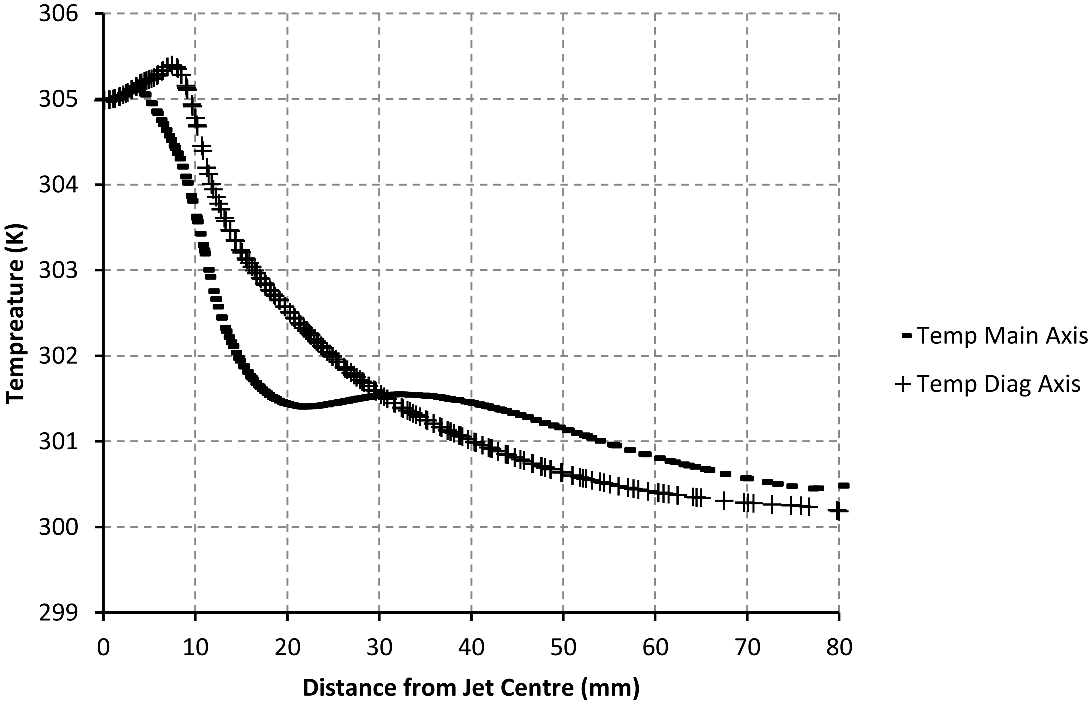

Figure 9-11: Comparative graph of predicted temperatures along the main and diagonal axes

Another important factor that was noted when examining the shear force equation is the fact that the air flow data examined so far was in the form of Mach number, not actual flow velocity. Since the speed of sound is dependent on temperature, as shown in the ideal gas equation below, the compounded effect of temperature on viscosity and velocity could explain the discrepancy in shear forces.

$$a = \sqrt{\gamma RT}$$

Equation 9-2

Where:

a = Speed of Sound (m/s)

γ = Ratio of Specific Heats

R = Specific Gas Constant (J/kgK)

T = Air temperature (K)

However upon examination of the velocity plot, shown in Figure 9-12, the velocity along the diagonal axis is still lower than that on the main axis. The two curves also show very similar trends to those observed in the Mach number plots above. The difference in temperatures does not appear to have a marked effect on flow velocity.

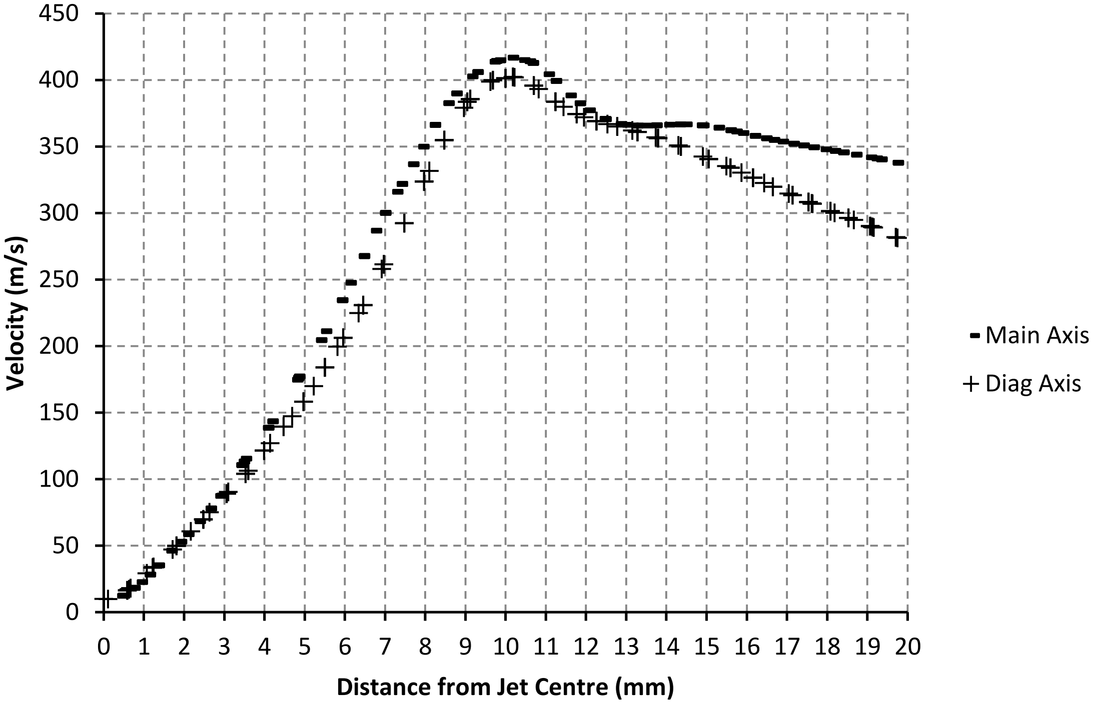

Figure 9-12: Plot of velocity profiles along the main and diagonal axes

That being said, the plot of temperature and shear force shown in Figure 9-13 shows that, for the diagonal plane, the temperature peak occurs the same distance from the jet centre as the shear force peak. The fact that the maximum temperature coincides with the point of maximum shear force cannot be ignored. However performing the same compound plot along the main axis, as shown in Figure 9-14, the maximum temperature value occurs well before the peak in shear force. Therefore, whilst temperature does seem to have an effect on shear force, it is clearly not the only factor to consider. In fact the plots of all commonly considered flow variables (Mach No, Density, Pressure), respectively shown in Figure 9-15, Figure 9-16 and Figure 9-17 do not show any coincidence between their peak values and that of shear force. The relationship between these variables and the shear force across the plate is therefore a much more complex one than was originally thought and requires more in depth investigation outside of the scope of this investigation.

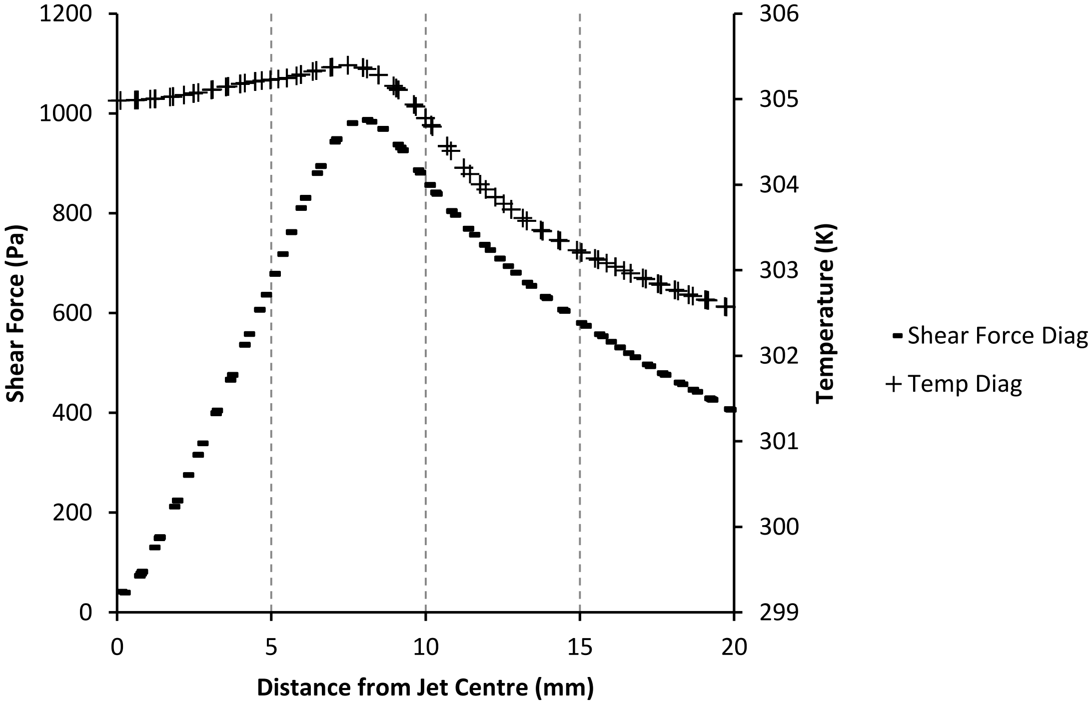

Figure 9-13: Plot of temperature and shear force along the diagonal axis

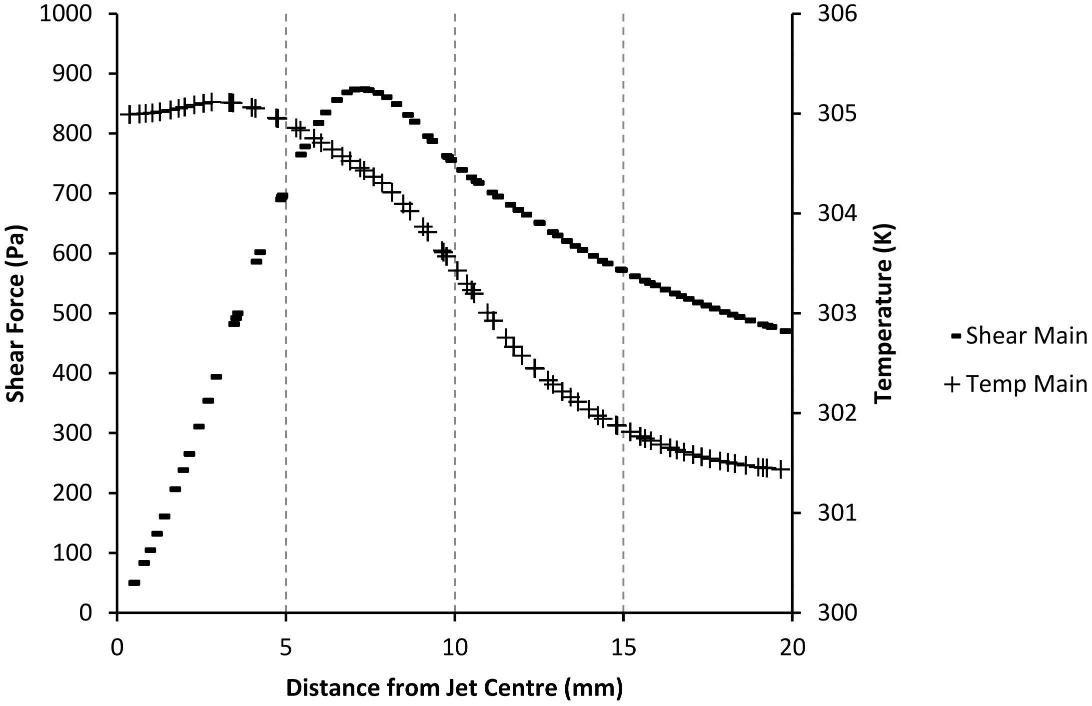

Figure 9-14: Plot of shear force and temperature along the main axis

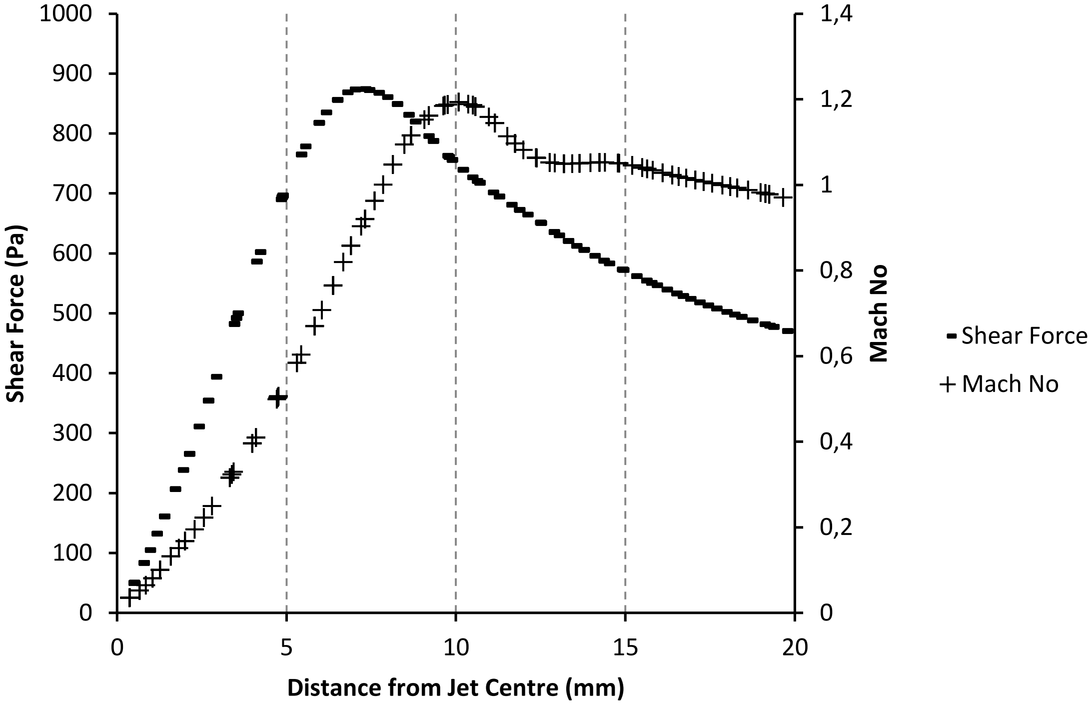

Figure 9-15: Plot of Shear Force and Mach number along the main axis

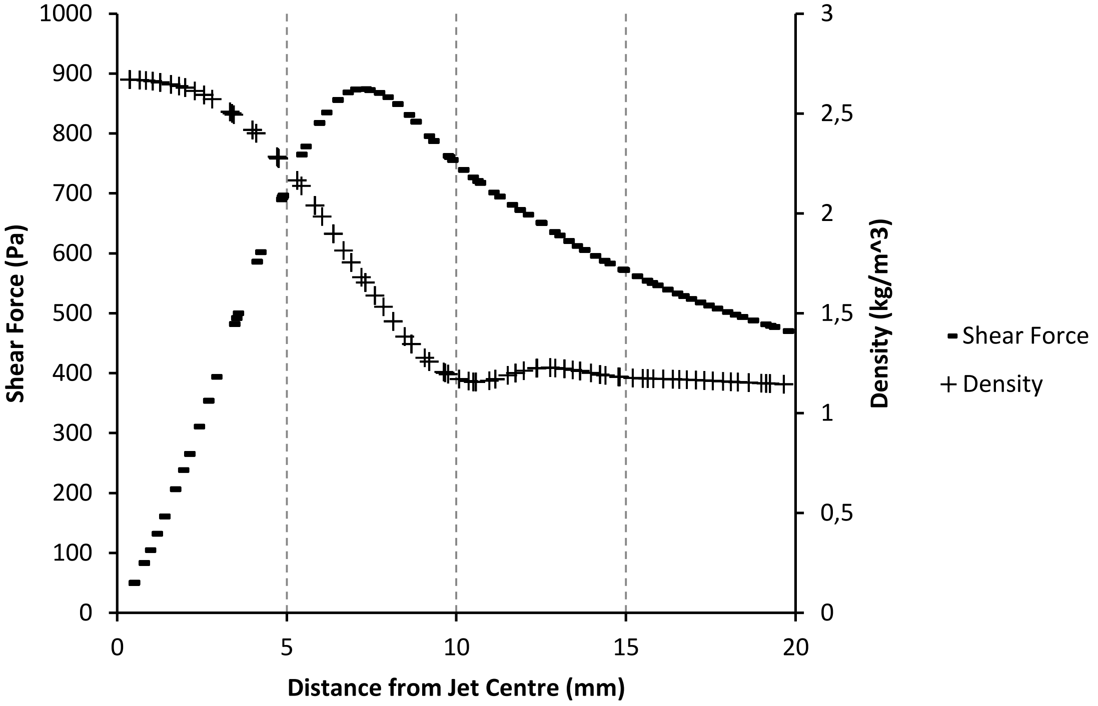

Figure 9-16: Plot of Shear Force and Density along the main axis

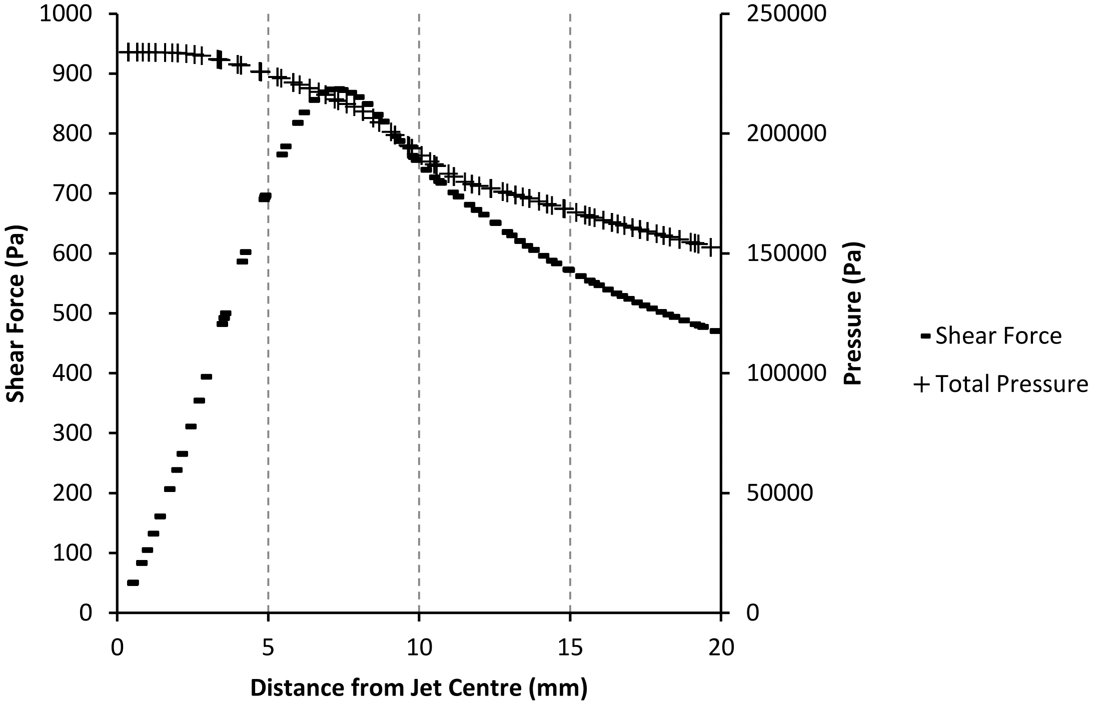

Figure 9-17: Shear Force and Pressure along the main axis

Turning now to the results from the oil film interferometry experimentation, which was the main objective of this investigation. As stated in the Observations in Section 6, the attaining of fringe images that could be analysed proved to be more difficult than originally thought. That being said the final experimental method generated some very good fringe images that allowed for both qualitative and quantitative analysis. The fringe images in Figure 9-1 and Figure 9-2 allowed for the visualisation of the general flow patterns on the plate and a general comparison with CFD results, as discussed above. The real test of the overall objective of this investigation came when the single drop fringe images were taken through the analysis process detailed in Section 7 and the results compared to the predicted results from CFD.

Figure 9-18 and Figure 9-19 show the resultant fringe patterns from single drops of oil placed at distinct points on the plate. Starting with the fringe pattern in the bottom left of both images and moving round anti-clockwise the drops were placed 10mm, 20mm, 30mm and 40mm from the centre of the plate. For both images the oil viscosity, jet NPR and run time were the same. The only difference between the two images is the orientation of the drops in respect to the axes of the jet. In Figure 9-18 drops were placed along the main axis of the jet whist the drops in Figure 9-19 were aligned with the diagonal plane. Comparing the fringe patterns in the two images the difference in shear force along the two planes is immediately apparent.

Looking at the 10mm fringes in the two images, the spacing between drops along the diagonal plane is much greater than those on the main axis. Another point worth noting is the slanting of the fringes in the oil in Figure 9-18. Since the appearance of fringes indicates a line of constant oil thickness, this slanting of the fringes shows a constant increase in shear force across the width of the fringe, moving towards the diagonal plane. These two fringe patterns support the earlier conclusion that in close proximity to the impingement zone, the shear force is greater along the diagonal plane.

Examining the fringe patterns at 20mm from the centre in the two images, the inverse appears to be true. The fringes along the main axis appear to be slightly further apart than those on the diagonal, supporting the CFD that predicted the shear force is greater along the main axes further out from the jet centre. That being said, the difference in fringe spacing is much less obvious than the 10mm fringes and could be a result of differing camera zoom and angle in the two photographs. Looking at the other two fringe patterns in both figures, the main axis fringes once again appear to be further apart but the difference is so subtle the only way to be certain of any difference is to compare the resultant shear data.

However before considering the shear data a curious pattern in the fringes in Figure 9-19 should be noted. Although it is visible in Figure 9-19, for the purpose of clarity Figure 9-20 shows an extreme close up of the 10mm oil coating with the area of interest highlighted.

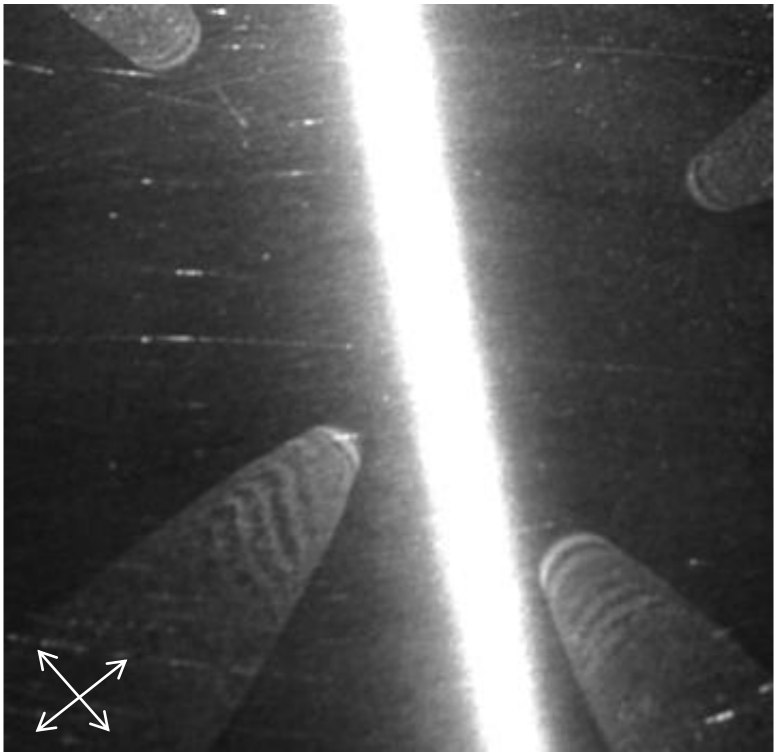

Figure 9-18: Main plane drops, NPR=1, n/d=2, v=550cSt, t=20s

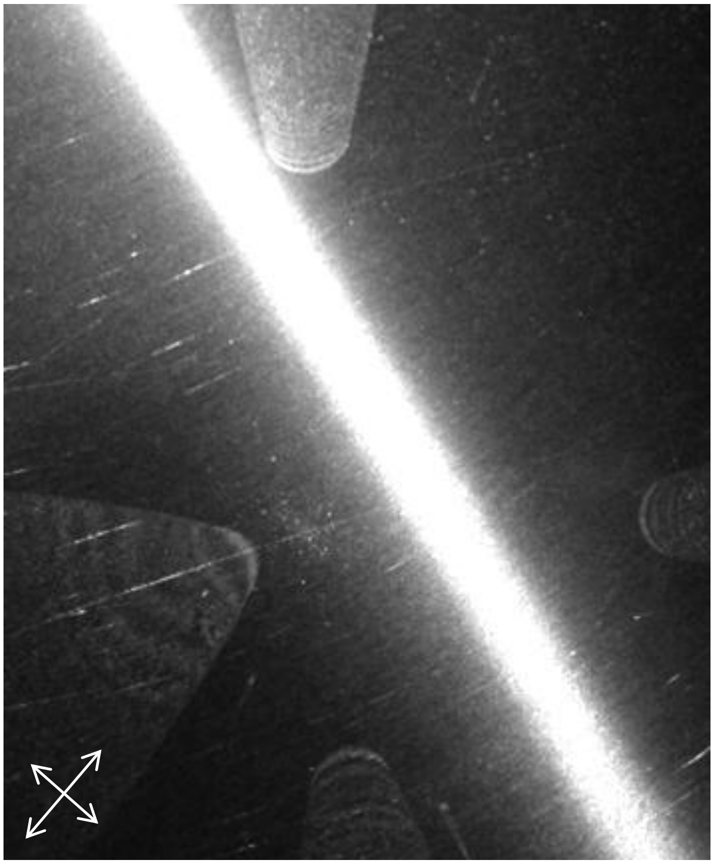

Figure 9-19: Diagonal plane drops, NPR=1, n/d=2, v=550cSt, t=20s

On the bottom edge of the oil coating a secondary fringe pattern is visible, as highlighted by the white circle. The oval shape of this fringe pattern indicates the presence of a recirculation zone at this point. The fact that it appears slightly clearer than the main fringes, as well as the fact that it shares the same boundary as the main fringes indicates that this fringe pattern was generated after the main oil thinning process had occurred. This fact gives an indication of the behaviour of the oil and the airflow during the impingement process.

As was mentioned in the Observations it takes approximately five seconds for the airflow to reach the desired pressure. During this start up process the initial thinning of the oil occurs, setting up the initial fringe patterns. Once this has occurred the oil has thinned to a sufficient point that the secondary flow conditions present on the plate can have an effect on the oil coating, setting up the fringe patterns shown in the figure. Since it takes approximately five seconds for the jet to get up to pressure, it is reasonable to assume that it will take a further two to three seconds to reach steady state conditions and all the stagnation points and recirculation zones to full evolve.

Comparing this apparent recirculation zone to those noted in Figure 9-1 and Figure 9-2, it appears to be closer to the main axis of the flow and several millimetres further out from the centre. Using the pixel measurement technique detailed in Section 7, the recirculation zones in Figure 9-1and Figure 9-2 are centred 8-9mm from the centre, whilst this zone is centred approximately 15mm from the jet centre. It is possible that this fringe pattern in fact points to the position of the main axis stagnation points predicted by Menon and Skews [5].

Unfortunately fringes shown in Figure 9-19 and Figure 9-20 were the only case where this secondary fringe pattern was observed. Further test runs under the same conditions failed to generate any of these smaller fringes. Thus the explanation detailed above is purely supposition and further investigation would be required to provide a definitive conclusion.

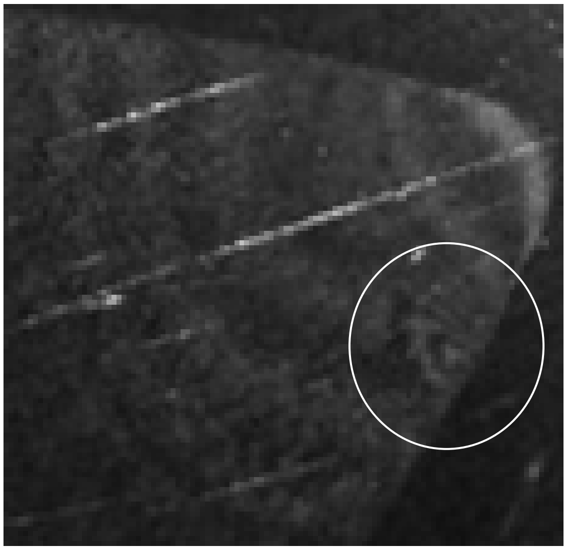

Figure 9-20: Close up of the 10mm fringe pattern in the diagonal plane

Moving back to the actual data from the experimentation, Figure 9-21 shows a plot of the shear forces calculated for the two fringe images discussed above. Although this raw data shows some clearly erroneous values, specifically the increase in shear force towards the tail end of the first fringe pattern on the diagonal axis, the overall trend of the data appears to be more or less in agreement with the predicted trends shown in the CFD data. The shear along the diagonal axis starts higher than that on the main axis and then drops off rapidly. After the 10mm mark the main axis shear remains above the diagonal shear along the rest of the plate. Overall the experimental data appears in agreement with the CFD data. However when comparing the two sets of data, as shown in Figure 9-22 and Figure 9-23, this agreement becomes somewhat more tenuous.

Figure 9-22 and Figure 9-23 were generated by plotting the shear data from all tests run under each flow condition, indicated by the + and x data points, then selecting all data points that showed a general trend, indicated by the o data points. These data points were then used to generate a best fit trend line, the type of trend line based on the highest R^2 values. Finally the CFD data was overlaid on each plot.

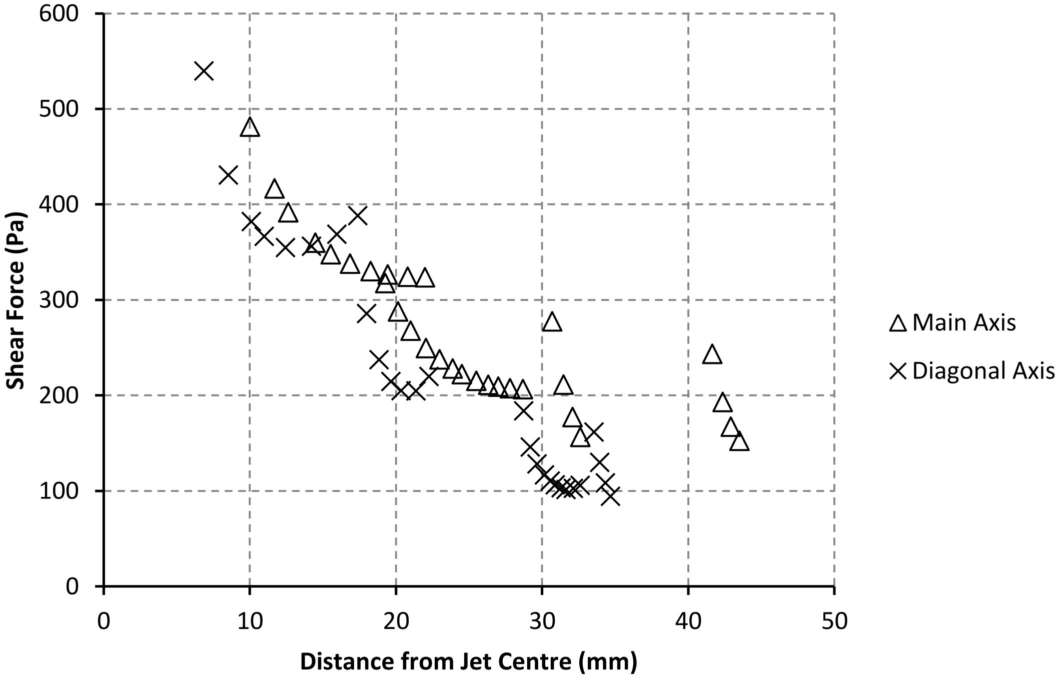

Figure 9-21: Experimental results. Shear force along main and diagonal axes

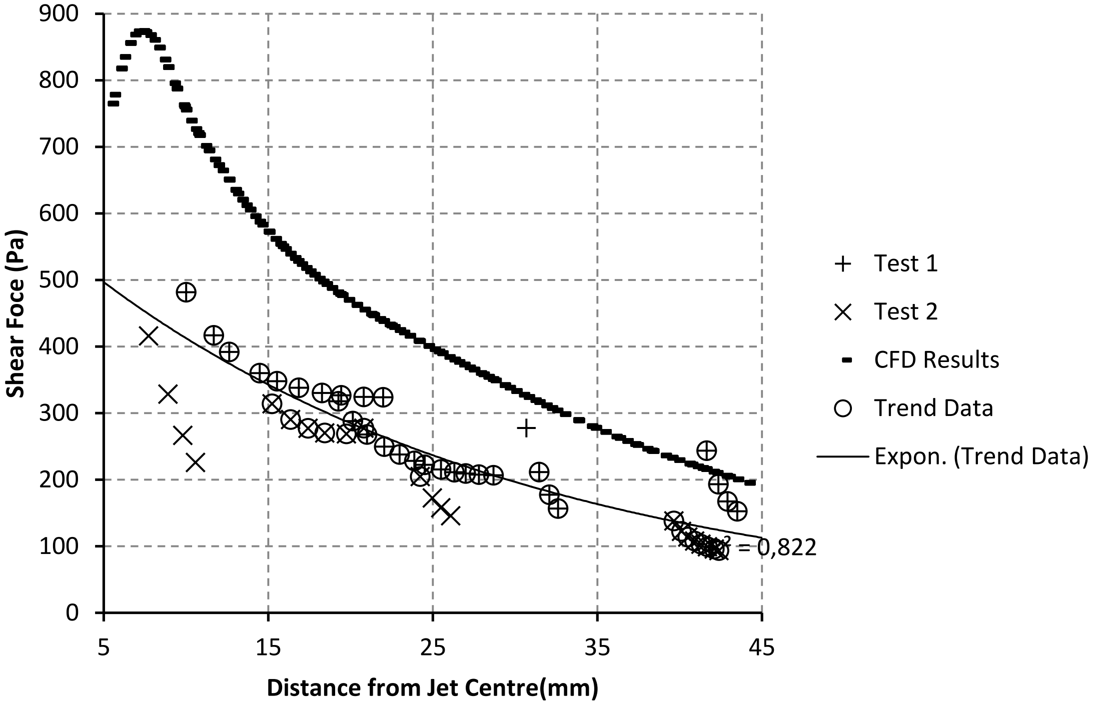

Figure 9-22: Experimental shear versus CFD shear along the main axis

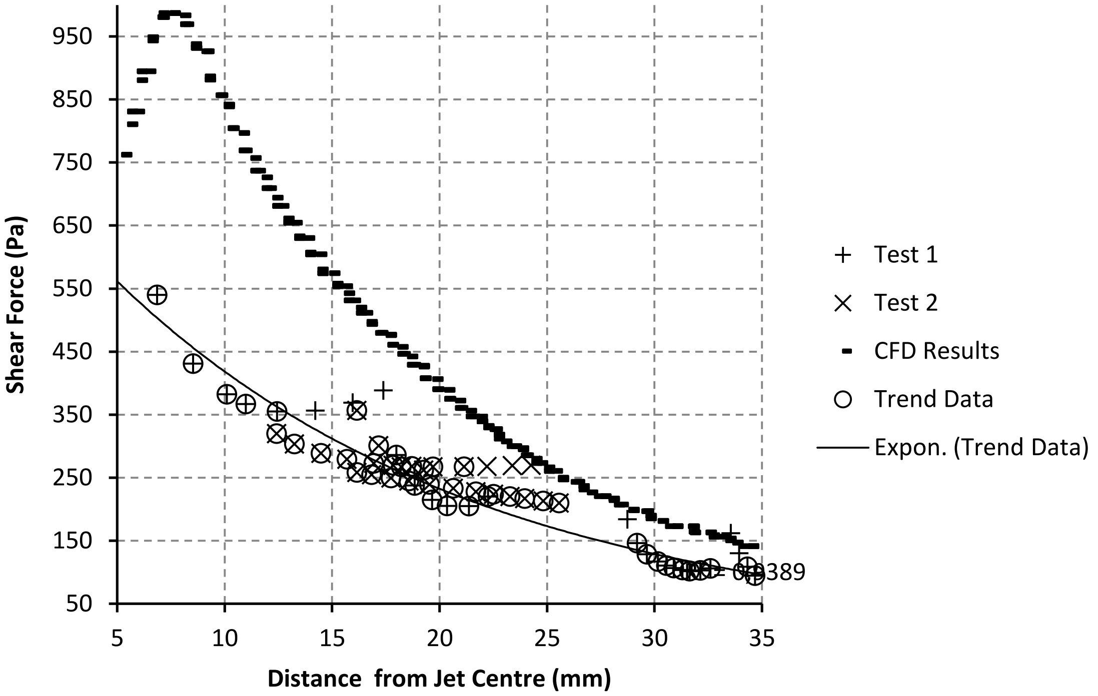

Figure 9-23: Experimental shear versus CFD shear along the diagonal axis

It is immediately apparent when examining both figures that the oil film interferometry data severely underestimates the shear forces close to the centre of impingement (in both cases the maximum experimental shear is approximately 60% less than the CFD shear at the same point). Moving out from the plate centre this disparity between results becomes somewhat reduced, however the interferometry shear data remains significantly lower than that predicted by CFD simulations. There is also no indication of the predicted peak values in the interferometry data.

In order to make the data clearer in the plots the error bounds have been left off. However even though the calculated shear has a rather large uncertainty (16.7% as discussed in section 8) the large difference between interferometry and CFD shear values is still higher than the uncertainty bounds close to the jet centre, as shown in Figure 9-24 and Figure 9-25 below. Even when including the uncertainty, the experimental shear along the both axes still falls short of that predicted by CFD.

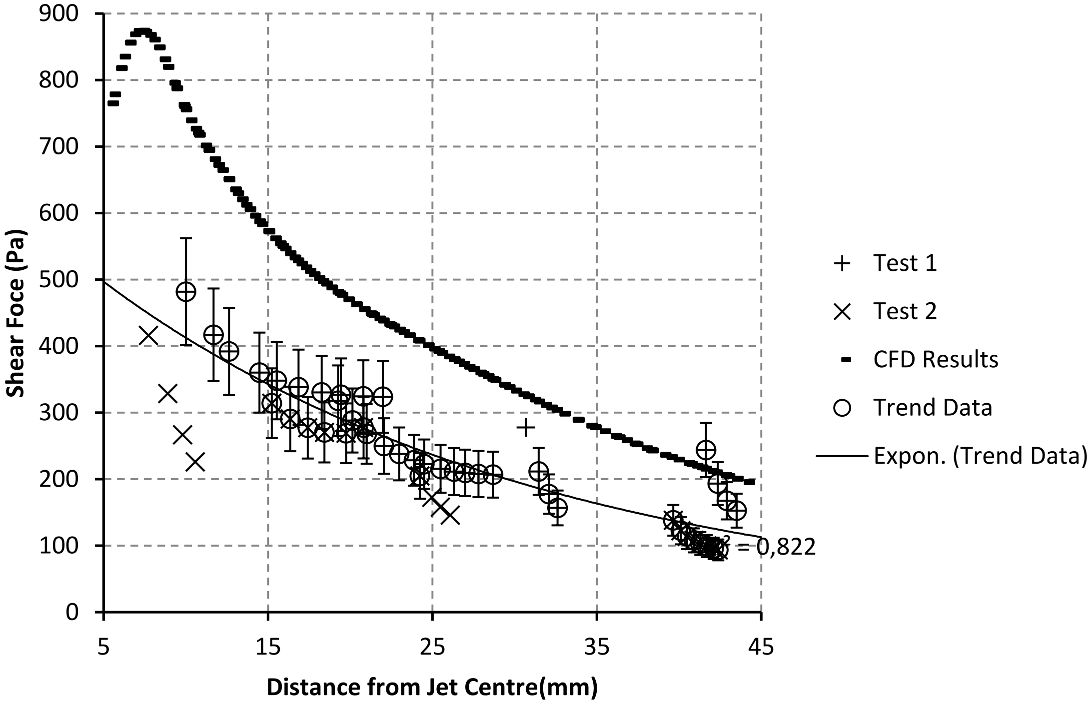

Figure 9-24: Main axis shear data with error bars

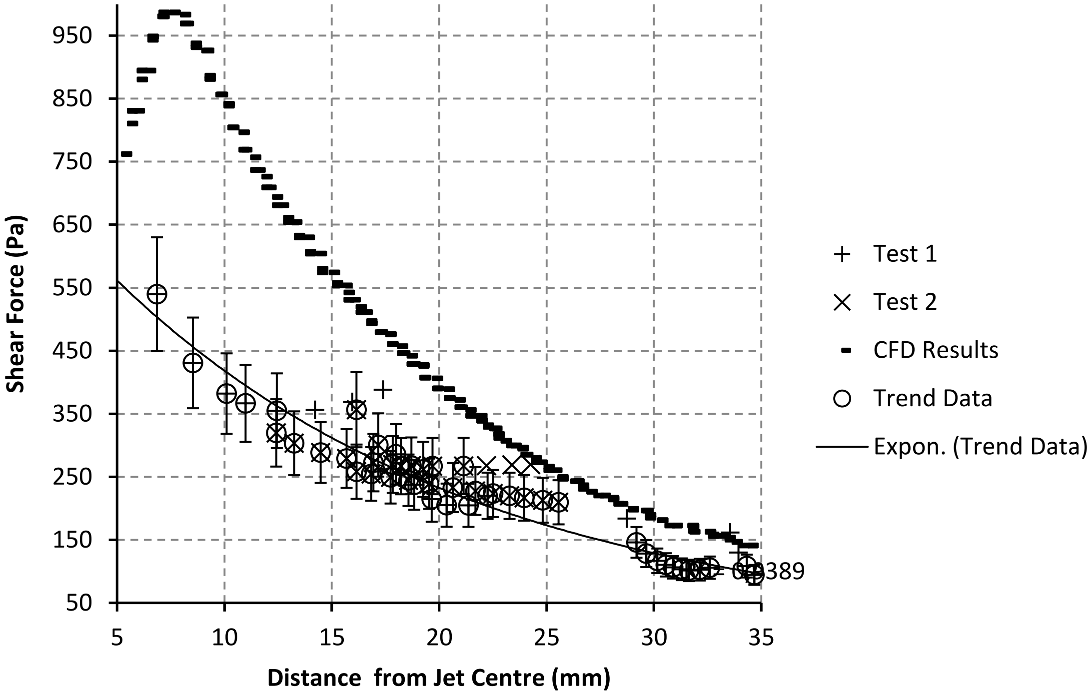

Figure 9-25: Diagonal axis shear data with error bars

A portion of this difference may be explained by the fact that the flow conditions simulated in the CFD model were possibly slightly higher than the conditions during experimentation. Looking at the Mach number plots shown in Figure 9-26 and Figure 9-27, the clearly defined shock diamonds within the jet core indicates the jet is operating well within the moderately under-expanded range, and not the perfectly under-expanded condition as hoped (even though the conditions at the pressure inlet and pressure farfield boundaries were set with a ratio of 1.8929:1 to give the critical nozzle pressure ratio of 1). That being said, the experimental runs were carried out under the same pressure ratio conditions, so results should be comparable. However, as was mentioned at the beginning of this report, it is very difficult to ensure a jet is operating under perfectly expanded conditions. Therefore, although the operating pressures were set to the theoretically correct values, any slight variations in the test conditions could have resulted in the physical jet operating at lower flow conditions than the simulated jet.

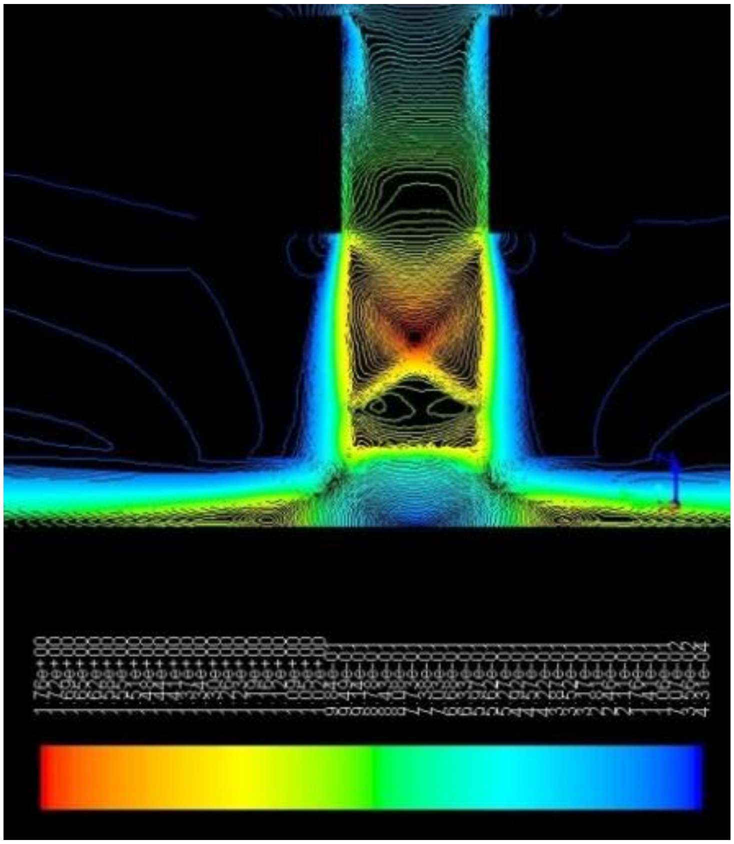

Figure 9-26: Mach number in the jet core along the main axis

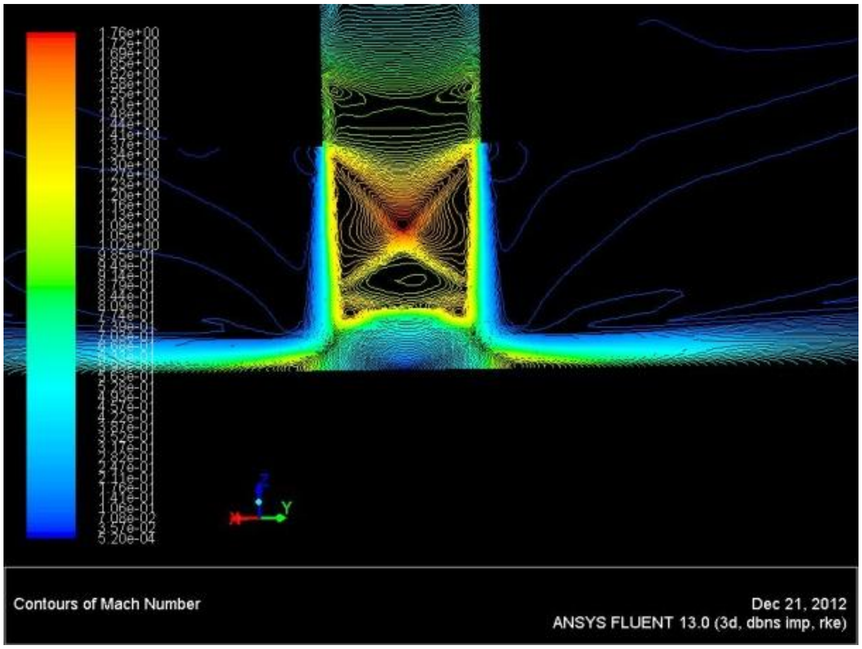

Figure 9-27: Mach number in the jet core along the diagonal axis

In conclusion then, even when taking into account the considerable level of uncertainty in the experimental data, the general trend for the interferometry method to underestimate the shear forces on the plate cannot be fully rectified. This is, however, only for one flow condition and a general conclusion about the effectiveness of oil film interferometry for this application cannot be made until the data for all tested flow conditions has been considered.

9.2 Square Nozzle, NPR=2, n/d=2

For the square convergent nozzle case, when the nozzle pressure ratio is increased to two, the impinging jet begins to take on the characteristics of an axisymmetric jet. Examining the fringe patterns shown in Figure 9-28, the overall shape of the fringes is more or less circular, in sharp contrast to the fringe patterns observed for the NPR=1 case. The circular pattern of the fringes indicates that the shear forces, in the impingement zone at least, are approximately equal in all directions. An initial examination of the CFD predicted shear forces, shown in Figure 9-29, seems to agree with this assessment.

This being said, there still appears to be some affect of the non-axisymmetric nature of the jet nozzle on the airflow. A closer look at the CFD shear contour plot shown in Figure 9-30, reveals the occurrence of the same cross pattern within the recirculation zone as was noted in the NPR=1 case. As before this cross pattern points to the presence of the diagonal lines of recirculation noted by Menon and Skews [5]. However the fringe patterns in Figure 9-28 do not show any areas of recirculation as was noted in the previous case. This is possibly due to the much higher shear forces and flow velocities dominating the oil flow, meaning the more subtle recirculation areas and stagnation points are obscured.

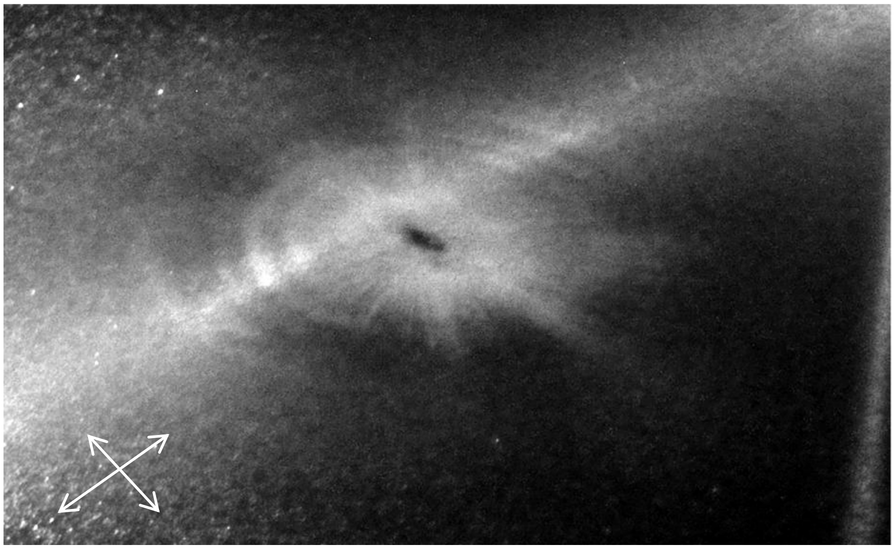

Figure 9-28: Central Blob, NPR=2, n/d=2, v=550cSt, t=70s

Another point highlighted in the CFD case that is not shown in the fringe patterns is the slightly higher shear values along the main plane at the recirculation zone boundary, an observation in direct contrast to the shear data from the lower pressure ratio. However the size of the difference is much smaller, as visible in the graph in Figure 9-31. Only when zooming in on the data in the vicinity of the recirculation zone does any difference in shear forces become apparent (Figure 9-32). Examining shear data plots, the difference between peak values is only 22.02 Pa (max 1260.08 Pa on the main axis, max 1238.06 Pa on the diagonal). This small difference in maximum shear values can possibly account for the fact that it this occurrence is not visible in the fringe image shown above (Figure 9-28).

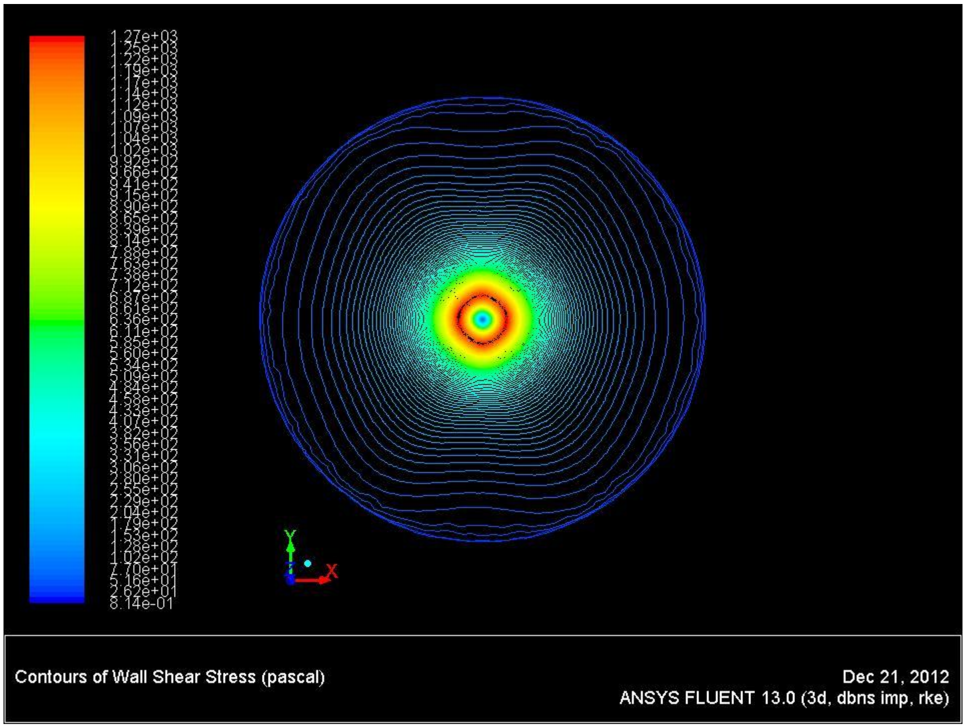

Figure 9-29: CFD shear forces across the whole plate for NPR=2

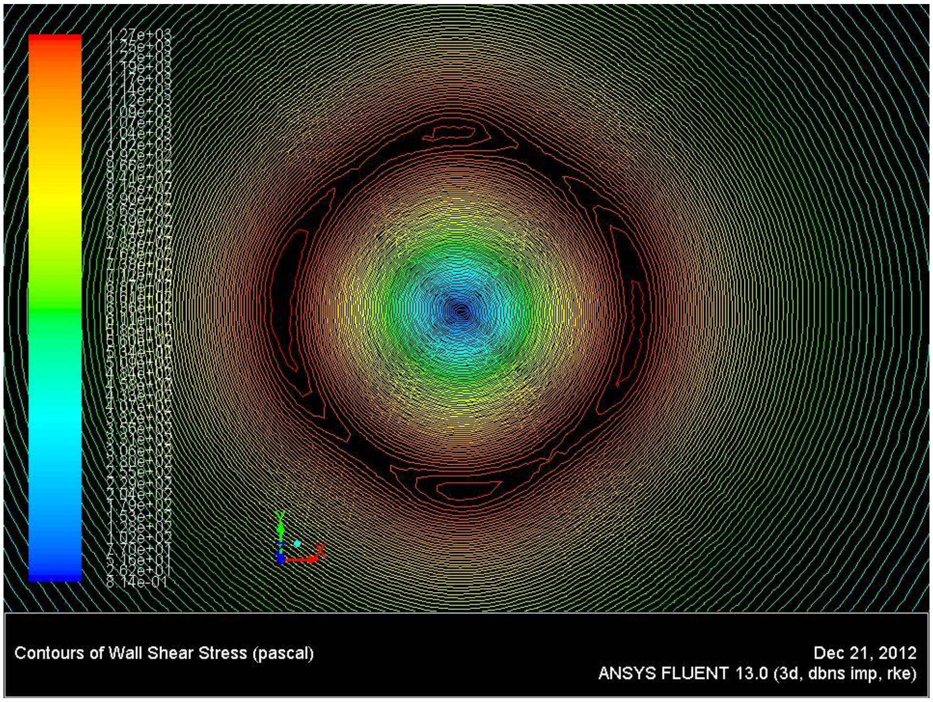

Figure 9-30: CFD plate shear in the impingement zone

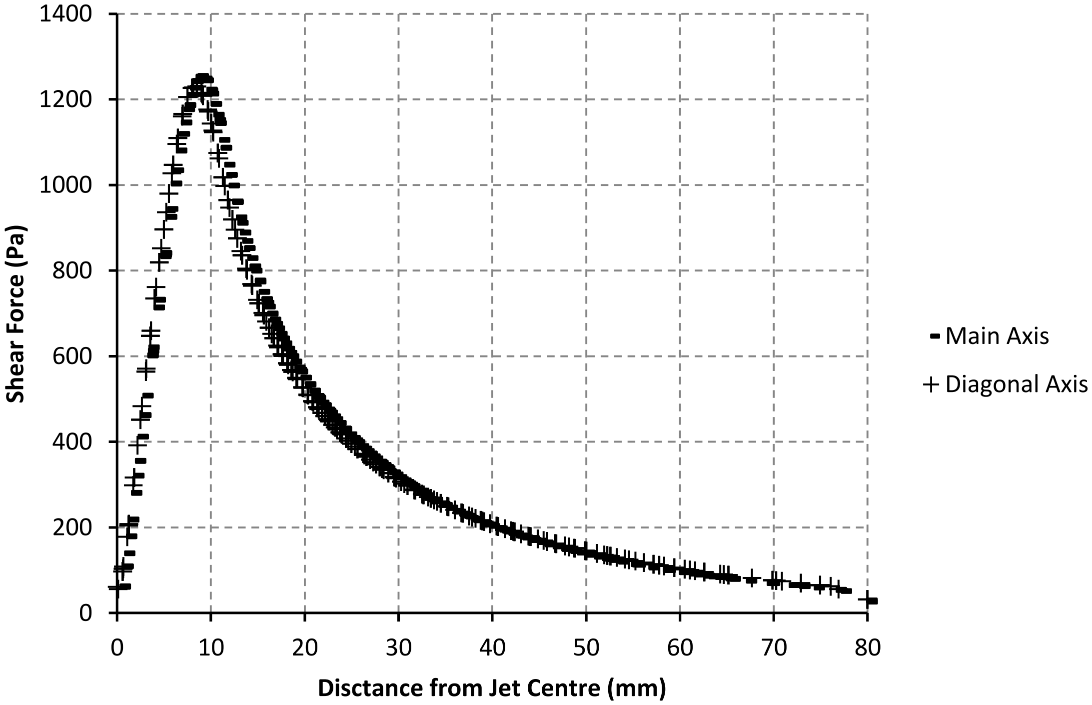

Figure 9-31: Plot of shear force along main and diagonal axes

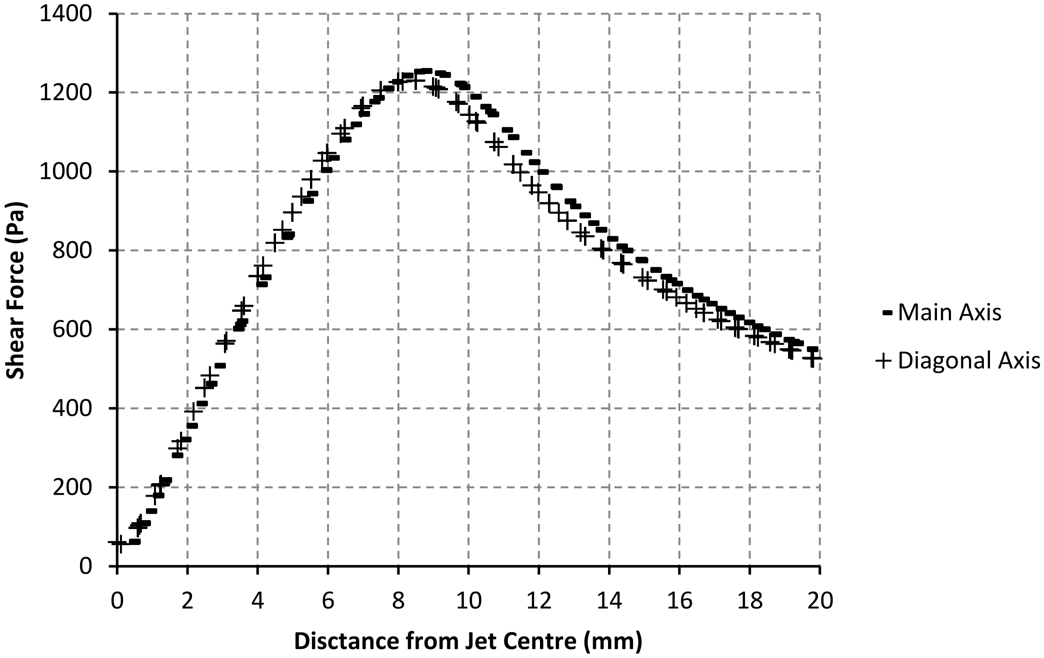

Figure 9-32: Shear force along the main and diagonal axes near the centre of impingement

Looking at the flow velocities across the plate, another interesting occurrence was noted. Examining the Mach contour plot shown in Figure 9-33, the flow over the whole plate appears relatively uniform in both planes. There is, however, an interesting cross pattern visible in the plot, aligned with the diagonal plane. Unlike the cross patterns noted in the shear contour plots discussed previously, this cross appears in the Mach contours of the wall jet, outside of the recirculation zone. This observation points to a slight difference in flow rates along the two planes. Examining the actual Mach data plotted in Figure 9-34, the two curves show only a very slight difference between the two planes. At this scale, however, it is impossible to draw any conclusions about the Mach number data near the recirculation zone.

As in the NPR=1 case the data has been re-plotted to consider only the first 20mm of the plate, as shown in Figure 9-35.

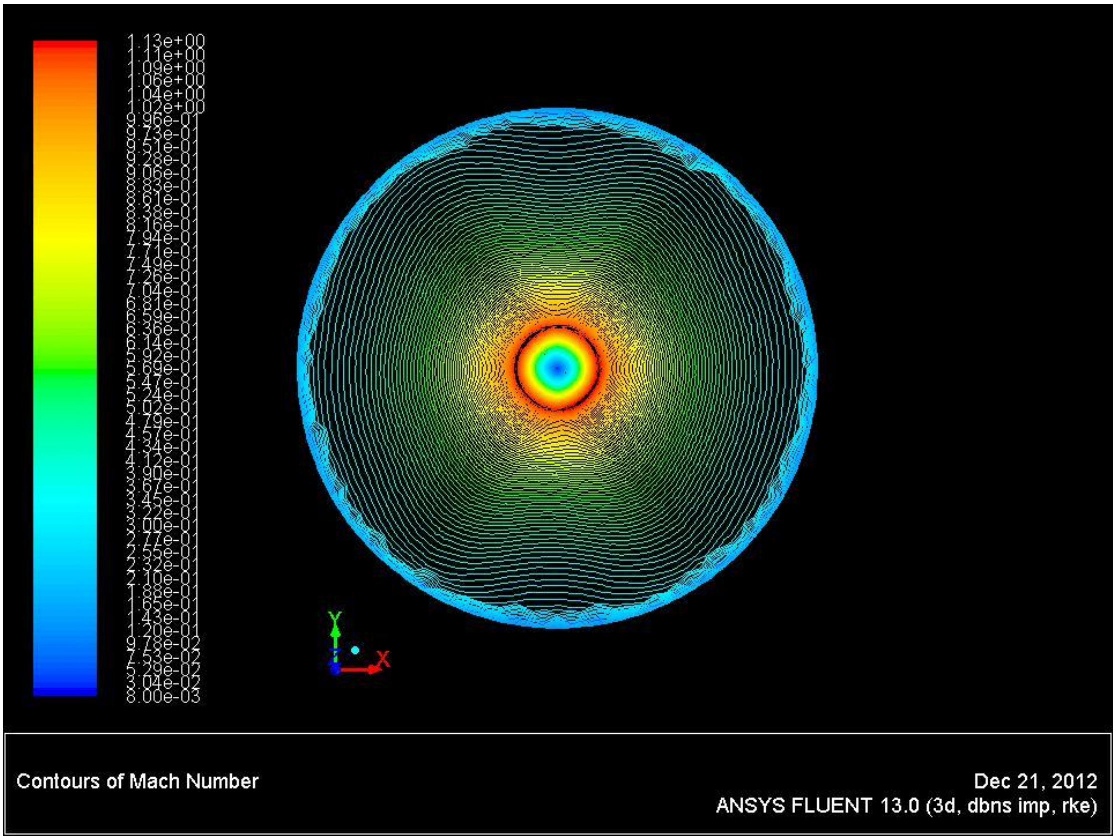

Figure 9-33: Mach number contour plot over the whole plate

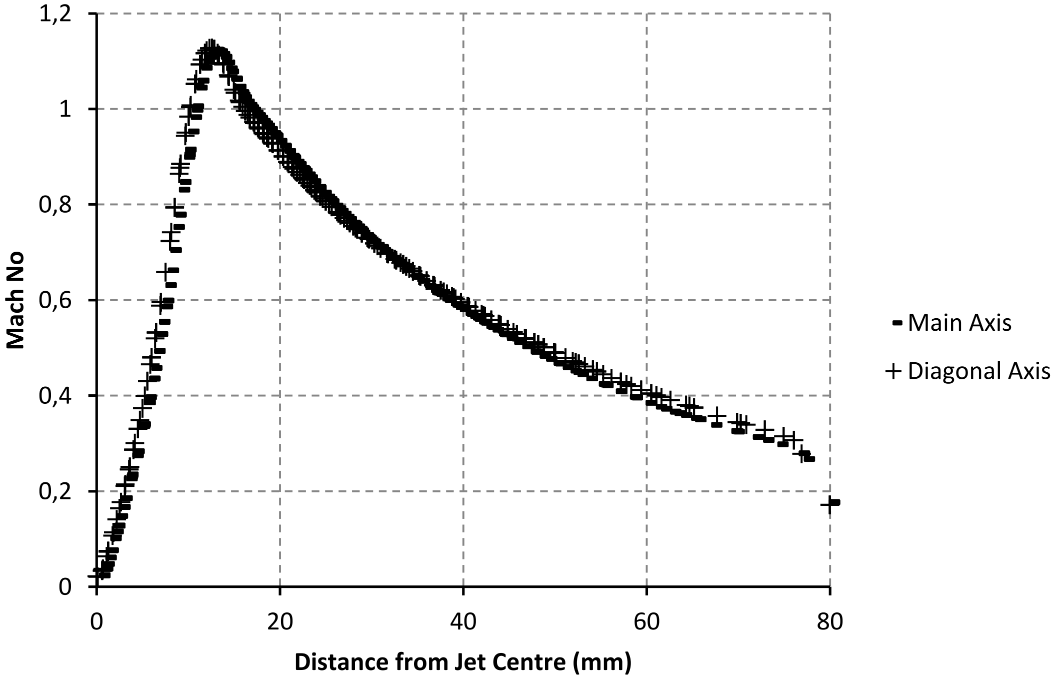

Figure 9-34: Plot of Mach number across the plate for the main and diagonal axes

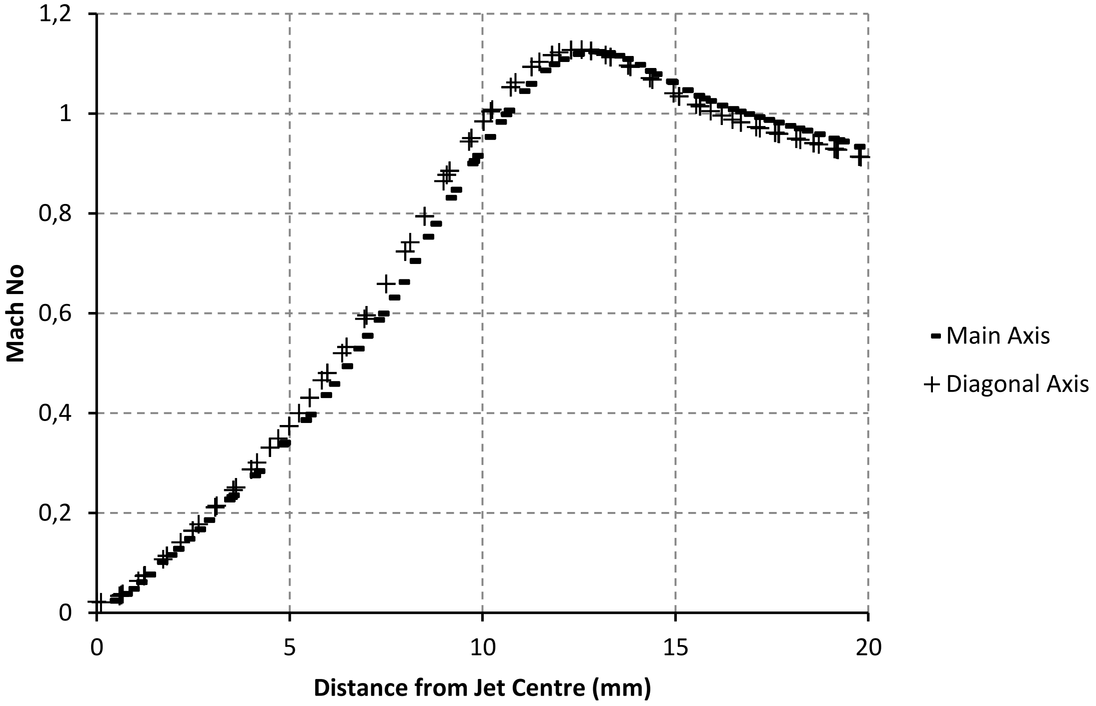

Figure 9-35: Mach number near the recirculation zone along the main and diagonal axes

In this case the Mach plots show the opposite trend to those of the NPR=1 case, with higher Mach numbers predicted along the diagonal plane. However, with a total difference of 0.0037 between the two peaks, the magnitude of the difference is too small to draw any definite conclusions.

In the NPR=1 case discussed previously the point of maximum shear coincided with the point of maximum temperature. Therefore the temperature variation across the plate has been considered for this case. Figure 9-36 shows the contours of temperature over the whole plate. The temperature variation across the plate seems approximately equal in all planes, with a possible slight increase in temperature on the main plane. This is confirmed when examining the plot of temperature variation for the two axes shown in Figure 9-37. However, as with the Mach number plot, the difference between the two curves is very small, with a maximum temperature difference of less than half a degree. At the recirculation zone boundary this difference is approximately 0.2^{o}K.

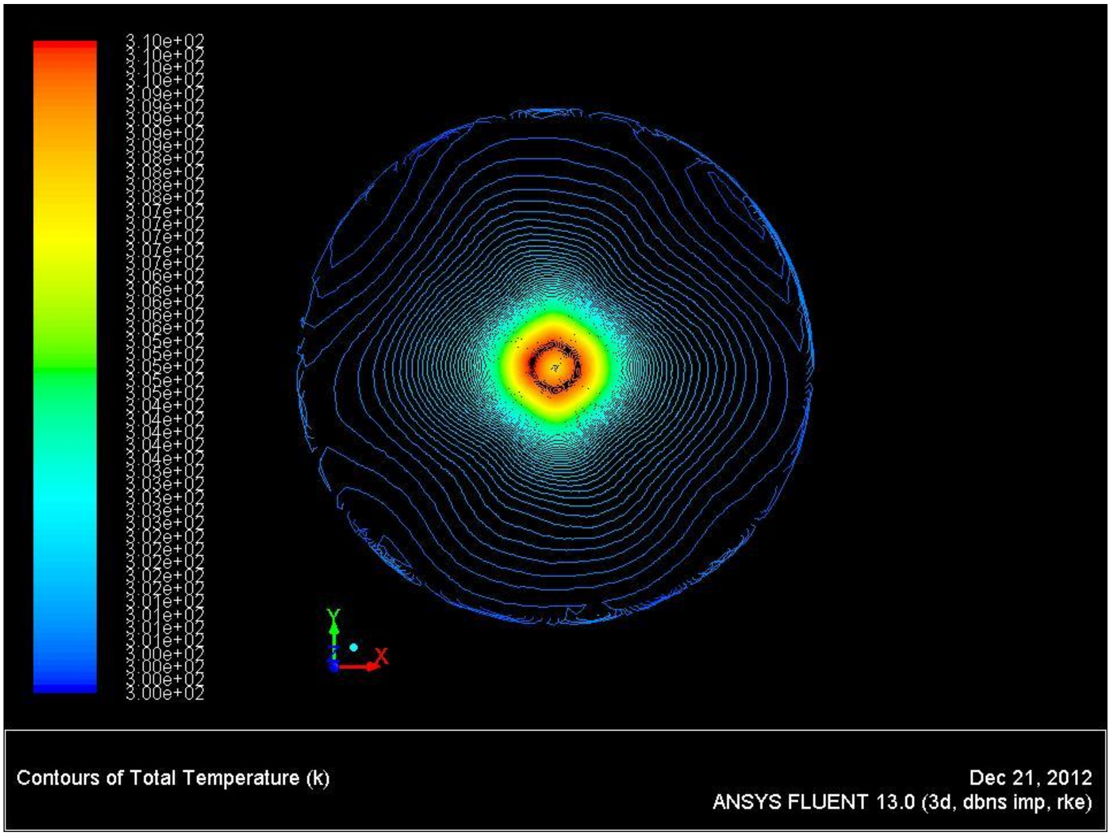

Figure 9-36: Contour plot of total temperature across the whole plate

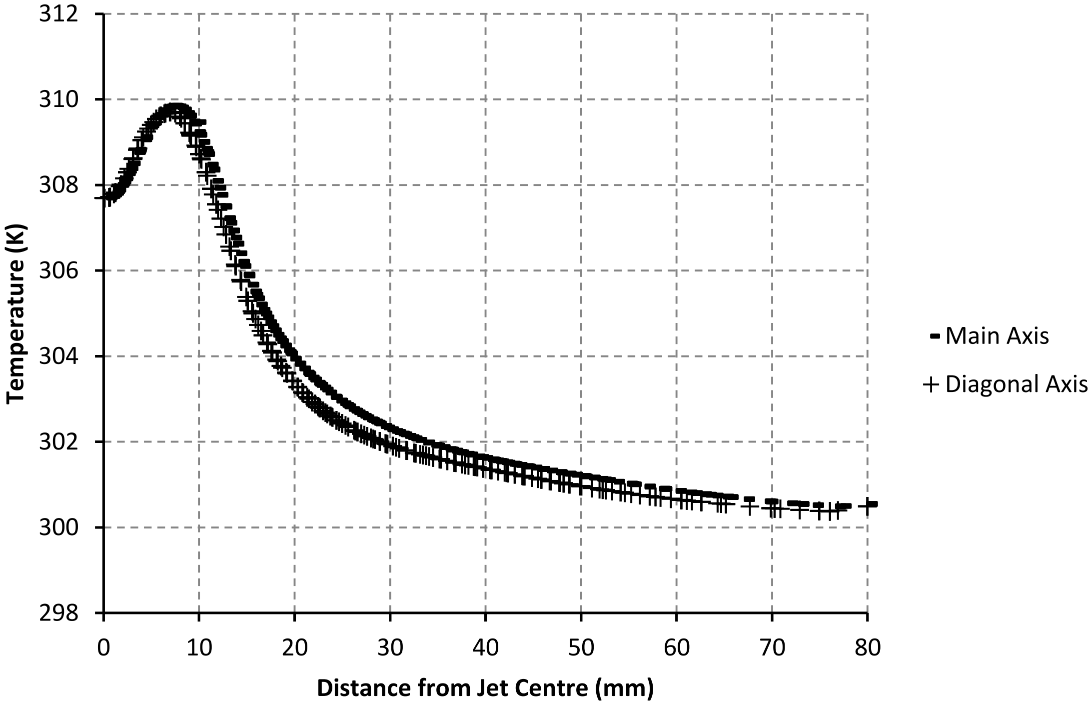

Figure 9-37: Temperature plot along the main and diagonal axes

Unlike the NPR=1 case, the peaks in temperature do not coincide with the shear force peaks on either axes, as evidenced by the two figures below. This fact calls into question the conclusion made previously regarding the effects of temperature on shear force.

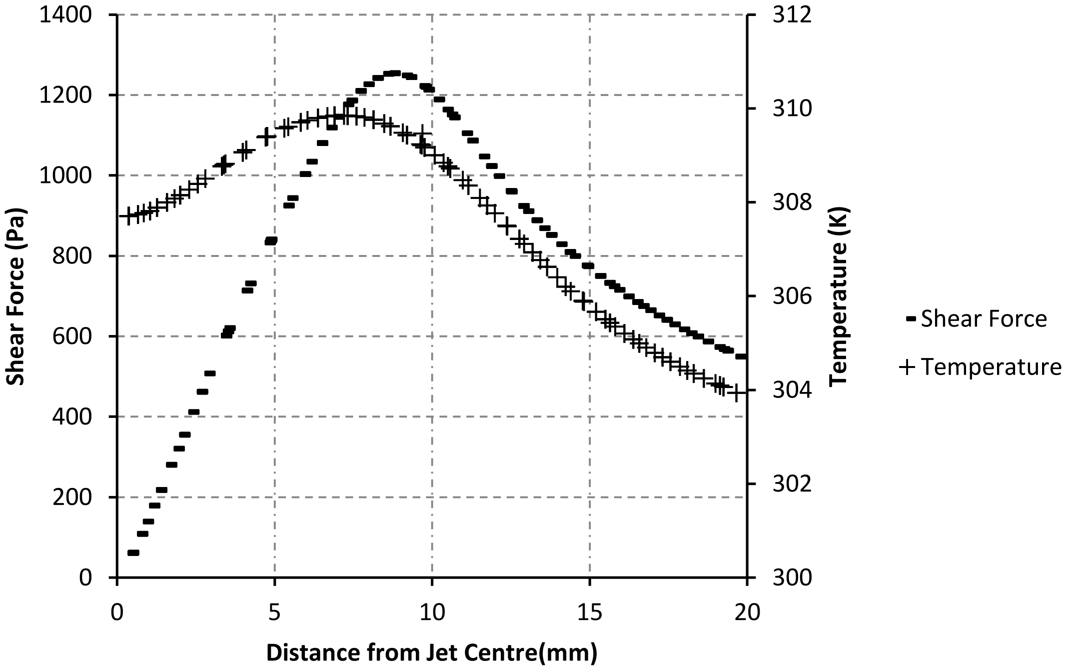

Figure 9-38: Shear force vs temperature along the main axis

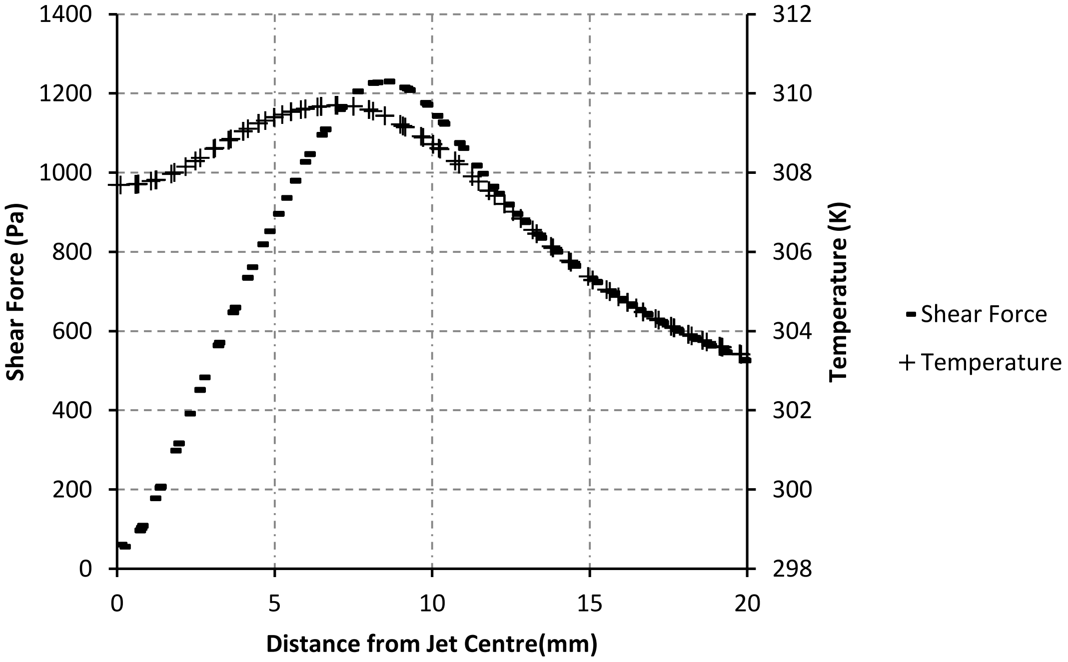

Figure 9-39: Shear force vs temperature along the diagonal axis

Moving now to comparing the experimental shear data with the CFD data discussed above, the interferometry data shows much better agreement with the simulation data than for the NPR=1 case. Although along both the main axis (Figure 9-40) and the diagonal axis (Figure 9-41) the experimental shear is lower than the CFD predictions close to the centre of impingement, the data matches much more closely further out along the plate. Even without removing outliers, the raw data in Figure 9-40 agrees very closely with the CFD.

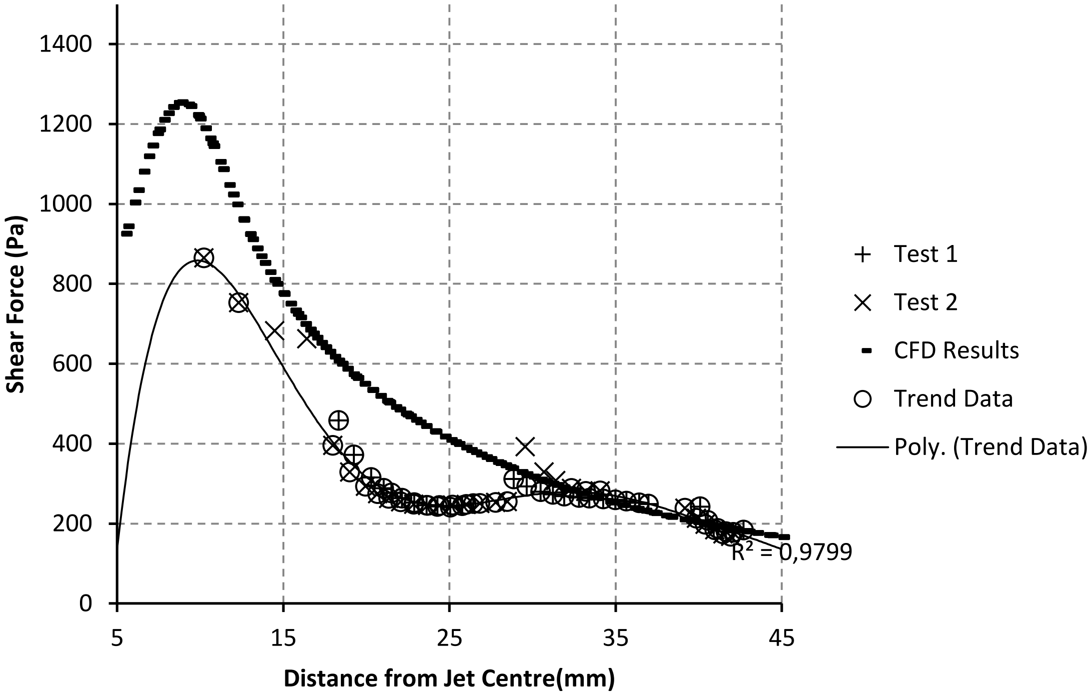

Figure 9-40: Plot of experimental and CFD shear data along the main axis

Although the there are a significant number of outliers in the data shown in Figure 9-41, the general trend of the data matches the CFD predictions very closely all the way along the curve. That being said, it is obvious from examining the graph that a large number of data points were excluded from the trend data to generate the best fit curve shown. So whilst the interferometry tests did generate closely matched data, the large difference between the two experimental data sets brings into question the repeatability of this method.

The actual fringe images generated from this test case once again showed some interesting qualitative results. Looking at the fringe image shown in Figure 9-42, the flow of the oil from the 10mm drop is unique in the flow patterns observed in this investigation. The flow pattern shown was the only case in this investigation where the oil was actually drawn towards the centre of the plate, into the recirculation zone. Measuring the distance of the leading edge of the original drop from the jet centre, the recirculation zone for the NPR=2 case appears to extend approximately 8mm from the jet centre along the main axis.

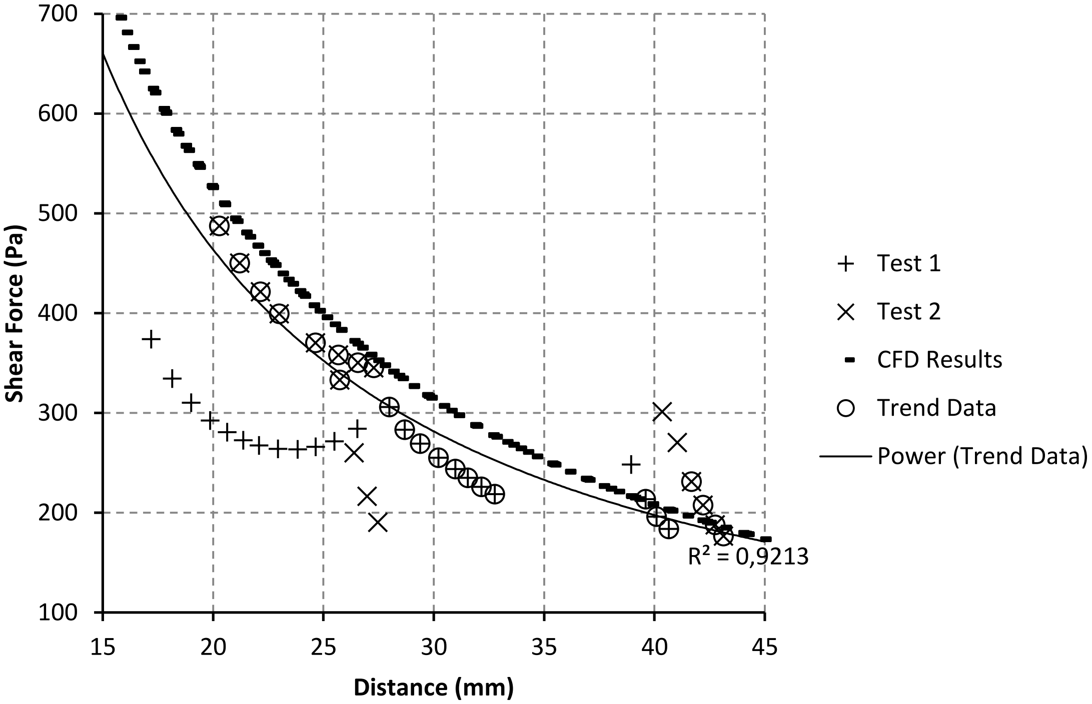

Figure 9-41: Plot of experimental and CFD shear data along the diagonal axis

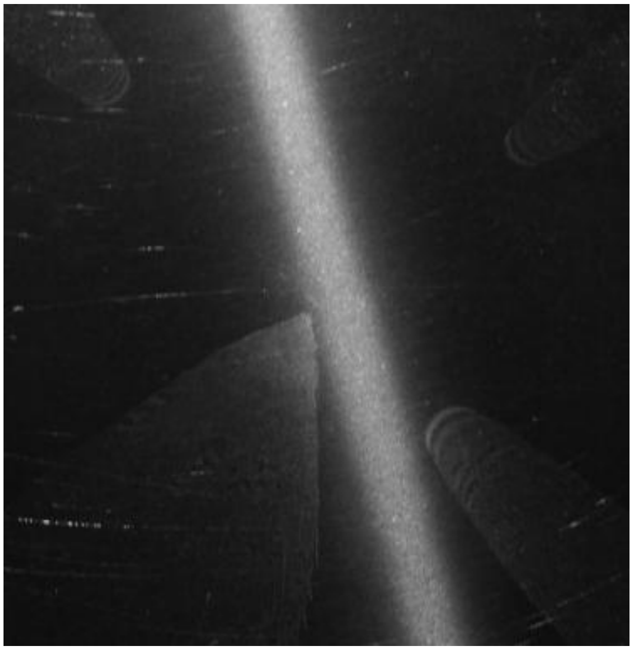

Figure 9-42: Single drop fringe patterns, v=600cSt, t-15s

Looking briefly at the Mach contours within the jet core along the main and diagonal planes (Figure 9-43 and Figure 9-44 respectively), the effects of the higher under expansion ratio is immediately clear. The choking shock wave has moved up into the nozzle, a result of the higher inlet pressure causing an increase in flow acceleration. The shock diamonds that were clearly evident in the NPR=1 case are not apparent in these images. The diagonal lines radiating out from the stand-off shock, most noticeable in the diagonal plane, indicate that the first shock diamond has moved further downstream of the nozzle exit to a point where it has been absorbed by the dominating stand-off shock. The stand-off shock is also much more clearly defined and occurs further from the plate surface than in the lower pressure case.

What is most interesting when examining these images is that fact that they show such different flow conditions. Unlike the flow patterns on the impingement surface, the jet core shows a distinct difference in behaviour between the two planes. Most notable is the difference in the extent of the jet boundary. As with the NPR=1 case, the jet core widens as it moves downstream from the exit on the main axis, whilst remaining more or less constant width in the diagonal plane. As mentioned above the deceleration shocks in the jet core are much more clearly defined along the diagonal plane.

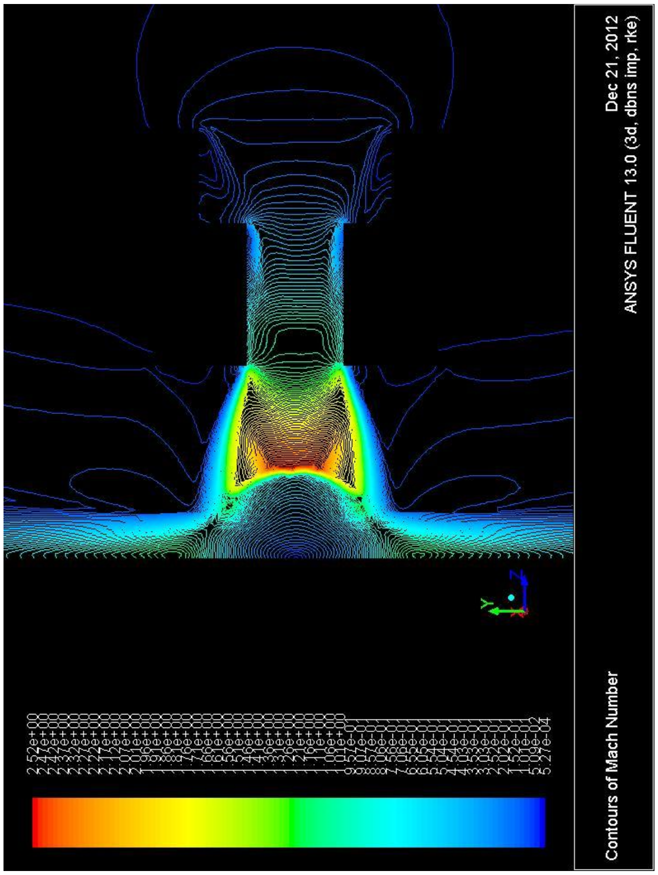

Figure 9-43: Mach contours within the jet along the main axis

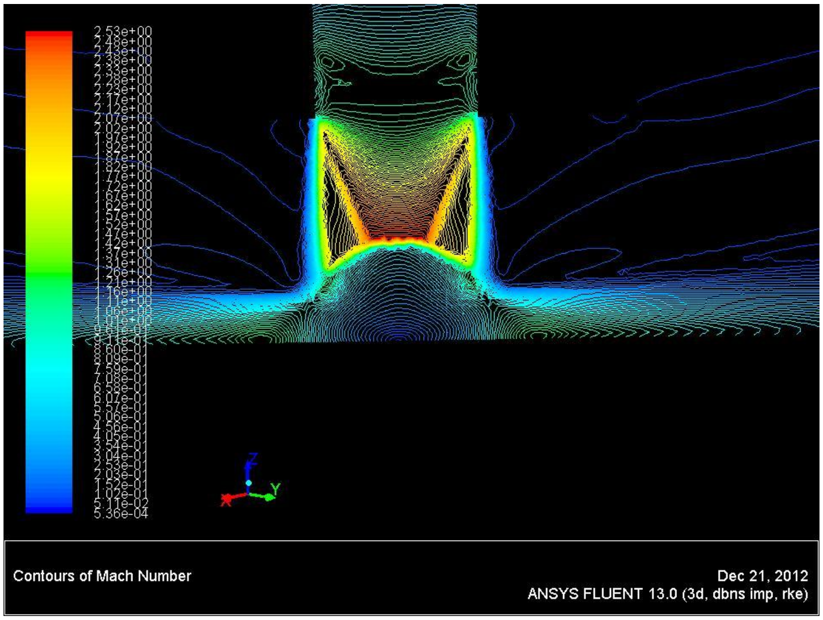

Figure 9-44: Mach contours in the jet core along the diagonal axis

9.3 Rectangular Nozzle, AR=4, NPR=1, n/d=2

When examining the results for the rectangular jet nozzle there is a third plane that needs to be considered. The schematic in Figure 9-45 below shows the definition of these planes. The Major Plane was taken as being parallel to the narrow side of the nozzle, the Minor Plane parallel to the long side. Whilst this definition may seem the wrong way round in terms of the geometry, it makes sense when considering the major direction of flow across the plate (which will be shown later to be along the major axis as defined here). Since the corners of the jet nozzle are not at 45^o to either of the other two axes, this set of axes has been re-defined as the Oblique Plane rather than the Diagonal Plane as in the Square Nozzle case.

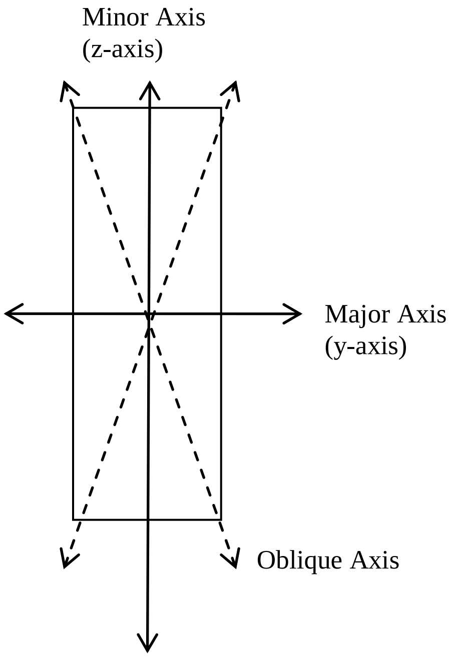

Figure 9-45: Axis definition for rectangular nozzles

In all images to follow the alignment of the major and minor axes has been indicated in the bottom left hand corner of the image. For clarity the oblique plane has been left off of the reference axes on the image. Since the results discussed here deal only with flow from a nozzle with an aspect ratio of four, the position of the oblique axes can be taken to be 14^o from the minor axis and 76^o from the major axis.

Now that the reference planes have been defined for this nozzle case, the resultant data can be examined with more clarity. As above, starting with the qualitative fringe images a dramatic difference from either square nozzle case is immediately apparent. Examining the whole plate surface in Figure 9-46, the first thing to note is the fact that the oil has not been spread out over the whole plate. The distinct lack of oil on the outer portions of the plate in the bottom left and top right hand corners indicates that the airflow over the plate has occurred almost entirely along the main axis, with very low velocity flow on the minor axis. This shows that the wall jet in this case is solely aligned with the major plane. This observation is supported by the CFD Mach number plot shown in Figure 9-47 (as with the experimental images, in the CFD images to follow the y-axis indicates the major plane, the z-axis the minor plane)

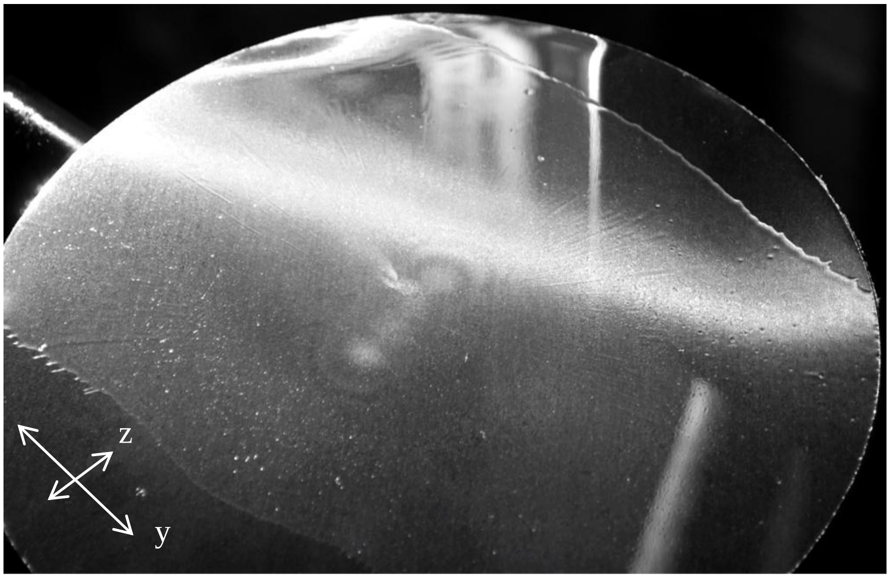

Figure 9-46: Central Blob, AR=4, NPR=1, n/d=2, v=550cSt, t=30s

When examining the CFD images another interesting flow pattern is also visible. Whilst the wall jets are approximately in line with the major plane, as indicated by the oil coating in Figure 9-46, these wall jets actually occur along four separate lines, angled slightly out from the major axis. Unfortunately none of the experimental images showed any sign of this wall jet alignment. Also, since the main objective of this investigation was focused on shear forces, the positioning of these wall jets was not discovered until very late into the experimental process so no single-drop interferometry experimentation along these lines was carried out. The positioning of these wall jets is something that requires further investigation.

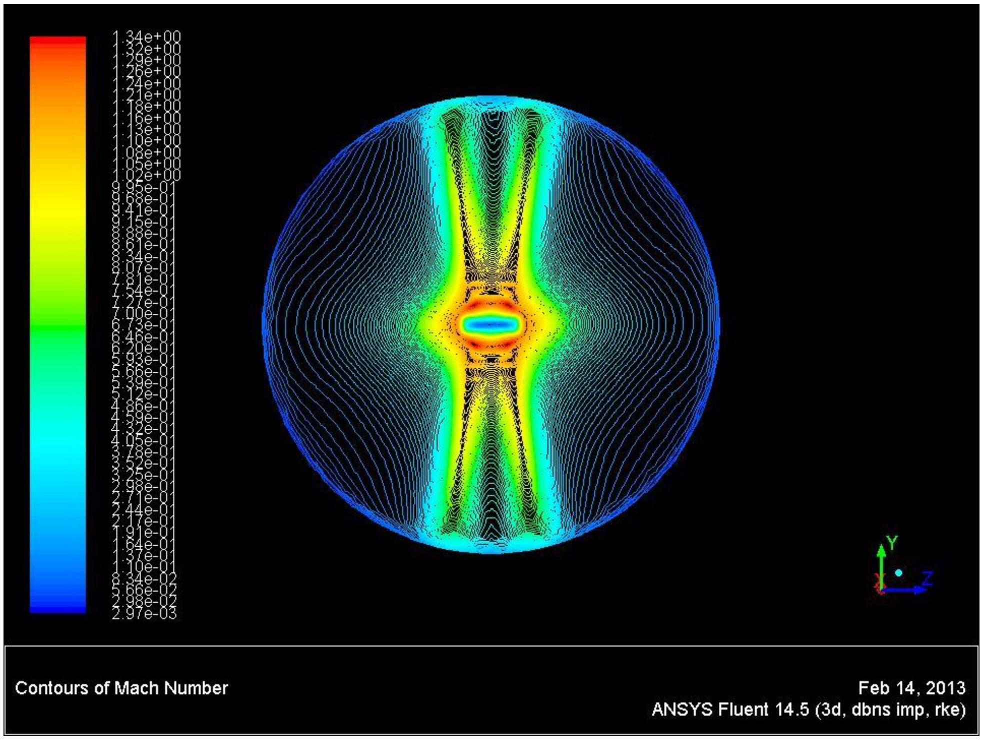

Figure 9-47: Contours of Mach Number on the impingement plate

Zooming in on the impingement zone at the centre of the plate, the fringe patterns shown in Figure 9-48 indicate the same shear force trends as were noted in the NPR=1 square nozzle case, with areas of maximum shear occurring along the plane of minimum wall jet flow rate. Apart from the general shear force trends, the two white ovals visible in the oil coating, highlighted by the two arrows in the figure, indicate the presence of either recirculation zones or areas of stagnation. The dark fringes surrounding these areas suggest a flow gradient; however it is unclear whether the flow is into or out of the area. An examination of the CFD shear forces on the plate shown in Figure 9-49 tends towards a conclusion for stagnation points, since these white areas in the photograph appear to coincide with the two end points of the recirculation zone. The CFD shear plot also shows the zones of maximum shear aligned with the jet’s minor axis.

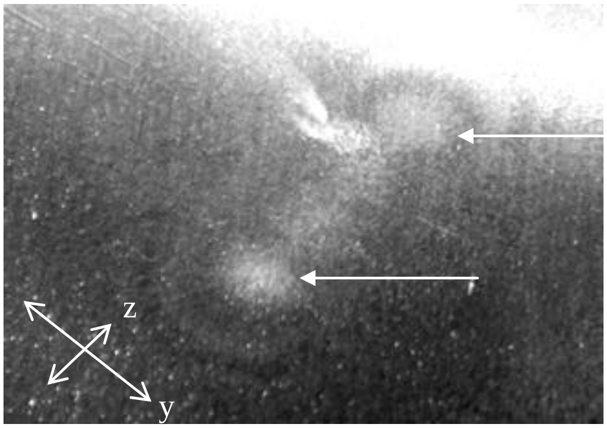

Figure 9-48: Impingement zone fringe patterns. AR=4, NPR=1, n/d=2, v=550cSt, t=30s

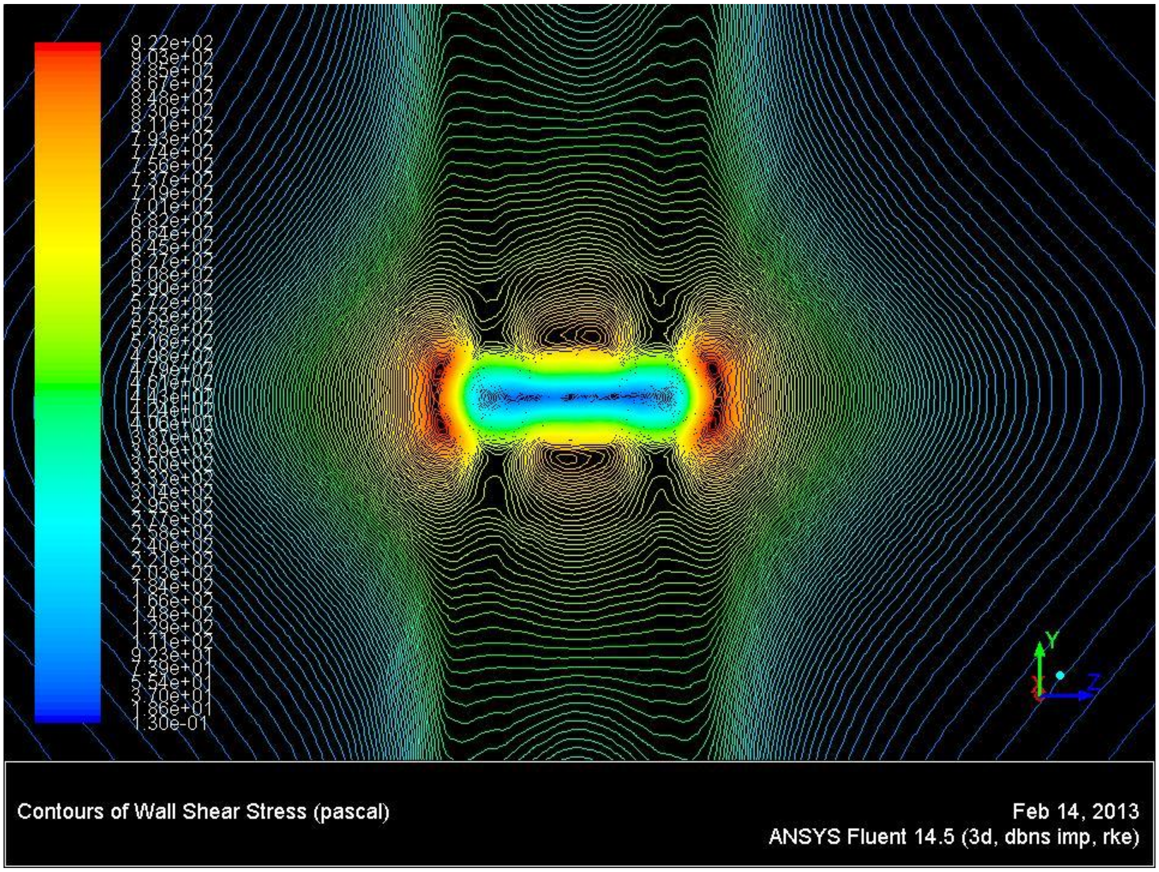

Figure 9-49: CFD contour plot of shear forces at the centre of the plate

A less surprising, yet no less noteworthy, flow characteristic shown in both the experimental and CFD images is the elongated nature of the recirculation zone. This is no doubt a result of the high aspect ratio of the nozzle as well as the small distance between the nozzle exit and the plate (20mm). Although the elongation of the recirculation zone was something to be expected, the actual shape of this zone is rather interesting. The zone is slightly squashed along the major axis, with two zones of high shear near the top and bottom borders. Moving along the minor axis the recirculation zone widens out slightly and terminates in two semi-circles, the zone bounded by the two areas of maximum shear which have a distinct kidney shape. Between the four zones of high shear are four zones of approximately constant shear.

Looking at a close up of the Mach contours in the same region (Figure 9-50), the areas of highest Mach number appear to coincide with the areas of constant shear noted above, with areas of lower Mach along the major and minor axes, where the shear force is higher. Unfortunately the results from this case did not give any further clarity on the inverse relationship between shear force and Mach number in the vicinity of the recirculation zone.

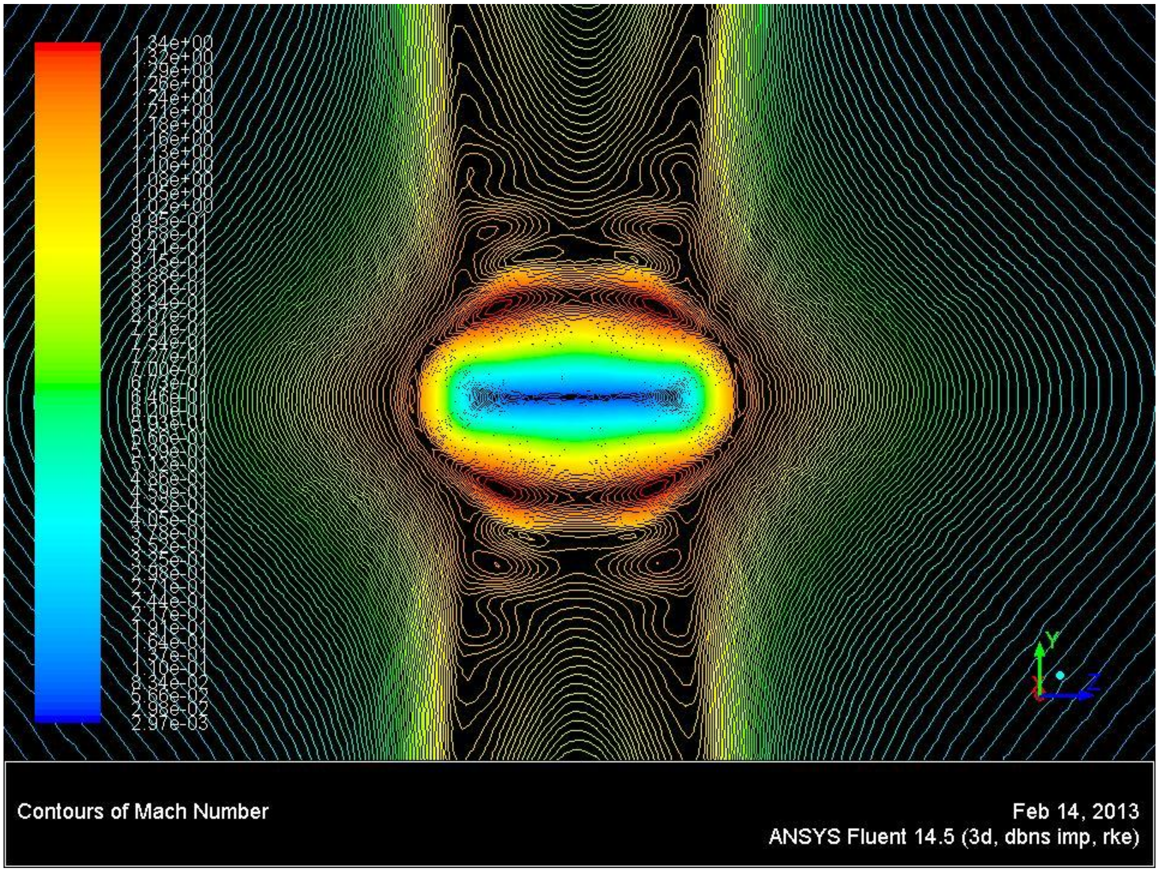

Figure 9-50: Mach number contours at the centre of the plate

Turning to the actual data predicted by the simulations, there is a large difference in maximum shear forces along the two planes, similar to the NPR=1 square nozzle case. Another similarity between the square and rectangular cases is the sharp drop off in shear force on the curve that shows maximum shear near the recirculation zone. Further out along the plate surface the shear force is dominated by the flow velocity, resulting in a higher shear along the major axis.

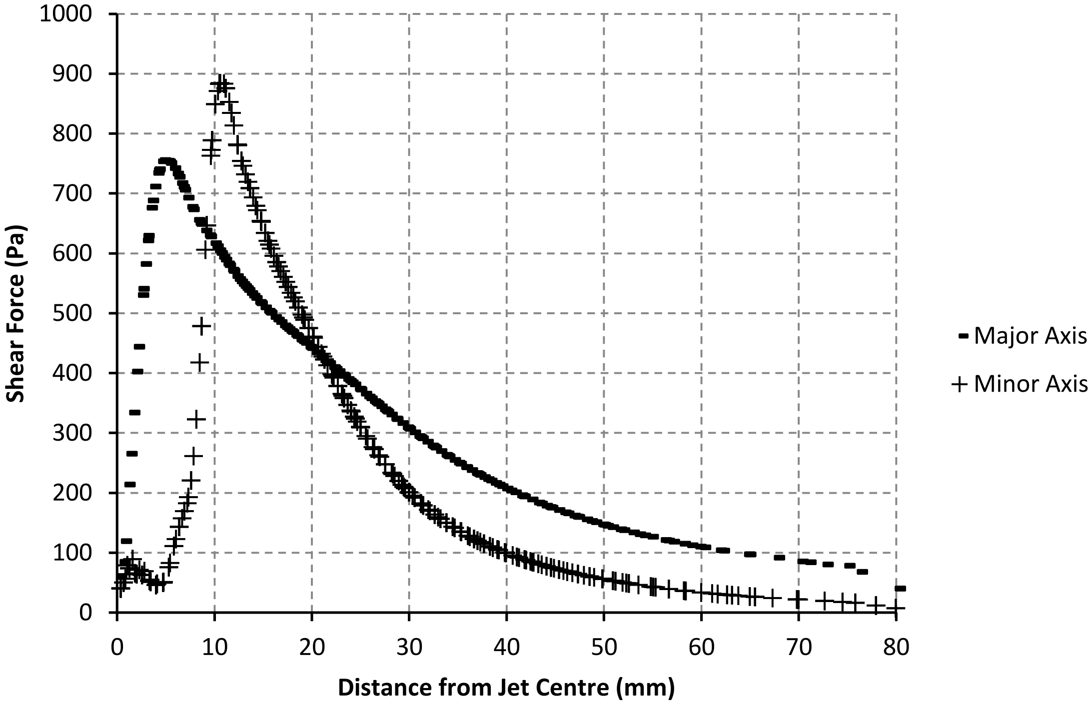

Figure 9-51: Shear forces along the major and minor axes

Closer examination of the shear data along the minor axis shows some interesting behaviour within the recirculation zone that was not evident in the square nozzle experimentation. The initial increase, followed by the short drop in shear force, which then increases sharply to the peak value possibly indicates the presence of a secondary recirculation zone within the main zone.

Comparing the experimental shear data with the CFD data for the major and minor axes, as shown in Figure 9-52 and Figure 9-53 respectively, the interferometry data once again underestimates the shear forces. Although the degree of this underestimation decreases further along the plate, the overall trend of the data is still somewhat lower than the CFD predictions. This difference in experimental and simulated data is most apparent between the 10 and 20mm marks on the major axis.

Looking at the graph it should be noted that there are a series of data points within the 10-20mm region that have been excluded from the trend data, even though they show significantly higher shear values. The reason for this data being excluded was the fact that more than double the number of data points in this region occurred in the lower shear regions. Since the goal of this comparative plotting process was to determine how accurately the interferometry method can predict shear forces, the relative density of data points meant that this higher-shear data had to be excluded from the trend data. Similarly in Figure 9-53, more data points predicted the higher shear values than the lower values, meaning they were chosen as trend points for the best fit curve.

These two plots shown below serve to illustrate once again the non-repeatable nature of the resultant data from the interferometry technique used in this application.

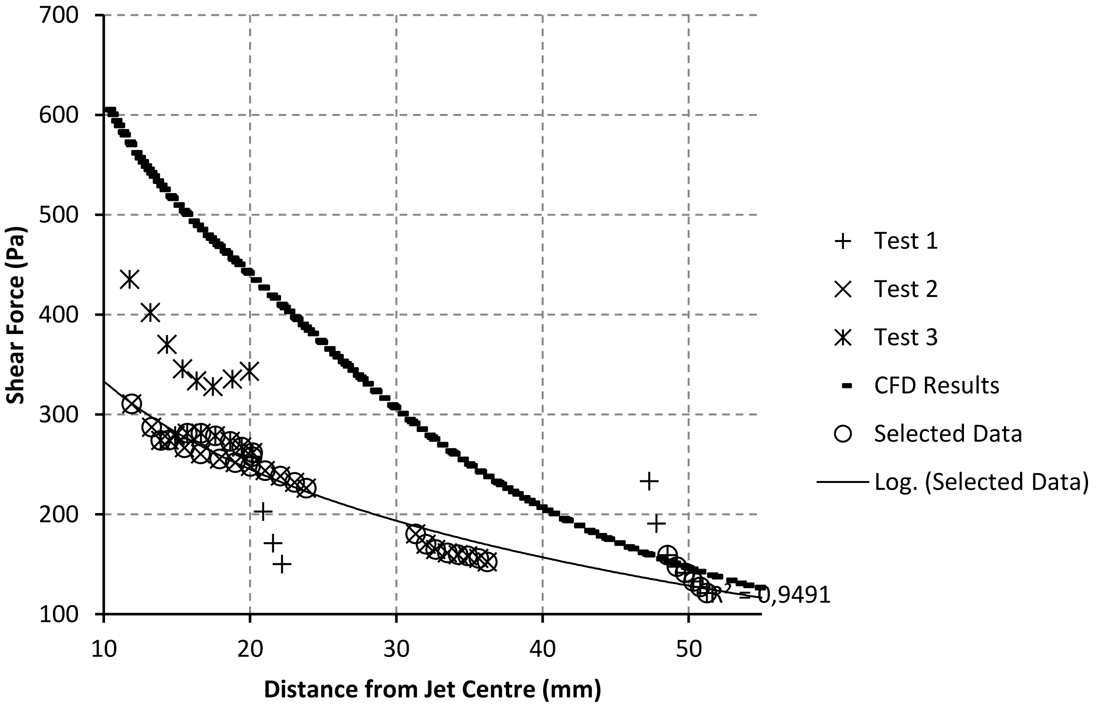

Figure 9-52: Experimental and CFD shear force curves along the main axis

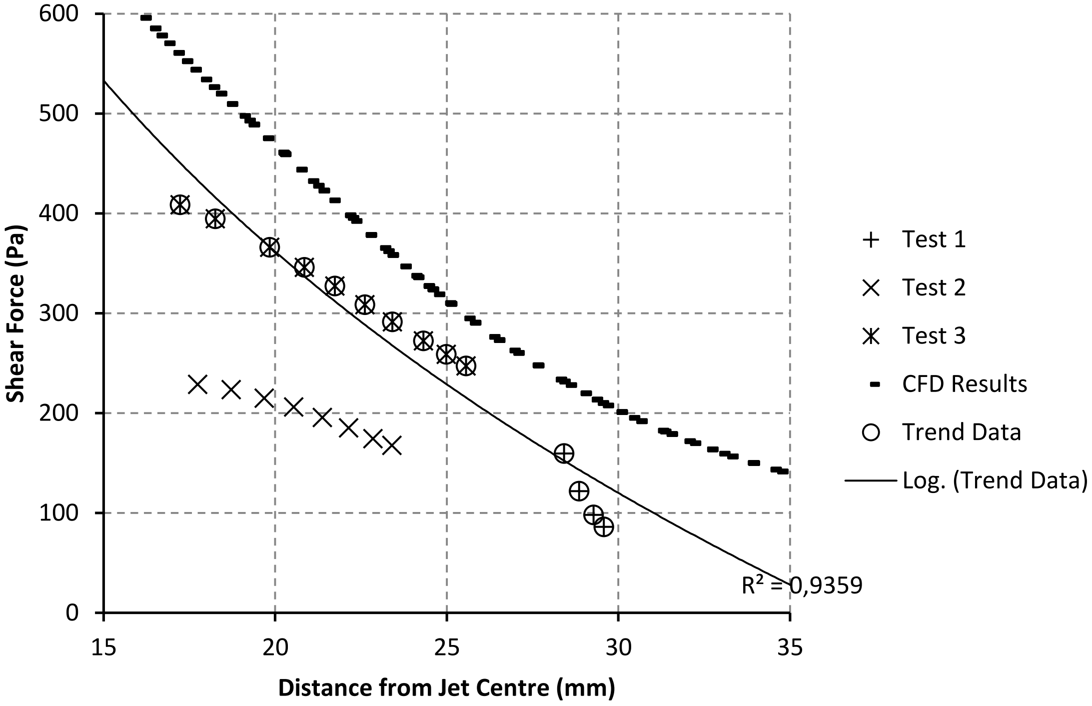

Figure 9-53: Experimental and CFD shear force curves along the diagonal axis

Examining the flow conditions in the jet core, the Mach contour plots shown in Figure 9-54, Figure 9-55 and Figure 9-56 show some completely unexpected results. Looking along the main axis (Figure 9-54), it appears that the first shock cell in the jet core occurs within the throat of the nozzle. Instead of being choked by a normal shock wave, the nozzle is choked by two oblique shocks which meet at the centre of the throat just before the nozzle exit plane. After exiting the nozzle the flow undergoes rapid acceleration and deceleration within the first 10mm of the flow.

The contour plot along the oblique axis (Figure 9-56) shows more or less the same flow patterns as those on the main axis. This is most probably due to the fact that the oblique axis is so close to the main axis. Conversely, the flow in the core along the minor axis (Figure 9-55) shows almost no distinct flow patterns.

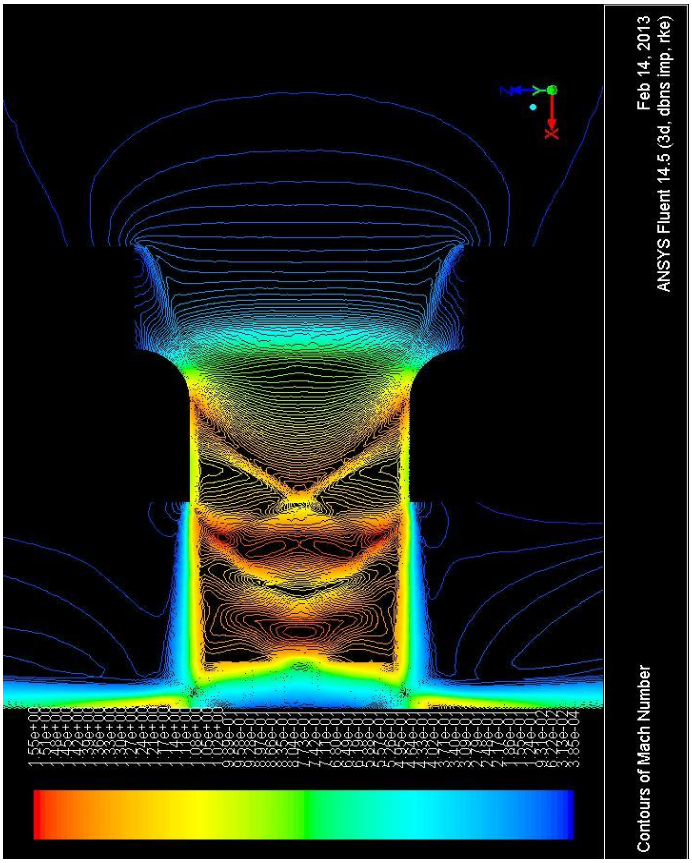

Figure 9-54: Mach contours in the jet core along the major axis

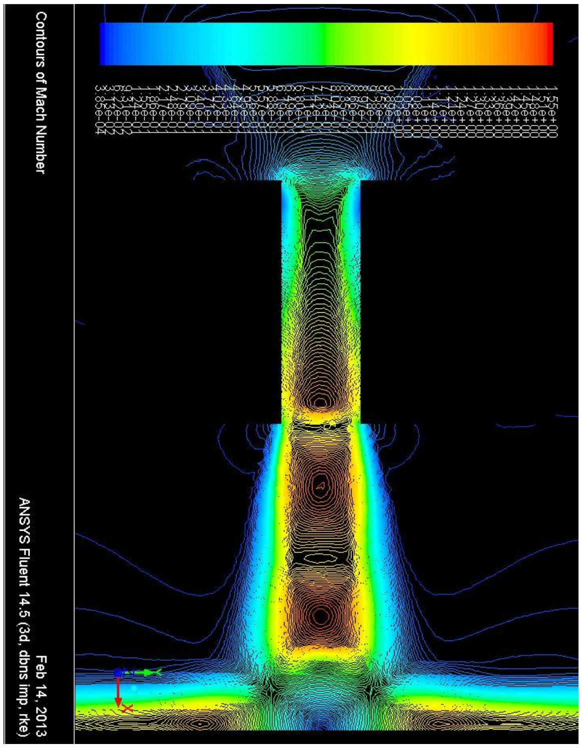

Figure 9-55: Mach contours in the jet core along the minor axis

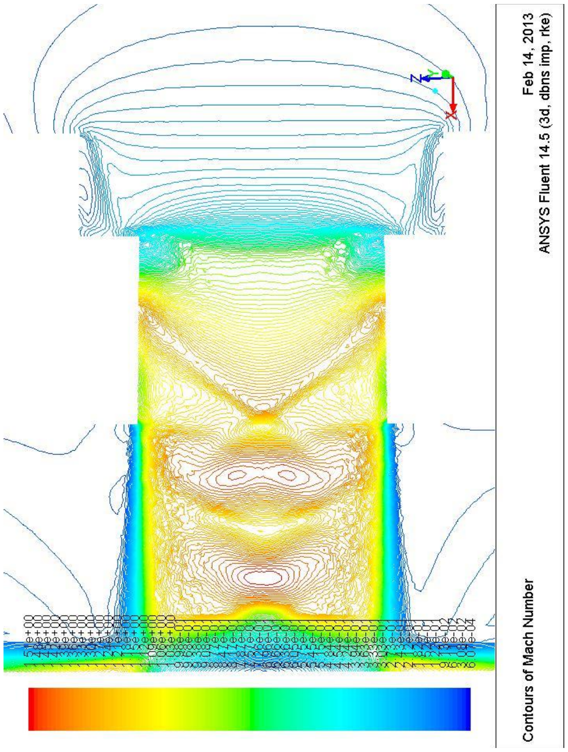

Figure 9-56: Mach contours in the jet core along the oblique plane

9.4 Rectangular Nozzle, AR=4, NPR=2, n/d=2

Unlike the square nozzle case, the impingement of a higher nozzle pressure ratio jet from the AR 4 rectangular nozzle does not result in the shear forces across the plate becoming more symmetric across the different axes. The high aspect ratio of the nozzle means that there is still a large difference between the shear forces along the major and minor axes. Figure 9-57 shows the result of running the jet for 20 seconds with a nozzle pressure ratio of two (NPR=2). A globule of 550cSt oil was placed at the centre of the plate. As is apparent, the fringe patterns are much less visible in this image than for any of the previous cases. Although no quantitative analysis could be carried out on any of the images generated from central globules, the fringes present are sufficient to show the general variation of the shear force within the vicinity of the impingement zone.

As with the lower NPR case, the highest shear appears to occur along the minor plane. However what is even more interesting than the fringe patterns are the white striations that are visible in line with the major axis. As was noted in the observations section, the presence of these white striations indicates the direction of flow of the wall jet.

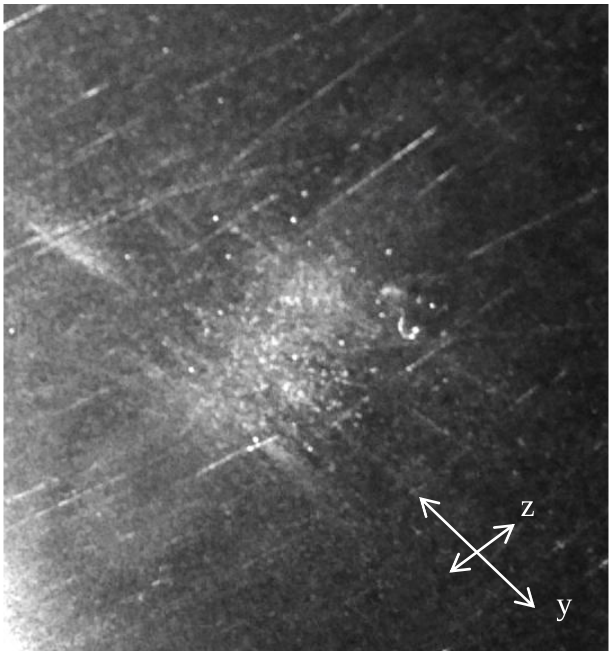

Figure 9-57: Central blob. AR=2, NPR=2, n/d=2, v=550cSt, t=20s

Both suppositions regarding the flow patterns visible in the above image are supported by the CFD data. The shear forces over the plate shown in Figure 9-58 show that the shear is still higher along the minor plane, however the extent of this region of high shear is significantly less than that of the NPR=1 case. An examination of the Mach number variation over the plate, as shown in Figure 9-59, shows that the wall jets once again occur along the major axis, as was indicated by the striations noted in Figure 9-57.

A further examination of the two CFD plots shows that the majority of the flow patterns noted in the NPR=1 case still occur. The wall jets still occur along four distinct lines angled slightly away from the major axis. The recirculation zone has the same elongated shape, although it has a much more uniform thickness along the minor axis than in the previous case. The zones of constant shear are also aligned with the wall jets. A closer examination of the Mach plot shown in Figure 9-60 also indicates that the zones of constant shear coincide with the zones of maximum Mach number.

There are also a number of unique flow patterns visible in these images. The shear plot of the impingement area (Figure 9-58) shows two different areas of constant shear: The first occurs along the main axis at the border of the recirculation zone, the second slightly farther out from the centre of the plate occurring between the two oblique axes across the major axis. The close-in plot of the Mach number contours (Figure 9-60) also show two distinct regions of approximately constant Mach. The first region is, as expected, on the boundary of the recirculation zone, indicating the position of the wall expansion fan. Just after this region the flow appears to undergo sharp deceleration after which is another region of constant Mach running between the two oblique axes, across the minor plane.

Plotting the shear forces and Mach numbers for all three planes (Figure 9-61 and Figure 9-62 respectively) shows similar trends. Although neither the shear forces nor the Mach numbers are in fact constant along any of these axes, there is a drop in their values in the areas mentioned. Along the major axis the shear force decreases sharply from 5 to 10mm from the plate centre. This drop off levels out at approximately 11mm, at which point it increases slightly, before gradually decreasing along the rest of the plate. The shear forces on the minor and oblique planes are considerably higher than that along the major axis. Although it is not as pronounced, there is a slight gradient change in the minor and oblique axis curves. This gradient change should coincide with the second constant shear zone mentioned above.

Examining the Mach number graph in Figure 9-62, the peak value on the major axis occurs at approximately 10mm and is, as expected, greater than the peak Mach value for the minor and oblique planes, which occur about 2mm after this peak. As with the shear data, the Mach curves along the minor and oblique planes undergo a sharp change in gradient, indicating the position of the second zone of apparent constant Mach.

In both the shear and Mach cases the areas identified in the contour plots are not in fact areas where the values are constant, but areas where these values undergo a sharp change in gradient.

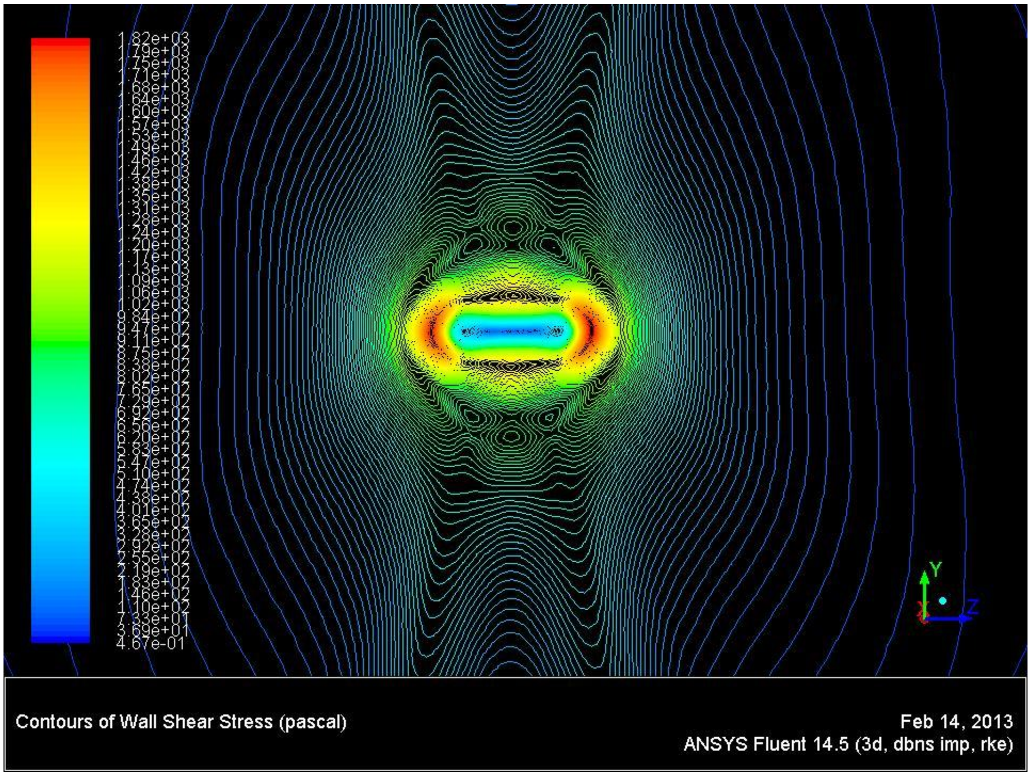

Figure 9-58: Shear force contour plot on the plate for AR=4 nozzle, NPR=2 jet

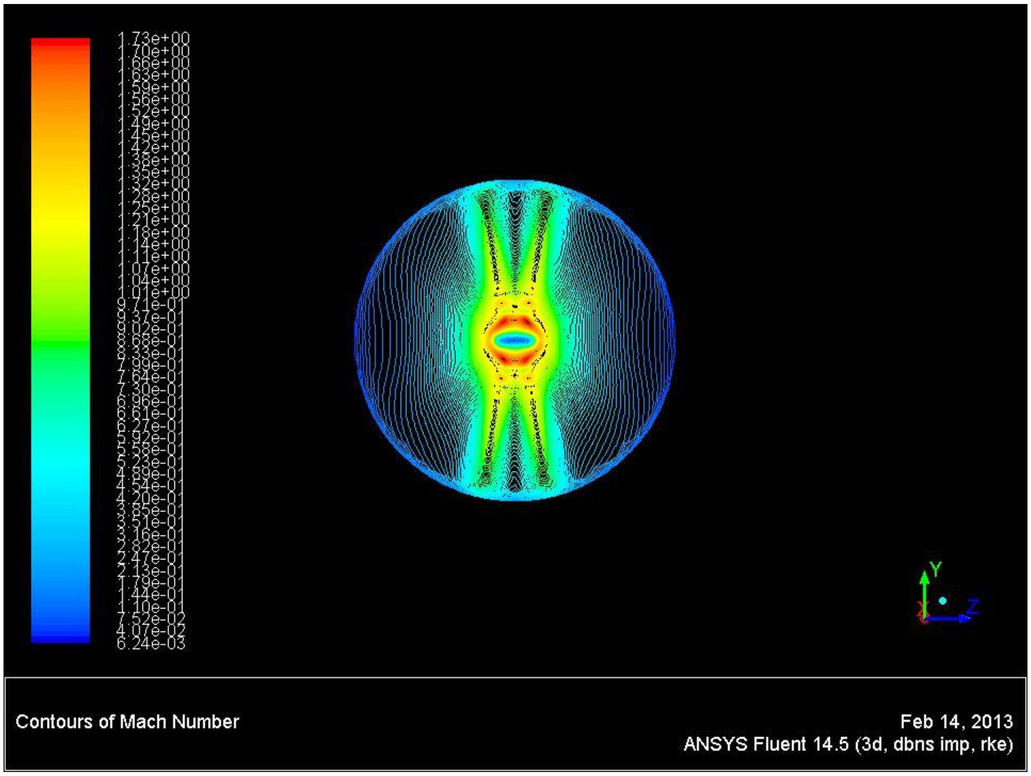

Figure 9-59: Mach contour plot over the plate for AR=4 nozzle, NPR=2 jet

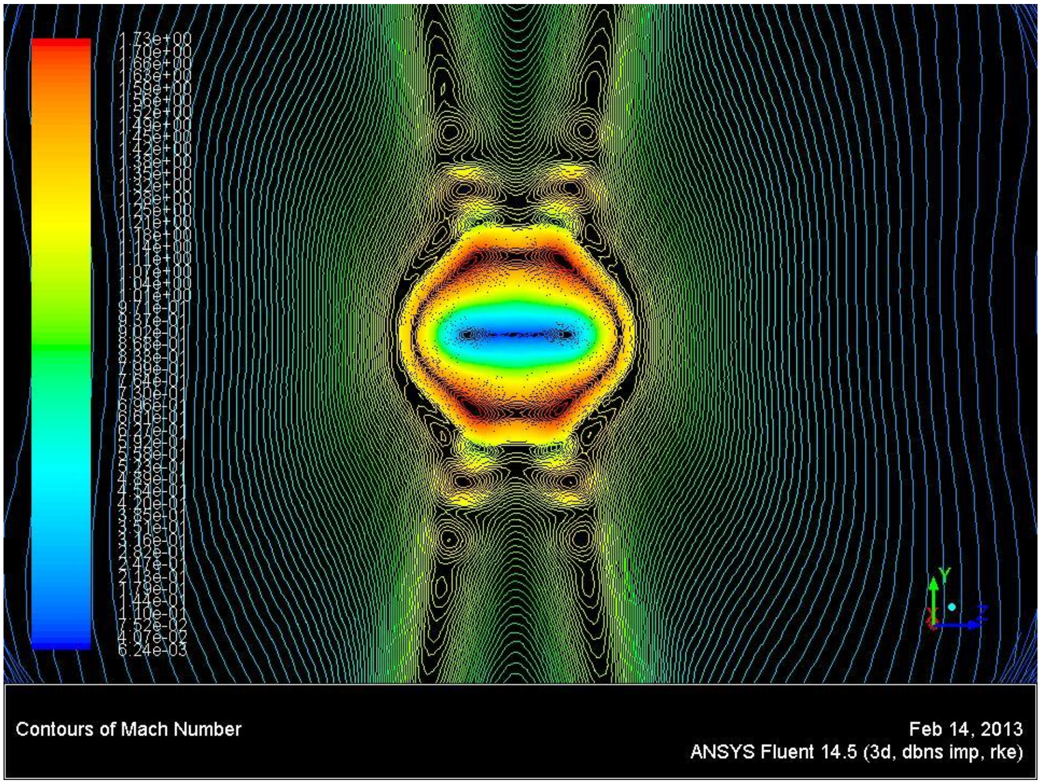

Figure 9-60: Mach contour plot of the impingement zone

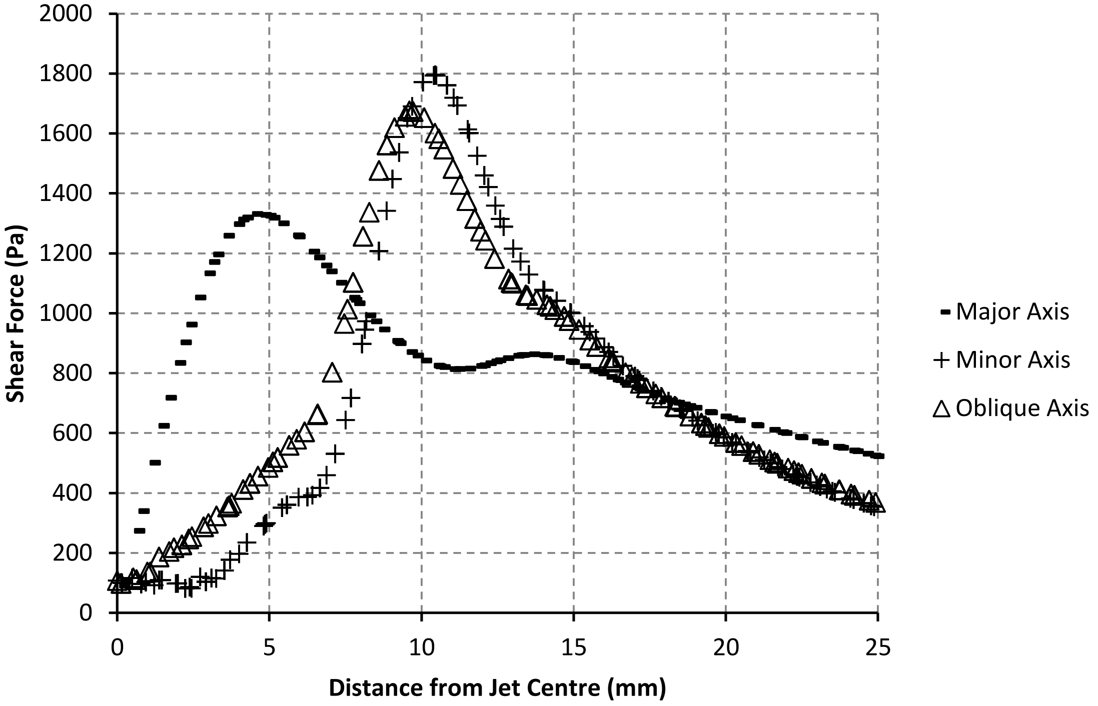

Figure 9-61: Plot of Shear Force near the impingement zone for all three planes

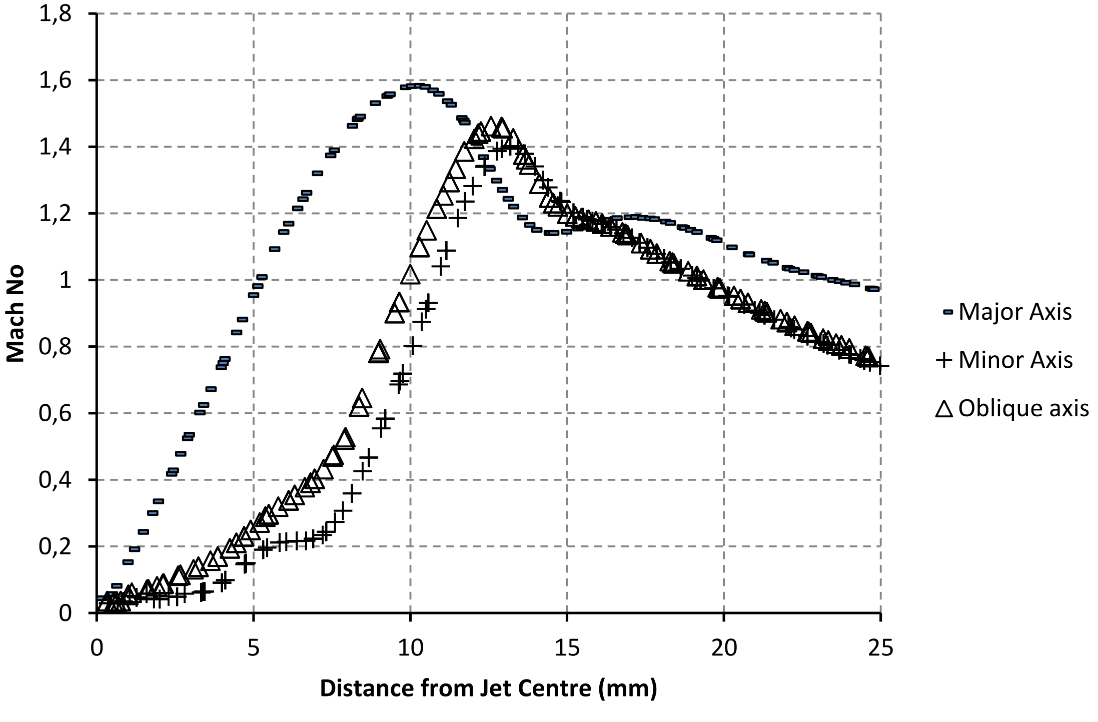

Figure 9-62: Plot of Mach number near the impingement zone for all three planes

Once again comparing the shear data generated from the oil film interferometry experiments to the data from the CFD, the familiar patterns are once again apparent. Whilst the experimental data shows good agreement with the CFD data on the outer portions of the plate, closer in to the recirculation zone the experimental data values are significantly lower than the CFD values. There is also a large difference between values calculated for different test runs, even though they were all carried out under the same conditions.

That being said, the shear plot along the minor axis shown in Figure 9-64 shows very good agreement between the experimental and CFD data. Although there are four data points towards the origin that show much lower shear values, these data points were in fact generated from an oil film that was not properly aligned with the minor axis (see Figure 9-66) and were thus considered erroneous and treated as outliers.

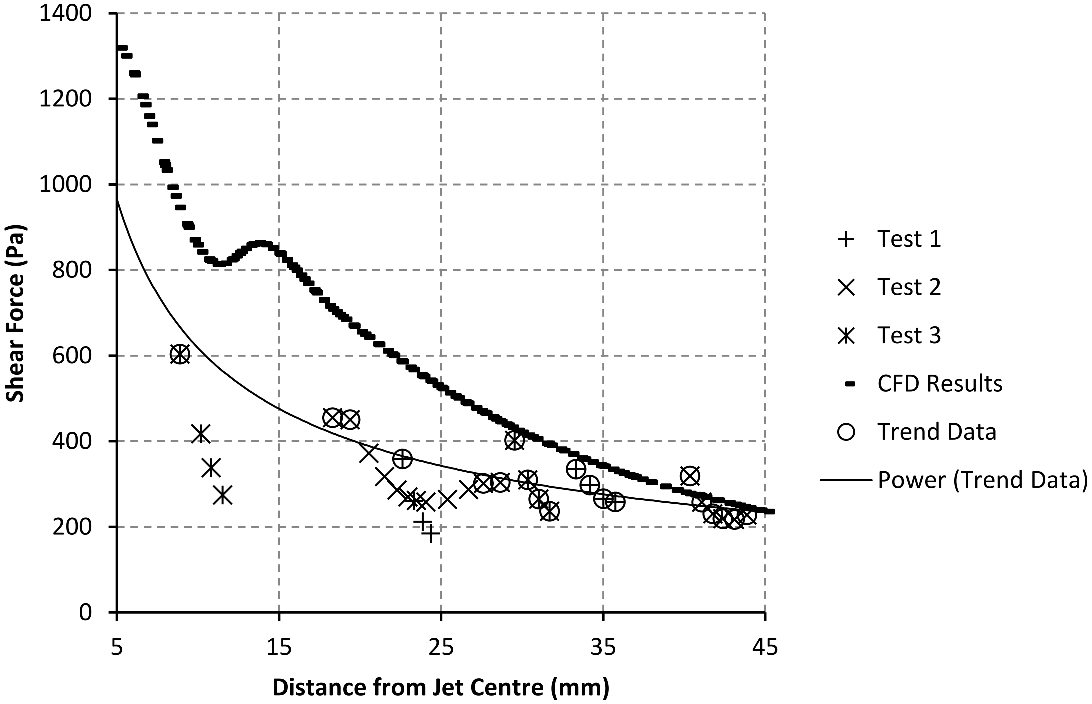

Figure 9-63: Experimental versus CFD shear along the main axis

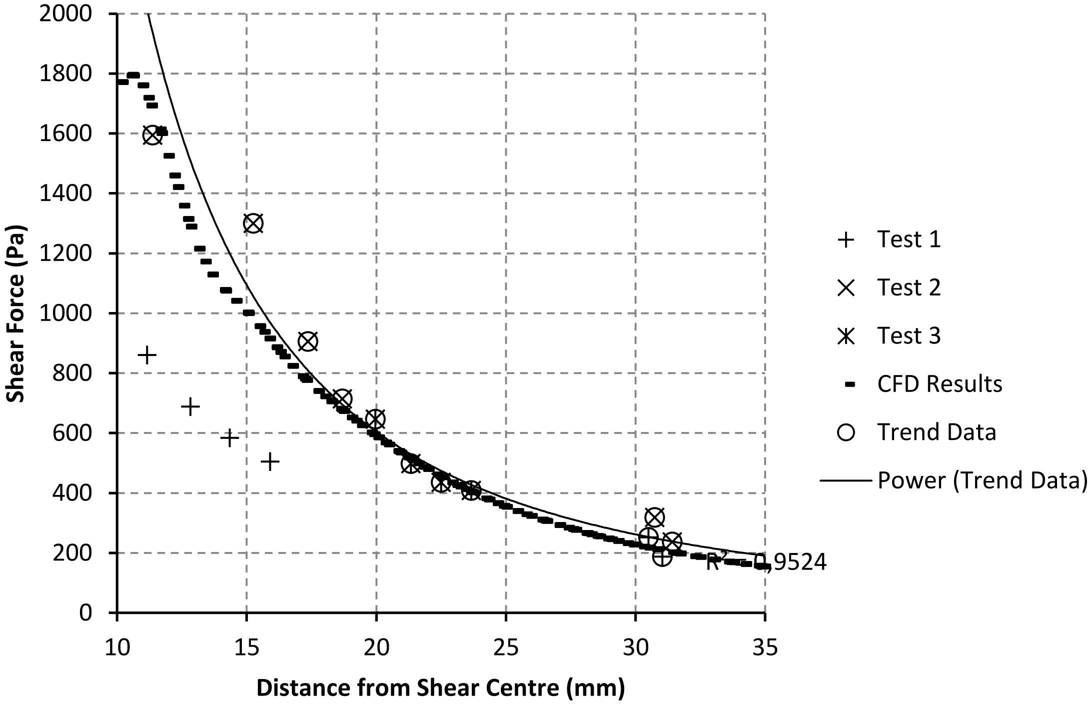

Figure 9-64: Experimental versus CFD shear along the minor axis

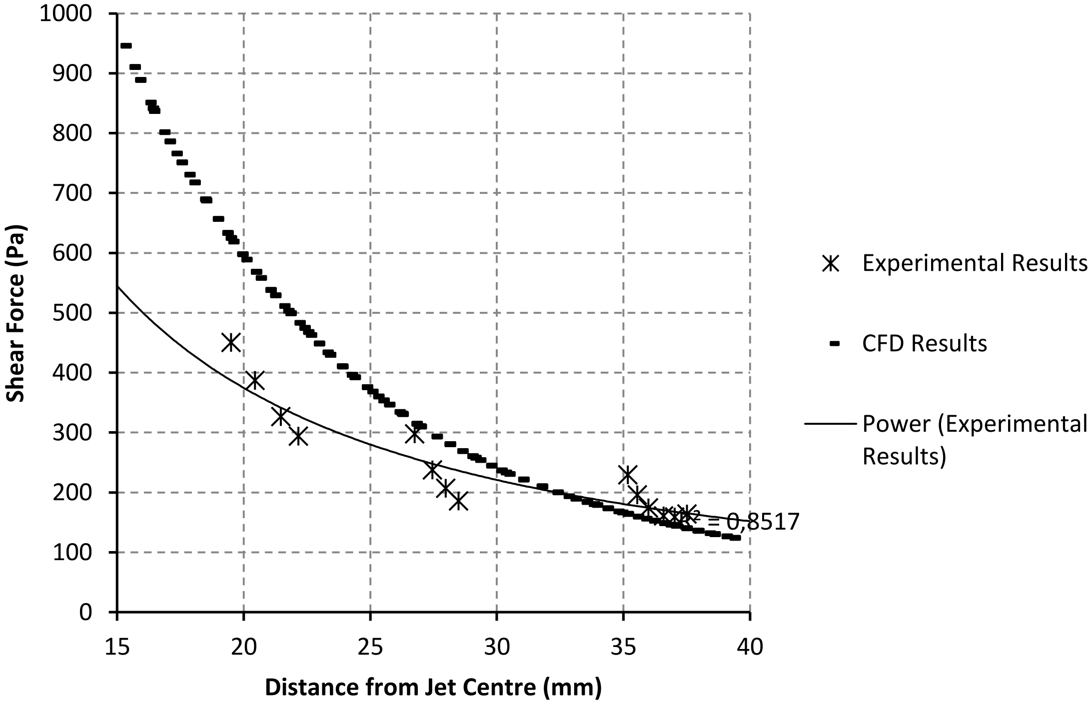

Figure 9-65: Experimental versus CFD shear on the oblique axis

Even though some of the fringe patterns generated show some questionable results, examination of the actual fringe images show some interesting qualitative results as well. Figure 9-66 highlights the unique nature of the airflow pattern over the plate. The oil film in the bottom left hand quadrant of the image was generated when the 10mm oil droplet was placed slightly out of alignment with the minor axis. Although this misalignment was not more than 1-2mm, the airflow such a small distance from the minor axis appears to push the oil towards the wall jet along the major axis.

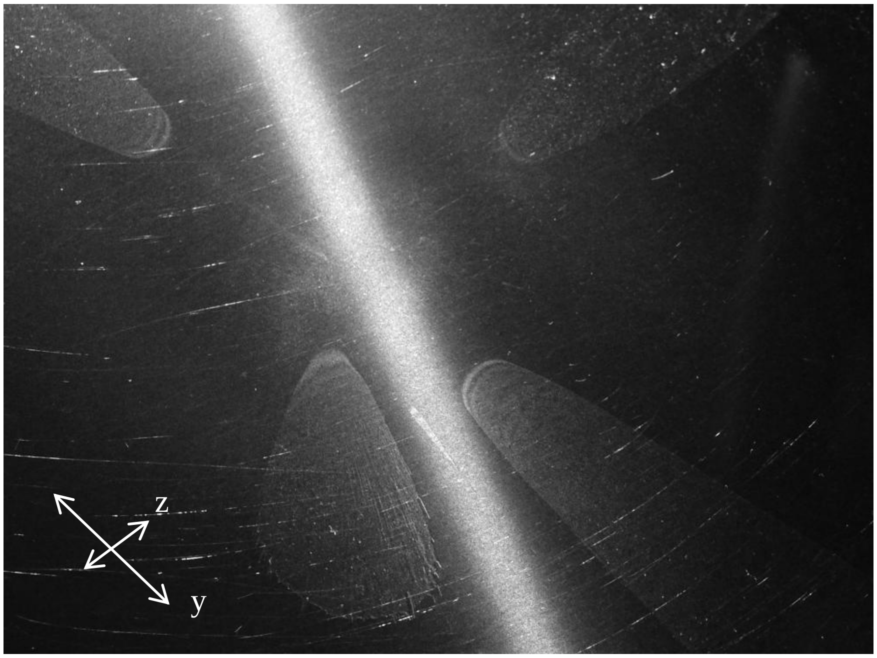

Figure 9-66: Droplet oil flow patterns for AR=4, NPR=2, v=550cSt, t=15s

Examining the fringe patterns generated in the second test under the same conditions, this time with the 10mm drop aligned correctly, further qualitative data is apparent. The oil coating in the bottom left hand quadrant of the image seems to have been generated from the oil drop being placed on the border of the recirculation zone. The fact that the leading edge of the drop is clearly visible means that the oil was not pulled into the recirculation zone, as occurred in the square NPR=2 case noted previously. The large light fringe pattern evident at the front of the oil film indicates that this oil experienced very high shear (this is in fact the fringe pattern responsible for the high shear values present in the minor axis shear graph above).

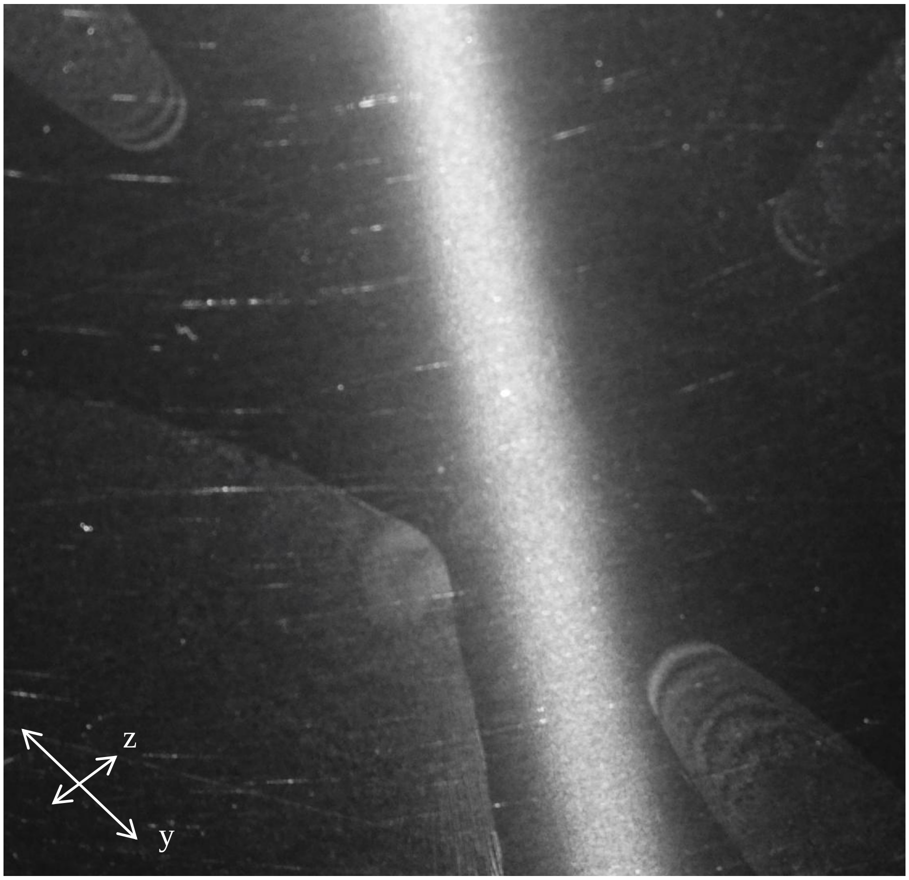

Figure 9-67: Droplet fringes, AR=4, NPR=2, v=550cSt, t=15s

Examining the Mach contour plots in the jet core, as shown in Figure 9-68, Figure 9-69 and Figure 9-70, the same unique flow characteristics are visible as were noted for the NPR=1 case, namely the occurrence of the oblique shocks within the nozzle throat. On top of this is the fact that the flow in the jet core seems to be dominated by the second shock cell, which extends from the nozzle exit plane down to the top of the plate recirculation bubble. Unlike the square NPR=2 case, the stand-off shock has not moved further up into the jet core and appears to be weaker than that for the NPR=1 case.

Once again the jet core along the oblique axis shows very similar flow patterns to the major axis, whilst there are no sharp velocity changes notable in the jet core along the minor axis. That being said, the stand-off shock is clearly visible above the plate in Figure 9-69. This indicates that the flow within the jet core has a complex three-dimensional nature that should be investigated further.

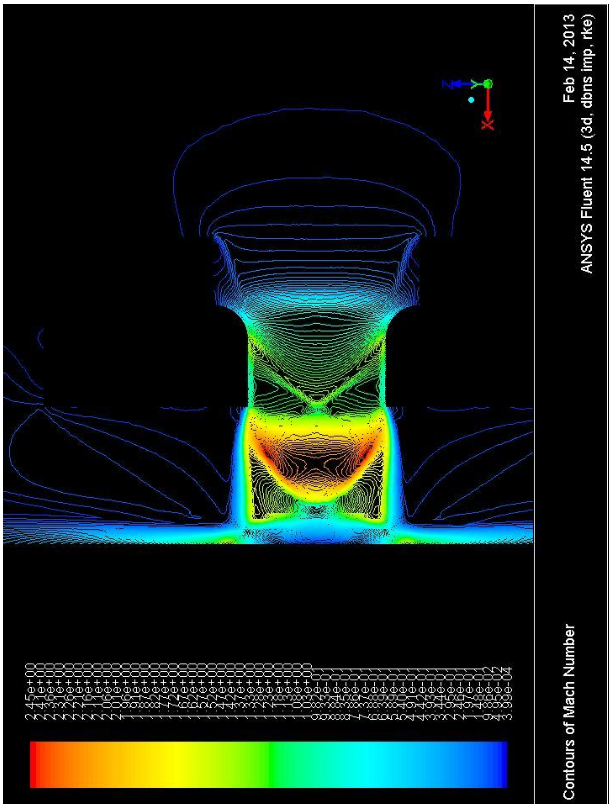

Figure 9-68: Mach contours in the jet core along the major axis

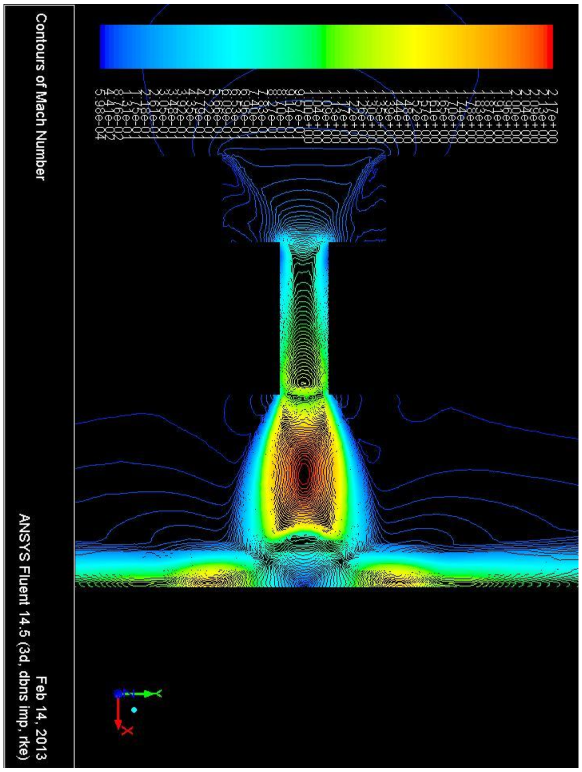

Figure 9-69: Jet contours in the jet core along the minor axis

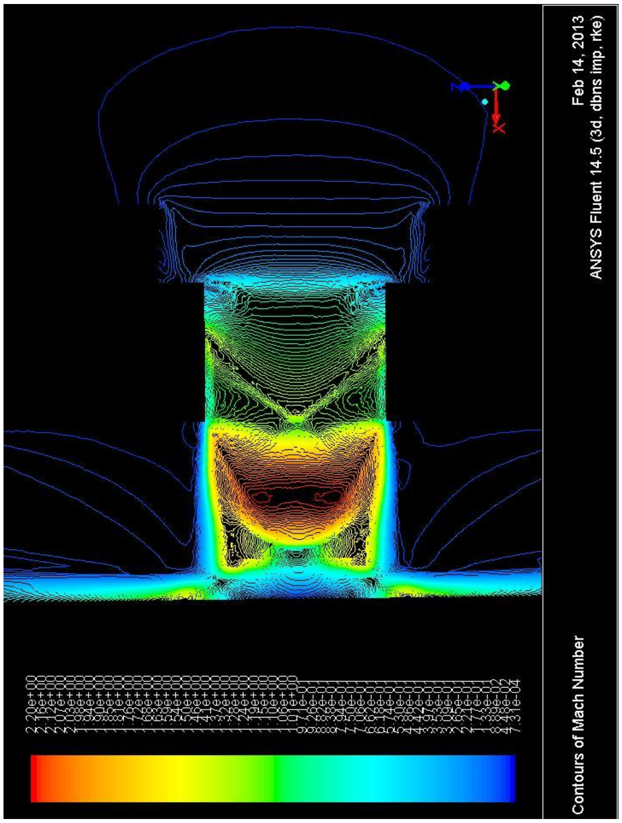

Figure 9-70: Mach contours in the jet core along the oblique axis

10 Discussion and Conclusions

Whilst the oil film interferometry technique is a relatively straightforward and simple process in theory, the trial and error process detailed in the observations section shows that it is in fact a rather complex process to get right. Finding the correct combination of oil viscosity, oil application technique, flow run time, surface coating, light source position and intensity, and camera position and set-up for this application was a much more laborious and time consuming process than was originally assumed.

It was discovered through the course of this investigation that, for this application, oils with a viscosity of between 500 and 650 cSt gave the best fringe definition. The optimal viscosity range for the impinging jets is significantly higher than that used in the majority of the experimentation detailed in the literature (typical oil viscosities are below 100cSt). This is no doubt due to the high mass flow rates experienced over the plate surface in this case.

A complex relationship exists between oil viscosity, jet under-expansion ratio and jet run time, and finding the right combination for each flow case was once again a process of trial and error. The higher the oil viscosity, the longer the jet needs to run before the oil has thinned out enough to generate discernible fringes. Also higher viscosity oils generated better results at higher under-expansion ratios. However, at higher under-expansion ratios the jet run time has to be reduced to ensure that the oil does not thin out to a point where the fringes are too widely spaced for accurate analysis.

Over the course of this investigation the following relationships were found to give the best overall fringe results:
At both under-expansion ratios tested, the best fringe images were generated using the 550cSt oil. At NPR=1, a jet run time of 30 seconds for the square nozzle, and 20 seconds for the AR=4 rectangular nozzle gave the best quality fringes. At NPR=2, the run time

was limited to 15 seconds for both nozzles, with longer run times causing severe degradation of the fringe patterns.

In terms of oil application technique, it was found that the central globule technique generated the best qualitative images, showing the general shear force distribution across the plate. However, as mentioned previously, the analysis technique utilised here did not allow for any shear force data to be calculated from these images, since the position of the leading edge of the oil is not known. Thus the discrete droplet technique was utilised to generate images for quantitative analysis.

Another advantage of droplet technique is the fact that it allowed for the visualisation of shear forces further out from the impingement zone. The fringe patterns visible in all of the central blob images were limited to the area in the immediate vicinity of the impingement zone.

As discussed in the apparatus section it was decided to utilise a light shroud and alter camera aperture and shutter speed in an effort to replicate the effects of a beam splitter. Whilst this was mostly successful, since ultimately fringe patterns were photographed, this required a great deal of fine tuning of the relative camera and light positioning as well as the camera settings and the amount of shrouding of the light. However, when examining the sample of fringe images shown in this report, the direction of the main beam from the light source is clearly evident on all the images. This bright line across the plate meant that the camera light sensitivity had to be limited to stop over-exposure, resulting in less-than-optimal fringe definition in the images. Also, since the data analysis process involved adjusting the contrast of the image, in the cases where the light beam occurred close to the fringe pattern being analysed, the first fringe often appeared over-exposed and the downstream fringes were under-exposed. This meant that the filtering of the intensity graph was skewed towards the bright fringes, with the boundaries of the less visible fringes being blurred and lost in the background noise.

Another important point to note when discussing the data analysis is the location of the leading edge of the oil coating. As discussed in the data analysis section, this point was located in the intensity plots by identifying the starting point of the zeroth fringe. However when looking at the fringe images, the dark fringes have approximately the same intensity as the surrounding plate and are only easily identified due to the light fringes directly in front and behind. Therefore disseminating the boundaries of the zeroth order fringe from the background radiation was often rather difficult. This fact is evident when examining the large difference in shear data between successive tests noted in the results. During the data analysis process it was noted that the position of the leading edge of the oil had a dominant effect on the resultant shear forces. Between two consecutive analysis runs on the same fringe pattern, the run with the largest difference between the leading edge and the first maximum fringe point generated significantly higher shear forces, not just in the first fringe but over the whole length of the fringe pattern.

In conclusion then, when examining the experimental data, it is clear that the large disparity observed is mostly due to the analysis techniques utilised and not the actual images. In the numerous investigations carried out by Naughton, in collaboration with other authors [7, 8, 10, 11], the analysis techniques utilised were able to generate very good shear data from fringe images that were often much more noisy and less well defined than the images shown here. Although the analysis technique utilised here was based on Naughton’s technique, there were certain steps that did not work correctly in this case and had to be altered, specifically the noise filtering technique used.

Moving now to the CFD data and the general trends they illustrate, there are a number of points of interest as highlighted in the results section.

Looking first at the square nozzle results, the behaviour of the jet core along the two planes of interest shows good agreement with the conclusions drawn by Menon and Skews [6]. Examining the Mach number contour plots for both NPR=1 and NPR=2 cases along the main and diagonal planes (Figure 9-26, Figure 9-27, Figure 9-43, and Figure 9-44) the jet core expands as it moves downstream of the nozzle exit along the main axis, whilst it remains more or less constant along the diagonal axis. This agrees with the conclusions put forward by Menon and Skews that the jet behaves as an under-expanded jet along the main axis and an over-expanded jet along the diagonal axis.

Comparing the two sets of images for the two under-expansion ratios, the extent of the expansion of the jet along the main axis is, as expected, far greater for the higher NPR case. However along the diagonal plane, the jet core in the NPR=2 case does not show the same level of over-expansion as that in the NPR=1 case, and shows a small amount of expansion about halfway down the jet core. This behaviour suggests that, at the higher under-expansion ratios, the small plate distance results in a very strong stand-off shock above the plate which dominates the flow; with the jet core becoming ‘squashed’ and not exhibiting the same level of over-expansion along the diagonal axis. This could also explain the size of the difference in under-expansion between the two main axes compared to the difference along the diagonal axes.

Examining the jet core for the AR4 rectangular nozzle for both flow cases (Figure 9-59, Figure 9-60, Figure 9-61, Figure 9-68, Figure 9-69 and Figure 9-70) several interesting flow patterns are evident.

The first, most surprising result is the occurrence of a shock diamond inside the actual jet nozzle. In both the NPR=1 and NPR=2 cases the nozzle is choked along the major axis by two oblique shocks that meet just before the flow exits the nozzle. This is in sharp contrast to the behaviour of the flow through both the axisymmetric nozzle and the square nozzle, where the flow is chocked by a normal shock. These oblique shocks within the throat of the nozzle indicate a certain level of under-expansion occurring in the flow before it even exits into atmosphere. This points to the presence of an extended subsonic boundary layer along the nozzle walls allowing for pressure signals to be transmitted upstream of the nozzle exit.

The next noteworthy observation when examining the Mach plots for the main axis is that the jet core exhibits over-expanded characteristics, narrowing as it moved downstream.

As was noted in the square nozzle case, the amount of narrowing is somewhat less for the higher under-expansion ratio.

The final curious and surprising flow behaviour shown in the Mach plots along the major axis for these two flow cases is the behaviour of the stand-off shock. For the NPR=1 case, the stand-off shock is slightly curved at the centre, but is relatively straight moving out towards the edge of the jet core. Even more surprising than the curious nature of the stand-off shock shape in the NPR=1 case is the fact that in the NPR=2 case the stand-off shock is not the dominant shock pattern in the jet core.

As noted in the NPR=2 case for the square nozzle, the stand-off shock is very strong and occurs well into the core of the jet flow. This is not the case of the AR4 nozzle. For the NPR=2 case, because the initial flow deceleration occurs within the jet core, the positioning of the shock diamonds is somewhat shifted. Instead of having two oblique expansion fans after the first oblique shock waves, the confines of the jet nozzle mean that the initial acceleration occurs through a strong normal expansion fan at the nozzle exit. This means that there is sufficient space between the nozzle exit and the impingement plate for the flow to undergo a second round of deceleration through the oblique shocks that extend almost through the entire jet core. Since the flow reaching the plate has already been decelerated significantly, the stand-off shock is not nearly as strong and, in fact, is non-existent at the centre of the plate. Because the stand-off shock is much weaker, the recirculation bubble is also much smaller.

Due to the high aspect ratio of the nozzle, there is very little difference between the jet core along the major and oblique axes, and both sets of plots for both flow conditions show more or less the same results.

Examining the Mach plots along the minor axis for the two flow conditions, as shown in Figure 9-55 and Figure 9-69, there are no clearly defined shock waves or expansion fans visible in the jet core. There are some variations in the flow velocity; however they are not nearly as sudden as those shown along the major axis. This indicates that the shock waves and expansion fans present in the jet core occur from nozzle corner to corner, along the oblique plane. However looking at the boundaries of the jet core, which extend as the flow moves downstream of the nozzle exit, the jet can be seen to exhibit under-expanded behaviour along this plane. The occurrence of the stand-off shock is also clearly evident for the NPR=2 case.

Turning finally to the flow patterns observed on the impingement surface, the CFD data once again shows a number of interesting trends. The non-axisymmetric nature of the jet nozzles is clearly evident in the recirculation zone, particularly for the rectangular nozzle.

Although the recirculation zone for the square nozzle operating at NPR=1 appears more or less circular, the areas of high shear aligned with the corners of the nozzle visible in Figure 9-3, as well as the faint cross pattern along the diagonal axes of the plane indicate the flow is not emanating from a circular nozzle. A quick glance at the Mach contours across the plate, as shown in Figure 9-6, shows that the jet nozzle is definitely not axisymmetric. The high velocity wall jets occur along the main axes of the nozzle.

However when the jet is operated at higher under-expansion ratios, the non-axisymmetric nature of the nozzle is very hard to determine from examination of the plate flow patterns by themselves. Only when zooming right in on the recirculation zone is any difference between the square nozzle and the axisymmetric nozzle apparent. The difference between the shear forces and Mach numbers along each plane is so small that only when the scale of the plots of this data is reduced significantly is any variation visible.

This is most definitely not the case for the rectangular nozzle. The recirculation zones for both rectangular nozzle flow cases are aligned with the axes of the jet nozzle and show approximately the same rectangular shape. Whilst the difference in shear forces along the major and minor planes is slightly less for the NPR=2 case, there is still a very large difference.

A further comparison of the recirculation zones for the square and rectangular nozzles highlights another interesting property of the rectangular nozzle flow cases. At centre of the square nozzle recirculation zones is a central stagnation point, as is the case for the axisymmetric nozzle. However in the rectangular nozzle cases the stagnation is not limited to a single point and in fact extends in a line along the minor axis.

Concluding this examination of the CFD data generated for the two nozzles investigated here, the simulated flow cases have served to illustrate some extremely interesting phenomena that are unique to these non-axisymmetric nozzles. The data generated in this investigation for the square nozzle has consistently supported the conclusions put forth by Menon and Skews [5]. To summarise these conclusions, the jet behaves as an under-expanded jet along the main axis, and an over-expanded jet along the diagonal axis. The impingement zone is also punctuated by the occurrence of two lines of recirculation along the diagonal plane. But by far the most interesting flow phenomena observed in this investigation was the behaviour of the flow within the jet core of the rectangular nozzle. The fact that the nozzle throat is not choked by a normal shock as in the circular and square nozzle cases, but by two oblique shock is a most surprising result and one that definitely requires further examination.

11 Recommendations

At the outset of this investigation there were two major choices made regarding the apparatus that were in direct contrast to the optimal apparatus set up suggested by the literature; namely the plate surface coating and the imaging apparatus.

Although it was stated by Naughton and Sheplak [11] to give the worst comparative fringe definition, it was decided to use polished aluminium as the interferometry surface. Whilst the reasoning for this choice at the time was sound, several drawbacks of this surface coating were noted during the course of this investigation, chief among them being the softness of the material and the susceptibility of the highly polished surface to damage and degradation. Even when using a micro-fibre cloth to clean the plate surface between runs, any small dust or grit particles moved across the surface would generate scratches. The adverse effects of these surface scratches can be seen in a number of the interferometry images presented here. Therefore it is recommended that for any further interferometry investigations carried out a more durable impingement surface is used.

The second problematic apparatus choice made in this investigation was the decision to forego the use of a beam splitter when capturing the fringe images. Although numerous steps were taken to minimise the effects of the direct reflection of the main light beam off the plate, it is highly possible that a number of these steps would not have to be taken if a beam splitter was utilised as part of the imaging apparatus. Thus finding a way to incorporate a beam splitter into the apparatus set up will be advantageous in any future interferometry experimentation.

While on the point of the imaging apparatus, a further recommendation can be made regarding the positioning of the camera and light source. As was discussed in the observations section, finding the optimal position of camera and light source was not an easy task. Even after this position had been found, a certain amount of fine-tuning was necessary for every experimental run. This was due to the fact that the camera was moved out of the way during each jet run, as well as being removed from the laboratory room at the end of each day. It is therefore recommended that some form of calibrated apparatus be designed to ensure the camera and light source can be located in the same position for every test.

Turning now to the data analysis procedure, the numerous issues with this process have already been discussed. A large amount of further work needs to be done on the MATLAB code to make the results more repeatable, and bring the values of the output data closer in line with the shear data predicted by CFD simulation. A large part of the non-repeatability stems from the identification of the leading edge of the oil coating. Finding a more reliable way to determine the exact position of the leading edge, or manipulating the shear force equation such that it does not rely on the position of this point being known will probably go a long way in increasing the accuracy and repeatability of the analysis technique.

Although it will not fix the repeatability issues, reducing the uncertainty in the shear data will also aid greatly in improving the accuracy of the results from the analysis process. As noted above, the two major contributors to this uncertainty are the potential error in the oil dynamic viscosity and the error in the oil height calculations. Reducing the oil viscosity uncertainty can be obtained by increasing the accuracy of the oil measurement technique, either using a burette for accurate volume measurement or a chemical balance for mass measurement. Obviously the simplest way of removing this uncertainty completely is to obtain the correct viscosity oils from the manufacturer. However, as mentioned, the South African distributors only supply these oils in industrial-scale quantities.

Reducing the uncertainty in the oil height is a slightly more complex process, since the level of this uncertainty is dependent on the equation of the best fit curves. It can be reduced significantly by finding a way to calculate the unique distance values from the best fit curves, but all this does is shift the uncertainty onto another variable. That being said, having the uncertainty in the x values rather than the h values may significantly reduce the shear uncertainty, since the x variable only occurs once in the shear equation. The effects of this shift need to be investigated and the overall curve-fitting process used should be reviewed.

Turning finally to the CFD simulations, a direct validation process needs to be carried out to cross-check the accuracy of the simulated results. Although the simulations give a very good indication of the expected flow fields, the large amount of turbulence present in the flow mean that the actual quantitative results may not be as accurate as hoped. Since turbulence is something that has always been extremely difficult to simulate, any further investigations should included detailed pressure and temperature mapping over the impingement plate surface in order to validate the data obtained from the CFD.

Although the reasons may in fact become clear during the validation process, two major flow phenomena were observed that warrant closer examination:

The first is the fact that, in the vicinity of the recirculation zones, the areas of high shear seem to coincide with the areas of low velocity. As was noted in the results, none of the other flow data sets show any significant variation at the points of maximum shear. The location of these points remains largely unexplained at this stage.

The second flow phenomenon that should be investigated further is the occurrence of the oblique shocks within the throat of the AR=4 rectangular nozzle. As discussed above these oblique shocks seem to indicate that the first shock cell has retreated into the jet nozzle. It is most likely that this is due to the width of the nozzle along this plane, however this is only supposition and further investigation is required to determine the cause of these shock patterns.

12 References

[1] C. D. Donaldson and R. S. Snedekker, "A Study of Free Jet Impingement. Part 1. Mean Properties of Free and Impinging Jets," *Journal of Fluid Mechanics,* vol. 45, pp. 281-319, 1971.

[2] J. C. Carling and B. L. Hunt, "The near wall jet of a normally impinging, uniform, axisymmetric, supersonic jet," *Journal of Fluid Mechanics,* vol. 66, pp. 159-176, 1974.

[3] G. T. Kalghatgi and B. L. Hunt, "The Occurrence of Stagnation Bubbles in Supersonic Jet Impingement Flows," *Aeronautical Quarterly,* pp. 169-185, August 1976 August 1976.

[4] P. J. Lamont and B. L. Hunt, "The Impingement of Underexpanded, Axisymmetric Jets on Perpendicular and Inclined Flat Plates," *Journal of Fluid Mechanics,* vol. 100, pp. 471-511, 1980.

[5] N. Menon and B. W. Skews, "Non-axisymmetric Supersonic Jet Impingement," in *25th International Symposium on Shock Waves,* Bangalor, India, 2005, pp. 319-324.

[6] N. Menon and B. W. Skews, "Rectangular Under Expanded Gas Jets: Effect of Pressure Ratio, Aspect Ratio and Mach Number," in *26th Iternational Symposium on Shock Waves,* Gottingen, Germany, 2007.

[7] C. Davy, F. S. Alvi, and J. W. Naughton, "Surface Flow Measurement of Micro-Supersonic Impinging Jets," in *1st Flow Control Conference 22nd AIAA Aerodynamic Measurement Technology and Ground Testing Conference* St. Louis, Missouri: AIAA, 2002.

[8] R. K. Decker and J. W. Naughton, "Improved Fringe IMagin Skin Friction Analysis Using Automated Fringe Identification," in *39th AIAA Aerospace Sciences Meeting and Exhibit* Reno, Nevada, USA: AIAA, 2001.

[9] B. W. Skews, "MECN 4004 - Gas Dynamics and Propulsion Course Notes," University of the Witwatersrand, Johannesburg, South Africa: School of Mechanical, Industrial and Aeronautical Engineering, 2008.

[10] J. L. Brown and J. W. Naughton, "The Thin Film Equation," Moffet Field, California: NASA Ames Research Centre, 1999.

[11] J. W. Naughton and M. Sheplak, "Modern Skin Friction Measurement Techniques: Decription, Use, and What to do With the Data," in *21st AIAA Aerodynamic Measurement Technology adn Ground Testing Conference* Denver, CO: AIAA, 2000.

[12] www.alanod.com.

[13] "A Note on Uncertainty Analysis," in *MECN 247 Mechanical Engineering Laboratory* Johannesburg: University of the Witwatersrand, 2006.

[14] E. Hecht, "Optics," 4th ed San Francisco: Addison Wesley, 2002.

[15] L. H. Tanner and L. G. Blows, "A study of the motion of oil films on sufraces, in air flows with application to the measurement of skin friction," *Journal of Physics E: Scientific Instruments,* vol. 9, pp. 194-202, March 1976 1976.

13 Appendix A

13.1 Derivation of the oil thickness equation

The following derivation was taken from chapter 9 of *Optics* [14]

Figure 13-1 below shows the behaviour of a single light beam as it moves through the oil film.

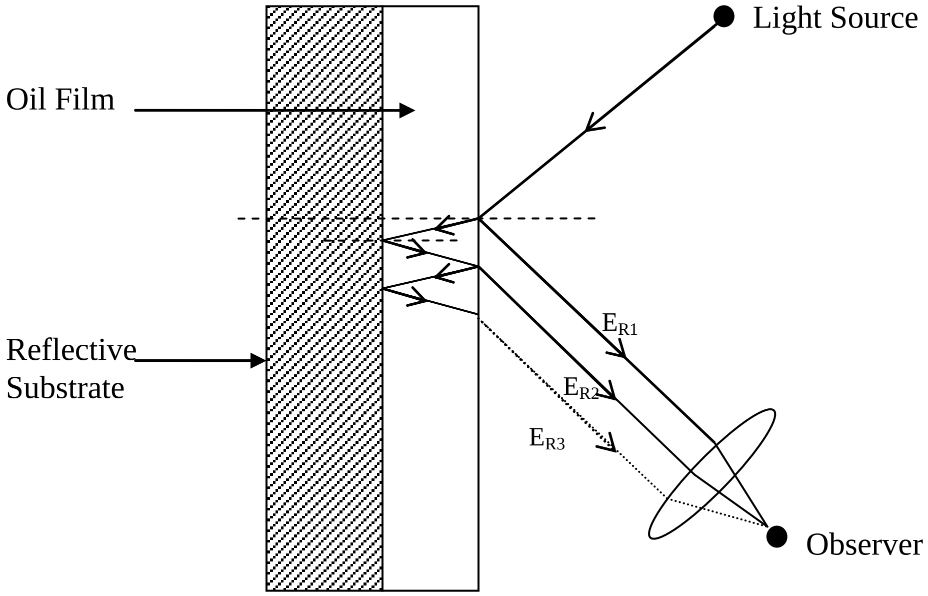

Figure 13-1: Schematic showing the path of light through the oil film

As the light hits the surface of the oil the beam is split. A portion of the light is reflected off the surface and travels to the observer along path E_{R1}. The other portion passes through the oil and is refracted through a certain angle due to the change in optical density. This portion of the beam is then reflected off the reflective substrate and moves back to the outer surface of the oil. Once it reaches this surface, once again a portion is reflected off the surface and a portion passes through the boundary into the air. It is once again refracted as it changes optical mediums and travels to the observer along path E_{R2}. This process of partial refraction and partial reflection continues with ever decreasing intensity since at each interface point the beam is split. According to Hecht [14] after the first set of reflections and refractions (path lines E_{R1} and E_{R2}) the intensity of the light drops off very rapidly. As such path line E_{R3} is represented here by a dashed line.

Figure 13-2 shows an exaggerated close up of the light path for the first set of reflections and refractions.

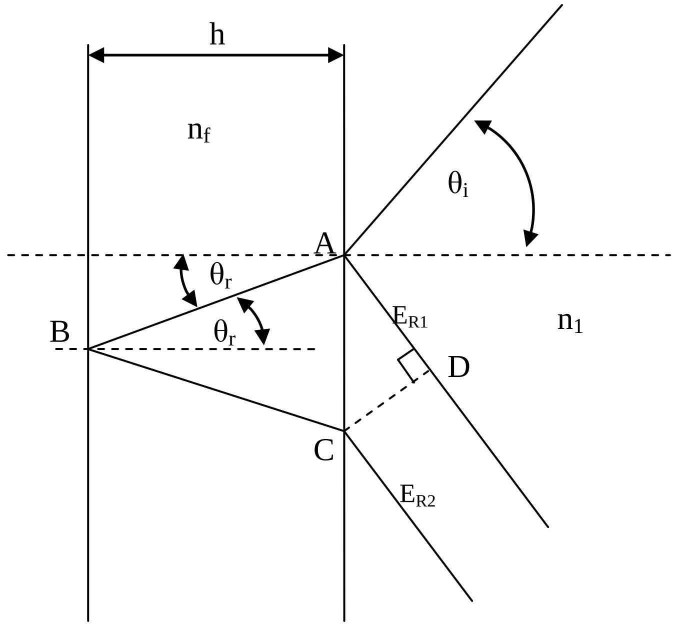

Figure 13-2: Close up of the path of a single light beam through the oil

In the above diagram:

θ_i – light angle of incidence
θ_r – light angle of refraction
h – oil thickness
n_1 – refractive index of air
n_f – refractive index of oil
A – point of initial reflection/refraction
B – point of secondary reflection
C – point of secondary refraction
D – point on E_{R1} parallel to C

As is evident from the diagram the light in path line E_{R2} has to travel a lot further to the light in path line E_{R1}. Let Λ represent this optical path length difference. From the diagram

$$\Lambda = n_f[(\overline{AB}) + (\overline{BC})] - n_1(\overline{AD})$$

Using basic trigonometry it can be shown that

$$\overline{AB} = \overline{BC} = \frac{h}{\cos\theta_r}$$

$$\Rightarrow \Lambda = \frac{2n_f h}{\cos\theta_r} - n_1(\overline{AD})$$

Once again from trigonometry:

$$\overline{AD} = \overline{AC}\sin\theta_i$$

$$\overline{AC} = 2h\tan\theta_r$$

$$\Rightarrow \overline{AD} = 2h\tan\theta_r\sin\theta_i$$

From Snell's Law:

$$\sin\theta_i = \frac{n_f}{n_1}\sin\theta_r$$

$$\Rightarrow \overline{AD} = 2h\tan\theta_r\frac{n_f}{n_1}\sin\theta_r$$

$$= \frac{2hn_f}{n_i}\sin\theta_r\left(\frac{\sin\theta_r}{\cos\theta_r}\right)$$

$$= \frac{2hn_f}{n_1\cos\theta_r}\sin^2\theta_r$$

$$\Rightarrow \Lambda = \frac{2hn_f}{\cos\theta_r} - \frac{2hn_f}{\cos\theta_r}\sin^2\theta_r$$

$$= \frac{2hn_f}{\cos\theta_r}(1 - \sin^2\theta_r)$$

$$\therefore \Lambda = 2hn_f\cos\theta_r$$

Equation 13-1

Defining the phase difference δ as

$$\delta = k_0\Lambda \pm \pi$$

$$k_0 = \frac{2\pi}{\lambda_0}$$

Where λ_0 is the incident light wavelength

Rearranging and substituting into Equation 13-1 gives

$$\delta = \frac{4\pi h n_f}{\lambda_0} \cos\theta_r \pm \pi$$

Equation 13-2

For a monochromatic light source total constructive interference will occur when both light waves are in phase.

$$\Rightarrow \delta = 2\pi m \text{ where } m \in \mathbb{Z} \geq 0$$

$$\Rightarrow 2\pi m = \frac{4\pi h n_f}{\lambda_0} \cos\theta_r \pm \pi$$

$$= \frac{4\pi h n_f}{\lambda_0} \cos\theta_r \pm \pi \frac{\lambda_0}{\lambda_0}$$

$$2m\pi + \pi = \frac{4\pi n_f h \cos\theta_r}{\lambda_0}$$

$$\frac{\lambda_0}{4\pi n_f}(2m\pi + \pi) = h \cos\theta_r$$

$$\Rightarrow h = (2m + 1)\frac{\lambda_0}{4n_f \cos\theta_r}$$

Similarly for total destructive interference the phase shift will be

$$\delta = \pi m$$

$$\Rightarrow h = 2m\frac{\lambda_0}{4n_f \cos\theta_r}$$

Taking a general solution the oil thickness can be described by:

$$h = k\frac{\lambda_0}{4n_f \cos\theta_r}$$

Equation 13-3

With light fringes where k is odd and dark fringes where k is even.

Equation 13-3 allows for the oil thickens at each fringe to be determined based on the incident light wavelength, the oil refractive index and the angle of refraction. However the angle of refraction is rather difficult to measure. This equation would be much more useful if it was in terms of the light's incident angle:

Taking the denominator of Equation 13-3:

$$n_f \cos\theta_r = \sqrt{n_f^2 \cos^2\theta_r}$$

$$\cos^2\theta = 1 - \sin^2\theta$$

$$\Rightarrow n_f \cos\theta_r = \left(n_f^2 - n_f^2 \sin^2\theta_r\right)^{1/2}$$

Once again applying Snell's Law:

$$n_1 \sin\theta_i = n_f \sin\theta_r$$

$$n_1^2 \sin^2\theta_i = n_f^2 \sin^2\theta_r$$

$$\Rightarrow n_f \cos\theta_r = \left(n_f^2 - n_1^2 \sin^2\theta_i\right)^{1/2}$$

Substituting back into Equation 13-3:

$$h = \frac{k\lambda_0}{4} \cdot \frac{1}{\left(n_f^2 - n_1^2 \sin^2\theta_i\right)^{1/2}}$$

Equation 13-4

13.2 Derivation of the shear force equation

The following derivation was taken from Brown and Naughton [10]

Consider a wedge of oil with air flow acting over it as shown in Figure 13-3 below. Taking a small control volume of the oil film with width Δz, length Δx and thickness h as shown. This control volume is subjected to a pressure force P and a shear force τ due to the airflow. The shear force τ causes a change in the thickness of the oil. Thus the value of h varies along the x direction.

The oil mass in the control volume is given by:

$$m_{cv} = \rho_0 h \Delta x \Delta z$$

Equation 13-5

Where:

ρ_0 – oil density

h – oil thickness

Δx – length along the x-axis

Δz – length along the z-axis

During time interval Δt the oil thickness h and thus the control volume mass m_{cv} changes by Δm_{cv}. Using the continuity equation:

$$\frac{\Delta m_{cv}}{\Delta t} + \Delta_{\mathrm{x}} F + \Delta_{\mathrm{z}} G = 0$$

Equation 13-6

Where:

$\Delta_x F$ – mass flux in the x-direction

$\Delta_z G$ – mass flux in the z-direction

F and G are defined by the following equations:

$$F = \iint \rho_0 u \, dA = \int_0^h \rho_0 u \, dy \Delta z = \rho_0 U_c h \Delta z$$

$$\text{and}$$

$$G = \iint \rho_0 w \, dA = \int_0^h \rho_0 w dy \, \Delta x = \rho_0 W_c h \Delta x$$

U_c – flow rate in the x direction

W_c – flow rate in the z direction

Substituting into Equation 13-6:

$$\frac{\rho_0 h \Delta x \Delta z}{\Delta t} + \rho_0 U_c h \Delta z + \rho_0 W_c h \Delta x = 0$$

Taking the limits as Δx, Δz and Δt tend to zero:

$$\frac{\partial h}{\partial t} + \frac{\partial}{\partial x}(U_c h) + \frac{\partial}{\partial z}(W_c h) = 0$$

Equation 13-7

$$where$$

$$U_c h = \int_0^h u dy \ and \ W_c h = \int_0^h w dy$$

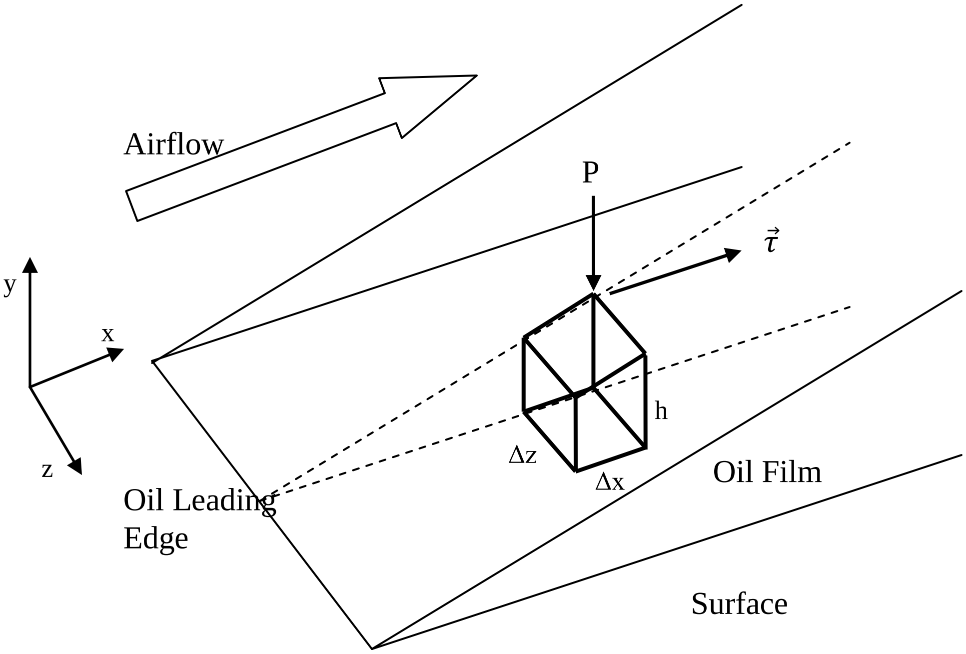

Figure 13-3: Oil film on a test surface

To be able to utilise Equation 13-7, u and w need to be evaluated. However these flow rates cannot be measured directly. Therefore expressions for u and w in terms of values that are available need to be determined. This can be done by considering the momentum equations in the x-direction:

$$\frac{\partial \tau_{x,o}}{\partial y} - \frac{\partial P_o}{\partial x} + \rho_o g_x = 0$$

Equation 13-8

It should be noted that the inertial terms have been ignored in this equation. An evaluation of the Reynolds number within the fluid shows that viscous effects dominate over inertial effects, allowing for this omission:

Taking the fluid Reynolds number as a ratio of inertial to viscous effects:

$$Re_f = \frac{\frac{\rho_0 U_c^2}{L}}{\frac{\mu_0 U_c}{h^2}} = \left(\frac{\rho_0 U_c h^2}{\mu_0 L}\right)$$

Using the expression for U_c as derived by Tanner and Blows [15]:

$$U_c = \frac{\tau h}{2\mu_0}$$

$$\Rightarrow Re_f \approx \frac{\tau h^3 \rho_0}{2\mu_0^2 L} = \frac{\tau h^3}{2\rho_0 \nu_0^2 L}$$

Equation 13-9

Taking a sample calculation with the following values:

$h = 10^{-6}$m

$L = 10^{-2}$m

$\tau = 20$N/m^2

$\rho_0 = 1000$kg/m^3

$\nu_0 = 100$ cSt $= 1\text{x}10^{-4}$m^2/s

This gives a fluid Reynolds number of $1\text{x}10^{-10}$. The extremely low Reynolds number shows that in the fluid viscous effects dominate over inertial effects.

Moving back to Equation 13-8:

$$\frac{\partial \tau_{x,o}}{\partial y} = \frac{\partial P_o}{\partial x} - \rho_o g_x$$

Equation 13-10

Taking the integral of Equation 13-10 from the oil-air boundary into the oil:

$$\int_h^y \frac{\partial \tau_{x,o}}{\partial y} dy = \int_h^y \left(\frac{\partial P_o}{\partial x} - \rho_o g_x \right) dy$$

$$\tau_{x,o} - \tau_{x,a} = \left(\frac{\partial P_o}{\partial x} - \rho_o g_x \right)(y - h)$$

Equation 13-11

In the above equation the subscripts *a* and *o* are introduced to differentiate between the shear stress within the oil and the aerodynamic shear stress on the oil surface due to the airflow. The pressure through the oil thickness has also been assumed to be constant.

Now integrating Equation 13-11 from the surface outwards:

$$\int_0^y \tau_{x,o} dy = \int_0^y \left[\tau_{x,a} + \left(\frac{\partial P_o}{\partial x} - \rho_o g_x\right)(y - h)\right] dy$$

$$taking\ \tau_{x,o} = \mu_0 \frac{\partial u}{\partial y}$$

$$\Rightarrow \int_0^y \tau_{x,o} dy = \int_0^y \mu_0 \frac{\partial u}{\partial y} dy$$

Integrating both sides:

$$\mu_0 u = \tau_{x,a} y + \left(\frac{\partial P_0}{\partial x} - \rho_0 g_x\right)\left(\frac{y^2}{2} - hy\right)$$

$$\Rightarrow u = \frac{\tau_{x,a} y}{\mu_0} + \frac{\left(\frac{\partial P_0}{\partial x} - \rho_0 g_x\right)\left(\frac{y^2}{2} - hy\right)}{\mu_0}$$

Equation 13-12

Performing the same process with the momentum equation in the z-direction:

$$w = \frac{\tau_{z,a} y}{\mu_0} + \frac{\left(\frac{\partial P_0}{\partial z} - \rho_0 g_z\right)\left(\frac{y^2}{2} - hy\right)}{\mu_0}$$

Equation 13-13

Using the definition in Equation 13-7:

$$U_c h = \int_0^h u dy = \int_0^h \left[\frac{\tau_{x,a} y}{\mu_0} + \frac{\left(\frac{\partial P_0}{\partial x} - \rho_0 g_x\right)\left(\frac{y^2}{2} - hy\right)}{\mu_0}\right] dy$$

$$\Rightarrow U_c h = \frac{\tau_{x,a} h^2}{2\mu_0} + \frac{\left(\frac{\partial P_0}{\partial x} - \rho_0 g_x\right)\left(\frac{h^3}{2.3} - \frac{h^2}{2}\right)}{\mu_0}$$

$$U_c h = \frac{\tau_{x,a} h^2}{2\mu_0} + \frac{h^3 \left(\frac{\partial P_0}{\partial x} - \rho_0 g_x\right)\left(\frac{y^2}{2} - hy\right)}{\mu_0}$$

Equation 13-14

Similarly

$$W_c h = \frac{\tau_{z,a} h^2}{2\mu_0} - \frac{h^3 \left(\frac{\partial P_0}{\partial z} - \rho_0 g_x\right)}{3\mu_0}$$

Equation 13-15

Due to the extremely thin nature of the film flows being discussed here, it can be assumed that the effects of pressure and gravity on the oil are negligible. Therefore Equation 13-14 and Equation 13-15 can be reduced somewhat:

$$U_c \approx \frac{\tau_x h}{2\mu_0}$$

$$W_c \approx \frac{\tau_z h}{2\mu_0}$$

Substituting this into Equation 13-7 gives the general differential equation for thin film flows:

$$\frac{\partial h}{\partial t} + \frac{\partial}{\partial x}\left(\frac{\tau_x h^2}{2\mu_0}\right) + \frac{\partial}{\partial z}\left(\frac{\tau_z h^2}{2\mu_0}\right) = 0$$

Equation 13-16

14 Appendix B

Manufacturing Drawings

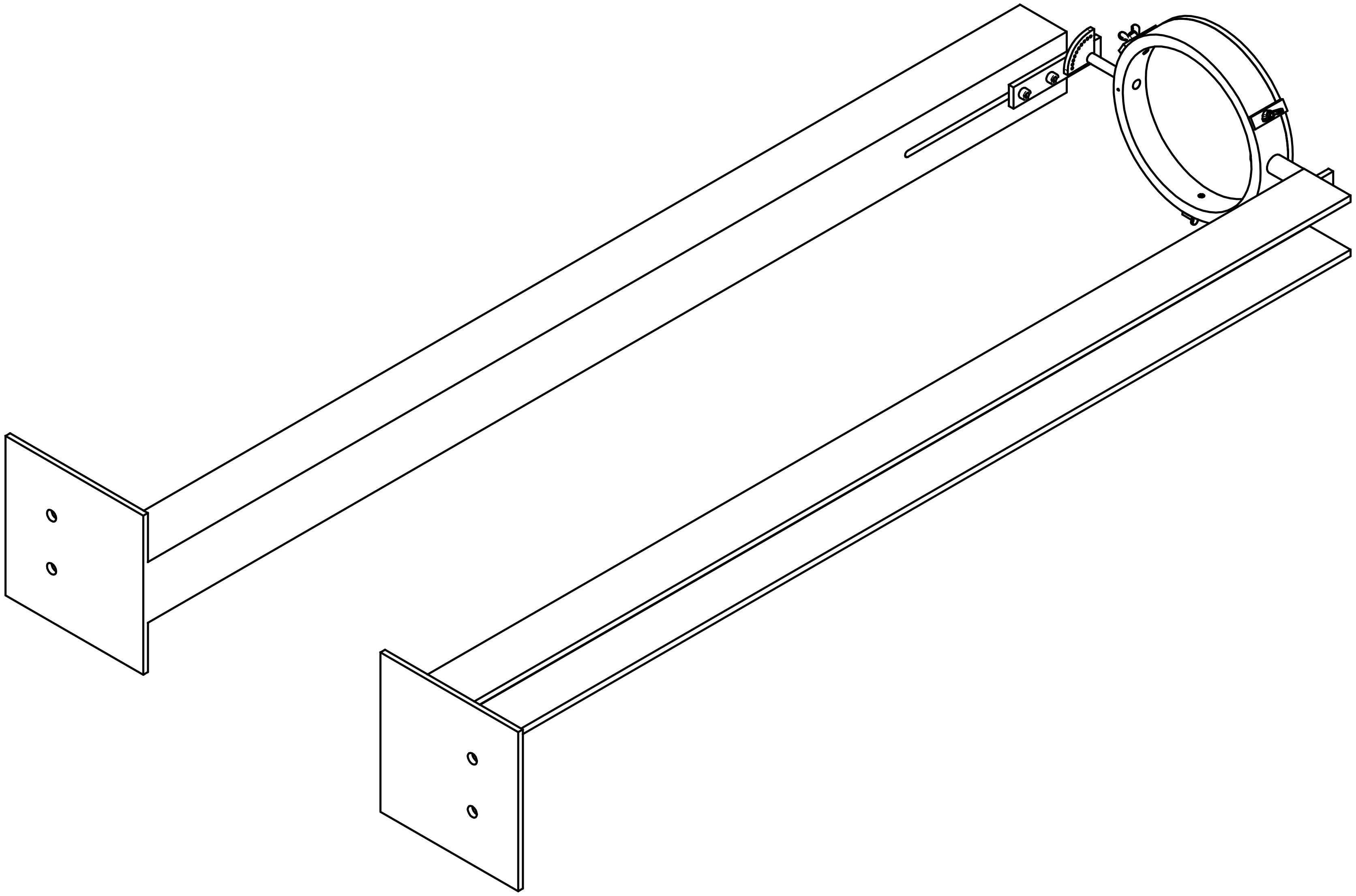

Jet Impingement Apparatus	
DRAWING	Isometric View
PROJECT NO	
AUTHOR	Louis Biebuyck
SUPERVISOR	Prof. B.W. Skews

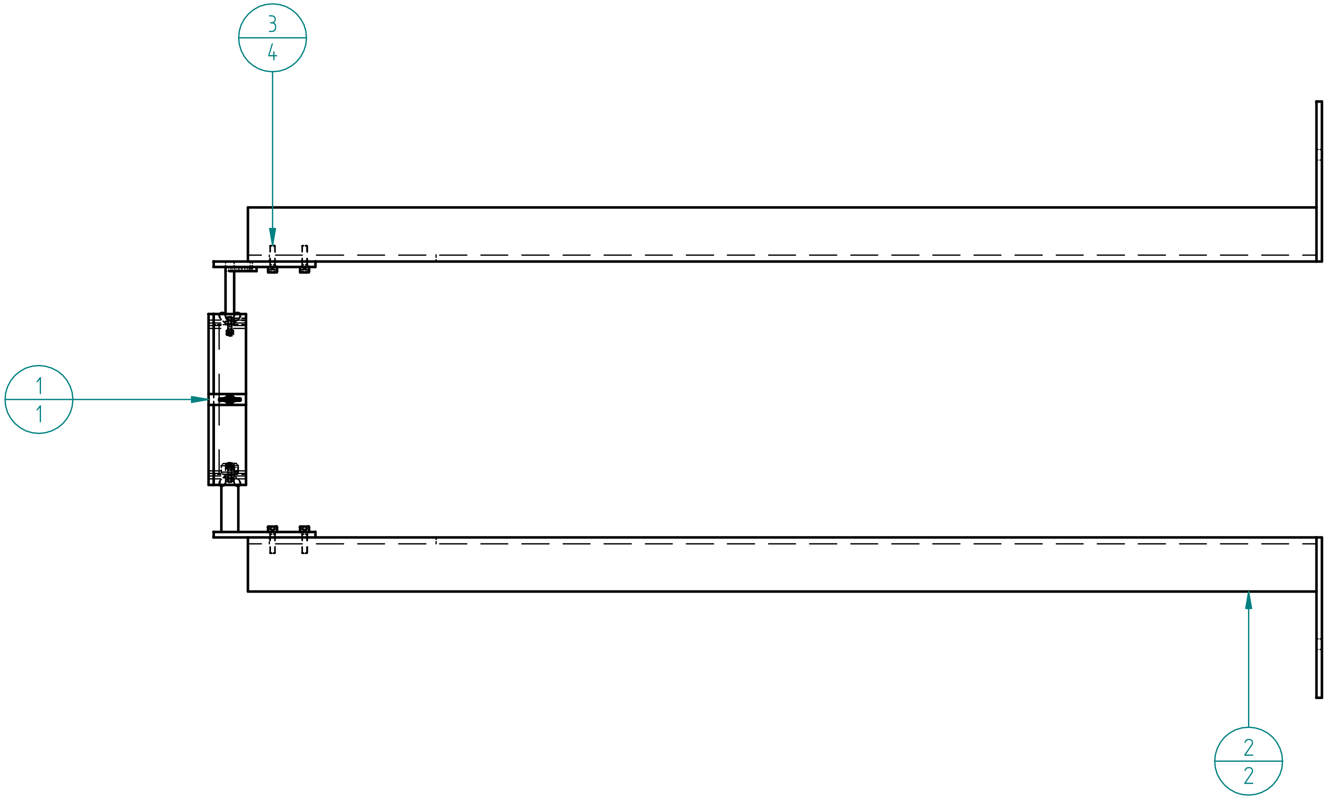

Item Number	Title	Material	Quantity
1	Impingement Plate		1
2	Stand Beam	Steel	2
3	M5 Cap Skrew	Steel	4

Jet Impingement Apparatus	
DRAWING	Parts List
PROJECT NO	
AUTHOR	Louis Biebuyck
SUPERVISOR	Prof. B.W. Skews

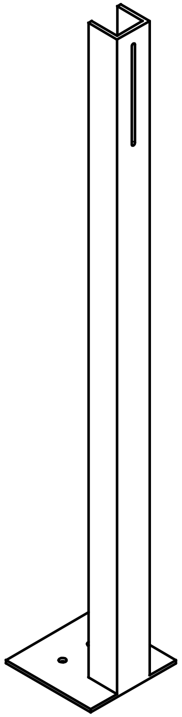

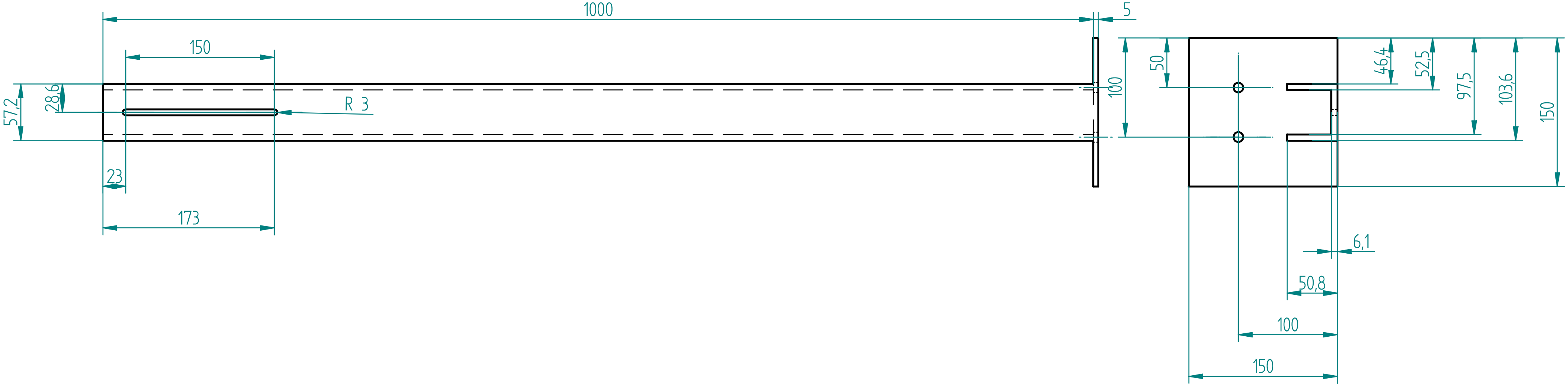

Jet Impingement Apparatus	
DRAWING	Stand Beam
PROJECT NO	
AUTHOR	Louis Biebuyck
SUPERVISOR	Prof. B.W. Skews

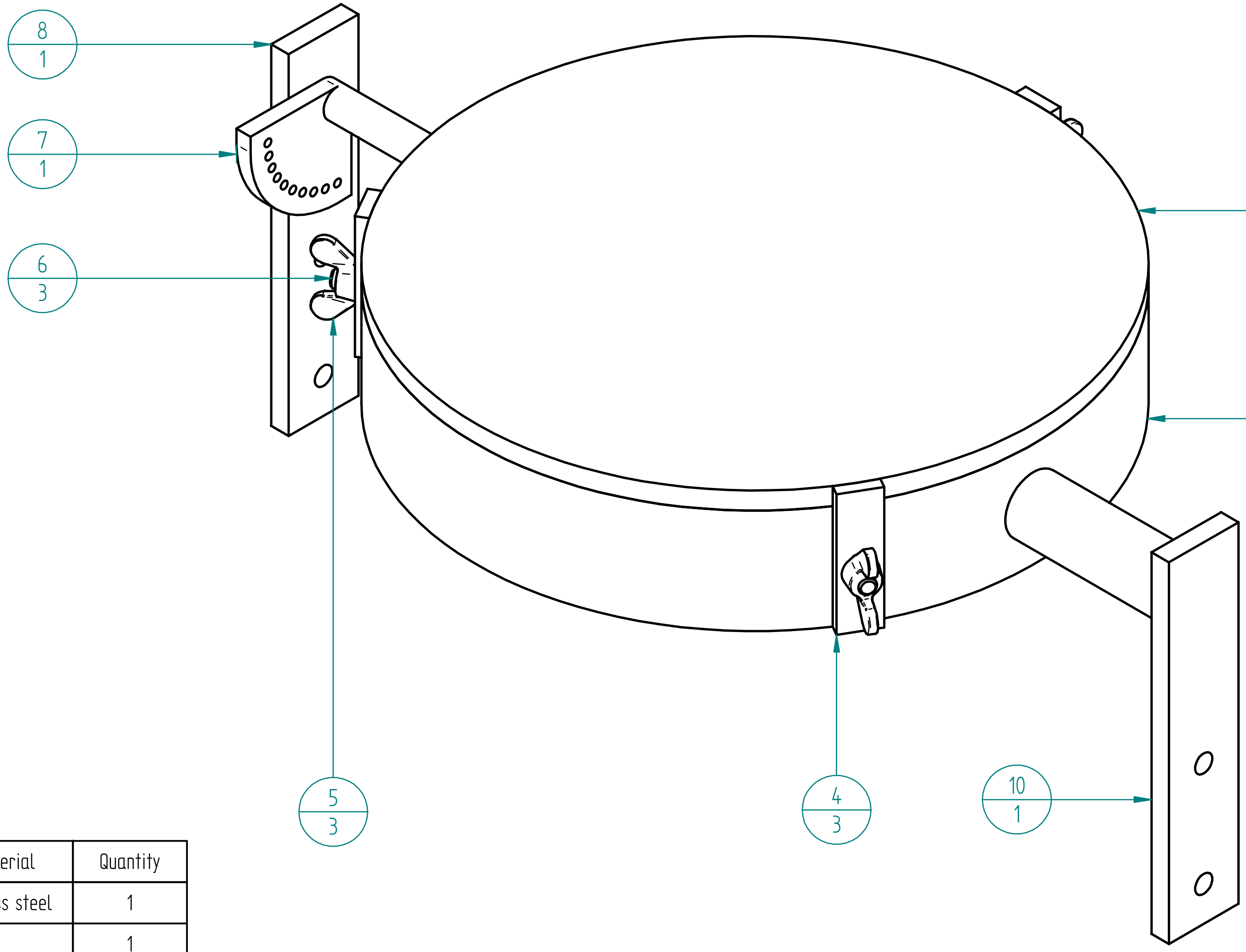

Item Number	Title	Material	Quantity
1	Impingement Plate	Stainless steel	1
2	Mount Collar	PVC	1
4	Plate Clamps	Steel	3
5	M4 Wing Nut	Steel	3
6	M4 Cap Screw	Steel	3
7	Hinge pin with locating holes	Steel	1
8	Sliding Mount	Steel	1
9	Lockiing Collar	Steel	1
10	Sliding Mount 2	Steel	1

Jet Impingement Apparatus	
DRAWING	Impingement Plate Parts List
PROJECT NO	
AUTHOR	Louis Biebuyck
SUPERVISOR	Prof. B.W. Skews

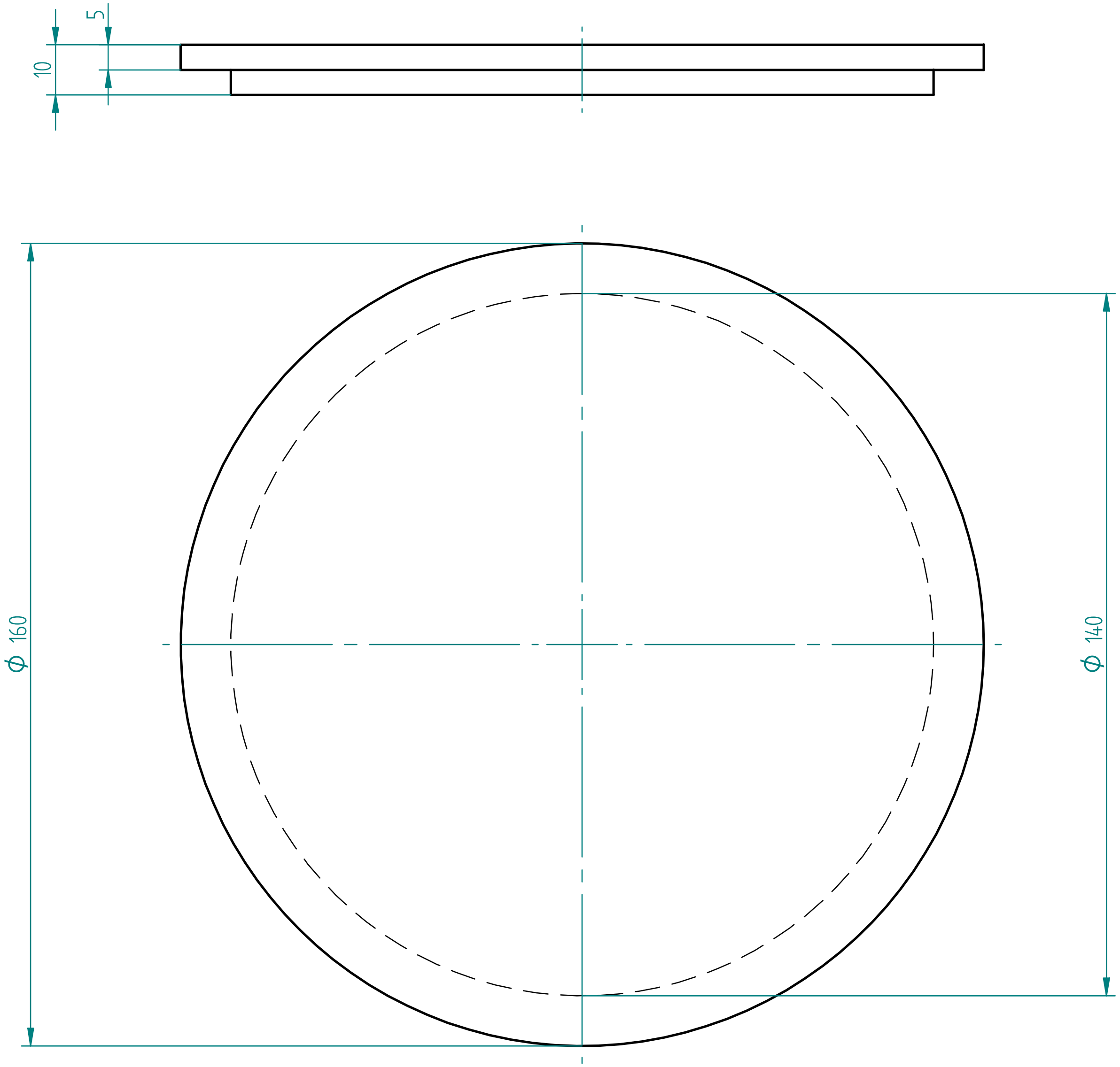

Jet Impingement Apparatus	
DRAWING	Impingement Plate
PROJECT NO	
AUTHOR	Louis Biebuyck
SUPERVISOR	Prof. B.W. Skews

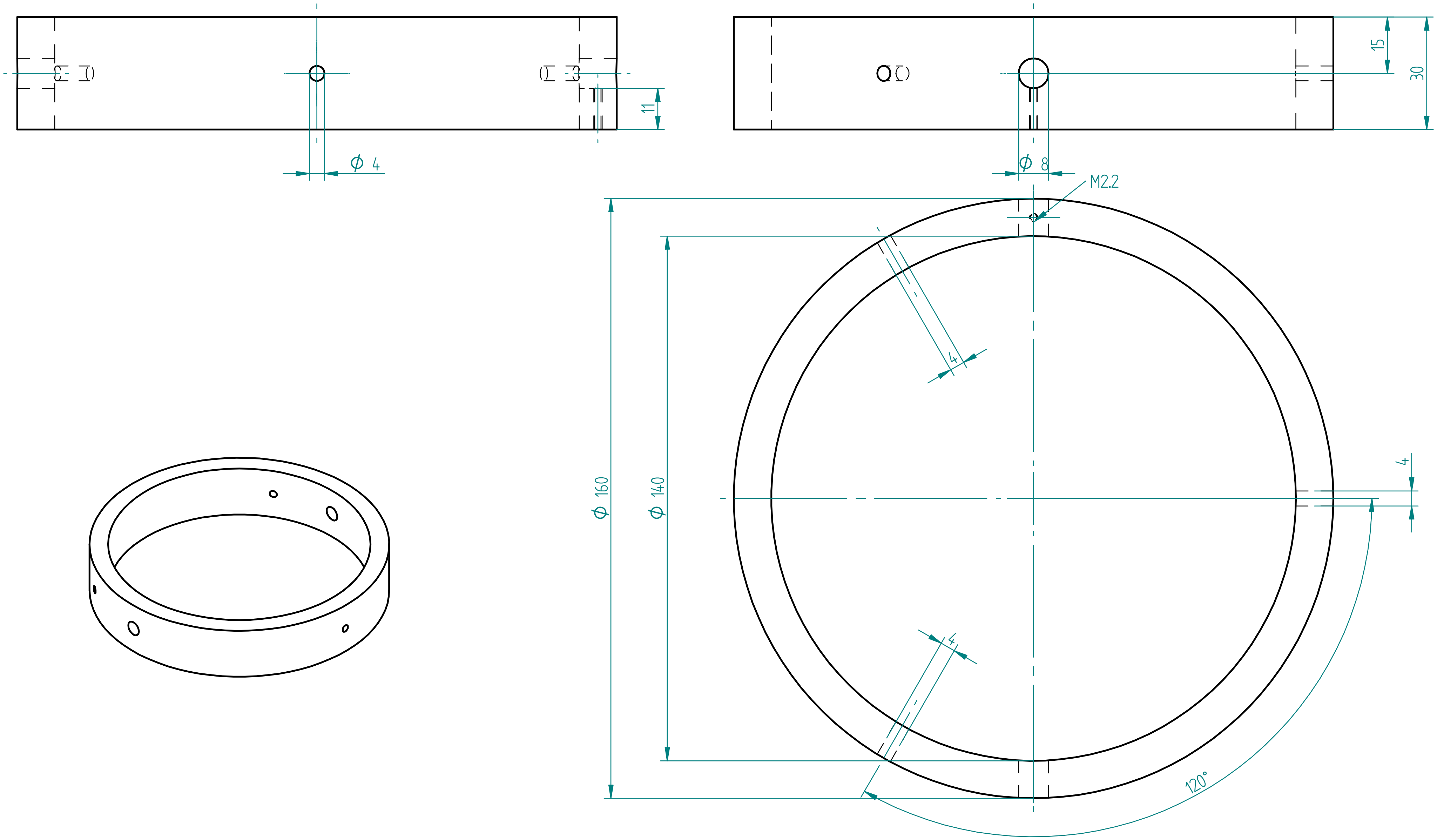

Jet Impingement Apparatus	
DRAWING	Mount Collar
PROJECT NO	
AUTHOR	Louis Biebuyck
SUPERVISOR	Prof. B.W. Skews

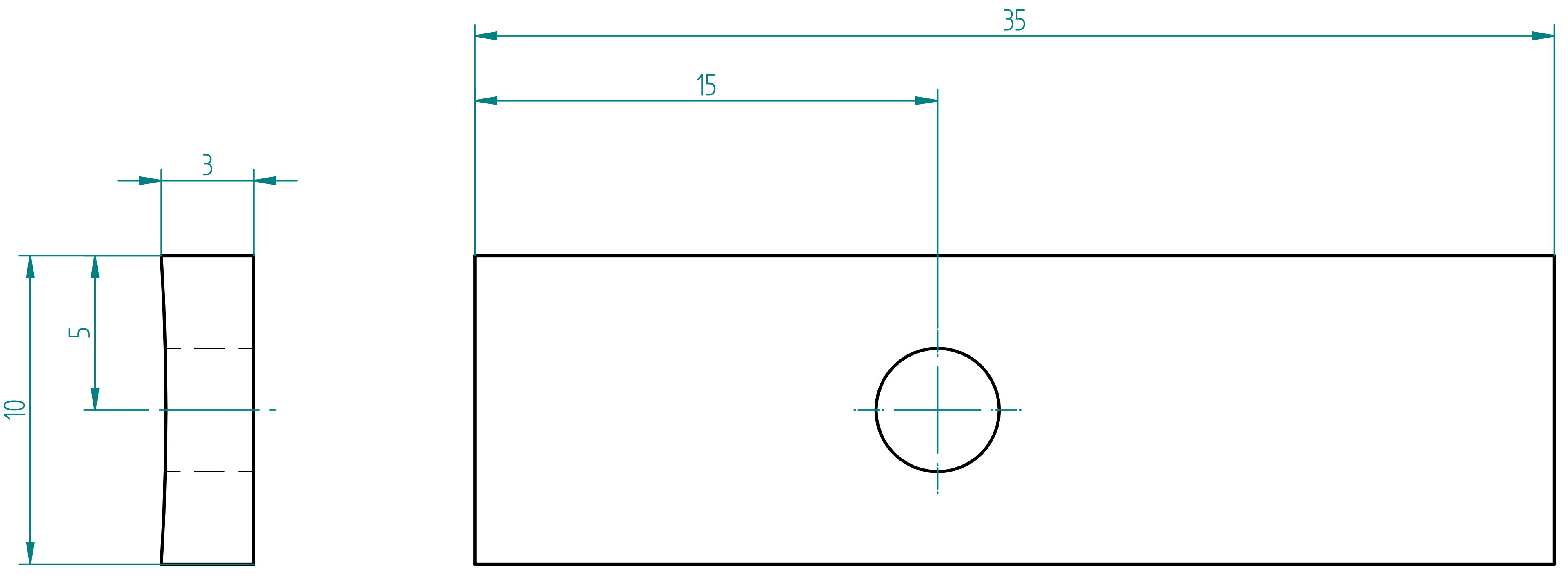

Jet Impingement Apparatus	
DRAWING	Plate Clamp
PROJECT NO	
AUTHOR	Louis Biebuyck
SUPERVISOR	Prof. B.W. Skews

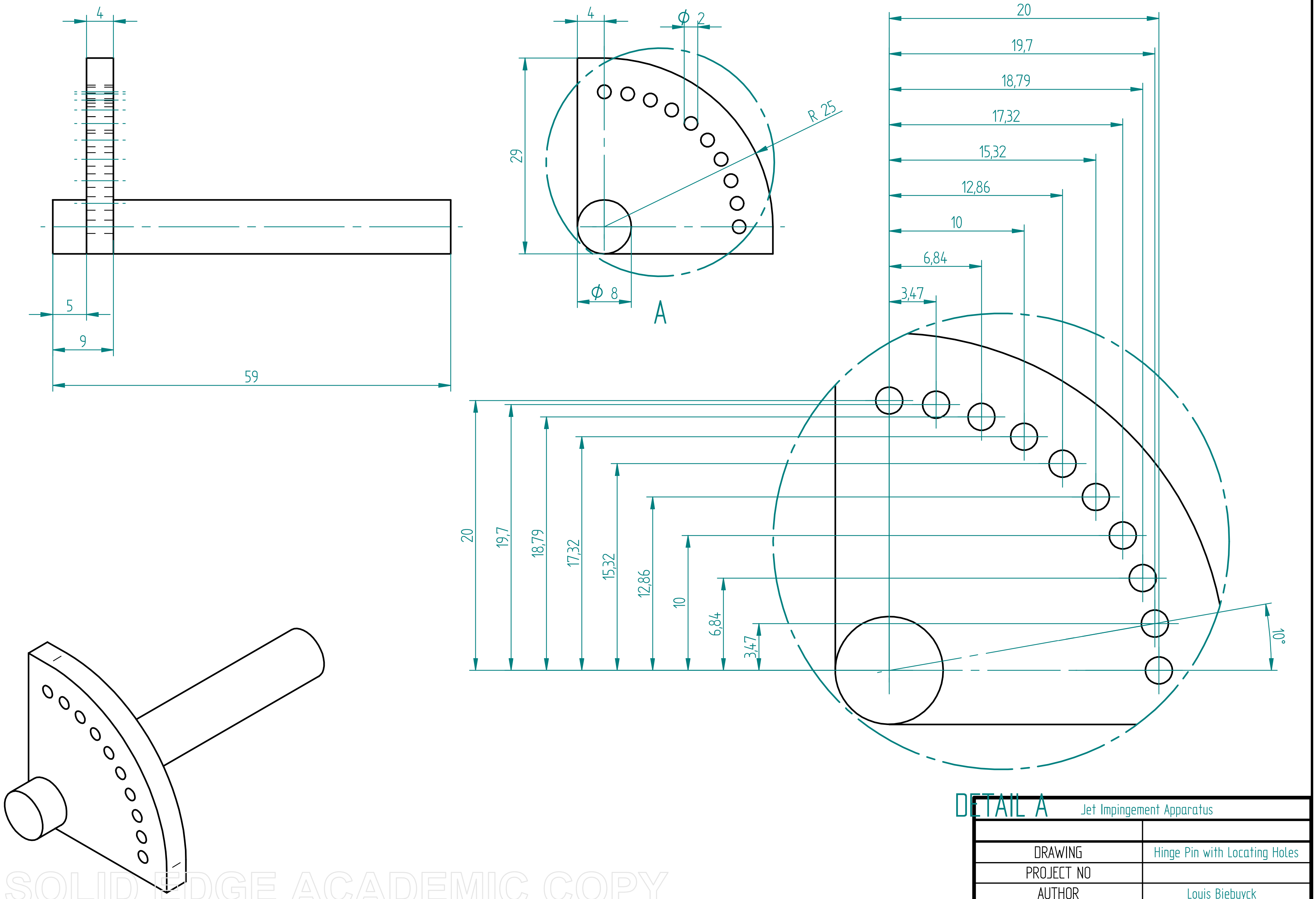

Jet Impingement Apparatus	
DRAWING	Hinge Pin with Locating Holes
PROJECT NO	
AUTHOR	Louis Biebuyck
SUPERVISOR	Prof. B.W. Skews

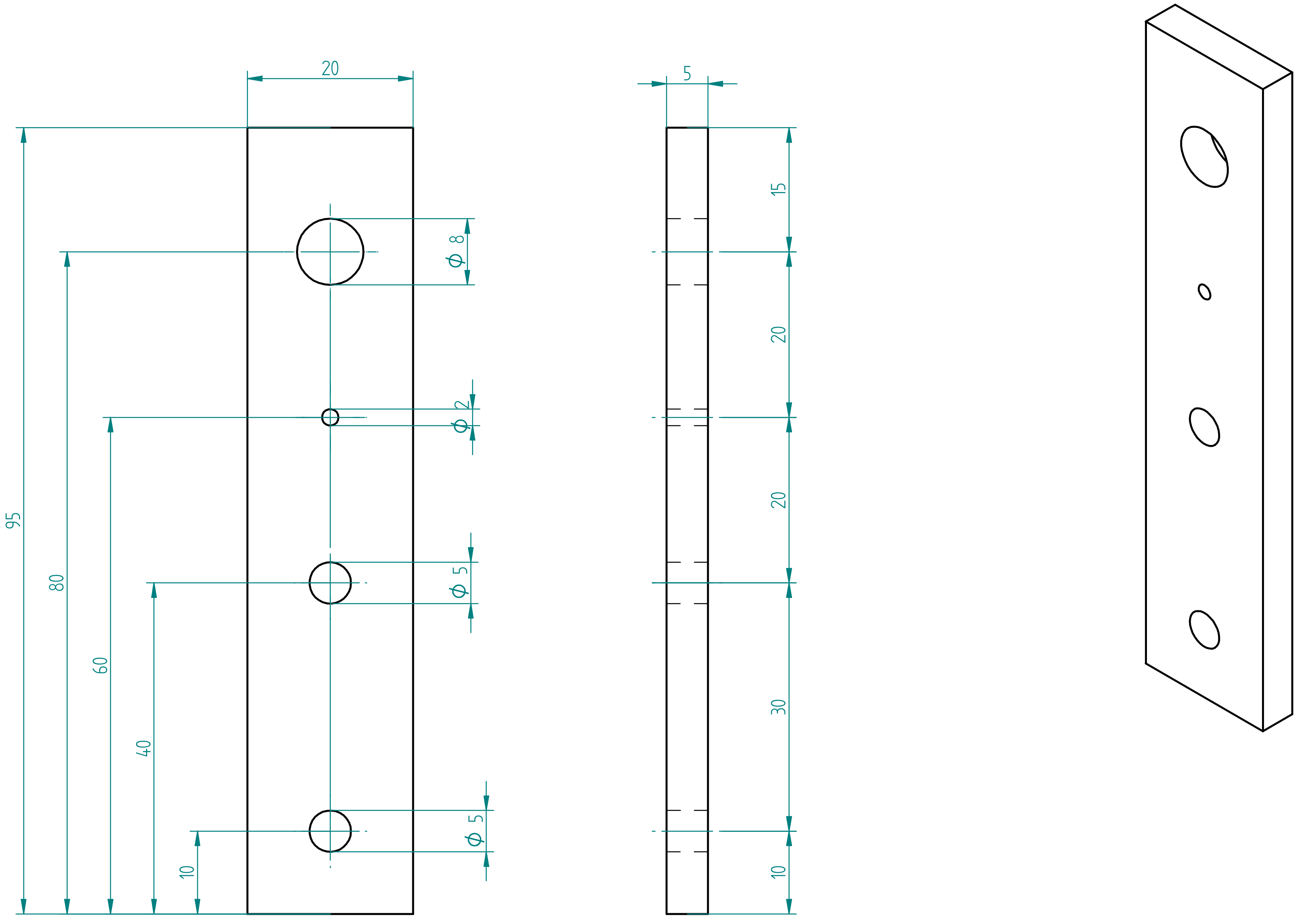

Jet Impingement Apparatus	
DRAWING	Sliding Mount
PROJECT NO	
AUTHOR	Louis Biebuyck
SUPERVISOR	Prof. B.W. Skews

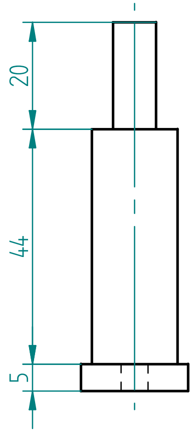

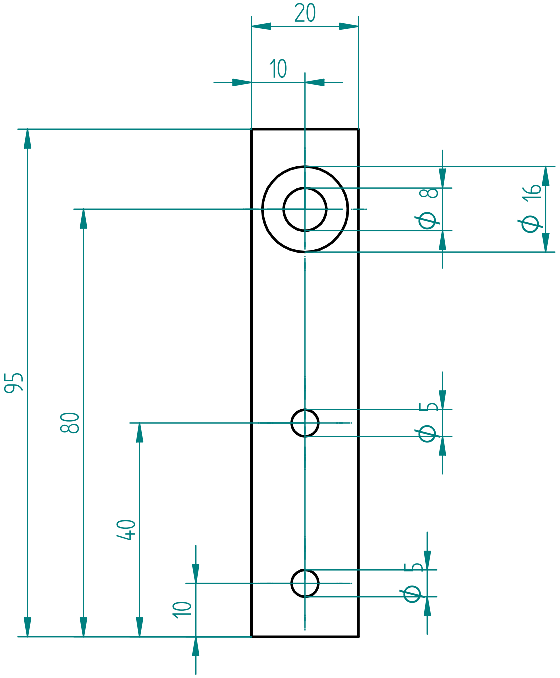

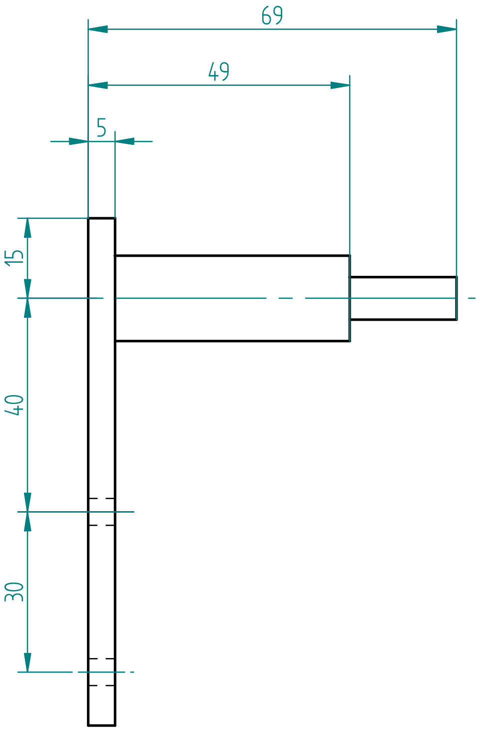

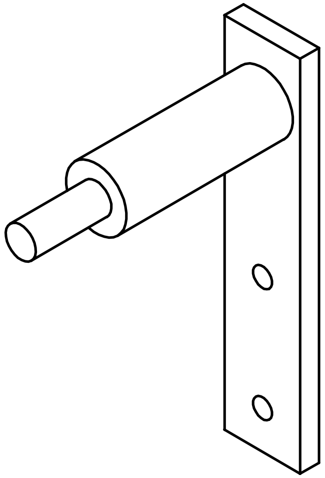

Jet Impingement Apparatus	
DRAWING	Sliding Mount 2
PROJECT NO	
AUTHOR	Louis Biebuyck
SUPERVISOR	Prof. B.W. Skews

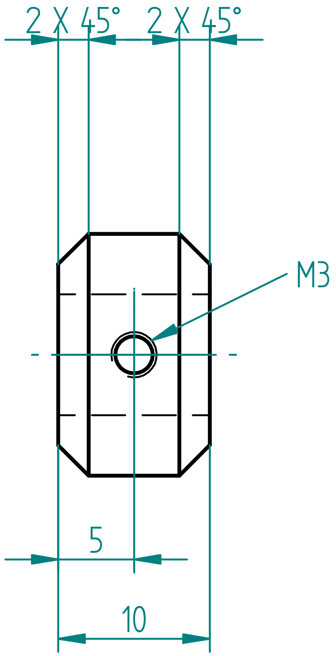

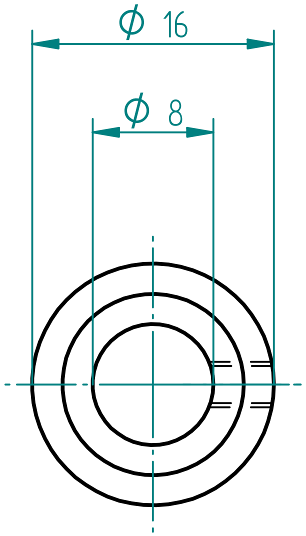

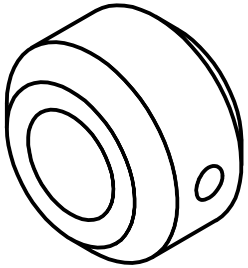

Jet Impingement Apparatus	
DRAWING	Locking Nut
PROJECT NO	
AUTHOR	Louis Biebuyck
SUPERVISOR	Prof. B.W. Skews

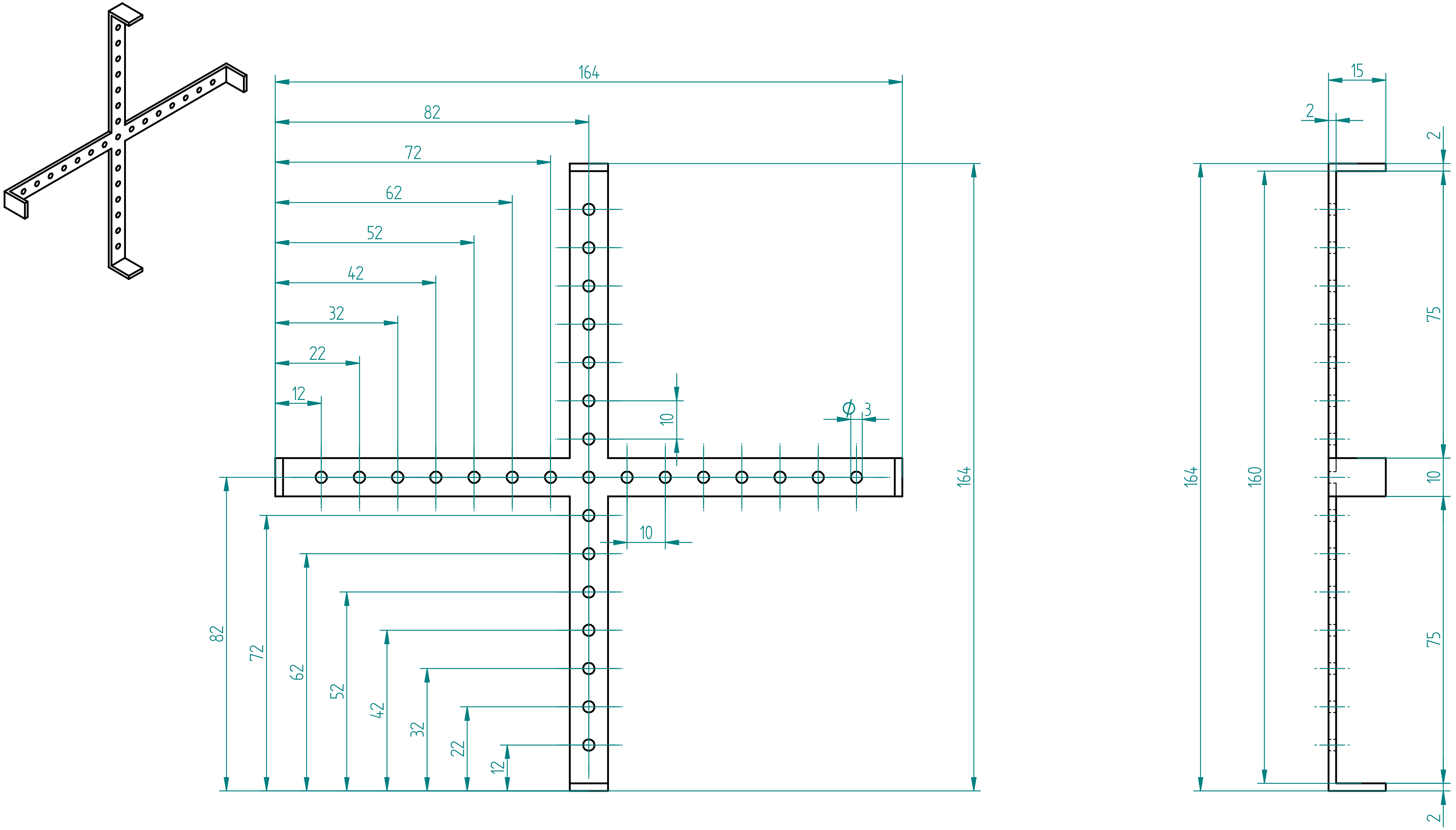

Jet Impingement Apparatus	
DRAWING	Oil Applicator
PROJECT NO	
AUTHOR	Louis Biebuyck
SUPERVISOR	Prof. B.W. Skews

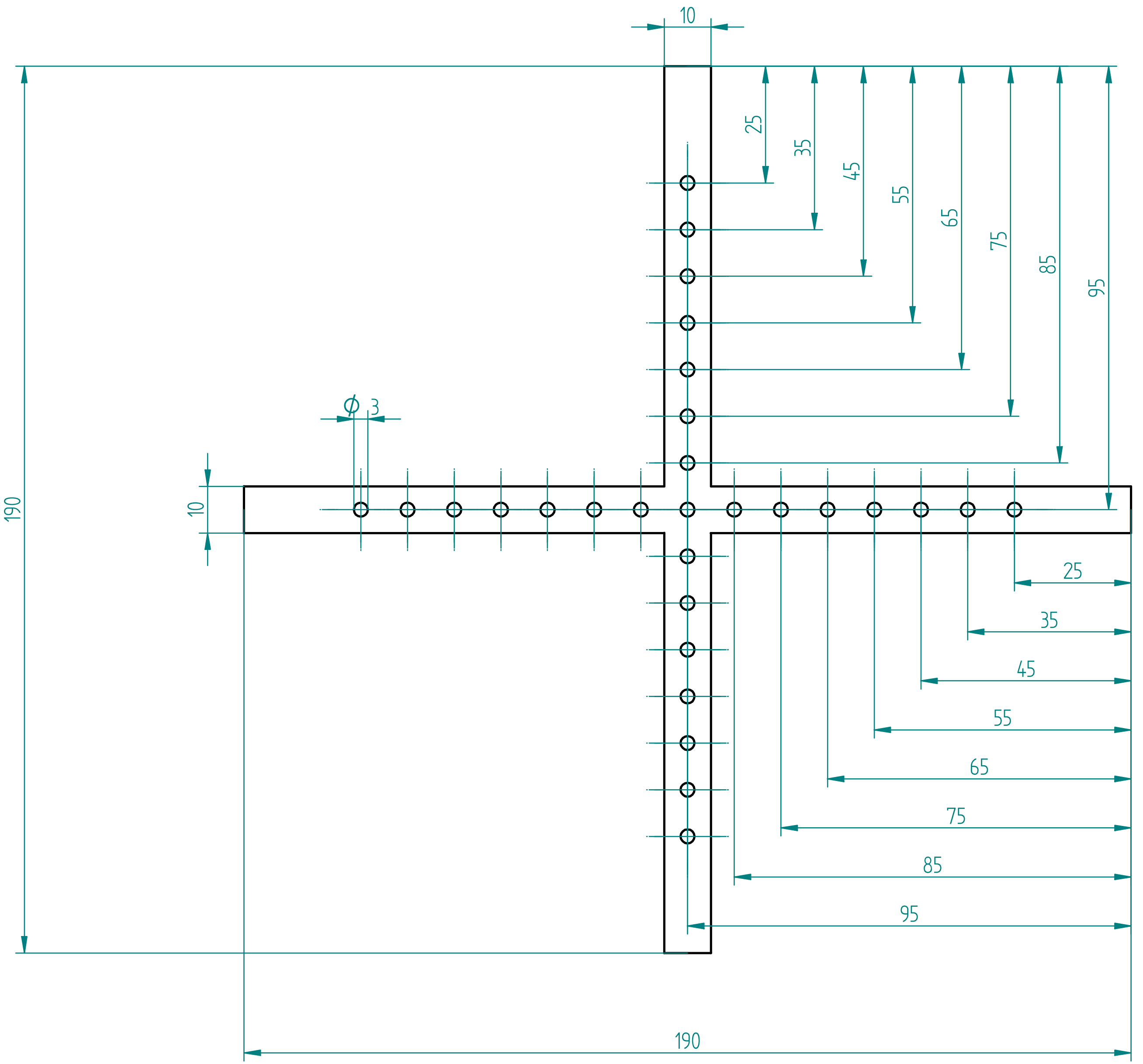

Jet Impingement Apparatus	
DRAWING	Oil Applicator Flat
PROJECT NO	
AUTHOR	Louis Biebuyck
SUPERVISOR	Prof. B.W. Skews

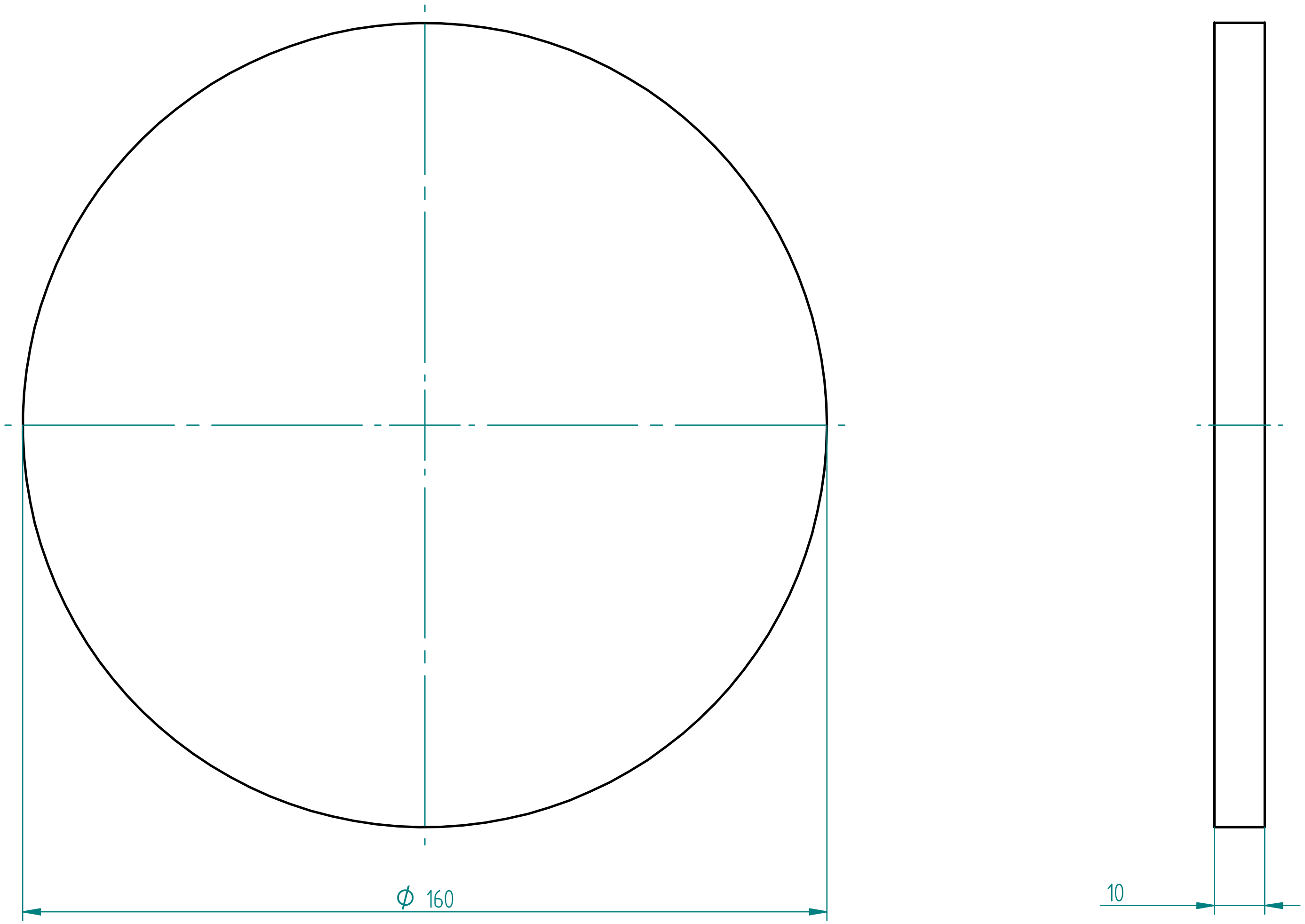

Item	Material	Quantity
10 mmImpingement Plate	Standard Float Glass	1

Jet Impingement Apparatus	
DRAWING	10mm Glass Imping. Plate
PROJECT NO	
AUTHOR	Louis Biebuyck
SUPERVISOR	Prof. B.W. Skews

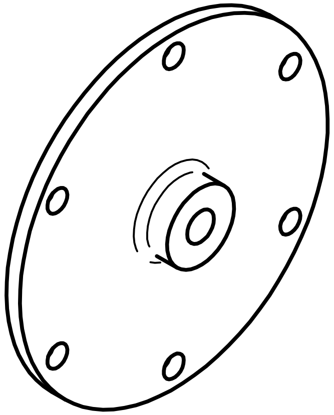

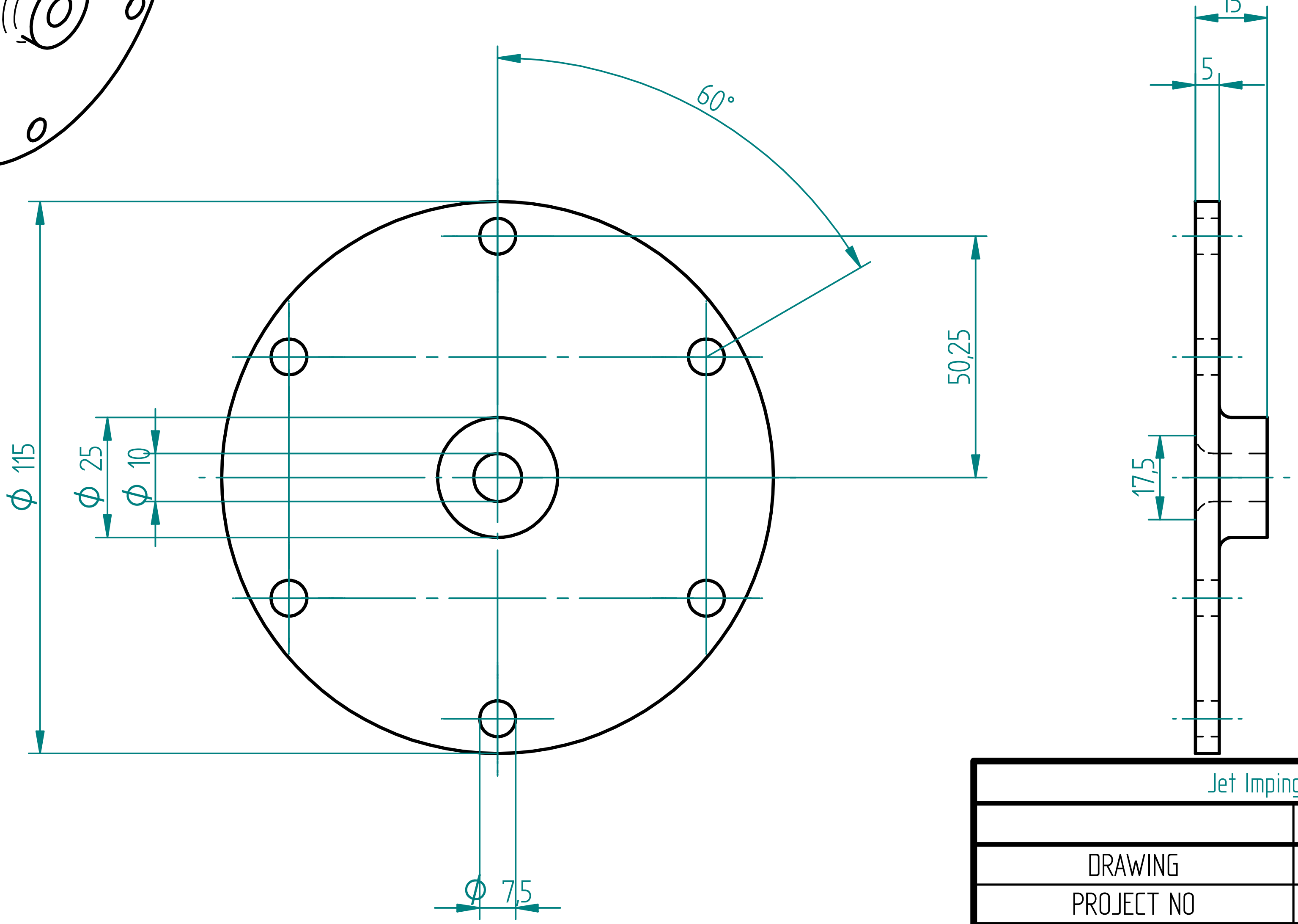

Jet Impingement Apparatus	
DRAWING	Axisymmetric Nozzle Plate
PROJECT NO	Louis Biebuyck
AUTHOR	
SUPERVISOR	Prof. B.W. Skews

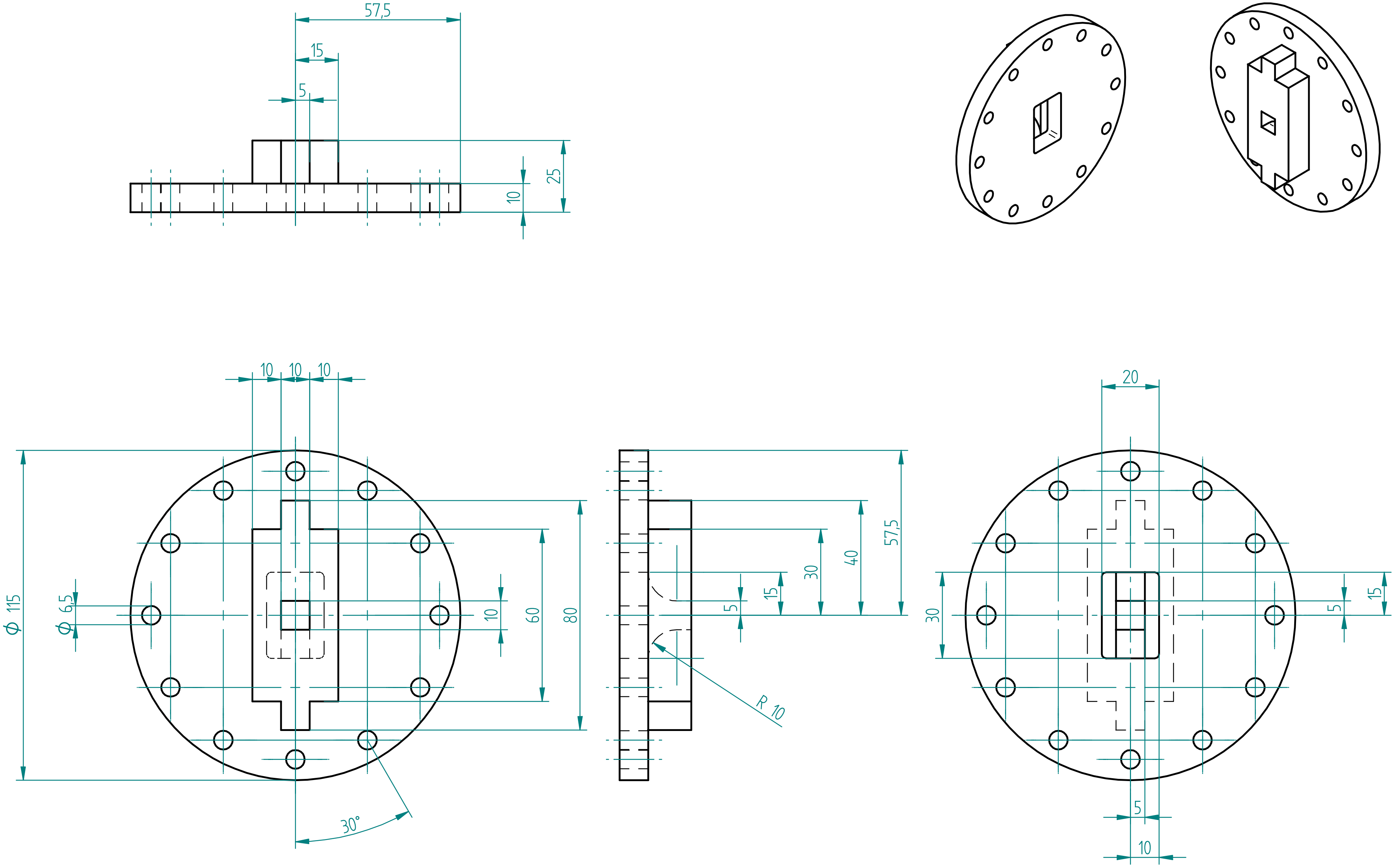

Jet Impingement Apparatus	
DRAWING	Sqaure Nozzle Plate
PROJECT NO	
AUTHOR	Louis Biebuyck
SUPERVISOR	Prof. B.W. Skews

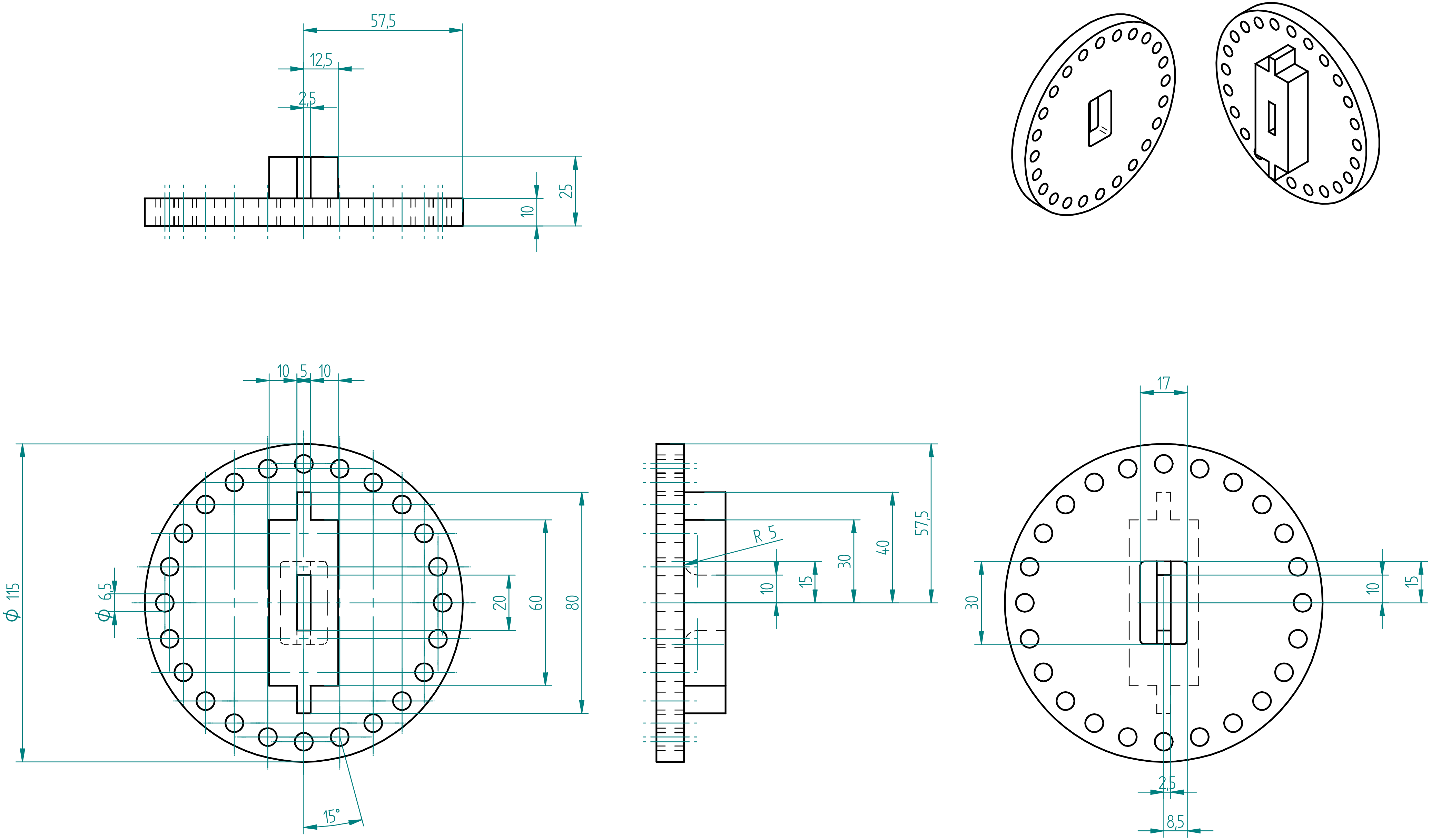

Jet Impingement Apparatus	
DRAWING	AR 4 Rectangular Nozzle
PROJECT NO	
AUTHOR	Louis Biebuyck
SUPERVISOR	Prof. B.W. Skews

15 Appendix C

Data sheets

Product Information

XIAMETER® PMX-200 Silicone Fluid, 50-1,000 cSt

Colorless, clear polydimethylsiloxane fluid

FEATURES

- Ease of application and rubout
- Ease of buffing
- Enhances color
- High water repellency
- High compressibility
- High shearability without breakdown
- High spreadability and compatibility
- Low environmental hazard
- Low fire hazard
- Low reactivity and vapor pressure
- Low surface energy
- Good heat stability
- Essentially odorless, tasteless and nontoxic
- Soluble in a wide range of solvents

BENEFITS

For personal care applications
- Skin protection
- Imparts soft, velvety skin feel
- Spreads easily on both skin and hair
- De-soaping (prevents foaming during rubout)

For industrial applications
- High dielectric strength
- High damping action
- Oxidation-, chemical- and weather-resistant

COMPOSITION

- Polydimethylsiloxane polymers
- Chemical composition $(CH_3)_3SiO[SiO(CH_3)_2]_nSi(CH_3)_3$

APPLICATIONS

- Active ingredient in a variety of automotive, furniture, metal and specialty polishes in paste, emulsion and solvent-based polishes and aerosols
- Various applications including cosmetic ingredient, elastomer and plastics lubricant, electrical insulating fluid, foam preventive or breaker, mechanical fluid, mold release agent, surface active agent, and solvent-based finishing and fat liquoring of leather

DESCRIPTION

XIAMETER® PMX-200 Silicone Fluid is a polydimethylsiloxane polymer manufactured to yield essentially linear polymers in a wide range of average kinematic viscosities.

The viscosities generally used in formulating polishes are between 100 and 30,000 cSt. To obtain optimum results, in terms of ease of application and depth of gloss, it is preferable to use a blend of a low-viscosity fluid and a high-viscosity fluid (e.g. 3 parts XIAMETER® PMX-200 Silicone Fluid 100 cSt and 1 part XIAMETER® PMX-200 Silicone Fluid 12,500 cSt). The low-viscosity silicone fluid acts as a lubricant to make polish application and rubout easier, whereas the high-viscosity silicone fluid produces a greater depth of gloss. Since these polymers are inherently water-repellent, they will cause water to bead up on a treated surface rather than penetrate the polish film.

HOW TO USE

XIAMETER PMX-200 Silicone Fluid is highly soluble in organic solvents such as aliphatic and aromatic hydrocarbons, and the halocarbon propellants used in aerosols. The fluid is easily emulsified in water with standard emulsifiers and normal emulsification techniques. XIAMETER PMX-200 Silicone Fluid is insoluble in water and many organic products.

Additive quantities as small as 0.1% may suffice where XIAMETER PMX-200 Silicone Fluid is to be used as a surface agent or for de-soaping creams and lotions. However, 1-10% is needed for applications such as hand creams and lotions to form a more uniform film and effective barrier.

HANDLING PRECAUTIONS

XIAMETER PMX-200 Silicone Fluid may cause temporary eye discomfort.

PRODUCT SAFETY INFORMATION REQUIRED FOR SAFE USE IS NOT INCLUDED IN THIS DOCUMENT. BEFORE HANDLING, READ PRODUCT AND SAFETY DATA SHEETS AND CONTAINER LABELS FOR SAFE USE, PHYSICAL AND HEALTH HAZARD INFORMATION. THE SAFETY DATA SHEET IS AVAILABLE ON THE XIAMETER WEBSITE AT XIAMETER.COM, OR FROM YOUR XIAMETER REPRESENTATIVE OR DISTRIBUTOR, OR BY CALLING YOUR GLOBAL XIAMETER CONNECTION.

USABLE LIFE AND STORAGE

When stored at or below 25°C (77°F) in the original unopened containers, this product has a usable life of 36 months from the date of production.

TYPICAL PROPERTIES

Test	Unit	Result			
		50 cSt	**100 cSt**	**200 cSt**	**300 cSt**
Appearance		Crystal clear	Crystal clear	Crystal clear	Crystal clear
Specific Gravity at 25°C (77°F)		0.960	0.964	0.967	0.968
Refractive Index at 25°C (77°F)		1.4022	1.4030	1.4032	1.4034
Color, APHA		5	5	5	5
Flash Point, Open Cup	°C (°F)	318 (605)	>326 (>620)	>326 (>620)	>326 (>620)
Acid Number, BCP		trace	trace	trace	trace
Melt Point	°C (°F)[1,2]	-41 (-42)	-28 (-18)	-27 (-17)	-26 (-15)
Pour Point	°C (°F)	-70 (-94)	-65 (-85)	-65 (-85)	-65 (-85)
Surface Tension at 25°C (77°F)	dynes/cm	20.8	20.9	21.0	21.1
Volatile Content, at 150°C (302°F)	percent	0.3	0.02	0.07	0.09
Viscosity Temperature Coefficient		0.59	0.60	0.60	0.60
Coefficient of Expansion	cc/cc/°C	0.00104	0.00096	0.00096	0.00096
Thermal Conductivity at 50°C (122°F)	g cal/cm·sec·°C	-	0.00037	-	0.00038
Solubility Parameter[3]		7.3	7.4	7.4	7.4
Solubility in Typical Solvents					
Chlorinated Solvents		High	High	High	High
Aromatic Solvents		High	High	High	High
Aliphatic Solvents		High	High	High	High
Dry Alcohols		Poor	Poor	Poor	Poor
Water		Poor	Poor	Poor	Poor
Fluorinated Propellants		High	High	High	High
Dielectric Strength at 25°C (77°F)	volts/mil	400	400	400	400
Volume Resistivity at 25°C (77°F)	ohm-cm	$1.0\text{x}10^{15}$	$1.0\text{x}10^{15}$	$1.0\text{x}10^{15}$	$1.0\text{x}10^{15}$

		350 cSt	**500 cSt**	**1,000 cSt**
Appearance		Crystal clear	Crystal clear	Crystal clear
Specific Gravity at 25°C (77°F)		0.969	0.970	0.970
Refractive Index at 25°C (77°F)		1.4034	1.4035	1.4035
Color, APHA		5	5	5
Flash Point, Open Cup	°C (°F)	>326 (>620)	>326 (>620)	>326 (>620)
Acid Number, BCP		trace	trace	Trace
Melt Point	°C (°F)[1,2]	-26 (-15)	-25 (-13)	-25 (-13)
Pour Point	°C (°F)	-50 (-58)	-50 (-58)	-50 (-58)
Surface Tension at 25°C (77°F)	dynes/cm	21.1	21.2	21.2
Volatile Content, at 150°C (302°F)	percent	0.15	0.11	0.11
Viscosity Temperature Coefficient		0.60	0.61	0.61
Coefficient of Expansion	cc/cc/°C	0.00096	0.00096	0.00096
Thermal Conductivity at 50°C (122°F)	g cal/cm·sec·°C	-	0.00038	0.00038
Solubility Parameter[3]		7.4	7.4	7.4
Solubility in Typical Solvents				
Chlorinated Solvents		High	High	High
Aromatic Solvents		High	High	High
Aliphatic Solvents		High	High	High
Dry Alcohols		Poor	Poor	Poor
Water		Poor	Poor	Poor
Fluorinated Propellants		High	High	High
Dielectric Strength at 25°C (77°F)	volts/mil	400	400	400
Volume Resistivity at 25°C (77°F)	ohm-cm	$1.0\text{x}10^{15}$	$1.0\text{x}10^{15}$	$1.0\text{x}10^{15}$

[1] The melt point temperature is a typical value and may vary somewhat due to molecular distribution (especially 50 cSt). If the melting point is critical to your application, then several lots should be thoroughly evaluated.

[2] Due to different rates of cooling, this test method may yield pour points lower than the temperature at which these fluids would melt.

[3] Fedors Method: R.F. Fedors, *Polymer Engineering and Science*, Feb. 1974.

LIMITATIONS

This product is neither tested nor represented as suitable for medical or pharmaceutical uses. Not intended for human injection. Not intended for food use.

HEALTH AND ENVIRONMENTAL INFORMATION

To support customers in their product safety needs, Dow Corning has an extensive Product Stewardship organization and a team of Product Safety and Regulatory Compliance (PS&RC) specialists available in each area.

For further information, please see our website, xiameter.com, or consult your local XIAMETER representative.

LIMITED WARRANTY INFORMATION – PLEASE READ CAREFULLY

The information contained herein is offered in good faith and is believed to be accurate. However, because conditions and methods of use of our products are beyond our control, this information should not be used in substitution for customer's tests to ensure that *Dow Corning*® and XIAMETER® products are safe, effective, and fully satisfactory for the intended end use. Suggestions of use shall not be taken as inducements to infringe any patent.

Dow Corning's sole warranty is that *Dow Corning* or XIAMETER products will meet the sales specifications in effect at the time of shipment.

Your exclusive remedy for breach of such warranty is limited to refund of purchase price or replacement of any product shown to be other than as warranted.

DOW CORNING SPECIFICALLY DISCLAIMS ANY OTHER EXPRESS OR IMPLIED WARRANTY OF FITNESS FOR A PARTICULAR PURPOSE OR MERCHANTABILITY.

DOW CORNING DISCLAIMS LIABILITY FOR ANY INCIDENTAL OR CONSEQUENTIAL DAMAGES.

DOW CORNING® 200 FLUID

CHART FOR BLENDING STANDARD VISCOSITY GRADES TO OBTAIN AN INTERMEDIATE VISCOSITY

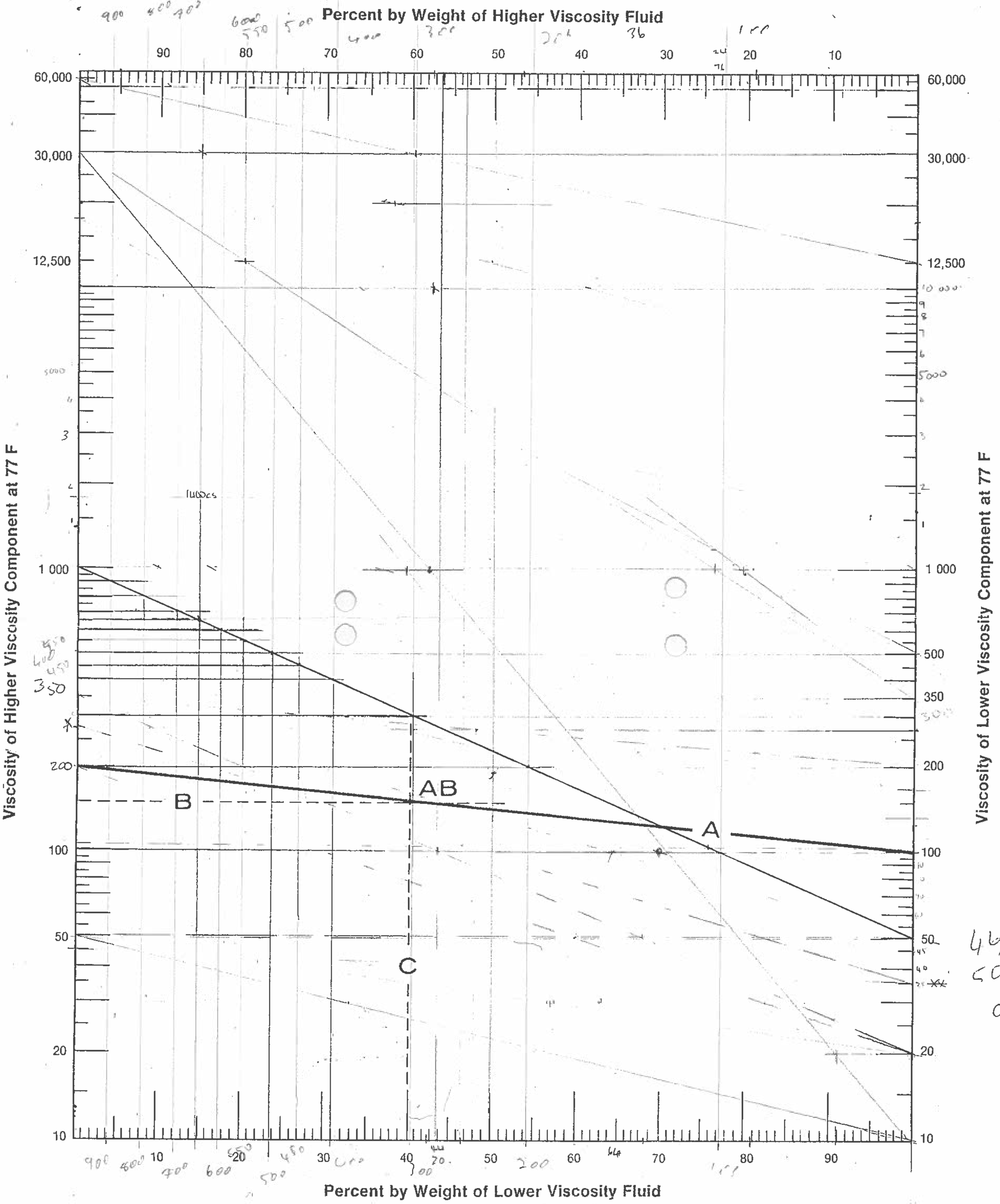

46,752
50,648
97,4

47,04
50,96

48% of 200.

52% of 350.

DOW CORNING INT. LTD., CHAUSSÉE DE LA HULPE, 177, B-1170 BRUSSELS, BELGIUM

® Denotes registered trademark of Dow Corning Corporation.

DOW CORNING

Printed in Belgium

Piérard's/3 M/1.74

Safety data for toluene

Click here for data on toluene in student-friendly format, from the HSci project

---

Glossary of terms on this data sheet.

The information on this web page is provided to help you to work safely, but it is intended to be an overview of hazards, not a replacement for a full Material Safety Data Sheet (MSDS). MSDS forms can be downloaded from the web sites of many chemical suppliers.

General

Synonyms: methylbenzene, phenylmethane, toluol, antisal 1A, CP 25, methacide, methylbenzol, NCI-C07272, RCRA waste number U220, tolu-sol
Uses: Solvent
Molecular formula: C_7H_8
CAS No: 108-88-3
EC No: 203-625-9
Annex I Index No: 601-021-00-3

Physical data

Appearance: Colourless liquid with a benzene-like odour (odour threshold 0.17 ppm)
Melting point: -93 C
Boiling point: 110.6 C
Specific gravity: 0.865
Vapour pressure: 22 mm Hg at 20 C (vapour density 3.2)
Flash point: 4 C
Explosion limits: 1% - 7%
Autoignition temperature: 536 C

Stability

Stable. Substances to be avoided: oxidizing agents, oxygen, moisture. Highly flammable. Hygroscopic.

Toxicology

Harmful if inhaled, especially if breathed in over long periods. May cause drowsiness. Possible risk of harm to the unborn child. May cause lung damage if swallowed. Serious irritant. Experimental teratogen. STEL (EU Directive 2006/15/EC) 100 ppm.

Toxicity data

(The meaning of any abbreviations which appear in this section is given here.)

ORL-RAT LD50 636 mg kg^{-1}

IPR-RAT LD50 1332 mg kg^{-1}

ORL-HMN LDLO 50 mg kg^{-1}

IPR-MUS LD50 59 mg kg^{-1}

IHL-MAM LC50 30 g m^{-3}

Irritation data

(The meaning of any abbreviations which appear in this section is given here.)
EYE-HMN 300 ppm.
SKN-RBT 435 mg mild.

Risk phrases

(The meaning of any risk phrases which appear in this section is given here.)
R11 R20 R48 R63 R65 R67.

Hazard statements

(The meaning of any hazard statement codes which appear in this section is given here.)
H225 H304 H315 H336 H361d H373.

Precautionary phrases

P210 P261 P281 P301 P310 P331.

Transport information

(The meaning of any UN hazard codes which appear in this section is given here.)
Hazard class 3.0 Packing group II. UN No 1294. IMDG class 3.

Personal protection

Safety glasses. Good ventilation.

Safety phrases

(The meaning of any safety phrases which appear in this section is given here.)
S16 S25 S29 S33.

[Return to Physical & Theoretical Chemistry Lab. Safety home page.]

This information was last updated on December 17, 2010. Although we have tried to make it as accurate and useful as possible, we can take no responsibility for its use or misuse.

Note also that the information on the PTCL Safety web site, where this page was hosted, has been copied onto many other sites, often without permission. If you have any doubts about the veracity of the information that you are viewing, or have any queries, please check the URL that your web browser displays for this page. If the URL **begins** "http://msds.chem.ox.ac.uk/" the page is maintained by the Safety Officer in Physical Chemistry at Oxford University. If not, this page is a copy made by some other person and we have no responsibility for it.

Product data sheet

4400GP, MIRO® 4

Product	Miro®, Extra Bright Rolled, reflection	
Delivery options	Coil, strip, sheet, blanks	
Thickness of up	[mm]	0,30 - 0,80
Width of up to max	[mm]	1250,00

Optical Properties		**Front (S1)**	**Rear (S2)**
Total light reflection[1]	[%]	≥ 95	
Diffuse light reflection	[%]	< 12	
Total light reflection[2]	[%]	≥ 95	
Brightness[3] along		89	
across		88	

Surface Properties

Treatment (S1)	brightened, anodised and PVD-coated
PVD Coating (S1)	PVD AL 99.99
Iridescence Assessment (S1)	Absolutely free of interference colors
Treatment (S2)	anodised

Material / Alloy[5]		AL 99.85
Hardness[6]		Hard
Mechanical Properties		
Tensile strength	[MPa]	160 - 200
Yield strength	[MPa]	140 - 180
Elongation (A50)	[%]	≥ 2
Deformation / Bending	[Bending radius]	≥ 1,5 x gauge of material

Tolerances

Gauge	[mm]	0,30 - 0,50 ± 0,04	0,61 - 0,80 ± 0,06
	[mm]	0,51 - 0,60 ± 0,05	
Width / Coil	[mm]	+ 3,00 / - 0,00	
Width Slit Coil	[mm]	± 0,20 Standard	± 0,05 Special
Longitudinal Curvature	[mm]	≤ 1,00 on a measuring length of 1000 mm	
Sheet	[mm]	0,00 - 600,00 + 1,00 - 0,00	1500,00 - 2500,00 + 2,50 - 0,00
	[mm]	600,00 - 1500,00 + 1,50 - 0,00	2500,00 - 3500,00 + 3,50 - 0,00
Transversal divergency	[mm]	≤ 1,50 (D1-D2)	
Flatness	[mm]	1,00% of wavelength maximum 8,00 [mm]	

PE-Film	Protective film 50-60 µm

---

[1] DIN 5036-3 (U-Globe)
[2] ASTM E-1651 (TR-2)
[3] ISO 7688 (60° / calibrated 91.8)
[4] ASTM E-430 (Hunter Dorigon, Tricor DOI Hazemeter)
[5] acc. to DIN EN 573-3/Millsnorm/Other
[6] acc. to DIN EN 485-2 / Millsnorm / Other

TYPICAL PROPERTIES

Test	Unit	Result			
		50 cSt	**100 cSt**	**200 cSt**	**300 cSt**
Appearance		Crystal clear	Crystal clear	Crystal clear	Crystal clear
Specific Gravity at 25°C (77°F)		0.960	0.964	0.967	0.968
Refractive Index at 25°C (77°F)		1.4022	1.4030	1.4032	1.4034
Color, APHA		5	5	5	5
Flash Point, Open Cup	°C (°F)	318 (605)	>326 (>620)	>326 (>620)	>326 (>620)
Acid Number, BCP		trace	trace	trace	trace
Melt Point	°C (°F)[1,2]	-41 (-42)	-28 (-18)	-27 (-17)	-26 (-15)
Pour Point	°C (°F)	-70 (-94)	-65 (-85)	-65 (-85)	-65 (-85)
Surface Tension at 25°C (77°F)	dynes/cm	20.8	20.9	21.0	21.1
Volatile Content, at 150°C (302°F)	percent	0.3	0.02	0.07	0.09
Viscosity Temperature Coefficient		0.59	0.60	0.60	0.60
Coefficient of Expansion	cc/cc/°C	0.00104	0.00096	0.00096	0.00096
Thermal Conductivity at 50°C (122°F)	g cal/cm·sec·°C	-	0.00037	-	0.00038
Solubility Parameter[3]		7.3	7.4	7.4	7.4
Solubility in Typical Solvents					
Chlorinated Solvents		High	High	High	High
Aromatic Solvents		High	High	High	High
Aliphatic Solvents		High	High	High	High
Dry Alcohols		Poor	Poor	Poor	Poor
Water		Poor	Poor	Poor	Poor
Fluorinated Propellants		High	High	High	High
Dielectric Strength at 25°C (77°F)	volts/mil	400	400	400	400
Volume Resistivity at 25°C (77°F)	ohm-cm	1.0x10^{15}	1.0x10^{15}	1.0x10^{15}	1.0x10^{15}

		350 cSt	**500 cSt**	**1,000 cSt**
Appearance		Crystal clear	Crystal clear	Crystal clear
Specific Gravity at 25°C (77°F)		0.969	0.970	0.970
Refractive Index at 25°C (77°F)		1.4034	1.4035	1.4035
Color, APHA		5	5	5
Flash Point, Open Cup	°C (°F)	>326 (>620)	>326 (>620)	>326 (>620)
Acid Number, BCP		trace	trace	Trace
Melt Point	°C (°F)[1,2]	-26 (-15)	-25 (-13)	-25 (-13)
Pour Point	°C (°F)	-50 (-58)	-50 (-58)	-50 (-58)
Surface Tension at 25°C (77°F)	dynes/cm	21.1	21.2	21.2
Volatile Content, at 150°C (302°F)	percent	0.15	0.11	0.11
Viscosity Temperature Coefficient		0.60	0.61	0.61
Coefficient of Expansion	cc/cc/°C	0.00096	0.00096	0.00096
Thermal Conductivity at 50°C (122°F)	g cal/cm·sec·°C	-	0.00038	0.00038
Solubility Parameter[3]		7.4	7.4	7.4
Solubility in Typical Solvents				
Chlorinated Solvents		High	High	High
Aromatic Solvents		High	High	High
Aliphatic Solvents		High	High	High
Dry Alcohols		Poor	Poor	Poor
Water		Poor	Poor	Poor
Fluorinated Propellants		High	High	High
Dielectric Strength at 25°C (77°F)	volts/mil	400	400	400
Volume Resistivity at 25°C (77°F)	ohm-cm	1.0x10^{15}	1.0x10^{15}	1.0x10^{15}

---

[1] The melt point temperature is a typical value and may vary somewhat due to molecular distribution (especially 50 cSt). If the melting point is critical to your application, then several lots should be thoroughly evaluated.

[2] Due to different rates of cooling, this test method may yield pour points lower than the temperature at which these fluids would melt.

[3] Fedors Method: R.F. Fedors, *Polymer Engineering and Science*, Feb. 1974.

LIMITATIONS

This product is neither tested nor represented as suitable for medical or pharmaceutical uses. Not intended for human injection. Not intended for food use.

HEALTH AND ENVIRONMENTAL INFORMATION

To support customers in their product safety needs, Dow Corning has an extensive Product Stewardship organization and a team of Product Safety and Regulatory Compliance (PS&RC) specialists available in each area.

For further information, please see our website, xiameter.com, or consult your local XIAMETER representative.

LIMITED WARRANTY INFORMATION – PLEASE READ CAREFULLY

The information contained herein is offered in good faith and is believed to be accurate. However, because conditions and methods of use of our products are beyond our control, this information should not be used in substitution for customer's tests to ensure that *Dow Corning*® and XIAMETER® products are safe, effective, and fully satisfactory for the intended end use. Suggestions of use shall not be taken as inducements to infringe any patent.

Dow Corning's sole warranty is that *Dow Corning* or XIAMETER products will meet the sales specifications in effect at the time of shipment.

Your exclusive remedy for breach of such warranty is limited to refund of purchase price or replacement of any product shown to be other than as warranted.

DOW CORNING SPECIFICALLY DISCLAIMS ANY OTHER EXPRESS OR IMPLIED WARRANTY OF FITNESS FOR A PARTICULAR PURPOSE OR MERCHANTABILITY.

DOW CORNING DISCLAIMS LIABILITY FOR ANY INCIDENTAL OR CONSEQUENTIAL DAMAGES.

16 Appendix D

Fringe Identification

```
%low pass filtering

close all
clc

%only have to go through the picture cropping process once per
%data set
if (countmaster<=1)

    clear I I2
    I=imread(I_file);
    I=rgb2gray(I);
    imshow(I), axis on, grid on
    I2=imcrop;                          % crop image to area of
interest
    I2=imadjust(I2);                    % adjust contrast of image
    imshow(I2), axis on, grid on        % show cropped image
    filename2=[num2str(pos) 'mm ' 'cropped image '];

end

imshow(I2), axis on, grid on

%plot raw pixel intensity data
clear c xs f xi yi ri ri_round
xi(1,1)=input('start x-value: ');
yi(1,1)=input('start y-value: ');
xi(1,2)=input('end x-value: ');
yi(1,2)=input('end y-value: ');
ri=sqrt((xi(1,1)-xi(1,2))^2+(yi(1,1)-yi(1,2))^2);
ri_round=round(ri);
c=improfile(I2, xi, yi, ri_round);
% c=improfile;
xs=size(c);
xs=xs(1,1);
f=linspace(0,1,xs);
figure, plot(c);
grid on, xlabel ('distance (pixels)'), ylabel ('intensity');
filename3=[num2str(pos) 'mm ' 'Initial Intensity Graph '
num2str(countmaster)];
print('-f2', '-djpeg', filename3);

%generate FFT of raw data to determine cut-off frequency for filter
clear C fcut
C=fft(c);           % take Fourier transform to determine cut-off
frequency
C(1,1)=0;                   % set first value to zero to improve
resolution
figure, bar(f(1:xs/2),abs(C(1:xs/2)));
xlabel ('frequency'), ylabel ('FFT magnitude');
```

```
fcut=input('input cut-off frequency ');          % define cut-off
frequency
n=5;                                         % level of smoothing of
filter
a=1;                                             % filter denominator
coeff
filename4=[num2str(pos) 'mm ' 'FFT Graph ' num2str(countmaster)];
print('-f3', '-djpeg', filename4);

%filter raw data
clear filt y ymin ymax
filt=fir1(n,fcut);                       % lowpass filter
y=filter(filt,a,c);                      % apply lowpass to data
ymin=min(c);
ymax=max(c);

%plot new filtered data for analysis
close all
imshow(I2), axis on, grid on
figure, plot(y), ylim([ymin (ymax+ymin/2)]);
grid on, xlabel ('distance (pixel)'), ylabel ('intensity');
filename5=[num2str(pos) 'mm ' 'Smoothed Intensity Graph '
num2str(countmaster)];
print('-f2', '-djpeg', filename5);


%ensure that each pass deals with the same number of fringes
%if fringe number changes, averaging function will not work
if (countmaster<=1)
    countmax=input('number of fringes: ');
end

clear count x_zero xp
count=1;

%capture pixel distance of each fring point
x_zero=input('input first min point: ');            %starting datum
point
while (count<=2*countmax)

    xp(count)=input('next fringe point: ');

    count=count+1;

end

%shift pixel data according to datum point
xp=xp-x_zero;
%xp=[0 xp];
```

Error of Paralax Conversion

```
%correct for error of paralax
close all
clc

space=5;    % line spacing in mm

%read in image data and convert to grayscale for analysis
I_ref=imread(I_reffile);
I_ref=rgb2gray(I_ref);

%crop image down to area of interest
imshow(I_ref), axis on, grid on
I2_ref=imcrop;
I2_ref=imadjust(I2_ref);
imshow(I2_ref), axis on, grid on

%plot pixel intensity graph
xi_ref(1,1)=input('start x-value: ');
yi_ref(1,1)=input('start y-value: ');
xi_ref(1,2)=input('end x-value: ');
yi_ref(1,2)=input('end y-value: ');
ri_ref=sqrt((xi_ref(1,1)-xi_ref(1,2))^2+(yi_ref(1,1)-yi_ref(1,2))^2);
ri_roundref=round(ri_ref);
c_ref=improfile(I2_ref, xi_ref, yi_ref, ri_roundref);

% c_ref=improfile;
xs_ref=size(c_ref);
xs_ref=xs_ref(1,1);
f_ref=linspace(0,1,xs_ref);
plot(c_ref), grid on, xlabel ('distance (pixels)'), ylabel
('intensity');
C_ref=fft(c_ref);                           % take Fourier transform to
determine cut-off frequency
C_ref(1,1)=0;                           % set first value to zero to
improve resolution
figure, bar(f_ref(1:xs_ref/2),abs(C_ref(1:xs_ref/2))), xlabel
('normalised frequency'), ylabel ('FFT magnitude')
fcut_ref=input('input cut-off frequency '); % define cut-off frequency
for lowpass
n_ref=5;                                    % level of smoothing of
filter
a_ref=1;                                    % filter denominator coeff

filt_ref=fir1(n_ref,fcut_ref);                     % lowpass filter
y_ref=filter(filt_ref,a_ref,c_ref);                     % apply lowpass
to data
y_refmin=min(c_ref);
y_refmax=max(c_ref);

close all
%imshow(I2_ref), axis on, grid on
plot(y_ref), ylim([y_refmin y_refmax]), grid on
```

```
filename6=[num2str(pos) 'mm ' 'reference intensity ',
num2str(countmaster)];
print('-djpeg', filename6);

%save intensity graph
filename6=[num2str(pos) 'mm ' 'reference intensity ',
num2str(countmaster)];
print('-djpeg', filename6);

%user defines how many reference line the interogation line passes
through
count_ref=1;
count_refmax=input('number of local min: ');

%read in pixel values for each reference line
while (count_ref<=count_refmax)

    x_ref(count_ref)=input('enter local min x-value: ');
    count_ref=count_ref+1;

end

%determine distance between each line
count2_ref=1;
while (count2_ref<=count_refmax-1)

    size_ref(count2_ref)=x_ref(count2_ref+1)-x_ref(count2_ref);
    count2_ref=count2_ref+1;

end

ymean=mean(size_ref);             %calculate the average distance between
lines
pix_dens=ymean/space;             %calculate the average number of pixels
per mm
```

Oil Height Calculation

```
%calculate matrix for oil height

close all
clc

lamda_0=589*10^-9;                  % light wavelenght
n_f=1.40;                           % oil refractive index
n_1=1.0;                            % air refractive index
theta_i=theta*2*pi/360;             % convert to radians

k=1;                                % phase shift (k odd light fringes,
k even dark fringes)
kmax=max(size(xp));                 % ensure size of oil height vector
is the same size as the size of the distance vector
clear h

%determine the oil height at each light and dark fringe
while (k<=kmax)

    h(k)=(k*lamda_0/4)*(1/sqrt(n_f^2-n_1^2*(sin(theta_i))^2));
    k=k + 1;

end
```

Oil Density and Viscosity Calculations

```
% mixing table calculation for oil density

rho_50=960;                % kg/m^3 density 50cSt oil
rho_1000=970;              % kg/m^3 density 1000cSt oil

%takes the correct density ratio for the specified oil viscosity
if (v<=100)
    p1=0.775;
else if (v<=200)
        p1=0.545;
    else if (v<=300)
            p1=0.405;
        else if(v<=400)
                p1=0.31;
            else if(v<=450)
                    p1=0.27;
                else if(v<=500)
                        p1=0.24;
                    else if(v<=550)
                            p1=0.2;
                        else if(v<=600)
                                p1=0.175;
                            else if(v<=650)
                                    p1=0.15;
                                else if(v<=700)
                                        p1=0.12;
                                    else if(v<=800)
                                            p1=0.08;
                                        else if(v<=900)
                                                p1=0.04;
                                            end
                                        end
                                    end
                                end
                            end
                        end
                    end
                end
            end
        end
    end
end

%calculate the actual oil density based on the density ratios
calculated
%from the mixing graph
p2=1-p1;
rho=rho_50*p1+rho_1000*p2;
```

Shear Force Calculation

```
%determine shear force

close all
clc
clear v1 meu_0 x_f h_f

v1=v*10^-6;                                 % convert from cSt to m^2/s
meu_0=v1*rho;                               % dynamic viscousity

%convert distance in pixels to metres
x_f=[0 xp]/pix_dens*10^-3;
h_f=[0 h];

syms x;
quest='n';
clear n p eval_max eval_min x_eval f
clc

%generate best fit curve for data
%loop runs until the user is happy with the fit of the curve
while (quest == 'n')

    n=input ('select degree of polynomial for best fit: ');
    p=polyfit(x_f, h_f, n);
    eval_max=max(x_f)+x_f(1,2);
    eval_min=x_f(1,2)*3;
    x_eval=(-eval_min:1e-8:eval_max);
    f=polyval(p, x_eval);
    plot(x_f, h_f, 'o', x_eval, f, '-'), grid on;
    quest = input('is this fit ok? y/n: ', 's');
    close figure 1;

end

%write bestfit graph to file
plot(x_f, h_f, 'o', x_eval, f, '-');
grid on, xlabel('Fringe Spacing (m)'), ylabel('Oil Height (m)');

filename7=[num2str(pos) 'mm ' 'Oil Height Best Fit '
num2str(countmaster)];
print('-djpeg', filename7);

%use the best fit curve as a calibration curve
f_x=poly2sym(p);
h_new=subs(f_x, x, x_f);        %calulate the calibrated height values

%write new graph to file
plot(x_f, h_new, '*', x_eval, f, '-');
grid on, xlabel('Fringe Spacing (m)'), ylabel('OIl Height (m)');
filename8=[num2str(pos) 'mm' 'Calibrated Oil Height'
num2str(countmaster)];
print ('-djpeg', filename8);
```

```
clear counter countermax tau sf2
counter=1;
countermax=max(size(xp));

%calculate the shear force at each data point
while (counter<=countermax)

    tau=(2*meu_0/((h_new(counter+1))^2*t))*(int(f_x,0,x_f(counter+1)));
    sf2(counter)=tau;
    counter=counter+1;
end

%save the graph shear vs distance from oil leading edge
clear x_f1
sf2=double(sf2);
x_f1=x_f*1e3;
x_f1(:,1)=[];
ymax=max(sf2)+min(sf2)/4;
figure, plot(x_f1, sf2, '*'), grid on;
xlabel ('Distance (mm)'), ylabel ('Shear Force (Pa)'), ylim([0, ymax]);
filename9=[num2str(pos) 'mm ' 'Shear Force ' num2str(countmaster)];
print('-f2', '-djpeg', filename8);
```

Master Run File

```
% %Run this file, make sure all others are in same directory file

clear all
close all
clc

%initialise required variables
countmaster=1;
%level 1 counter
countmastermax=input('select number of iterations: ');
%User define number of passes for averaging
shear_ave=[];
%initialise shear average vector for while loop
x_posave=[];
%initialise position average vector for while loop
shear_ave1=[];
x_posave1=[];

%user inputs about test data
pos=input('approximate position of oil: ');
%position of oil drop from jet centre
v=input('specify viscosity of oil in cSt: ');
%oil viscosity
t=input('run time in s: ');
%jet run time
theta=input('angle of camera from vertical: ');
%camera angle
I_file=input('specify image file ','s');
%fringe photo
I_reffile=input('specify reference image file ','s');
%reference photo
I_or=input('Original oil position picture: ', 's');

%determine distance from jet centre to edge of oil drop
I_or=imread(I_or);
I_or=rgb2gray(I_or);
imtool(I_or);
oil_drop=input('Pixel distance: ');
imtool close all
clc

filename=[num2str(pos) 'mm ' 'shear.txt'];
%define name of file for writing data
fid=fopen(filename, 'w');
%create data file and allow write privaledges

%write initial test conditions to file
fprintf(fid, '\r\nOil Viscosity (cSt)=');
fprintf(fid, '  %i', v);
fprintf(fid, '\r\nRun Time (s)=');
fprintf(fid, '  %i', t);
fprintf(fid, '\r\nCamera Angle (degrees)=');
fprintf(fid, '  %i', theta);
```

```
%run code to determine other physical parameters for calculations
mixing
paralax
fprintf(fid, '\r\nPixel Density (pixel/mm)=');
fprintf(fid, '  %f', pix_dens);

%iterate through the picture analysis process
while (countmaster<=countmastermax)

    %code to calculate fringe spacing, oil height and shear values
    lowpass
    oil_height
    shear_2

    %save all data to file
    fprintf(fid, '\r\n\r\nRun Number: ');
    fprintf(fid, '% u', countmaster);
    fprintf(fid, '\r\n\r\n Fringe Spacing (pixels)');
    fprintf(fid, '\r\n %i', xp);
    fprintf(fid, '\r\n\r\n Measured Fringe Spacing (m)');
    fprintf(fid, '\r\n %e', x_f);
    fprintf(fid, '\r\n\r\n Oil Height (m)');
    fprintf(fid, '\r\n %e', h_f);
    fprintf(fid, '\r\n\r\n Corrected Oil Height (m)');
    fprintf(fid, '\r\n %e', h_new);
    fprintf(fid, '\r\n\r\n Shear Force (Pa)');
    fprintf(fid, '\r\n %f', sf2);

    %generate matrices for averaging
    shear_ave=[shear_ave;sf2];
    x_posave=[x_posave;x_f1];
%     shear_ave1=[shear_ave1;sf2'];
%     x_posave1=[x_posave1;x_f1'];
    countmaster=countmaster+1;

end

clc

%remove any outlying data sets
%loop runs till user is happy there are no outlying data sets
quest='y';
while (quest=='y')

    plot(shear_ave'), legend('toggle');
    quest=input('Are there outliers? (y/n): ', 's');

    if(quest=='y')

        cleaner=input('data set number: ');
        shear_ave(cleaner,:)=[];           %removes entire row from
matrix.
        x_posave(cleaner,:)=[];                                   %If
one data point erroneous,
                                           %the rest calculated in that
```

```
                                        %set will be too.
    end
    close all
end

close all
clc

%calculate distance from jet centre
oil_space=oil_drop/pix_dens;

m_tot=size(shear_ave, 1);
m=1;
shear_ave1=[];
x_posave1=[];
while (m<=m_tot)
    x_posave1=[x_posave1; x_posave(m, :)'];
    shear_ave1=[shear_ave1; shear_ave(m, :)'];
    m=m+1;
end
x_posave=x_posave+oil_space;
x_posave1=x_posave1+oil_space;

%generate matrix of all calculated shear and distance values
shear=[x_posave1 shear_ave1];
shear_total=sortrows(shear);

clc

%save graph of raw data
plot(shear_total(:,1), shear_total(:,2), '*');
grid on, ylim([0, max(shear_ave1)+5]);
xlabel('fringe spacing (mm)'), ylabel('shear force (Pa)');
filename10=[num2str(pos) 'mm ' 'final shear values'];
print('-djpeg',filename10);

%write raw data to file
fprintf(fid, '\r\nDistance From Centre (mm) Shear Force (Pa)');
dlmwrite(filename, shear_total, '-append', 'roffset', 1, 'delimiter',
'\t', 'newline', 'pc');
fclose(fid);

%generate matrix of average shear and distance values
countmaster2=1;
row=size(shear_ave);
row=row(1,2);

while (countmaster2<=row)
    ave_shear(countmaster2)=mean(shear_ave(:,countmaster2));
    ave_x(countmaster2)=mean(x_posave(:,countmaster2));
    countmaster2=countmaster2+1;
end

%save graph of averaged data
```

```
figure, plot(ave_x, ave_shear, '*'), ylim([0, max(ave_shear)+5]), grid
on;
xlabel('Fringe Spacing (mm)'), ylabel('Shear Force (Pa)');
filename11=[num2str(pos) 'mm ' 'average shear values'];
print('-djpeg',filename11);

%save final averaged data to a seperate file for
%overall analysis and comparison
SHEAR_FINAL=[ave_x' ave_shear'];
fid=fopen(filename, 'a');
fprintf(fid, '\r\n\r\nAverage Shear Force (Pa)');
dlmwrite(filename, SHEAR_FINAL, '-append', 'roffset', 1, 'delimiter',
'\t', 'newline', 'pc');
dlmwrite('final shear.txt', SHEAR_FINAL, '-append', 'roffset', 1,
'delimiter', '\t', 'newline', 'pc');

fclose(fid);
```

Uncertainty Analysis

```
% work out errors
clear all
close all
clc
v=input('oil viscosity: ');

%values from mixing table
if (v==100)
        p1=0.775;
        p2=1-p1;
elseif (v==200)
        p1=0.545;
        p2=1-p1;
elseif (v==300)
        p1=0.405;
        p2=1-p1;
elseif(v==400)
        p1=0.31;
        p2=1-p1;
elseif(v==450)
        p1=0.27;
        p2=1-p1;
elseif(v==500)
        p1=0.24;
        p2=1-p1;
elseif(v==550)
        p1=0.2;
        p2=1-p1;
elseif(v==600)
        p1=0.175;
        p2=1-p1;
elseif (v==650)
        p1=0.15;
        p2=1-p1;
elseif (v==700)
        p1=0.12;
        p2=1-p1;
elseif (v==800)
        p1=0.08;
        p2=1-p1;
elseif (v==900)
        p1=0.04;
        p2=1-p1;
else
        p1=0;
        p2=0;
end

%error values
e_w=2.5e-3; %mixing table measuring error
e_Vm=0.1; %syringe measuring error
e_theta=5*2*pi/360; %angle error
e_space=0.25; %printed line space error
e_xp=5; %pixel space error
e_pixref=2; %pixel space error
```

```
%oil values
rho1=0.960; %g/ml
rho2=0.970; %g/ml
v1=50; %cSt
v2=1000; %cSt

%input known parameters
pos=input('Approx oil position: ');
rt=input('run time: ');


%calculate errors in oil mixing
V=p1/rho1+p2/rho2;
pv1=p1/(rho1*V);
pv2=p2/(rho2*V);
e_V=sqrt((e_w/rho1)^2+(e_w/rho2)^2);
e_p1=sqrt((e_w/(rho1*V))^2+(p1/(rho1*V^2)*e_V)^2);
p_ep1=e_p1/pv1*100;
%calculate volume to make 10ml total
V1=10*pv1;
V2=10*pv2;
dvdp1=V1*v1;
%e_p1=rho1*e_w; %mixing table error
dvdp2=V2*v2;
e_p2=sqrt((e_w/(rho2*V))^2+(p2/(rho2*V^2)*e_V)^2);
p_ep2=e_p2/pv2*100;
%e_p2=rho2*e_w; %mixing table error
dvdV1=p1*v1;
e_V1=sqrt((10*e_p1)^2+e_Vm^2); %Volume error
p_eV1=e_V1/V1*100;
dvdV2=p2*v2;
e_V2=sqrt((10*e_p2)^2+e_Vm^2); %Volume error
p_eV2=e_V2/V2*100;

%viscosity error in cSt
e_v=sqrt((dvdp1*e_p1)^2+(dvdp2*e_p2)^2+(dvdV1*e_V1)^2+(dvdV2*e_V2)^2);
p_ev=e_v/v*100;

rho1_2=rho1*1000; %convert to kg/l
rho2_2=rho2*1000; %ditto

v=v*1e-6; %convert to m^2/s
e_v2=e_v*1e-6; %convert error to same

rho=rho1_2*p1+rho2_2*p2; %calculate density
e_rho=sqrt((rho1_2*e_w)^2+(rho2_2*e_w)^2); %density error
p_erho=e_rho/rho*100;

%dynamic viscosity error
meu=v*rho;
e_meu=sqrt((rho*e_v2)^2+(v*e_rho)^2); %dynamic viscosity error
p_emeu=e_meu/meu*100;

lamda_0=589*10^-9; %light wave length
```

```
n_f=1.4;
n_1=1;
theta=input('camera angle: ');
theta=theta*2*pi/360;
dhdtheta=(lamda_0*n_1^2*cos(theta)*sin(theta))/(4*(n_f^2-
n_1^2*(sin(theta))^2)^(3/2));

count=1;
countmax=input('number of points: ');
%capture pixel distance of each fring point

while (count<=countmax)

    xp(count)=input('next fringe point: ');
    h(count)=(count*lamda_0/4)*(1/sqrt(n_f^2-n_1^2*(sin(theta))^2));
    e_h(count)=count*dhdtheta*e_theta; %initia oil height error
    p_eh(count)=e_h(count)/h(count)*100;
    count=count+1;

end

pix_dens=input('pixel density: ');
xp=[0 xp];
x_f=(xp/pix_dens)*1e-3; %pixel distance to metre distance
h=[0 h];
e_h=[0 e_h];

%best fit curve
quest='n';
while (quest == 'n')

    n=input ('select degree of polynomial for best fit: ');
    p=polyfit(x_f, h, n);
    eval_max=max(x_f)+x_f(1,2);
    eval_min=x_f(1,2);
    x_eval=(-eval_min:1e-8:eval_max);
    f=polyval(p, x_eval);
    plot(x_f, h, 'o', x_eval, f, '-'), grid on;
    hold on;
    errorbar(x_f, h, e_h, 'o');
    hold off;
    quest = input('is this fit ok? y/n: ', 's');
    close figure 1;

end

%calulate new oil height values based on best fit curve
syms x
f_x=poly2sym(p);
h_new=subs(f_x, x, x_f);        %calulate the calibrated height values
plot(x_f, h_new, '*', x_eval, f, '-');
grid on, xlabel('Fringe Spacing (m)'), ylabel('OIl Height (m)');
hold on;

%calculate error in paralax conversion
```

```
space=5;
ymean=pix_dens*space;
dpixdy=1/space;
dpixdspace=-ymean/(space^2);
e_pixdens=sqrt((dpixdy*e_pixref)^2+(dpixdspace*e_space)^2); %pixel
density error

dxdxp=1/pix_dens;

count=1;

%x-distance error & best fit height error
while (count<=countmax+1)

    dxdpix(count)=-xp(count)/(pix_dens)^2;
    e_x(count)=sqrt((dxdxp*e_xp)^2+(dxdpix(count)*e_pixdens)^2);
%distance error
    e_x1=e_x*1e-3; %convert error to meters
    df_x=diff(f_x);
    e_hnew(count)=subs(df_x, x, x_f(count))*e_x1(count); %error in best
fit height
    count=count+1;

end

e_hnew=e_hnew+e_h; %height error best fit error plus equation error
p_ehnew=e_hnew./h_new*100;

errorbar(x_f, h_new, e_hnew, '*'); %plot error bars on best fit
hold off
filename=[num2str(pos) 'mm' ' Best fit height errors'];
print('-djpeg', filename);

close all
%remove zero values from front of matrices
x_f(:,1)=[];
h_new(:,1)=[];
e_h(:,1)=[];
e_hnew(:,1)=[];

%error in shear force
syms meu_0 h t x
tau=(2*meu_0/((f_x)^2*t))*(int(f_x)); %shear force equation
dtaudmeu=diff(tau, meu_0);
dtaudt=diff(tau, t);
dtaudx=diff(tau, x);
e_t=0.5;

clear count
count=1;

while (count<=countmax)

    tau1(count)=subs(tau, {meu_0, x, t}, {meu, x_f(count), rt});
```

```
e_tau(count)=sqrt((dtaudmeu*e_meu)^2+(dtaudt*e_t)^2+(dtaudx*e_x1(count)
)^2);
    e_tau1(count)=subs(e_tau(count),{meu_0,t,x}, {meu,rt,x_f(count)});

    count=count+1;

end

pe_tau1=e_tau1./tau1*100;
pe_ave=mean(pe_tau1);
close all
errorbar(x_f*1e3, tau1, e_tau1, '*'), grid on;
xlabel ('Distance (mm)'), ylabel('Shear Force (Pa)');
clear filename
filename=[num2str(pos) 'mm Shear Force Errors'];
print('-djpeg', filename);

tau_error=[tau1' e_tau1' pe_tau1'];
clear filename
filename=['error analysis.txt'];
fid=fopen(filename, 'a');
fprintf(fid, 'Shear Force Error');
dlmwrite(filename, pos, '-append', 'roffset', 1, 'delimiter', '\t',
'newline', 'pc');
dlmwrite(filename, tau_error, '-append', 'roffset', 1, 'delimiter',
'\t', 'newline', 'pc');

p_ep1
p_ep2
p_eV1
p_eV2
p_ev
p_erho
p_emeu
p_eh
p_ehnew
pe_tau1

% dlmwrite(filename, tau1, '-append', 'roffset', 1, 'delimiter', '\t',
'newline', 'pc');
% dlmwrite(filename, e_tau1, '-append', 'roffset', 1, 'delimiter',
'\t', 'newline', 'pc');
% dlmwrite(filename, pe_tau1, '-append', 'roffset', 1, 'delimiter',
'\t', 'newline', 'pc');
% dlmwrite(filename, pe_ave, '-append', 'roffset', 1, 'delimiter',
'\t', 'newline', 'pc');

fclose(fid);
```

17 Appendix E

17.1 Initial Measurement Uncertainties

$\Delta\%_W = 0.25\ \%$

$\Delta V_m = 0.1\ ml$

$\Delta\theta = 5^0$

$\Delta LS = 0.25\ mm$

$\Delta x_{pix} = 5\ pixels$

$\Delta PS_{ref} = 2\ pixels$

$\Delta t = 0.5\ s$

Where:

$\Delta\%_W$ – Uncertainty in required mass percentage read from the mixing table

ΔV_m – Uncertainty in syringe oil volume measurement

$\Delta\theta$ - Camera angle uncertainty

ΔLS - Printed line spacing uncertainty in error of parallax conversions

Δx_{pix} – Measured pixel distance uncertainty

ΔPS_{ref} – Reference photograph pixel uncertainty

Δt - Run time uncertainty

17.2 Uncertainties in oil viscosity

Total volume of oil:

$$V = \frac{\%_{W1}}{\rho_1} + \frac{\%_{W2}}{\rho_2}$$

Uncertainty in total volume due to mixing table measurement uncertainty:

$$\Delta V = \sqrt{\left(\frac{\Delta\%_W}{\rho_1}\right)^2 + \left(\frac{\Delta\%_W}{\rho_2}\right)^2}$$

Respective required oil volume percentages:

$$\%_{V1,2} = \frac{\%_{W1,2}}{\rho_{1,2} \cdot V}$$

Respective volume percentage uncertainty:

$$\Delta\%_{V1,2} = \sqrt{\left(\frac{\Delta\%_W}{\rho_{1,2} \cdot V}\right)^2 + \left(\frac{\%_{W1,2} \cdot \Delta V}{\rho_{1,2} \cdot V^2}\right)^2}$$

Required volume of each oil to make 10ml

$$V_{1,2} = 10 \cdot \%_{V1,2}$$

Uncertainty in required volumes

$$\Delta V_{1,2} = \sqrt{\left(10 \cdot \Delta\%_{V1,2}\right)^2 + \Delta V_m{}^2}$$

Final uncertainty of the resultant oil viscosity:

$$\Delta\nu = \sqrt{(V_1 \cdot \nu_1 \cdot \Delta\%_{W1})^2 + (V_2 \cdot \upsilon_2 \cdot \Delta\%_{W2})^2 + (\%_{W1} \cdot \upsilon_1 \cdot \Delta V_1)^2 + (\%_{W2} \cdot \upsilon_2 \cdot \Delta V_2)^2}$$

Final oil density

$$\rho = \rho_1 \cdot \%_{W1} + \rho_2 \cdot \%_{W2}$$

Oil density uncertainty

$$\Delta\rho = \sqrt{(\rho_1 \cdot \Delta\%_W)^2 + (\rho_2 \cdot \Delta\%_W)^2}$$

Dynamic Viscosity:

$$\mu = \upsilon \cdot \rho$$

Dynamic Viscosity Uncertainty:

$$\Delta\mu = \sqrt{(\rho \cdot \Delta\nu)^2 + (\nu \cdot \Delta\rho)^2}$$

17.3 Uncertainty in Oil Height

Oil height equation (Equation 3-8)

$$h = \frac{k\lambda_0}{4} \frac{1}{\sqrt{n_f^2 - n_1^2 \sin^2\theta_i}}$$

Oil height uncertainty:

$$\Delta h = k \cdot \frac{\partial h}{\partial \theta} \cdot \Delta \theta$$

Where:

$$\frac{\partial h}{\partial \theta} = \frac{\lambda \cdot {n_1}^2 \cdot cos\theta \cdot sin\theta}{4 \cdot \left({n_f}^2 - {n_1}^2 sin^2\theta\right)^{\frac{3}{2}}}$$

17.4 Uncertainty in Fringe Spacing

Error of parallax pixel density:

$$\rho_{pix} = \frac{\bar{y}}{LS}$$

Where

$\bar{y}$ - mean pixel distance between lines

LS – physical distance between lines (5mm)

Uncertainty in error of parallax pixel density:

$$\Delta\rho_{pix} = \sqrt{\left(\frac{1}{LS} \cdot \Delta PS_{ref}\right)^2 + \left(-\frac{\bar{y}}{LS^2} \cdot \Delta LS\right)^2}$$

Fringe spacing (in mm):

$$x = \frac{x_{pix}}{\rho_{pix}}$$

Where

x – fringe spacing in mm

x_{pix} – fringe spacing in pixels

Uncertainty in fringe spacing

$$\Delta x = \sqrt{\left(\frac{1}{\rho_{pix}} \cdot \Delta x_{pix}\right)^2 + \left(-\frac{x_{pix}}{{\rho_{pix}}^2} \cdot \Delta\rho_{pix}\right)^2}$$

17.5 Uncertainty in Shear Force

Shear force equation (Equation 3-7)

$$\tau = \frac{2\mu_0}{h^2 t}\int_0^x h\,dx$$

Shear force uncertainty:

$$\Delta\tau = \sqrt{\left(\frac{\partial\tau}{\partial\mu}\cdot\Delta\mu\right)^2 + \left(\frac{\partial\tau}{\partial t}\cdot\Delta t\right)^2 + \left(\frac{\partial\tau}{\partial x}\cdot\Delta x\right)^2 + \left(\frac{\partial\tau}{\partial h}\cdot\Delta h\right)^2}$$

Due to the fact that the equation of fringe spacing vs. oil height (x vs. h) was calculated separately for each test run, a single general solution for the integral cannot be given. Adding to this the fact that the fringe spacing (x) is in turn dependant on the oil viscosity (μ) and run time (t), it becomes very difficult to determine a single expression for the partial differentials present in the uncertainty equation. These partial differentials where therefore calculated using the *diff* function in MATLAB.